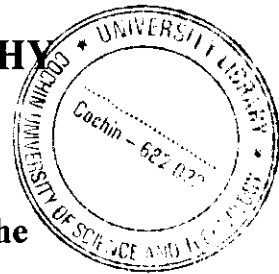


REFERENCE UNI .

G9021

**DEVELOPMENT OF ACTIVE MICROWAVE
IMAGING TECHNIQUES FOR APPLICATIONS
IN MAMMOGRAPHY**



Thesis submitted to the

COCHIN UNIVERSITY OF SCIENCE AND TECHNOLOGY

by

BINDU. G

In partial fulfillment of the requirements for the degree of

DOCTOR OF PHILOSOPHY

under the Faculty of Technology

DEPARTMENT OF ELECTRONICS

COCHIN UNIVERSITY OF SCIENCE AND TECHNOLOGY

KOCHI - 682 022

November 2005

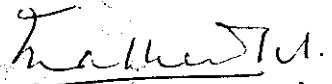
Jan. 2007

CERTIFICATE

This is to certify that the thesis entitled **“Development of active microwave imaging techniques for applications in mammography”** is a bona fide record of the research work carried out by Ms. Bindu. G under my supervision in the Department of Electronics, Cochin University of Science and Technology. The results embodied in this work or parts of it have not been presented for any other degree.

Cochin

23rd ~~November~~ ^{January} 2008



Dr. K.T.Mathew

(Supervising guide)

Professor,

Department of Electronics,
Cochin University of Science and
Technology, Cochin

DECLARATION

I hereby declare that the thesis entitled **“Development of active microwave imaging techniques for applications in mammography”** is based on original work done by me under the supervision of Dr. K.T.Mathew, in the Department of Electronics, Cochin University of Science and Technology and no part of the work has been presented for the award of any other degree.

Cochin

23rd ~~November 2005~~ *January 2007*

Bindu G

Bindu. G

Acknowledgements

I would like to express my deepest sense of gratitude to my research guide, Dr. K.T.Mathew, Professor, Department of Electronics, Cochin University of Science and Technology for his excellent guidance and incessant encouragement. It has been a great pleasure and privilege to work under him. He was always there when I needed help and had even granted me freedom to pursue the research on my line of thought. This remarkable insight has been an illuminating introduction to put together this work.

I am much grateful to Dr. Vasudevan, Professor and Head, Department of Electronics, CUSAT, for the whole hearted support and constant encouragement.

I would like to express my sincere thanks to Prof. K.G.Balakrishnan, former Head, Department of Electronics, CUSAT, for his valuable suggestions and constant support.

I am much indebted and thankful to Dr. C.K.Aanandan, Reader of this department for the timely help, proper guidance and invaluable suggestions. Through out the course of the work he has shown keen interest in the work and has given persistent support.

Sincere thanks are due to Dr. P. Mohanan, Prof.P.R.S.Pillai and Dr. Tessamma Thomas for providing adequate help and fruitful suggestions.

May I express my heart felt indebtedness and gratitude to Dr. Santhosh John Abraham, Department of Surgery, Lourde Hospital, Kochi, for the help and support provided. His active interest in the work and the timely help and advice, helped me to unfurl this research findings into an expression of this volume.

During the period of my research I was financially supported by CSIR, through Senior Research Fellowship. I sincerely acknowledge their help.

Last but not the least, I am grateful to my husband, son and parents for their moral support, loving care and immense patience which gave me the strength to complete this thesis successfully.

Bindu. G

ABSTRACT

Breast cancer is the most common cause of non-skin malignancy in women and a leading cause of female mortality. A potentially important strategy for reducing this menace is the detection at an early stage. However, conventional mammographic detection techniques have many drawbacks and often cause harm to patients. The invention of non-invasive and non-ionizing microwave technique, to reveal the internal structure of biological objects thus became a break through in the field of medical diagnostics. When exposed to microwaves, breast tumor exhibits electrical properties that are significantly different from that of healthy breast tissue and hence false free detection of the tumor in terms of dielectric contrast is possible. An introductory chapter which deals with various imaging techniques, their advantages and disadvantages is given as Chapter 1 of this thesis. The advantages of microwave imaging for breast cancer detection, its classifications and the two approaches of active microwave imaging – microwave tomographic imaging with measured scattered signals and confocal microwave imaging with measured reflected signals are also addressed here.

The variation of dielectric properties of tissues upon exposure to microwaves is the underlying principle of microwave imaging. Hence a good understanding of the behavior of biological tissues when interacted with microwave energy is essential to study the variations of the electrical properties of the tissues. This is explained in Chapter 2 of the thesis. Also the various techniques to study the dielectric properties such as rectangular and coaxial cavity perturbation techniques, their theoretical analysis, and the calibration of the experimental set up for data acquisition are also explained in this chapter.

The design of a single transmitter-receiver combination suitable for both microwave tomographic imaging and confocal microwave imaging is a challenging task in microwave breast imaging. As microwave tomographic imaging is a frequency domain approach, the antenna should exhibit good matching at the desired resonant frequency. More over the antenna should exhibit less edge reflections for better coupling of electro magnetic energy into the tissue and should be compact enough for the ease in system implementation and data acquisition. Time domain confocal microwave technique requires wide band antenna to transmit short transient pulses. The antenna should efficiently focus the microwave signal towards the target and collect the back-scattered energy. A novel coplanar strip line fed bow tie antenna capable of using for both these applications is designed and

developed and is discussed in Chapter 3. An in depth study of the new antenna is performed in terms of radiation characteristics, return loss and bandwidth to assess the feasibility of using the antenna for microwave breast imaging. Theoretical analysis of the antenna is performed using FDTD method and good agreement is observed. The chapter also gives a literature survey of the various antennas that are tried for microwave imaging. The literature review shows that even though microstrip bow tie antennas with coaxial feed have been simulated for microwave imaging, their experimental feasibility is not reported. Also some of these antennas reported erratic response when immersed in water.

Evaluation of the performance of microwave imaging prototypes requires imaging and interpretation of test objects or phantoms. The dielectric properties of the breast equivalent material should yield close match to the actual tissue conditions. In microwave imaging, the object immersed in a coupling medium is subjected to microwave illumination and the reflected / transmitted energy is analyzed to study the dielectric profile of the object. The specific use of suitable coupling medium enhances the coupling of electromagnetic energy to the object as well as increases the resolution. Chapter 4 discusses the development of a single material to be suitable as both phantom and coupling medium in microwave breast imaging. The dielectric parameters of the material are studied in detail and the performance of the antenna when immersed in this medium is also studied. The new material exhibits matching values of dielectric constant with that of the breast tissues with less propagation loss.

Chapter 5 discusses the development of 2-D microwave tomographic images on breast phantoms and breast tissues in the presence of matching coupling medium. Here the object is illuminated by a microwave signal and 2- D images are reconstructed from the collected scattered fields using distorted Born iterative method in terms of dielectric constant. A detailed literature survey of the various algorithms used in microwave tomographic breast imaging is also discussed in the chapter. To the best of our knowledge and belief, ours is the only 2-D microwave tomographic approach that has been tried on an actual breast model in the presence of a matching coupling medium and accurate determination of the presence of tumor is achieved.

Time domain Confocal Microwave Technique implemented on real time breast model to locate the position of the tumor is discussed in Chapter 6. Here the object is illuminated by a microwave signal and the time domain response of the reflected signal is analyzed to locate the tumor. The point of dielectric contrast is represented as a sharp peak in the response. Experimental analysis is substantiated by FDTD method and good

agreement is observed. A detailed literature survey of the various time domain approaches used in microwave breast imaging is also discussed in this chapter.

For the techniques discussed in Chapters 5 and 6, same breast tissue samples are used. Microwave tomographic imaging of the samples provides valuable diagnostic information about the shape and quantitative description of the dielectric constant profile of the object, rather than identifying the location of the tumor. The time domain CMT identifies the presence and location of regions of dielectric contrast of the object rather than completely reconstructing the dielectric property profile. Thus the advantages of two techniques are explored and are put together in this doctoral work for a reliable and assertive detection of breast cancer.

Conclusion and further extension of the work to 3-D analysis is discussed in Chapter 7. Three Appendices are included showing the associated studies performed by the author. They are - microwave tomographic imaging of wax samples, microwave studies of poly vinyl acetate based phantom and details of the driver circuit used for data acquisition.

The thesis concludes with the index, list of publications of the author and a brief resume.

CONTENTS

CHAPTER 1

Introduction	1
1.1 Industrial Scientific and Medical Applications	5
1.1.1 Industrial Applications	6
1.1.2 Scientific Applications	8
1.1.3 Medical Applications	8
1.2 Various Imaging Techniques	10
1.2.1 X – ray	10
1.2.2 Magnetic Resonance Imaging	11
1.2.3 Ultrasound Imaging	11
1.2.4 Optical Imaging	11
1.2.5 Microwave Imaging	12
1.3 Microwave for Breast Cancer Detection	12
1.3.1 Passive Microwave Imaging	13
1.3.2 Hybrid Microwave Imaging	14
1.3.3 Active Microwave Imaging	14
1.3.3.1 Confocal Microwave Technique	14
1.3.3.2 Microwave Tomographic Imaging	15
1.4 Brief Sketch of the Present Study	15
1.5 References	18

CHAPTER 2

Dielectric Behavior of Biological Materials	23
2.1 Introduction	23
2.2 Effects of Microwaves	24
2.3 Dielectric Polarization	24
2.3.1 Polarization by Dipole Alignment	25
2.4 Dielectric Spectrum of Biological Tissues	32
2.5 Dielectric Studies Using Cavity Perturbation Technique	33
2.5.1 Coaxial Cavity Perturbation Technique	34
2.5.2 Rectangular Cavity Perturbation Technique	38
2.6 Experimental Setup and Calibration Procedure	41
2.7 References	45

CHAPTER 3

Design of Antenna for Microwave Breast Imaging 48

3.1 Introduction	48
3.2 Antennas for Medical Applications	49
3.2.1 Waveguide Antennas	49
3.2.2 TEM Waveguide Antenna	49
3.2.3 Ridged Waveguide Antenna	50
3.2.4 Ridged Horn Antenna	51
3.2.5 Microstrip Patch Antenna	52
3.2.6 Monopole and Dipole Antenna	52
3.2.7 Bowtie Antenna	53
3.3 Review of the past Work	53
3.4 Motivation for the Present Work	59
3.5 Design of Coplanar Strip line fed Bowtie Antenna	60
3.6 Theoretical Analysis	64
3.6.1 FDTD Modelling Theory	64
3.6.2 FDTD Problem Definition	67
3.6.3 FDTD Source Excitation and Principal Equations	68
3.6.4 Finite Difference Equations	70
3.6.5 Absorbing Boundary Conditions for the Finite Difference Approximation	72
3.6.6. Calculation of Scattering Parameters	75
3.6.7 Flow Chart of the Algorithm	76
3.6.8 FDTD Design of Bowtie Antenna	76
3.7 Results and Discussions	78
3.8 Conclusion	85
3.9 References	86

CHAPTER 4

Identification of Suitable Phantom and Coupling Medium for Microwave Mammography 90

4.1 Introduction	90
4.2 Review of the Past work	91
4.3 Motivation for the Present Work	98
4.4 Sample Preparation	98

4.5 Experimental Analyses	99
4.6 Conclusion	116
4.7 References	118

CHAPTER 5

Two Dimensional Microwave Tomographic Imaging of Breast Phantoms and Breast tissues 122

5.1 Introduction	122
5.2 Review of the Past Work	123
5.3 Motivation for the Present Work	130
5.4 The Wave Equation	131
5.4.1 Inverse Scattering	134
5.4.2 Non-Linear Inverse Scattering Method	136
5.4.3 Distorted Born Iterative Method	137
5.4.4 Discretization of the integral equation	141
5.4.5 Minimization of Cost (Error) Functional	142
5.4.6 Flow Chart of the Algorithm	145
5.5 Measurement Set Up	146
5.5.1 System Calibration	148
5.5.2 Data Acquisition	148
5.5.3 Measurement Configuration	148
5.5.3.1 Using Breast Phantoms	149
5.5.3.2 Using Breast Tissues	151
5.6 Results and Discussions	153
5.6.1 Comparison of the Results	156
5.7 Conclusion	158
5.8 References	170

CHAPTER 6

Detection of Dielectric Contrast of Breast Phantoms and Breast Tissues Using Confocal Microwave Technique 175

6.1 Introduction	175
6.2 Review of the Past Work	176

6.3 Motivation for the Present Work	180
6.4 Measurement Set Up	180
6.4.1 System Calibration	181
6.4.2 Data Acquisition	182
6.4.3 Measurement Configuration	182
6.4.3.1 Using Breast Phantoms	183
6.4.3.2 Using Breast Tissues	183
6.5 Analyses	184
6.5.1 Experimental Analysis	184
6.5.1.1 Flow Chart of the Algorithm	184
6.5.2 Numerical Analysis	185
6.5.3 FDTD Analysis	185
6.5.3.1 Analytical Model	189
6.5.3.2 Flow Chart of the FDTD Algorithm	190
6.6 Results and Discussions	190
6.6.1 Comparison of the Results	203
6.7 Conclusion	203
6.8 References	204

CHAPTER 7

Conclusion and Further Extension of the Work

7.1 Conclusion	207
7.2 Sources of Error	210
7.3 Future Extensions of the Work	211
7.4 References	213

APPENDIX A

2-D Microwave Tomographic Imaging of Some Biological Objects and Wax Sample	214
------------------------------------------------------------------------------------	-----

APPENDIX B

Microwave Studies of Poly Vinyl Acetate Based Phantom for Applications in Medical Imaging	221
--------------------------------------------------------------------------------------------------	-----

APPENDIX C

Driver Circuit used for the Measurement Setup	229
------------------------------------------------------	-----

INDEX

LIST OF PUBLICATIONS

RESUME

Chapter 1

INTRODUCTION

The science of magnetism began with Pierre de Maricot who, around 1269, identified the north and south poles of a magnet. Later John Mitchell showed that magnetic attraction varied inversely with the square of the distance between magnetic poles. Electricity began with Stephen Gray, but it was Jean-Theophile Desaguliers who showed that there are two types of materials - namely conductors and insulators. The relation between electricity and magnetism became apparent in 1819, when Christian Oersted observed that a magnetic needle oriented itself perpendicular to a wire carrying electric current. Later, in 1895 Andre Marie Ampere created a new science based on the work of Oersted. He elucidated the laws that governed the production of magnetic field by electric current and determined the forces acting between two conductors carrying current. In 1831, Michael Faraday demonstrated the existence of an induced current in a circuit placed in an alternating magnetic field. He also introduced the concept of a dielectric, defined as a medium in which electric induction can take place. The discovery of Maxwell that light, by its very nature, was electromagnetic was the starting point for the evolution of the concept of an electromagnetic spectrum that extends from dc to cosmic rays.

The knowledge of interaction between electron beam and electromagnetic field led to the evolution of microwave electronics. With the development of radar, microwave technology flourished tremendously during World War II. Development of devices that could operate in the UHF / microwave bands with high power became the next target. The outcome of this research was the conventional vacuum tube, which at the time seemed to be the best approach. But this device suffered two major problems - the inter electrode capacitance within the vacuum tube and the longer electron transit time. The inter electrode capacitance effectively shorting at higher frequencies and the longer transit time, restricted its use to lower frequencies.

A solution to the transit time problem was proposed in 1920 by German scientists H.Barkhausen and K.Kurz. Their solution was the Barhausen - Kurz oscillator, a special type of vacuum tube that generated high frequency signals. Another solution to these problems was proposed in 1921 by A.W. Hull, who used a magnetic field to influence the flow of electrons. His design was the original magnetron and modifications of his design are still in use today.

The power versus frequency dilemma remained unsolvable for many years. In the mid 1930s, a solution to this problem was proposed by Dr. W.W. Hansen and Dr. A. Heil when they turned the electron transit time into advantage with a mechanism called velocity modulation. Then in 1937, Varian brothers extended Dr. Hansen's work into the development of the klystron vacuum tube. It could be used either as an oscillator or as a power amplifier. With the production of these vacuum tubes, radar finally became a commercial, albeit a military success at microwave frequencies.

Also, this marked the opening of frequencies in the Giga Hertz range to communication engineers.

Military developments in the decades that followed continued to be in radar, while use of microwaves in the commercial sector was limited primarily to telephone companies. By 1960s, microwave communications had replaced 40 % of the telephone circuits. Microwave field became vitally important as man reached out to space. The consumer market saw an explosion in the early 1980s with the television broadcast service to the home of satellite TV transmissions. The 1990s saw a continuous evolution of microwave developments particularly in consumer market place.

Microwave frequencies occupy three decades of electromagnetic spectrum (300 MHz to 300 GHz) that lie between VHF radio waves and far infrared. The broad classification of the electromagnetic spectrum is summarized in Table 1.1.

Table 1.1 Broad classification of electromagnetic spectrum

Region	Frequencies
Audio Frequencies	30 – 30 x 10 ³ Hz
Radio Frequencies	30 x 10 ³ Hz – 3 x 10 ¹¹ Hz
Infrared	3 x 10 ¹¹ – 4.1 x 10 ¹⁴ Hz.
Visible	4.1 x 10 ¹⁴ – 7.5 x 10 ¹⁴ Hz
Ultraviolet	7.5 x 10 ¹⁴ - 10 ¹⁸ Hz
X- rays	> 10 ¹⁷ Hz
γ- rays	> 10 ²⁰ Hz
Cosmic rays	> 10 ²¹ Hz

Traditionally microwave domain is sub divided into bands which arises from physiological factors like modes of production and the specific properties of radiation. The division of electromagnetic bands is designated in Table 1.2.

Designation	Frequency range in Giga Hertz
HF	0.003 – 0.030
VHF	0.030 – 0.300
UHF	0.300 – 1.0
L band	1.0 – 2.0
S band	2.0 – 4.0
C band	4.0 – 8.0
X band	8.0 – 12.0
Ku band	12.0 – 18.0
K band	18.0 - 27.0
Ka band	27.0 – 40.0
Millimeter	40.0 – 300.0
Sub millimeter	> 300.0

Table 1.2. Various bands in the microwave domain

Microwave radiation obeys the laws of electromagnetism. Electromagnetic wave is a propagation phenomenon which requires no material support but only involves electric and magnetic fields, each of which is a function of time. Wavelengths at microwave frequencies are of the same order of magnitude as the dimensions of the circuit devices, and the time of propagation of electrical effects from one part of the circuit to the other is comparable to the period of oscillating currents and charges. Hence conventional circuit concepts of currents and voltages are replaced by field concepts.

Applications of microwaves can be mainly classified into two domains: information and power. Information domain deals with applications in the field of radar and communications. Power domain includes industrial, scientific and medical (ISM) applications. A chart of microwave applications is shown in Figure 1.1.

1.1 Industrial Scientific and Medical Applications

Microwaves do not provide universal solution to all the problems, but should be considered whenever all other processes fail to solve an industrial problem, in which case the advantages of microwaves become unique.

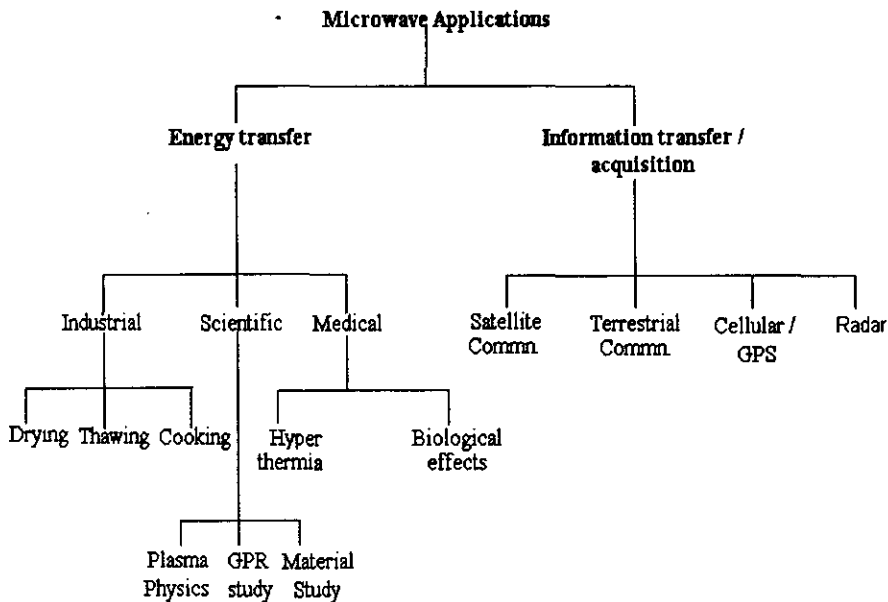


Figure 1.1 Classification chart of the applications of microwaves

Some of the advantages of microwaves are

- Speed of heating, better efficiency, savings in space and man power
- Ease of operation, instantaneous on and off operations.
- Ease of adaptation to existing on – line operations, possible combination with other thermal processes.
 - No energy loss by radiation, improved efficiency and working conditions, possibility of eliminating the need for temperature control of the environment

- Better thermal efficiency compared with traditional processes and improved quality.

The frequencies employed for these applications are 434, 915 and 2450 MHz and are called the Industrial Scientific and Medical Applications (ISM) band.

1.1.1 Industrial Applications

Many industrial processes involve one or more stages of product drying, which is often very expensive. Microwaves offer the most viable alternative in terms of energy efficiency. Microwave is used for drying humid materials, which occur in physiochemical forms (e.g., pastes, colloids, suspensions and porous solids containing absorbed liquid) [1]. In printing industry, for superior and well- defined quality results, microwave heating is adopted as it involves no risk of darkening or cracking of paper and no need of high temperature protection [2, 3]. Microwaves can also help in the drying of paper coatings that consist of a very thin layer of mineral particulate. Microwave drying tests on binding agents have demonstrated improved drying efficiency and better coating cohesion [4]. In leather industry microwave is used for the treatment of leather in steam heated dryer under vacuum as it results in high, uniform distribution of humidity thereby avoiding over drying and re-humidification [5]. Microwave drying is employed in textile industry for the treatment of tufts and yarns, and for dyeing and finishing [6]. Microwave is used for the processing of cardboard and paper bags, plywood, plaster, concrete and ceramics, photographic films and magnetic tapes [1]. Microwave treatment of wood avoids the creation of internal strains, ensures uniformity and controls insect attacks [7]. Microwave drying is recommended for drying polymers as it produces no changes in the molecular weights and hence no

damage to the product [8]. Microwaves find application in pharmaceutical industry for the drying of granules [1]. The use of microwave for vulcanization of rubber provides excellent results in terms of efficiency, reliability and adaptability to industrial environment [9, 10]. Microwaves are widely used to reticulate thermosetting resins and to polymerize plastic materials [1]. Large scale industrial applications of microwaves include de-waxing casting moulds [11], pyrolyzation of shale oil [12], gasification of coal [13], liquefaction of heavy oil prior to pumping [14], hardening of foundry mouldings [11], fast setting of concrete [15] and sintering of ferrites and ceramics [16]. In nuclear waste treatment, microwaves are being used to solidify droplets of radioactive wastes [17]. The contribution of microwaves in food industry includes cooking poultry, bacon, meat loaves, preparation of sprats, frying of fritters and doughnuts, baking of bread and reheating of prepared meals. Microwave cooking is superior in terms of speed, hygiene, nutrition and in sensory perception [18, 19]. Another successful application of microwaves in food industry lies in thawing and tempering [20, 21]. Microwaves can be used for food preservation by performing enzymatic inactivation, sterilization and pasteurization [22 - 24]. It can also be used for germination of dormant grains, disinfestations of stored cereals and in the making of wine [1].

Applications of microwaves in industry are attributed to the fact that microwave technology offers dust free operation, uniform drying, no accidental burns, no water pockets, energy saving, no environmental heating and prevention of over drying. The use of microwaves in industry has led to 50% improvement in productivity. More over the flexibility of the technique, precision and control, and the ease with which the whole

installation can be supervised, make microwave technology an attractive option for industrial applications than the conventional methods.

1.1.2 Scientific applications

Microwave is successfully used to determine basic semiconductor parameters such as resistivity [25], mobility of charge carriers [26], plasma density measurement [27], atmospheric absorption measurements [28] and ground penetrating radar studies [29]. It is also used as alternating voltage to accelerate electrons in linear accelerator, cyclotron [30], and synchrotron [31].

Material characterization [32-34] is another important scientific application of microwaves. The dielectric parameters over a wide range of temperatures on low loss dielectrics are needed to assess their suitability for use in telecommunications, dielectric waveguides, lenses, radomes, dielectric resonators and microwave integrated circuit substrates. Knowledge of the dielectric properties of biological materials is needed to estimate the electrical response of these materials when exposed to microwaves and is thus important in the development of phantoms and coupling media for biomedical applications.

A part of this thesis deals with the identification of suitable materials to be used as phantoms and coupling media for microwave breast imaging.

1.1.3. Medical applications

Microwave technology makes important contributions to both therapeutic and diagnostic medicine. A number of medical devices that use microwaves are in clinical use today [35, 36]. All these devices depend on the ability of microwaves to deeply penetrate into living tissues. The depth to which microwaves can penetrate tissues is primarily a function of the

dielectric property of the tissues and of the frequency of the microwaves. When microwaves penetrate into the tissues, they give up energy to the tissues. Thus, microwaves can be used to non-invasively produce hyperthermia, particularly in cutaneous and subcutaneous cancer sites, and in sites that are accessible via natural openings of the body [37]. This most promising therapeutic medical application of microwave seems to have no side effects and continues to be effective as the body does not get accustomed to it. Also it produces minimum discomfort for the patients. As the energy of photons in the microwave region is small, harmful ionization effects are avoided. The results are remarkable when microwave technology is combined with radiotherapy and chemotherapy. Microwave hyperthermia is also effective in relieving neurologic or arthritic pain [38] and for the treatment of prostate cancer [39]. Microwaves can be used for rapid re-warming after accidental hyperthermia or heart surgery. It is reported that high power microwave pulses can enhance the ability of certain chemotherapeutic agents to enter malignant cells. Since microwave pulses, unlike dc pulses, can non-invasively deeply penetrate the tissues, poration with microwave pulses offers the possibility of non-invasively treating more deep - seated malignancies than is possible with dc pulses [37]. Microwaves also find application in diathermy for mild orthopedic heating [40], microwave ablation [41], microwave assisted balloon angioplasty [42]. It is reported that microwaves are effective in tissue healing and rapid fixation of brain cells [37].

Microwave imaging is another new technology which has potential applications in the field of diagnostic medicine [43]. The basic motivation for this is improved physiologic and pathophysiologic correlation, especially in soft tissues. This expectation is based on the molecular

(dielectric) rather than atomic (density) based interactions of the radiation with the target when compared with X-ray imagery [44]. Due to the improved dielectric contrast, better tissue characterization too is possible. Microwaves can be used effectively for the detection of biological anomalies like tumor at an early curable stage itself.

1.2 Various Imaging techniques

Imaging an object, invisible to naked eyes, is an important quest of scientists. All systems for internal body imaging are based on the differentiation of tissue properties. The various imaging techniques are given below.

1.2.1 X-ray

The standard method of imaging human body is X-ray tomography. An X-ray picture is a shadow cast on a photographic film by denser media that are more opaque to X-rays compared with less dense media. Developing three dimensional pictures out of a series of shadows cast by X-rays is called as X-ray tomography which later developed as Computer – Aided Tomography. In X-ray tomography, a tissue is differentiated based on density. However in most cases, tissue density does not depend on tissue physiological state. Important tissue characteristics such as temperature, blood content, blood oxygenation and ischemia cannot be differentiated by X-ray tomography. For soft tissues like human breast, X-ray cannot image the breast anomalies, as there is no significant variation in density between normal and malignant breast tissues, and has proven to be insensitive to the presence of lesions in the breast. Many a times X- ray reported high false positive rates and high false negative rates [45, 46].

1.2.2 Magnetic Resonance Imaging (MRI)

MRI makes use of the fact that spin echoes of protons have different resonant frequencies depending on the ambient static magnetic field [47]. The body is immersed in a static magnetic field that has a linear gradient in a three dimensional space. The stronger the magnetic field the higher will be the resonant frequency of the proton spin and louder will be the gradient noise. Even though MRI is a non-ionizing technique, it has many disadvantages. MRI cannot be used for patients having implants, and is claustrophobic. The MRI machine makes tremendous amount of noise, which creates fear in patients. Also, patient should lie still for a long duration of time. Even a slight movement of the part being scanned can cause much distorted images.

1.2.3 Ultrasound imaging

Ultrasound is widely used as it is non-hazardous and can outline some organs which are not successfully imaged by X-rays. Ultrasound images are functions of the propagation velocity of sound waves in the medium. The ultrasound waves diffract around objects instead of travelling in straight lines [48]. Also, multiple scattering effects take place when these waves enter an object. In ultrasound imaging, the effects of diffraction and multiple scattering are not taken into account for image reconstruction and hence image distortion arises.

1.2.4 Optical imaging

Infrared signals have shorter wavelengths than microwaves and therefore have less penetration power. This limits the application of optical imaging to non-invasively image internal body parts [49]. Microwaves have wavelengths of the order of centimeters and so is its penetration strength.

Also, biological tissues are more translucent to microwaves than to infrared signals [49].

1.2.5 Microwave imaging

Microwave images are maps of the electrical property distributions in the body [43]. The electrical properties of various tissues may be related to their physiological state. Cancer detection with microwave imaging is based on this contrast of electrical properties. Tissue dielectric properties in the microwave region depend upon molecular constituents, ion concentration, mobility, concentration of free water & bound water and tissue temperature [50].

The motivation for developing a microwave imaging technique for detecting breast cancer is the significant contrast in dielectric properties of normal and malignant breast tissues at microwave frequencies [51, 52]. Further more microwave attenuation in normal breast tissue is low enough to make signal propagation feasible even through large breast volumes. In addition microwave technology is non-invasive, non-ionizing and eliminates uncomfortable breast compression. The small size and physical accessibility of the breast compared to other internal organs is also an added advantage.

As application of microwave imaging for breast cancer detection is the research area of this thesis, the technique is discussed in detail below.

1.3. Microwaves for Breast Cancer Detection

“Early detection is the best protection” is the philosophy that drives breast cancer screening programs. An integral component of these programs is X-ray mammography which is X-ray imaging of compressed breast. However the X-ray mammography suffers many limitations like, missing of 15% of breast cancer, difficulty in imaging women with dense breasts and

production of in-conclusive results [45, 46]. Diagnosis often involves waiting for further imaging or biopsies. These limitations of X-ray mammography provide clear motivation for the development of a complementary breast imaging tool to assist in detection and diagnosis. An ideal breast screening tool should have low health risk, be sensitive to tumors, detect breast cancer at a curable stage, be non-invasive and simple to perform, be cost effective and widely available, involve minimum discomfort, and provide easy to interpret and consistent results [51,52].

For reliable detection of small malignant tumors, a significant and consistent contrast between malignant and normal breast tissues is required. At microwave frequencies the sensitivity, specificity and the ability to detect small tumors is the dielectric contrast between normal and malignant breast tissues. Malignant breast tissues exhibit considerable increase in bound water content compared to the normal tissues and hence a high value of dielectric constant [50].

There are three methods of microwave breast imaging. They are passive, hybrid and active approaches.

1.3.1 Passive Microwave Imaging

The principle of operation relies on increased tumor temperature compared with healthy breast tissues, when exposed to microwaves. This method incorporates radiometers to measure temperature differences in the breast. Images display the temperature measured over a quadrant of the breast [53]. For diagnosis, images of the suspicious lesion and that of the corresponding area of the other breast are compared. Clinical results obtained with the French system ONCOSCAN suggest that microwave radiometry has the potential to assist in the diagnosis of suspicious areas on X-ray mammograms.

1.3.2 Hybrid Microwave Imaging

Hybrid approach, specifically microwave induced acoustic imaging uses microwaves to illuminate the breast. Due to higher conductivity of malignant breast tissue, more energy is deposited in tumors resulting in selective heating of these lesions. The tumors expand and generate pressure waves, which are detected by ultrasound transducers. Two methods of image reconstruction have been proposed, namely computed thermo-acoustic tomography (CTT) [54] and scanning thermo-acoustic tomography (STT) [55]. In CTT, the breast is placed in a water bath and illuminated at 434 MHz with a wave guide. Pulses of $0.5\mu\text{s}$ are used to generate ultrasound waves in the medical region. Ultrasound transducers are arranged on a bowl, and data is recorded as this bowl rotates through 360° . Image reconstruction uses filtered back propagation algorithms adapted from X-ray computed tomography. With STT approach, image reconstruction is simplified by employing focused transducers to record ultrasound waves. Here the object is illuminated by short duration pulses from a wave guide antenna. Ultrasound transducers record the signals transmitted through the object. The sample is scanned along the axis perpendicular to the transducer, time domain signals are recorded at a number of locations and the collection of signals is displayed as an image. By using focused transducer, this approach avoids complex image reconstruction algorithms.

1.3.3 Active Microwave Imaging

Two classifications of active microwave imaging are discussed here.

1.3.3.1 Confocal Microwave Technique

Confocal Microwave Technique (CMT) uses backscatter methods to infer the locations of significant microwave scatterers [56, 57]. The breast is

illuminated with a wide band pulse from a number of antenna locations and the same antenna collects the backscattered signals. The relative arrival times and amplitudes of the backscattered signal provide information to determine the scatterer location. This approach only identifies the presence and location of strong scatterers in the breast rather than completely reconstructing the dielectric properties profile.

1.3.3.2 Microwave Tomographic Imaging

Microwave tomographic imaging poses an inverse scattering problem where the breast is illuminated by a microwave transmitter, and scattered fields are measured at numerous locations [58, 59]. The shape of the object and spatial distribution of the complex permittivity are obtained from the transmitted and the collected scattered fields. Due to the relationship between the object dimensions, discontinuity, separation and contrast in properties of inhomogeneities compared to wavelength, the wave undergoes multiple scattering within the object. This results in a non-linear relationship between the measured scattered fields and the object function. In general, inverse scattering approach (especially for whole body imaging) suffers from non-uniqueness and multiple wrappings of the scattered field phases. However with smaller geometries, as in the case of breast imaging, these concerns are minimal.

1.4 Brief sketch of the present study

Development of active microwave imaging techniques for detection of breast cancer is presented in this thesis.

The thesis is organized in different chapters as given below.

Chapter 2 explains in brief the dielectric behavior of biological materials and the dielectric spectrum of biological tissues. Various polarization effects are discussed. Cavity perturbation techniques used for the measurement of dielectric parameters are also mentioned.

Chapter 3 gives the design of coplanar strip line fed bowtie antenna for microwave imaging, and optimization of the antenna dimensions. Experimental studies on the radiation characteristics of the antenna are discussed. Theoretical validation of the experimental observation is performed using finite difference time domain analysis.

Chapter 4 discusses the development of suitable phantoms and coupling media for microwave breast imaging. The dielectric constant and conductivity studies of the materials in different concentrations are performed using cavity perturbation technique. The results are compared with the available literature data on normal and malignant breast tissues. The performance of the antenna when immersed in the coupling medium is also studied.

Chapter 5 deals with two dimensional microwave tomographic imaging technique. Both breast phantoms and breast tissues are subjected to the study. Two dimensional images are reconstructed from the experimentally collected scattered fields using distorted Born iterative method and profiles of their dielectric constants are studied.

Chapter 6 deals with the confocal microwave technique for the detection of biological anomalies, using breast phantoms and breast tissues.

Experimentally collected backscattered waveforms are analyzed in the time domain and regions of dielectric contrast are determined. Experimental results are substantiated by finite difference time domain analysis.

The conclusions drawn from the studies and further extensions of the work are discussed in Chapter 7.

Related research works carried out by the author during this period are included in Appendices A & B.

Appendix A deals with 2-D microwave tomographic imaging of biological objects like calf femur, chicken thigh and wood sample, and wax cylinder with water inclusion.

Appendix B deals with the dielectric studies of mixture of carbon black powder, graphite powder and polyvinyl acetate based adhesive in definite proportions. The feasibility of using this material as phantom for low water content biological tissues and as absorbing material for microwave tomographic imaging is analyzed.

In **Appendix C**, the details of the driver circuit used to activate the stepper motor of the experimental set up for data acquisition is discussed.

1.5. References

1. Jacques Thurey, "Microwaves: Industrial Scientific and Medical Applications", Artech House, Inc., Norwood, MA 02062, 1992.
2. Roussy G, Thiebaut J, Charreyreneel M, Watelle G, "A chemical – physical model describing microwave paper drying", Journal of microwave power, vol. 19, pp. 243 – 250, 1984.
3. Moore D, "The rapid drying of print by microwave energy", Journal of Microwave Power, vol.3, pp. 158 – 165, 1968.
4. Goerz D, Jolly J, "The economic advantages of microwave energy in the paper industry", Journal of Microwave Power, vol.2, pp. 87 – 94, 1967.
5. "Microwave conditioning of leather", Case History, The Electricity Council, EC 3608 / 12/ 76. 1976.
6. Chabert J, Viallier P, Meisel N, "Microwave drying of untwisted roving sand yarns in the textile industry", Proceedings of the IMPI Symposium, Toronto, pp. 61 – 63, 1981.
7. Lofdahl C, "Microwave veneer redrying: a general report", Cryodry Corp. 4, pp. 45 – 50, 1968,
8. Vasilakos N, Magalhaes F, "Microwave during of polymers", Journal of Microwave Power, vol. 19, pp. 135 – 144, 1984.
9. Luypaert P, Reusens P, "A new microwave applicator for continuous vulcanization", Journal of Microwave Power, vol. 21, pp. 75 - 78, 1986.
10. Fix S, "Microwave devulcanization of rubber", Elastomers, vol.112, pp. 38 40, 1980.
11. Hulls P, "Development of the industrial use of dielectric heating in United Kingdom", Journal of Microwave Power, vol.17, pp. 29 - 38, 1982.
12. Briggs W, Lewis J, Tranquilla J, "Dielectric properties of new Brunswick oil shale", Journal of Microwave Power, vol.18, pp. 37 – 43, 1983.
13. Balanis C, "Electromagnetic techniques in the development of coal-derived energy sources – a review", Journal of Microwave Power, vol.18, pp.45 - 54, 1983
14. Gill H, "The electrothermic system for enhancing oil recovery", Journal of Microwave Power, vol. 18, pp. 107 - 110, 1983.
15. Tereschenko A, Kononov A, Kontar A, "On the application of microwave energy for acceleration of concrete hardening", Proceedings of IMPI – CFE, Monoca, pp. 136 – 140, 1979.

16. Kimrey H, White T, Bigelow T, Becher P, “ Initial results of a high power microwave sintering experiment at ORNL”, *Journal of Microwave Power*, vol.21 , pp. 81 – 82, 1986
17. Bonek E, Knotik K, Leichter P, Magerel G, Rohrecker L, “Microwave hardening of free-falling radioactive droplets”, *Proceedings of 12th European Microwave Conference, Helsinki*, pp. 610 – 614, 1982.
18. Ohlsson T, “Fundamentals of microwave cooking”, *Microwave World*, vol. 4, pp. 4 – 9, 1983.
19. Ohlsson T, Astrom A, “Sensory and nutritional quality in microwave cooking”, *Microwave World*, vol.3, pp. 15 –16, 1982.
20. Bialod D, Jolion M, Le Goff R, “Microwave thawing of food products using associated surface cooling”, *Journal of Microwave Power*, vol.13, pp. 269 - 1978.
21. Bezanson A, Edgar R, “Microwave tempering in the food processing industry”, *Electromagnetic Progress*, vol.18, pp. 8 – 12, 1976.
22. Aref M, Noel J, miller H, “Inactivation of alpha-amylase in wheat flour with microwaves”, *Journal of Microwave Power*, vol.7, pp. 215 -221, 1972
23. Ayoub J, Berkowitz D, Kenyon E, Wadsworth C, “Continuous microwave sterilization of meat in flexible pouches”, *journal of Food Science*, vol.39, pp.309 – 313, 1974.
24. Bengtsson N, Green W, del Valle F, “Radio frequency pasteurization of cured hams”, *Journal of Food Science*, vol. 35, pp. 681 – 687, 1974.
25. Liu J.H, Lin Y.C, Lue J.T and Wu C.J, “Resistivity measurements of layered metallic films at various microwave frequencies and temperatures using the micro-strip T-junction method”, *Measurement Science and Technology*, vol. 13, pp. 1132-1137, 2002
26. Warman J.M, Gelinck G.H and de Haas M.P, “The mobility and relaxation kinetics of charge carriers in molecular materials studied by means of pulse-radiolysis time-resolved microwave conductivity: dialkoxy-substituted phenylene-vinylene polymers”, *Journal of Physics: Condensed Matter*, vol. 14, pp. 9935-9954, 2002.
27. Bora D, Jayakumar R and Vijayashankar M.K, “A simple microwave technique for plasma density measurement using frequency modulation”, *Plasma Physics and Controlled Fusion*, vol. 26, pp. 853-857, 1984.
28. Dicke R.H, Beringer R, Kyhl R. L, Vane A.B, “ Atmospheric absorption measurements with a microwave radiometer”, *Physical Review*, vol.70, pp. 340-348, 1946.
29. Daniels D.J, “Surface Penetrating Radar”, the Institution of Electrical Engineers, London, 1996.

30. Pan W, Lai K, Bayrakci S.P, Ong N.D, Tsui D.C, "Cyclotron resonance at microwave frequencies in two-dimensional hole system in AlGaAs / GaAs quantum wells", Applied Physics Letters, vol. 83, pp. 3519 – 3521, 2003.
31. Kramer S.L, Podobedev B, "Coherent microwave synchrotron radiation in VUV ring", Proceedings of Accelerator Conference NIM A463, pp.387 – 389, 2001.
32. Murthy V.R.K, Sundaram S, Viswanathan B (Editors), "Microwave Materials", Vh. 2, Narosa Publishing House, 1993.
33. Afsar M.N, James R.B, Clarke R.N, "The measurement of the properties of materials", Proc.of IEEE, vol.74, pp. 183 – 199, Jan. 1986.
34. Polk C, Postov E, "CRC Handbook of Biological Effects of Electromagnetic Fields", CRC Press, Second Edition, 1995.
35. Rosen A, Rosen H.D, "New Frontiers in Medical Device Technology", Wiley, New York, 1995.
36. "Mini special issue of RF/Microwave applications in Medicine", IEEE Transactions on Microwave Theory and Techniques, vol.48, Nov. 2000.
37. Fred Sterzer, "Microwave medical devices", IEEE Microwave Magazine, vol. 3, 2002.
38. Dahl. O, Dalene R, Schem B.C, Mella .O, "Status of clinical hyperthermia", Acta Oncologica, vol.38, pp. 863 – 873, 1999.
39. Barlow O.W, "Epidemiology of prostate cancer" in Comprehensive textbook of genitourinary oncology, N.J Vogelzang, Eds. Philadelphia, PA:Lippincot, William & Wilkins, pp. 534 – 544, 2000.
40. Kantor G, "Evolution and survey of microwave and radio frequency applicators", Journal of Microwave Power, vol. 1.16, pp. 136 – 150, 1981.
41. Labonte S, Ali H, Roy L, "Monopoles for microwave catheter ablation of heart tissue", IEEE MTT Symposium Digest, pp. 303 – 306, 1995.
42. Liu P, Rappaport C, "Microwave assisted balloon angioplasty", IEEE Transactions on Microwave Theory and Techniques, vol. 44, pp. 1819 - 1831, 1996.
43. Larsen E.L, Jacobi J.H, "Medical Applications of Microwave Imaging", IEEE Press, The institute of Electrical and Electronic Engineers, Inc., New York, 1985.
44. Fear E C, Paul M Meaney, Maria A Stuchly " Microwaves for breast cancer detection?", IEEE Potentials, vol. 22 pp. 12 - 18, 2003.
45. Huynh P.T, Jarolimek A.M, Dayee S, "The false-negative mammogram", Radiographics, vol.18, pp. 1137 – 1154, 1998.

46. Elmore J.G, Barton M.B, Mocerri V.M, Polk S, Arena P.J, Fletcher S.W, "Ten year risk of false positive screening mammography and clinical breast examinations", *New England Journal of Medicine*, vol.338, pp. 1089 – 1096, 1998.
47. Lauterber P.C, "Medical imaging by nuclear magnetic resonance zeugmatography", *IEEE Transactions on Nuclear Science*, vol. 27, pp.2808 – 2811, 1973.
48. Lee H, Wade G, "Modern Acoustic Imaging", *IEEE Press*, New York, 1986.
49. McBride T.O, Pogue B.W, Shudong-Jiang, Osterberg U.L, Paulsen K.D, and. Poplack S.P, "Initial studies of *in vivo* absorbing and scattering heterogeneity in near-infrared tomographic breast imaging", *Optical Letters*, vol.26, pp. 822-824,2001.
50. Semenov S.Y, Svenson R.H,Souvorov A.E, Borisov V.Y, Sizov, Starostin V.N, Dezern K.R, Tatsis G.P, Baranov V.Y, "Microwave tomography: two-dimensional system for biological imaging", *IEEE Transactions on Biomedical Engineering*, vol. 43 , pp. 869 – 877, 1996.
51. Fear E.C, Stuchly M.A, "Microwave detection of breast cancer", *IEEE Transactions on Microwave Theory and Techniques*, vol. 48, pp. 1854 – 1863, 2000
52. Fear E.C,. Hagness S.C, Meaney P.M, Okoniewski M, Stuchly M.A, "Enhancing breast tumor detection with near field imaging", *IEEE Microwave magazine*, vol. 3, pp. 48 – 56, March 2002.
53. Bocquet B, van de Velde J.C, Mamouni A, Leroy Y, "Microwave radiometric imaging at 3 GHz for the exploration of breast tumors", *IEEE Transactions on Microwave Thoery and Techniques*, vol.38, pp. 791 – 791, June 1990.
54. Kruger R.A, Kopecky K.K, Aisen A.M, Reinecke, "Thermoacoustic CT with radio waves: A medical imaging paradigm", *Radiology*, vol.211, pp. 275 – 278, 1999.
55. Ku G, Wang M.W, "Scanning thermoacoustic tomography in biological tissue", *Medical Physics*, vol.27, pp. 1195 – 1202, 2000.
56. Hagness S.C, Taflove A, Brdiges J.E, "Three-Dimensional FDTD analysis of a pulsed microwave confocal system for breast cancer detection: design of an antenna-array element", *IEEE Transactions of Antennas and Propagation*, vol.47, pp.783 – 791, May 1999.
57. Hagness S.C, Taflove A, Brdiges J.E, " Two-Dimensional FDTD analysis of a pulsed microwave confocal system for breast cancer detection: fixed focus and antenna array sensors" , *IEEE Transactions of Biomedical Engineering*, vol.45, pp.1470 -1479, Dec.1998

58. Meaney P.M, Fanning M.W, Dun Li, Poplack S.P, Paulsen K.D, “ A clinical prototype of active microwave imaging of the breast”, IEEE Transactions on Microwave Theory and Techniques, vol. 48, pp. 1841 – 1853, Nov. 2000.
59. Bulyshev A.E, Semenov S.Y, Souvorov A.E, Svenson R.H, Nazarov A.G, Sizov Y.E, Tatsis G.P, “ Computational modeling of three-dimensional microwave tomography of breast cancer”, IEEE Transactions on Biomedical Engineering, vol. 48, pp. 1053 – 1056, Sept. 2001.

Chapter 2

DIELECTRIC BEHAVIOR OF BIOLOGICAL MATERIALS

2.1 Introduction

Electrical properties of a material are a measure of its ability to interact with electromagnetic energy. As this interaction results from the presence of components within the material that can be affected by the electric and magnetic forces generated by the electromagnetic (EM) fields, a material's electrical properties are a direct consequence of its composition and structure.

In non-magnetic materials such as biological tissues, an EM field primarily acts upon components within the material that possess a net electric charge and / or an electric dipole moment. Polar molecules are the main source of electric dipole moments in tissues. Protein structures, muscle, fat etc. are the additional sources. Due to the fact that the electrical properties of a tissue are determined by such a wide variety of components, as reflected in different dielectric dispersions, these properties exhibit significant variations as functions of parameters such as frequency, tissue type and vascularization. In turn, these variations in tissue electrical properties can serve as a measure of different physiological conditions.

When an object is exposed to microwaves, the release of heat is so instantaneous, that thermal phenomena of conduction, convection and radiation play only a secondary role in temperature equilibrium. The object is polarized, and dipolar rotation accompanied by intermolecular friction and hysteresis takes place [1, 2].

2.2 Effects of microwaves on dielectrics

Microwaves propagate in uniform dielectrics according to the relation,

$$E = E_0 e^{-\gamma z} \quad (2.1)$$

where E is the scalar instantaneous electric field in the dielectric at a distance z from the origin, E_0 is the electric field at the origin, and γ is the complex propagation constant [3-5]. The complex propagation constant is defined as

$$\gamma = \sqrt{(\sigma + j\omega\epsilon)j\omega\mu} \quad (2.2)$$

For perfect dielectrics, conductivity $\sigma = 0$, and hence eqn 2.2 will reduce to

$$\gamma = j\omega\sqrt{\mu\epsilon} \quad (2.3)$$

where ω represents the angular frequency, μ the magnetic (complex permeability) and ϵ the dielectric (complex permittivity) property of the medium. For perfect dielectrics, the magnetic properties are assumed to be those of free space, i.e. purely real with no attenuation or phase shift.

2.3 Dielectric polarization

The common feature of dielectric materials is their ability to store electromagnetic energy. This is accompanied by the displacement of positive and negative charges under the influence of the applied electric fields, against the force of atomic and molecular attraction [5]. The mechanism of charge displacement (polarization) depends on the type of dielectric material and the frequency of the applied field. The electric

equilibrium is disturbed because the applied field causes spatial separation of charges of opposite signs.

Space charge polarization occurs at low-frequency ranges such as VLF and LF bands. It occurs when the material contains free electrons whose displacements are restricted by obstacles such as boundaries. When an electric field is applied, the electrons accumulate on the obstacle, and the resulting charge separation polarizes the material. Entire regions of the material become either positive or negative.

Polarization by dipole alignment occurs at higher frequencies of the HF band and microwave region, at the molecular level. Dielectric heating takes place due to this phenomenon.

Ionic polarization takes place at infrared frequencies due to the separation of positive and negative ions in the molecule.

Electronic polarization occurs at very high frequencies close the ultraviolet region. The negative electronic cloud surrounding the positive nucleus is displaced in the direction of the applied field.

As polarization by dipole alignment is the phenomenon that occurs at microwave frequencies, it is discussed in detail below.

2.3.1. Polarization by dipole alignment

In a polar dielectric, the constituent molecules are neutral, but the centers of positive (+q) and negative (-q) do not geometrically coincide. This asymmetry is responsible for a permanent dipole moment given by

$$\vec{p} = q\vec{l} \quad (2.4)$$

where \vec{l} is the relative position vector of the positive and negative charges as shown in Figure 2.1

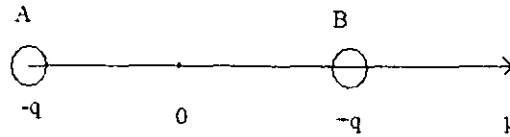


Figure 2.1 Molecular dipole moment

Non-polar molecules do not have a permanent dipole moment, but may acquire an induced moment by the molecular deformation in an applied electric field. The polarizability α' is a measure of the dipole moment induced by a unit field. In other words,

$$\vec{p} = \alpha' \vec{E}_{loc} \quad (2.5)$$

where \vec{E}_{loc} is the local field near the molecule. At the macroscopic level, alignment by the field is opposed by thermal agitation. A statistical equilibrium is then established in which, at a given temperature and in a given field, the number of aligned molecules per unit volume N remains constant. The total dipole moment is characterized by the polarization \vec{P} as [5],

$$\vec{P} = N\alpha' \vec{E}_{loc} \quad (2.6)$$

or in function of the applied field as,

$$\vec{P} = \chi E \quad (2.7)$$

In free space, the relation ship between induction and applied electric field \vec{E} is given by

$$\vec{D} = \epsilon_0 \vec{E} \quad (2.8)$$

and in a dielectric it becomes,

$$\vec{D} = \epsilon_0 \vec{E} + \vec{P} = (\epsilon_0 + \chi) \vec{E} = \epsilon \vec{E} \quad (2.9)$$

where χ is the dielectric susceptibility of the medium. Hence

$$\chi = \epsilon_r \epsilon_0 - \epsilon_0 = \epsilon_0 (\epsilon_r - 1) \quad (2.10)$$

The relative susceptibility $\chi_r = \frac{\chi}{\epsilon_0} = \epsilon_r - 1$ (2.11)

ϵ_r is the relative permittivity. Using eqns. 2.6 – 2.11, a relationship between relative permittivity which is the characteristics of the medium and polarizability which is the characteristics of the molecule can be established.

Hence
$$\frac{N\alpha'}{\epsilon_0} = \epsilon_r - 1 \quad (2.12)$$

For other media the local or Mosotti field [5] becomes,

$$\vec{E}_{loc} = \vec{E} + \frac{\vec{P}}{3\epsilon_0} = \vec{E} \left(1 + \frac{\chi}{3\epsilon_0}\right) = \frac{\epsilon_r + 2}{3} \vec{E} \quad (2.13)$$

From eqn. 2.5, polarization becomes,

$$\vec{P} = N\alpha' \frac{(\epsilon_r + 2)}{3} \vec{E} \quad (2.14)$$

Using eqn. 2.11,
$$\frac{N\alpha'}{3\epsilon_0} = \frac{(\epsilon_r - 1)}{(\epsilon_r + 2)} \quad (2.15)$$

which is known as the Clausius-Mosotti Formula.

Onsager [5] realized a molecular model where a molecule is represented as a point at the center of a cavity of molecular dimensions, volume $1/N$ and radius $(3/4\pi N)^{1/3}$. Hence the dipole moment contained by the cavity is calculated using eqn. 2.7,

$$\vec{p} = \text{Volume} \times P = \frac{4}{3} \pi a^3 P = \frac{4}{3} \pi a^3 \epsilon_0 (\epsilon_r - 1) E \quad (2.16)$$

Hence
$$E = \frac{3\vec{p}}{4\pi a^3 \epsilon_0 (\epsilon_r - 1)} \quad (2.17)$$

If the applied field is small compared to the thermal agitation energy, Onsager approximated the polarization of the medium using Langevin function [5] as

$$\bar{P} = \frac{N\bar{p}^2 \bar{E}_{loc}}{3kT} \quad (2.18)$$

where k represents Boltzman's constant and T the period of the applied field.

Making use of eqn. 2.18 in eqns. 2.5 to 2.11, the local field produced by \bar{E} in the empty cavity is calculated as,

$$\bar{E}_{loc} = \frac{3\epsilon_r}{2\epsilon_r + 1} \bar{E} \quad (2.19)$$

This field is called as the Onsager field.

The difference between Mosotti field and Onsager field is a reaction field due to the enclosed dipole moment [5]. This field is obtained by subtracting eqn. 2.19 from eqn. 2.13. The field is given by

$$\bar{E}_R = \frac{2(\epsilon_r - 1)^2}{3(2\epsilon_r + 1)} \bar{E} \quad (2.20)$$

Substituting eqn. 2.17 in eqn. 2.20,

$$\bar{E}_R = \frac{p}{4\pi\alpha^3 \epsilon_o} 2 \frac{\epsilon_r - 1}{2\epsilon_r + 1} = \frac{2pN}{3\epsilon_o} \frac{\epsilon_r - 1}{2\epsilon_r + 1} \quad (2.21)$$

The field \bar{E}_R is parallel to the dipole and does not affect it. The only force is the couple due to the Onsager field.

Using eqns 2.16, 2.18 and 2.21

$$\epsilon_o(\epsilon_r - 1)E = \frac{Np^2}{3kT} \frac{3\epsilon_r}{2\epsilon_r + 1} \quad (2.22)$$

and

$$p^2 = \frac{kT\epsilon_o}{N} \frac{(\epsilon_r - 1)(2\epsilon_r + 1)}{\epsilon_r} \quad (2.23)$$

The fields considered for eqns 2.5 – 2.23 were static. When an alternating field is applied, the orientation of a dipole varies cyclically with the period T of the field. At low frequencies, the dipoles readily synchronize their orientations with the applied field. But as the frequency increases, the inertia of the molecules and the binding forces become dominant. The medium becomes tetanized [5, 6] and the dipolar polarization ceases to contribute to the dielectric properties. The static relative permittivity tends toward optical relative permittivity ϵ_{∞} which is a function of the refractive index of the medium.

$$\epsilon_{\infty} = n^2 \quad (2.24)$$

where n is the optical index of the medium. To account for this phenomenon, the relationships established for the static field are modified to obtain the relationship for optical relative permittivity, so that eqn. 2.12 becomes

$$\frac{N\alpha'}{\epsilon_0} = \epsilon_{\infty} - 1 \quad (2.25)$$

Using eqns. 2.6, 2.18 and 2.19, the relationship between the relative permittivity and polarizability when a static field is applied can be written as,

$$\epsilon_{rs} - 1 = \frac{N}{\epsilon_0} \left(\alpha' + \frac{p^2}{3kT} \right) \quad (2.26)$$

Using eqns 2.25 and 2.26 the contribution of the permanent dipoles to the static relative permittivity is

$$\epsilon_{rs} - \epsilon_{\infty} = \frac{N}{\epsilon_0} \frac{p^2}{3kT} \quad (2.27)$$

The Clausius-Mosotti formula given in eqn 2.15 becomes,

$$\frac{N}{3\epsilon_0}(\alpha^2 + \frac{p^2}{3kT}) = \frac{\epsilon_{rs} - 1}{\epsilon_{r\infty} + 2} \quad (2.28)$$

Substituting eqns. 2.25, 2.27 and 2.28 in eqn. 2.23, the dipole moment [5]

$$p^2 = \frac{9kT\epsilon_0}{N} \frac{(\epsilon_{rs} - \epsilon_{r\infty})(2\epsilon_{rs} + \epsilon_{r\infty})}{\epsilon_{rs}(\epsilon_{r\infty} + 2)^2} \quad (2.29)$$

When the electric field that induces polarization in a dielectric is removed, the material takes a certain time to return to molecular disorder, and the polarization subsides exponentially with time constant τ which is called as the relaxation time [5-7]. This constant is the time taken for the polarization of the material to fall by a factor of e^{-1} .

If P_1 and P_2 are the polarization components due to deformation and dipole alignment, respectively, then in an alternating field $E = E_0 e^{j\omega t}$, P_2 tends exponentially to its maximum value [5],

$$P_2 = (P - P_1)(1 - e^{-t/\tau}) \quad (2.30)$$

According to eqns 2.7 and 2.10,

$$P = (\epsilon_{rs} - 1)E \quad (2.31)$$

$$P_1 = (\epsilon_{r\infty} - 1)E$$

From eqn. 2.30,

$$\frac{dP_2}{dt} = \frac{(\epsilon_{rs} - \epsilon_{r\infty})}{\tau} E_0 e^{j\omega t} - \frac{P_2}{\tau} \quad (2.32)$$

for which the solution is

$$P_2 = \frac{(\epsilon_{rs} - \epsilon_{r\infty})E}{1 + j\omega\tau} \quad (2.33)$$

The complex nature P_2/E applies the phase difference or hysteresis between the applied field and the polarization.

In biological materials, the dielectric properties are complex [4] when polarized by an electric field or when subjected to a time harmonic

electric field. This is due to the formation of both conduction and displacement currents. The conduction currents represent the current flow that is in phase with the applied voltage whereas the displacement currents are in phase quadrature with the applied voltage. The complex relative permittivity is represented as,

$$\epsilon_r = \epsilon_r' - j\epsilon_r'' \quad (2.34)$$

where ϵ_r' is the real part of complex relative permittivity known as the dielectric constant and ϵ_r'' is the imaginary part known as the dielectric loss. The real and imaginary parts of complex relative permittivity represent the complimentary processes of energy storage and dissipation respectively. Since heat production is related to the frequency and the dielectric loss factor, these are combined to be known as the conductivity σ as,

$$\sigma = \omega\epsilon_0\epsilon_r'' \quad (2.35)$$

and loss tangent as,
$$\tan \delta = \frac{\epsilon_r''}{\epsilon_r'} \quad (2.36)$$

The absorption coefficient α is given as

$$\alpha = \frac{\pi\epsilon_r'' f}{c\sqrt{(\epsilon_r')^2 + (\epsilon_r'')^2}} \quad (2.37)$$

where c is the velocity of light and f the frequency.

Debye has related the dielectric relaxation time with the complex relative permittivity in his equation [8],

$$\epsilon_r = \epsilon_{r\infty} + \frac{\epsilon_{rs} - \epsilon_{r\infty}}{1 + j\omega\tau} \quad (2.38)$$

where ϵ_{rs} is the static relative permittivity measured at dc / low frequencies, $\epsilon_{r\infty}$ is the optical relative permittivity measured at optical / very high frequencies, ω the angular frequency and τ the relaxation time. Equating 2.34 and 2.38, and rationalizing,

$$\text{Dielectric constant } \epsilon_r' = \epsilon_{r\infty}' + \frac{\epsilon_{rs}' - \epsilon_{r\infty}'}{1 + (\omega\tau)^2} \quad (2.39)$$

$$\text{and Dielectric Loss } \epsilon_r'' = \epsilon_{r\infty}'' + \frac{(\epsilon_{rs}' - \epsilon_{r\infty}')\omega\tau}{1 + (\omega\tau)^2} \quad (2.40)$$

Due to the highly asymmetric configuration, water molecule has an exceptionally high polarity and has a dipole moment of 0.62×10^{-29} C m. The water in aqueous media can take different forms. It can appear as ice, free water in cavities or capillaries, or spread on a solid surface with very different properties than those of pure water. It can also be bound water, whose properties are not well determined, but are intermediate between liquid water and ice. The higher the bound water content of a material, the more is its dipole moment, and hence more lossy is the material. Aqueous materials have a number of relaxation states that correspond to different forms of water.

2.4. Dielectric spectrum of biological tissue

The dielectric properties of biological tissues result from the interaction of electromagnetic energy with the tissue constituents at the cellular and molecular level, which depend greatly on the bound water content [9-10]. High water content tissues have dielectric constants and loss factors that are much higher than those of low water content tissues. The main features of the dielectric spectrum of biological tissues [11-14] are given below.

- The relative permittivity of a tissue reaches very high values at frequencies below 100 Hz.

- At high frequencies the relative permittivity decreases in three main steps known as α , β , and γ dispersions. Other dispersions may also be present.
- The low frequency α dispersion is associated with ionic diffusion processes at the site of the cellular membrane.
- The β dispersion, in the hundreds of kilohertz region, is mainly due to the polarization of cellular membranes which act as barriers to the flow of ions between the intra and extra cellular media. Other contributions to the β dispersion come from the polarization of protein and other organic macromolecules.
- The γ dispersion, in the gigahertz region is due to the polarization of water molecules.

The magnitude of dispersion is defined as $\Delta\epsilon = \epsilon'_{rs} - \epsilon'_{\infty}$.

However, the complexity of both the structure and composition of biological material is such that each dispersion region may be broadened by multiple contributions to it [11].

When an electromagnetic field is applied, the polarization of the sample will relax towards a steady state as a first order process characterized by the relaxation time τ . Each of these relaxation regions is the manifestation of a polarization mechanism [11] which gives the expression for complex relative permittivity as in Eqn. 2.34

2.5. Dielectric studies using cavity perturbation technique

Knowledge of microwave dielectric properties of human tissues is essential for understanding and developing medical microwave techniques. Microwave thermography, microwave hyperthermia and microwave imaging rely on processes fundamentally determined by the high frequency electromagnetic properties of human tissues [15-23]. Also it is very

essential for the development of suitable phantoms and coupling media for microwave imaging applications [24-25].

Among the available methods for the measurement of dielectric properties, cavity perturbation technique has a unique place, due to the accuracy in the measured values and the ease of operation [26-29]. When a material is introduced into a resonant cavity, the cavity field distribution and resonant frequency are changed depending on the geometry, electromagnetic properties and position of the sample in the fields of the cavity. Dielectric material interacts only with electric field in the cavity.

Broad band coaxial cavity perturbation technique and rectangular cavity perturbation technique are the techniques used in the present work to study the microwave dielectric properties of breast phantoms and breast tissues and are discussed in detail below.

2.5.1 Coaxial cavity perturbation technique

This technique uses a reflection type cylindrical cavity to resonate over a broad frequency band. The schematic diagram of the cavity resonator is shown in Figure 2.2. The cavity is interfaced with network analyzer and a computer, for data acquisition. The cavity is excited below the cut off for the TM_{01} mode. Along the axis of the waveguide there is a removable central conductor. Thus TEM mode can propagate up to the end of the central conductor. The length of the central conductor can be adjusted to obtain suitable resonance frequencies. A movable sample holder is attached around the resonator and a small hole is drilled in it for inserting the samples. A capillary tube made of low loss silica ($\tan \delta = 0.002$ at 3 GHz) having volume 0.063 cm^3 is used to hold the liquid sample (corn syrup / glycerine) and a cylindrical cup made of low loss Teflon ($\tan \delta = 0.0015$ at 3 GHz) having volume 0.052 cm^3 is used to hold the breast tissue

sample. On the wall of the resonator, a long narrow slot is provided to facilitate the movement of the samples along the length of the cavity. The resonant frequency f_o and the corresponding quality factor Q_o of each resonant peak of the cavity resonator with the empty capillary tube / Teflon cup placed at the maximum of electric field are noted. The position of the tube / cup is adjusted for maximum perturbation (i.e. maximum shift of resonant frequency with minimum amplitude for the peak). Similarly f_s and Q_s are determined for the cavity with the capillary tube / cup loaded with the samples.

The standing wave components of the resonant TEM mode are obtained by combining the forward and backward propagating waves [30] as,

$$E_{\rho s}^0 = \frac{A}{\rho} e^{j\beta z} + \frac{B}{\rho} e^{-j\beta z} \quad (2.41)$$

$$H_{\phi s}^0 = \frac{-A}{\eta\rho} e^{j\beta z} + \frac{B}{\eta\rho} e^{-j\beta z} \quad (2.42)$$

where η is the free space impedance and A and B are constants. The boundary conditions are applied to E and H fields at $z = 0$ and $z = L$ where L is the length of the central conductor. The first condition gives $A = -B$, while the second one gives the resonance condition.

The eqns . 2.41 and 2.42 become,

$$E_{\rho s}^0 = \frac{A}{\rho} \sin \beta z = E_{o,\max} \sin \beta z \quad (2.43)$$

$$H_{\phi s}^0 = \frac{A}{\eta\rho} \cos \beta z = H_{o,\max} \cos \beta z \quad (2.44)$$

The electrical energy stored in the cavity

$$w_e = \frac{\epsilon_o}{2} \int_{V_c} E_{\rho s}^0{}^2 dv \quad (2.45)$$

Substituting eqn. 2.43 in eqn. 2.45 we get,

$$w_e = \frac{\epsilon_o}{2} \int_0^L \int_a^b \int_0^{2\pi} E_{o,\max}^2 \sin^2 \beta z \rho d\rho d\phi dz \quad (2.46)$$

where b and a are the outer and inner radii respectively of the coaxial resonator.

When the sample is introduced in to the cavity the relative frequency shift is given by,

$$-\frac{d\Omega}{\Omega} \approx \frac{(\epsilon_r - 1)\epsilon_o \int_{V_s} E \cdot E_{o,\max}^* dV + (\mu_r - 1)\mu_o \int_{V_s} H \cdot H_{\max}^* dV}{\int_{V_c} (D_o E_{o,\max}^* + B_o H_{o,\max}^*) dV} \quad (2.47)$$

The numerator of this equation represents the energy stored in the sample. The denominator represents the total energy stored in the cavity which can be written as $4w_e$. When the dielectric sample is introduced in to the cavity at the position of the maximum electric field, the relative frequency shift is given by,

$$-\frac{d\Omega}{\Omega} \approx \frac{(\epsilon_r - 1)\epsilon_o \int_{V_s} E_{\rho s}^o E_{o,\max}^* dV}{4w_e} \quad (2.48)$$

Substituting eqn. 2.46 in eqn. 2.48 and simplifying,

$$-\frac{d\Omega}{\Omega} \approx \frac{(\epsilon_r - 1)V_s}{2 \times 2\pi \frac{b^2 - a^2}{2} \frac{L}{2}} \quad (2.49)$$

$$-\frac{d\Omega}{\Omega} \approx \frac{(\epsilon_r - 1)V_s}{\pi L(b^2 - a^2)} \quad (2.50)$$

Here $E_{\rho s}^o \approx E_o^*$ because the field inside the sample is assumed to be equal to the field inside the cavity. The volume of the sample

$V_s = \pi r^2(b-a)$ where r is the radius of the sample. Also $\epsilon_r = \epsilon_r' - j\epsilon_r''$.

Then eqn. 2.50 becomes,

$$-\frac{d\Omega}{\Omega} \approx \frac{(\epsilon_r' - 1)r^2}{L(b+a)} - j \frac{\epsilon_r'' r^2}{L(b+a)} \quad (2.51)$$

Hence
$$-\frac{d\Omega}{\Omega} \approx \frac{-(\epsilon_r' - 1)r^2}{L(b+a)} + j \frac{\epsilon_r'' r^2}{L(b+a)} \quad (2.52)$$

$$-\frac{d\Omega}{\Omega} \approx \frac{(f_s - f_o)}{f_s} + \frac{j}{2} \left[\frac{1}{Q_s} - \frac{1}{Q_o} \right] \quad (2.53)$$

From 2.52 and 2.53,

$$(\epsilon_r' - 1) = \frac{L(b+a)}{r^2} \frac{(f_o - f_s)}{f_s} \quad (2.54)$$

$$\epsilon_r'' = \frac{L(b+a)}{2r^2} + \left[\frac{1}{Q_s} - \frac{1}{Q_o} \right] \quad (2.55)$$

where ϵ_r' is the dielectric constant and ϵ_r'' is the dielectric loss of the sample. The dimensions L, b, a and r are as shown in Figure 2.2.

For a dielectric material having non-zero conductivity, Ampere's law in phasor form can be written as,

$$\nabla \times H = (\sigma + j\omega\epsilon)E = (\sigma + \omega\epsilon'')E + j\omega\epsilon'E \quad (2.56)$$

The loss tangent
$$\tan \delta = \frac{\sigma + \omega\epsilon''}{\omega\epsilon'} \quad (2.57)$$

The effective conductivity of the medium
$$\sigma_e = \sigma + \omega\epsilon'' \quad (2.58)$$

When σ is very small, the effective conductivity reduces as $\omega\epsilon''$. Hence effective conductivity

$$\sigma_e = \omega \epsilon'' = 2\pi f \epsilon_o \epsilon_r'' \quad (2.59)$$

And
$$\tan \delta = \frac{\omega \epsilon''}{\omega \epsilon'} = \frac{\epsilon_r''}{\epsilon_r'} \quad (2.60)$$

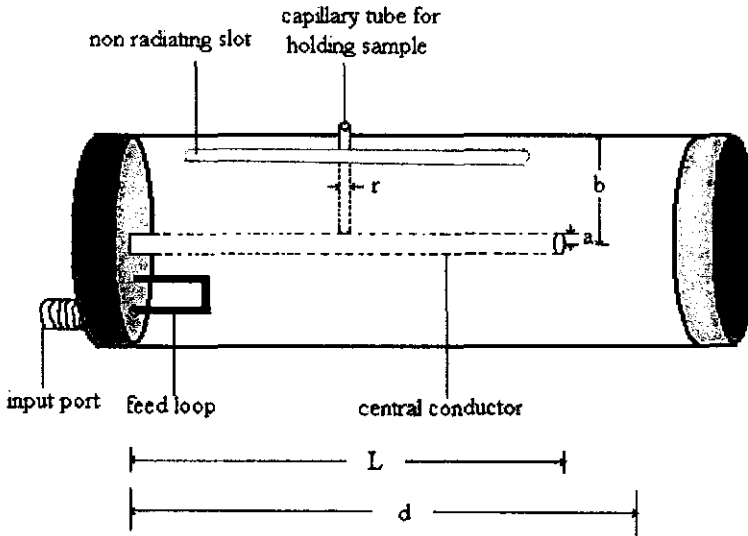


Figure 2.2. Schematic diagram of the coaxial cavity resonator

2.5.2. Rectangular Cavity Perturbation Technique

Here, a transmission type rectangular cavity is used to generate the resonant frequencies, as shown in Figure 2.3. The cavity is made from S - band waveguide with both ends closed. The length of the resonator determines the number of resonant frequencies. On the wall of the resonator, a long narrow slot is made to facilitate the movement of the samples along the length of the cavity. The resonator is excited in the TE_{10p} mode. The sample holders used and the procedure for obtaining the resonant frequencies f_o, f_s with the corresponding quality factors Q_o and Q_s , are the same as described in Section 2.5.1.

When a small sample is introduced in a cavity which has the electric field E_0 and magnetic field H_0 in the unperturbed state, the fields formed in the interior of the object be E and H . Beginning with the Maxwell's equations, an expression for the resonant frequency shift is obtained [30] as,

$$\frac{\omega - \omega_0}{\omega} = \frac{\int (\Delta\epsilon E \cdot E_0^* + \Delta\mu H \cdot H_0^*) dr}{\int (\epsilon E \cdot E_0^* + \mu H \cdot H_0^*) dr} \quad (2.61)$$

where dr is the elemental volume, μ and ϵ are the permeability and permittivity of the medium in the unperturbed cavity respectively, $\Delta\mu$ and $\Delta\epsilon$ are the changes in permeability and permittivity of the medium due to the introduction of the sample in the cavity. Without affecting the generality of Maxwell's equations, the complex frequency shift due to a lossy sample in the cavity is given by [30],

$$-\frac{d\Omega}{\Omega} \approx \frac{(\epsilon_r - 1)\epsilon_0 \int_{V_s} E \cdot E_0^* dV + (\mu_r - 1)\mu_0 \int_{V_s} H \cdot H^* dV}{\int_{V_c} (D_0 \cdot E_0^* + B_0 \cdot H_0^*) dV} \quad (2.62)$$

The numerator of the eqn. 2.62 represents the energy stored in the sample and the denominator represents the total energy stored in the cavity. When a dielectric sample is introduced at the position of maximum electric field, only the first term in the numerator is significant, since a small change in ϵ at a point of zero electric field or a small change in μ at a point of zero magnetic field does not change the resonance frequency. Hence eqn. 2.62 reduces to,

$$-\frac{d\Omega}{\Omega} \approx \frac{(\epsilon_r - 1) \int_{V_s} E \cdot E_{0,\max}^* dV}{2 \int_{V_c} |E_0|^2 dV} \quad (2.64)$$

Including the quality factors in eqn.2.64, the complex frequency shift [30], is obtained by,

$$-\frac{d\Omega}{\Omega} \approx \frac{d\omega}{\omega} + \frac{j}{2} \left[\frac{1}{Q_s} - \frac{1}{Q_o} \right] \quad (2.65)$$

Using eqn. 2.64 and eqn. 2.65,

$$\frac{(f_s - f_o)}{f_s} \approx \frac{(\epsilon'_r - 1) \int_{V_s} E \cdot E_{o,\max}^* dV}{2 \int_{V_c} |E_o|^2 dV} \quad (2.66)$$

and

$$\frac{1}{2} \left[\frac{1}{Q_s} - \frac{1}{Q_o} \right] = \frac{\epsilon''_r \int_{V_s} E \cdot E_{o,\max}^* dV}{2 \int_{V_c} |E_o|^2 dV} \quad (2.67)$$

Assume that $E=E_o$ and the value of E_o in TE_{10p} mode as $E_o = E_{c,\max} \sin(m\pi x/d) \sin(p\pi z/d)$ where a is the broader dimension of the waveguide and d is the length of the cavity. Integrating and rearranging the above equations,

$$\epsilon'_r - 1 = \frac{f_o - f_s}{2f_s} \left[\frac{V_c}{V_s} \right] \quad (2.68)$$

$$\epsilon''_r = \frac{V_c}{4V_s} \left[\frac{1}{Q_s} - \frac{1}{Q_o} \right] \quad (2.69)$$

The conductivity of the sample is calculated using eqns. 2.56 - 2.60.

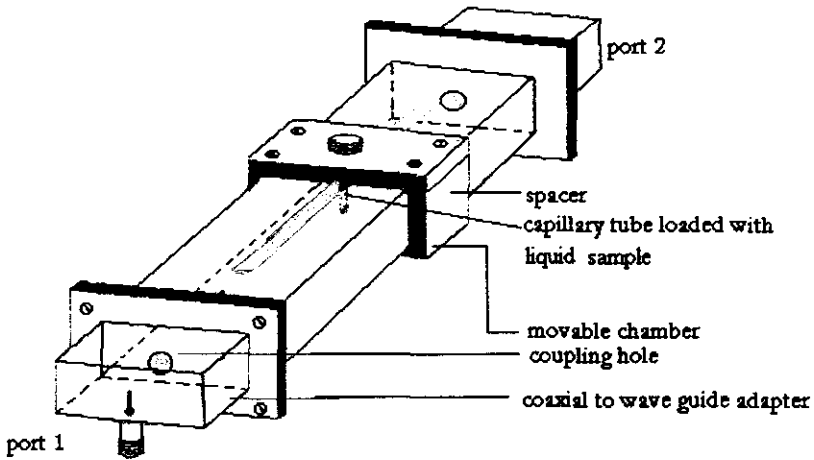


Figure 2. 3. Schematic diagram of rectangular cavity resonator

2.6 Experimental Set up and Calibration Procedures

The experimental set up used for the antenna studies, dielectric measurement using cavity perturbation technique and microwave imaging is discussed below.

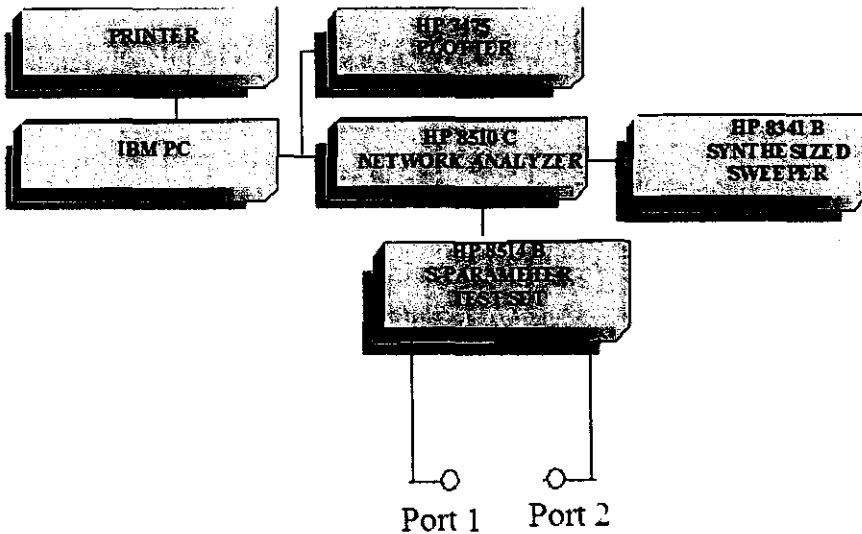


Figure 2.4. Experimental Set up

The set up consists of Vector Network Analyzer HP 8510C, S-parameter test set HP 8514B, Synthesized Sweeper HP 8341B and interfacing workstation as shown in Figure 2.4.

To begin with, the system is first calibrated using THRU-REFLECT-LINE (TRL) calibration. The process of implementing the TRL calibration in a specified environment is as follows.

1. Selecting standards appropriate for the application
2. Defining the standards by modification of the internal calibration kit registers
3. Performing the calibration
4. Checking the performance.

Requirements for TRL Standards

Standard	Requirements
Zero Length	S_{21} and S_{12} are defined equal to 1
THRU	S_{11} and S_{22} are defined equal to zero.
REFLECT	Phase of Γ (reflection coefficient) must be known within $\pm 1/4$ wavelength. Must be same on both the ports. May be used to set the reference plane if the phase response of the REFLECT is known and specified.
LINE	Z_0 of the LINE establishes the reference impedance after error correction is applied. Insertion phase of the LINE must never be same as that of the THRU. Optimal LINE length is $\pm 1/4$ wavelength or 90 degrees relative to the THRU at the center frequency. Insertion phase or electrical length need only be specified within $\pm 1/4$ wavelength.

Selection of Optimal Line Length

Optimal line length is $\pm 1/4$ wavelength or 90 degrees relative to the THRU at the center frequency. Line length is (LINE-THRU). If the lower and upper cut off frequencies of the bands are f_1 and f_2 GHz respectively, then

the electrical length, 'l' is $\frac{15}{f_1 + f_2}$, With this electrical length, insertion

phase is to be calculated using the expression $\frac{360 \times f \times l}{c} = 12 \times f \times l(\text{cm})$,

where f is the center frequency. The insertion phase for f_1 and f_2 is to be calculated and it should be in between 20 and 160 degrees. If this condition is not satisfied, line length is to be slightly adjusted for getting the insertion phase with in the specified range.

Defining TRL Standards

The standards selected should be entered into the calibration kit registers of the HP 8510C Network Analyzer. It can be done from the CAL menu and from the MODIFY CAL1/2. THRU options are set in the calibration standard number 14, REFLECT in the 18 and LINE options in 15 and 16. Multiple LINE lengths can be incorporated using the two LINE standards. The corresponding offset delays and impedances should be set for each standards and saved.

Performing the calibration

To begin with, the fixture is connected to the coaxial test ports and desired stimulus conditions for measurements such as start frequency, stop frequency, number of points, power level, averaging are set in the network analyzer. In the CAL menu, press TRL 2-PORT and this menu will give different options such as THRU, S11REFLECT, S22REFLECT, ISOLATION, and LINE. This can be performed in any convenient order.

Pressing SAVE TRL CAL will enable to save the calibration coefficients in the desired calibration number. Error correction is automatically turned on.

Checking the performance

Verification kits are available in the coaxial connector family. These kits contain devices whose characteristics are precisely and independently known. When these devices are measured, the difference between the displayed results and the known values indicate the level of measurement accuracy. In non-coaxial cases, these verification devices do not exist. However, there are some performance checks. Connection repeatability can be evaluated. Take a single S-parameter measurement and store its response into memory. Break the connection, reconnect the same device and then re-measure. This will give the performance calibration.

2.6 References

1. Von Hippel A.R, "Dielectrics and Waves", MIT Press, 1954.
2. Hasted J.B, "Aqueous Dielectrics", Chapman and Hall Publs., 1973.
3. Larsen L.E, Jacobi J.H, "Medical Applications of Microwave Imaging", pp. 118 – 137, IEEE Press 1985.
4. Grant E.H, Sheppard R.J, South G.P, "Dielectric Behavior of Biological Molecules in Solution", Oxford: Clarendon Press, 1978.
5. Jacques Thurey, "Microwaves: Industrial Scientific and Medical Applications", Artech House, Boston, MA 02062, 1992.
6. Copson D, "Microwave Heating", Avi Publ. Co., Westport, USA, 1975
7. Smith C, "Molecular relaxation processes", Proceedings of Chemical Society Symposium, Academic Press, London, pp. 1 – 13, 1966.
8. Debye P, "Polar Molecules", Dover Publications, New York, 1945.
9. Gabriel C, Gabriel S, Corthout E, "The dielectric properties of biological tissues: I. Literature survey", Physics in Medicine and Biology, vol. 41, pp. 2231 – 2249, 1996.
10. Schepps J. L, Foster K.R, "The UHF and microwave dielectric properties of normal and tumor tissues: variation in dielectric properties with tissue water content", Physics in Medicine and Biology, vol. 25, pp.1149 – 1159, 1980.
11. Gabriel S, Lau R.W, Gabriel C, "The dielectric properties of biological tissues: II. Measurements in the frequency range 10 Hz – 20 GHz", Physics in Medicine and Biology, vol. 41, pp. 2251 – 2269, 1996.
12. Gabriel S, Lau R.W, Gabriel C, "The dielectric properties of biological tissues: III. Parametric models for the dielectric spectrum of tissues", Physics in Medicine and Biology, vol. 41, pp. 2271 – 2293, 1996.
13. Schwan H.P, "Interaction of microwave and radio frequency radiation with biological systems", IEEE Transactions on Microwave Theory and Techniques, vol. 19, no.2, pp. 146 – 152, 1971.
14. Schwan, H.P, "Electrical properties of tissues and cell suspensions: mechanisms and models", Proceedings of the 16th International Conference of the IEEE Engineering in Medicine and Biology, pp. A70 - A71, 1994.
15. Pop M, Molckovsky A, Chin L, Kolios M.C, Jewett M.A.S , Sherar M, "Changes in dielectric properties at 460 kHz of kidney and fat during heating: importance for radio-frequency thermal therapy", Physics in Medicine and Biology, vol. 48, pp. 2509 – 2525, 2003.

16. Chin L, Sherar M, "Changes in dielectric properties of ex vivo bovine liver at 915 MHz during heating", *Physics in Medicine and Biology*, vol. 46, pp. 197 – 211, 2001.
17. Smith S.R, Foster K.R, "Dielectric properties of low-water content tissues", *Physics in Medicine and Biology*, vol. 30, pp. 965 – 973, 1985.
18. Campbell A.M, Land D.V, "Dielectric properties of human breast tissue measured in-vitro at 3.2 GHz", vol.37, pp. 193 – 210, 1992.
19. Chaudhary S.S, Mishra R. K, Swarup A, Thomas J. M, "Dielectric properties of normal and malignant human breast tissues at radio wave and microwave frequencies", *Indian Journal of Biochemistry and Biophysics*, vol. 21, pp. 76 – 79, 1984.
20. Foster K.R, Schwan H.P, "Dielectric properties of tissues and biological materials: a critical review", *Critical Review in Biomedical Engineering*, vol. 17, pp. 25 -104, 1989.
21. Suroweic A.J, Stuchly S.S, Barr J.R, Swarup A, "Dielectric properties of breast carcinoma and the surrounding tissues", *IEEE Transactions of Biomedical Engineering*, vol. 35, pp. 257 – 263, 1988.
22. Stuchly M. A, Stuchly S.S, " Dielectric properties of biological substances – tabulated", *Journal of Microwave Power*, vol. 15, pp. 19 26, 1986.
23. Peloso R, Tuma D.T, Jain R .K, "Dielectric properties of solid tumors during normothermia and hyperthermia", *IEEE Transactions on Biomedical Engineering*, vol. 31, pp. 725 – 728, 1984.
24. Bindu G, Lonappan A, Thomas V, Hamsakutty V, Aanandan C.K, Mathew K.T, "Microwave characterization of breast phantom materials," *Microwave and Optical Technology Letters*, vol. 43, pp. 506 – 508, 2004.
25. Kato H, Ishada T, "Development of an agar phantom adaptable for simulation of various tissues in the range 5-40 MHz. (Hyperthermia treatment of cancer)", *Physics in Medicine and Biology*, vol. 32, pp. 221-226, 1987.
26. Raveendranath U, Bijukumar S, Mathew K.T, "Broadband coaxial cavity resonator for complex permittivity measurements of liquids", *IEEE Transactions on Instrumentation and Measurement*", vol. 49, pp. 1305 – 1312, 2000.
27. Mathew K.T, Raveendranath U, *Sensors Update*, Wiley – VCH, Germany, pp.185 – 210, 1999.
28. Mathew K.T, Raveendranath U, "Waveguide cavity perturbation method for measuring complex permittivity of water", *Microwave and Optical Technology Letters*, vol.6, pp. 104 – 106, 1993.

29. Raveendranath U, Jacob J, Mathew K.T, "Complex permittivity measurement of liquids with coaxial cavity resonators using a perturbation technique", *Electronics Letters*, vol. 32, pp. 988 -990, 1996.
30. Raveendranath U, Ph.D Thesis "The study of the dielectric and magnetic properties of certain materials using modified cavity perturbation technique", May 1996, Cochin University of Science and Technology, Cochin.

Chapter 3

DESIGN OF ANTENNA FOR MICROWAVE BREAST IMAGING

3.1 Introduction

Rapid advances in technology have been accompanied by its increasing demand in medical field for improved health care. Interaction of scientists and engineers with medical people has resulted in significant developments of highly sophisticated medical equipments. Applications of electromagnetic energy in medical field involve the use of antennas of one kind or other, for coupling this energy into human body or into other biological systems.

Primarily, medical applications of microwaves can be divided into two categories: therapy and diagnostics. In therapy, antennas are used as system elements to produce hyperthermia for treating cancer. In diagnostics, antennas are used to couple electromagnetic energy into and out of the body. These signals are then monitored to study various physiological parameters.

While active microwave imaging has been hypothesized as a potentially powerful medical imaging modality for a number of years, there

has yet to be any significant realization of a clinically viable imaging system. The design and fabrication of suitable transmitting and receiving antennas and selection of proper coupling medium, present significant challenges in the implementation of these systems.

3.2 Antennas for medical applications

The antennas that are currently in use as transmitters and receivers for medical applications are given here.

3.2.1 Wave guide antennas

One class of commonly used antennas for coupling electromagnetic energy into the human body consists of open-ended wave guides. Such radiators have been primarily used to induce hyperthermia for cancer therapy, which requires effective heating of muscle tissue without excessive heating of the fat layer that overlies the muscle. Wave guide radiators provide good coupling of electromagnetic energy into the tissue, but they tend to be bulky and awkward. Since the wave guides are physically very large at low frequencies, they have been used mostly at frequencies of 915 MHz and above, although ridged waveguides loaded with water have been used at frequencies as low as 27 MHz for inducing hyperthermia. Loading a wave guide with a lossless dielectric of dielectric constant approximately equal to that of the tissue provides a good impedance match and ensures good transmission of energy into the tissue. The dielectric loading also reduces the size of the wave guide.

3.2.2 TEM wave guide antenna

Open ended wave guides are inhomogeneously loaded with dielectric material to generate TEM mode. For microwave hyperthermia treatment, a power absorption pattern that is uniform in the cross section of the region to be heated is required.

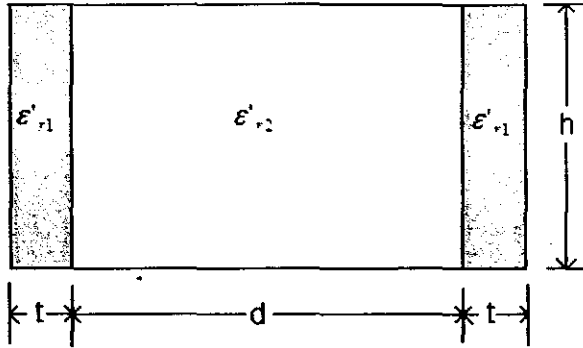


Figure 3 .1 TEM wave guide

Due to the uniformity of the fields across the aperture of the TEM wave guide antennas, it is more suitable for hyperthermia treatment than the TE_{10} mode wave guide antennas. For field patterns in the central portion of the wave guide to approximate to those of the TEM mode, the condition that needs to be satisfied is $t\sqrt{(\epsilon'_{r1}/\epsilon'_{r2}) - 1} = \lambda_1/4$, where λ_1 is the wavelength in the unbounded region of dielectric constant ϵ'_{r1} . The height h of the wave guide should not exceed $\lambda/2$ so that higher order modes will not propagate. The impedance of the antenna can be made to match with that of the tissue by using a material of dielectric constant ϵ'_{r2} approximately equals to that of the tissue. But a high value of ϵ'_{r2} requires a very heavy material which makes the antenna bulky and expensive. Since ϵ'_{r1} should be greater than ϵ'_{r2} and as the thickness t is directly related to $\epsilon'_{r1}/\epsilon'_{r2}$, finding a low loss material of high dielectric constant ϵ'_{r1} with reasonable thickness is difficult.

3.2.3 Ridged wave guide antennas

A method to reduce the size of a wave guide that will propagate waves at a given frequency is to add ridges. In addition to lowering the cut off

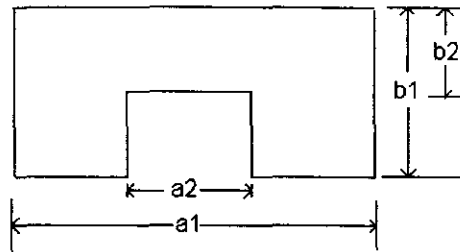


Figure 3.2 (a) Single ridged wave guide

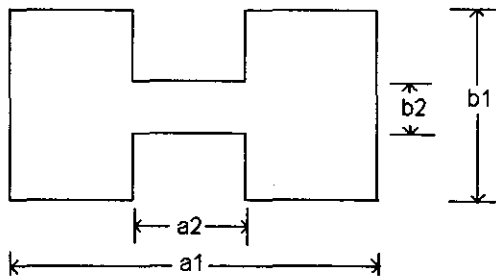


Figure 3.2 (b) Double ridged wave guide

frequency, the ridges also reduce the wave impedance, which makes it easier to match into the tissue. However ridged wave guides have the disadvantage of concentrating the electric field in the space above the ridge, which sometimes lead to undesirable hot spots, especially when $b1$ is small.

3.2.4 Ridged Horn Antennas

Horns are widely used antennas due to its simple construction, large gain and ease in excitation. Since they have limited bandwidth, great efforts have been made to enlarge the operational bandwidth. Ridges on the side flares are introduced to extend the bandwidth, similar to the ridges in a wave guide that lower the cut-off frequency. But the antenna is very bulky for microwave imaging applications.

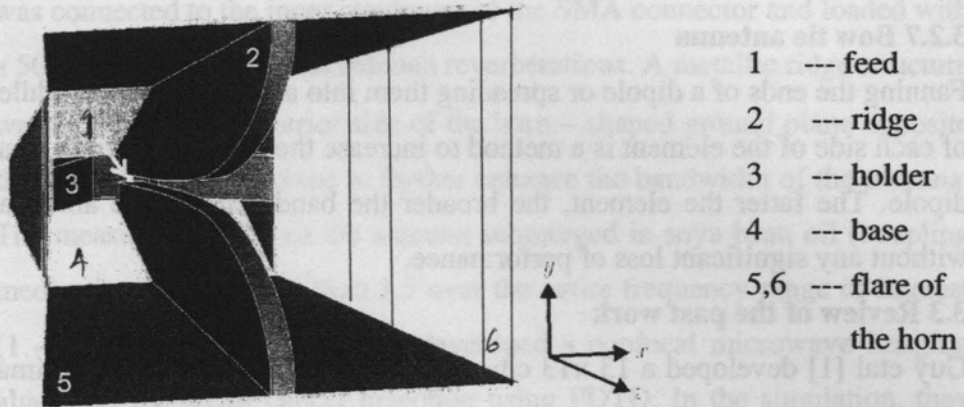


Figure 3.3 Double ridged horn antenna

3.2.5 Microstrip patch antennas

Microstrip patch antennas are attractive applicators to couple electromagnetic energy into biological systems because they are flat, compact and mechanically convenient. They are also easy to design and fabricate.

However they tend to be narrow band making it unsuitable for pulsed confocal microwave technique.

3.2.6 Monopole and Dipole antenna

Monopole and dipole antennas are compact and easy to use. The monopole is the inner conductor of a coaxial cable embedded in open air. The coaxial cable dimensions are set such that they result in good impedance matching. But when put to practice the poor bandwidth offered by the monopole restricts its use in pulsed confocal microwave technique. Dipole antenna too exhibits poor band width. Resistive loading is adopted in monopole and dipole antenna designs to enhance the band width, at the cost of radiation

efficiency. Also, the omni directional radiation patterns of these antennas reduce the amount of microwave energy coupled to the target.

3.2.7 Bow tie antenna

Fanning the ends of a dipole or spreading them into a bow about the middle of each side of the element is a method to increase the SWR bandwidth of a dipole. The fatter the element, the broader the bandwidth of the antenna without any significant loss of performance.

3.3 Review of the past work

Guy et al [1] developed a 13 x13 cm aperture applicator to provide optimal heating for fat – muscle configuration at 915 MHz. Open ended dielectric loaded wave guide antennas were used for the transmission of microwave energy into the tissue. Open ended TEM wave guide was designed as applicator for hyperthermia treatment by Cheung et al [2].

Large ridged wave guide applicators that operated at 27.12 MHz were developed by Sterzer and colleagues [3]. The antenna was loaded with de-ionized water to further reduce the size. Because it was operated at low frequency, it produced good deep regional heating.

Microstrip loop radiators were designed and tested for selective heating of the muscle phantom [4]. The heating was effective to a depth of approximately 1.6 cm at 433 MHz and 1.1 cm at 915 MHz.

Xu Li et al [5, 6] performed microwave imaging via space time beam forming for breast cancer detection. They used a 2-D antenna array for data acquisition. The brass antenna element had a pyramidal horn-shaped ground plane connected to the outer conductor of the coaxial feed via SMA connector. The height of the pyramidal horn was 1.3 cm and aperture dimensions were 2.5 x 2 cm. This ground plane configuration confined the main beam of the radiation pattern to the opening of the horn to ensure

minimum interference from undesired sources. A curved launching plane was connected to the inner conductor of the SMA connector and loaded with a 50Ω resistor to suppress antenna reverberations. A metallic ridge structure was attached to the interior side of the horn – shaped ground plane opposite the curved launching plane to further enhance the bandwidth of the antenna. The measured VSWR of the antenna submerged in soya bean oil (coupling medium) was no greater than 1.5 over the entire frequency range of interest (1 – 11 GHz). Same group [7] developed a confocal microwave imaging algorithm for breast cancer detection using FDTD. In the simulation, they modelled an antenna array consisting of 17 monopoles spanning 8 cm along the surface of the breast. Each antenna was excited individually with a short pulse and the backscatter response was collected by the same antenna element. Planar antenna array using resistively loaded bow tie antennas and cylindrical antenna array using resistively loaded dipole antennas were also simulated [8] for 3-D breast tumor localization. Each of the antennas in the array was excited with a Gaussian pulse centered at 6 GHz.

Meaney et al [9] developed an active microwave imaging system in the frequency range of 0.3 –1 GHz for reconstruction of 2-D electrical property distributions. They used water filled wave guide transmitters as its design was straightforward and it yielded a certain degree of directivity without increase in size. Monopole antennas were used as receivers because they closely emulated a point electric field detector in the 2-D plane. Studies performed in deionized water and 0.9 % saline solution showed that the system exhibited poor performance in this frequency range. Same measurement system was used in imaging multi target tissue equivalent phantoms [10] and error of 50% in the reconstructed image was reported. Same group designed a clinical prototype microwave imaging

system using monopole antennas [11] as transmitter and receiver in the frequency range of 0.3 - 1 GHz. Single and multi target imaging experiments were performed and the near field effects on the measurement data were studied. Images were reconstructed from the data collected by the monopole configuration. The analyses showed that there was a decrease of approximately 10% error in single target experiments and 20% in multi target cases, compared to the images reconstructed using wave guide data. They also reported that the image quality was improved with decreased array diameter. Microwave imaging experiments in ex-vivo breast tissues having saline inclusions using a 14 cm. diameter array of 16 monopole antennas were also conducted [12]. Satisfactory detection of the saline inclusion was reported.

Fear et al investigated microwave breast imaging using resistively loaded Wu-King dipole antennas [13-15]. Even though these antennas reported poor efficiency and directivity, they allowed the incorporation of physically small antennas with reasonable bandwidth and fidelity. Also it reduced the computational cost in modeling.

Hagness et al [16, 17] investigated the ultra wide band radar technology for early stage detection of breast tumors. For this application they designed a bowtie antenna of flare length 4 cm and flare angle 53° on thin metal sheet. The antenna was embedded in a large block of lossy dielectric material to match with the dielectric parameters of the biological tissue. A resistive voltage source coaxial feed was used to excite the antenna. The antenna exhibited wide band and reduced end reflections of -60 dB. However the antenna was bulky, and the significant back radiations reduced the amount of microwave energy coupled into the object. Same group [18] performed FDTD analysis of a pulsed confocal microwave

system for breast cancer detection. A dipole antenna having a resonant frequency of 6 GHz located at the focus, inside an elliptical reflector was excited with a Gaussian pulse for the study. They [19] modelled a 17 element electronically scanned monopole array in 2-D using FDTD. The monopoles were spaced at 0.5 cm intervals along the surface of a 0.1 cm. thick layer of skin. Each monopole element was excited one at a time using a 270 ps Gaussian pulse multiplying a 6 GHz sinusoid.

A microwave tomographic scanner for medical imaging operating at 2.45 GHz was realized by Joefre etal [20]. The system used an antenna array consisted of 64 water loaded wave guide antennas, flared in the E-plane forming a conformed sectorial horn (2.5 cm height and 2.5 cm length) providing a collimated field pattern of about 2 cm in the vertical plane. In the H plane, the antenna was an open wave guide with a quasi omni directional field pattern. Images reconstructed with the collected scattered fields were not promising.

The distortions in the scattered field measurements that arise due to non-active antenna element interactions in the frequency range of 500 - 900 MHz using 16 element monopole array were studied by Paulsen etal [21,22]. The non-active members of the antenna array were treated as impedance boundary conditions applied over a cylindrical surface of finite radius providing two parameters, the effective antenna radius and impedance factor. These parameters were introduced into the antenna compensation model and high quality images were reconstructed. Also the quantification of 3-D field effects of breast phantoms from the 2-D microwave data collected using 32 monopole antennas equally spaced around a 25 cm diameter annulus at a frequency of 500 MHz [23] were studied.

A liquid coupled non-contacting, microwave imaging system to exploit breast cancer diagnosis was developed by Dun Li et al [24]. A movable circular array of 16 monopole antennas operating over a frequency range of 0.5 - 3 GHz was used for data acquisition. Images reconstructed from the collected scattered fields could distinguish malignant and normal breast tissues. The same group [25] developed a parallel detection microwave spectroscopy system for breast imaging. The system implemented a parallel detection scheme that allowed signals to be sampled simultaneously at multiple receiving antenna sites. Monopole antennas having resonant frequencies 900 MHz were used in the array as they consumed less space and could be positioned in close proximity to the breast.

Stuchly et al [26,27] developed a confocal microwave system for breast tumor detection using resistively loaded Wu-King dipole antenna. The antenna exhibited a bandwidth of 6 GHz and a center frequency of 4GHz. The resistive loading reduced end reflections from the antenna, making the antenna suitable for radiating wideband signal. The characteristics of the antenna in various immersion media of dielectric constants 26, 15, 6 and 15 were also investigated [28]. Antenna exhibited wide band performance in all the media.

Bowtie patch antennas having coaxial feed were developed by Yun et al [29,30] for breast cancer detection in the frequency range of 2 – 4.3 GHz for studying the cross polarized reflections from tumor. The vertical bowtie element functioned as transmitter and the horizontal bowtie element received the cross polarized reflections from targets. Studies were performed for various tumor depths, locations and orientations. The antenna was found successful in detecting tumor.

A microwave tomographic imaging system operating at 2.45 GHz was developed by Semenov et al [31-33]. The system consisted of 64 wave guide antennas having aperture dimensions of 30 mm x 9 mm, divided into 32 emitters and 32 receivers. The antennas had narrow radiation pattern in the vertical direction and the field pattern in the horizontal projection was approximately three times wider than in the vertical one. Later they extended their studies using wave guides loaded with barium titanate [34] of dielectric constant 60 and better resolution of 2-D reconstructed images were reported.

Cross polarized resistively loaded bow tie patch antennas with coaxial feed of which one acted as transmitter and the other as receiver were simulated for confocal microwave imaging by Oral et al [35]. The transmitter was excited with a differentiated Gaussian pulse centered at 6 GHz and the corresponding reflections were recorded on the receiving antenna. Tumor detection was not accurate with this set up.

Rectangular array and circular array of monopole antenna configurations were investigated, for wide band confocal microwave imaging by Zhao et al [36]. Both arrays consisted of one transmitter and 24 receivers. The transmitter was excited with a wide band signal of 3.2 GHz and 3 dB bandwidth of 5 GHz. They obtained higher contrast imaging with circular antenna array and high resolution with rectangular antenna array.

Shannon et al [37] designed a Slot line Bowtie Hybrid (SBH) antenna for breast cancer detection. The SBH was a hybrid of a slot line circuit board antenna and bowtie horn. The broad bandwidth match was achieved by the slot widening with a Vivaldi profile. The antenna exhibited a bandwidth of 2-18 GHz and HPBW of 30°.

3.4 Motivation for the present work

Time domain confocal microwave technique requires wide band antenna to transmit short transient pulses. The antenna should efficiently focus the microwave signal towards the target and collect the back-scattered energy. As microwave tomographic imaging is a frequency domain approach, the antenna should exhibit good matching at the desired resonant frequency. More over the antenna should exhibit less edge reflections for better coupling of electro magnetic energy into the tissue and should be compact enough for the ease in system implementation and data acquisition.

A microstrip patch antenna consists of a conducting patch of any planar geometry on one side of a dielectric substrate backed by a ground plane. These antennas have several advantages compared to conventional microwave antennas such as light weight, low profile planar configurations and low fabrication costs. However it offers some disadvantages like narrow band width, poor isolation between feed and radiating elements and lower power handling capacity. Microstrip feed and coaxial feed are the commonly used feeding techniques for exciting microstrip antenna. However these feeds produce significant radiation and dispersion losses [38].

Following section deals with the development of an efficient bow tie antenna fed by a coplanar strip line, to be suitable for both confocal and microwave tomographic imaging applications. Coplanar strip line feeds are advantageous because they exhibit low radiation and dispersion losses due to their uniplanar nature and the ease in shunt connection [38].

Even though microstrip bow tie antennas with coaxial feed have been simulated for microwave imaging [16, 29,30,35] their experimental

feasibility is not reported. Also some of these antennas [16, 35] reported erratic response when immersed in water.

3.5. Design of coplanar strip line fed bowtie antenna

The substrate used for the development of the antenna is single layered FR4 Glass Epoxy having dielectric constant $\epsilon'_r = 4.28$ and thickness $h = 1.6$ mm.

Figures 3.4 (a) show the geometry of the antenna. As the first step of the design, a printed dipole antenna of dimension 4 x 4 cm is optimized by experimental iterations to have a resonant frequency of 3 GHz. The edges of the dipole are then flared to enhance the band width as shown in Fig.3.4 (b). The results of this optimum design are discussed in Section 3.7 of this chapter.

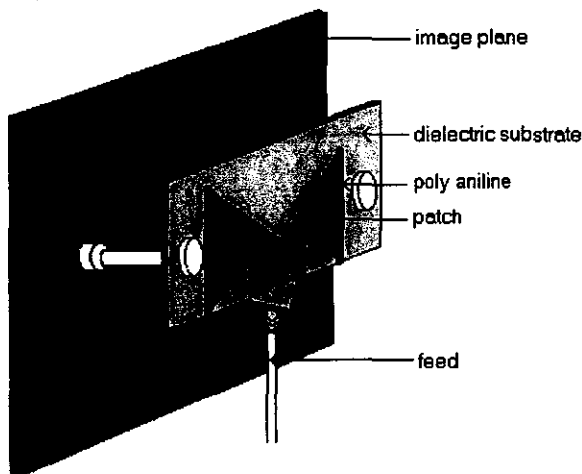


Figure 3.4 (a) Geometry of the antenna

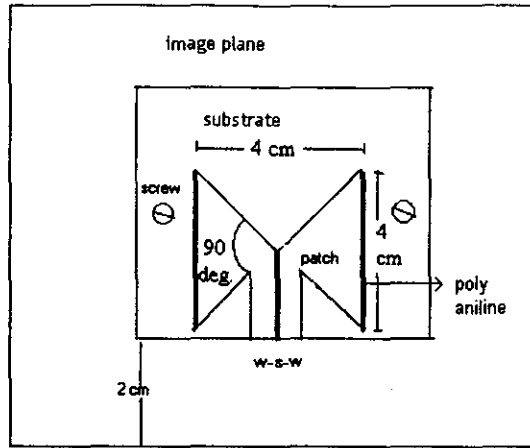


Figure 3.4 (b) Geometry of the antenna -Top view

w-s-w = 5 – 0.5 –5 (all mms.)

The coplanar strip line feed is designed using the Quasi-Static Analysis.

Figure 3.5 shows the geometry of the coplanar strip.

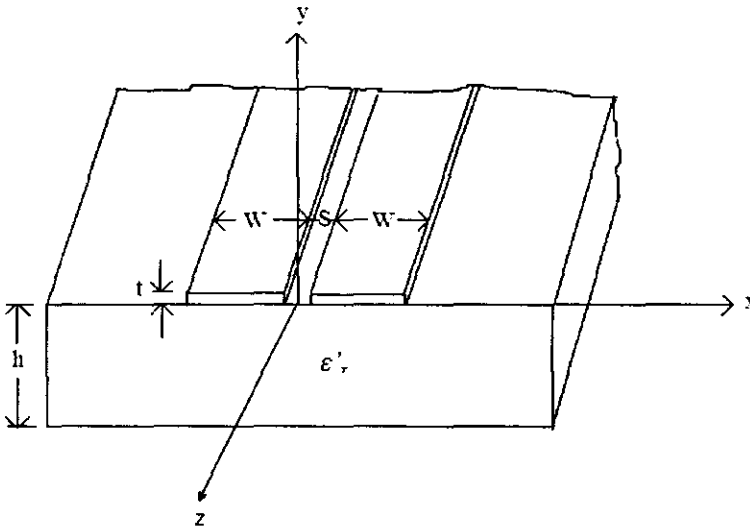


Figure 3.5. Geometry of the coplanar strip line.

Quasi static analysis of the coplanar strip line is carried out using the conformal mapping method where the dielectric substrate thickness h is sufficiently large and can be considered infinite in the analytic model

(Here the effective thickness of the substrate is large due to the presence of the ground plane attached at a distance.). The strip and the metallization thickness are considered negligible. The conformal transformation which maps the dielectric half plane z_1 (Figure 3.6 (a)) of coplanar strip into an interior of a rectangle in the z -plane (Figure 3.6 (b)), with conductor surface on the sides and air-dielectric interfaces on the top and the bottom is given by [38],

$$\frac{dz}{dz_1} = \frac{A}{(z_1^2 - a_1^2)^{1/2}(z_1^2 - b_1^2)^{1/2}} \quad (3.1)$$

where A is a constant. The a/b of the rectangle in the z -plane may be evaluated by carrying out the integration,

$$a + jb = \int_0^{b_1} \frac{Adz_1}{(z_1^2 - a_1^2)^{1/2}(z_1^2 - b_1^2)^{1/2}} \quad (3.2)$$

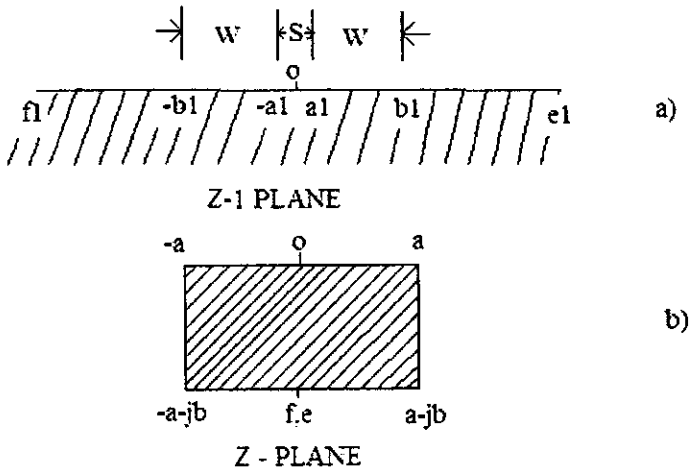


Figure 3.6. Conformal Transformation Planes for Coplanar Strip Analysis

and is given by,

$$\frac{a}{b} = \frac{K(k)}{K'(K)} \quad (3.3)$$

where $K(k)$ is the complete elliptic integral of the first kind and

$$k = \frac{a1}{b1} = \frac{S}{S + 2W} \quad (3.4)$$

$$k' = \sqrt{1 - k^2} \quad (3.5)$$

The total line capacitance per unit length of the line contributed by the dielectric half space may be written as,

$$C = (\epsilon_r' + 1)\epsilon_o(b/2a) \quad (3.6)$$

Using quasi static approximation the phase velocity can be written as

$$v_{cp} = \left(\frac{2}{\epsilon_r' + 1} \right)^{1/2} c \quad (3.7)$$

The characteristic impedance thus becomes,

$$Z_o = \frac{1}{Cv_{cp}} = \frac{120\pi}{\sqrt{\epsilon_r' + 1}} \frac{K(k)}{K'(k)} \quad (3.8)$$

The complete elliptic integral of first kind [38] takes the value,

$$\frac{K(k)}{K'(k)} = \frac{\pi}{\ln \left[2 \frac{1 + \sqrt{k'}}{1 - \sqrt{k'}} \right]} \quad \text{for } 0 \leq k \leq 0.707 \quad (3.9)$$

Using eqn. 3.8 and 3.9, the coplanar strip feed is designed for an impedance of 50Ω and hence S and W takes the values of 0.5 mm and 5 mm respectively.

For the present antenna an optimum distance of 2 cm is selected for the image plane, to obtain good bandwidth and maximum forward radiation in the operating band. The details of this optimum selection are discussed in Section 3.7. Thus the substrate thickness $(h + t)$ becomes 2.16 cm which is much greater than the strip width and hence suitable for the quasi static

analysis. This thickness parameter is conveniently incorporated in the numerical analysis of the antenna using FDTD analysis described in the following section.

To minimize the edge reflections of the antenna, a 1 mm wide coating of polyaniline is given at the edges. Results of this analysis are discussed in Section 3.7. Polyaniline having dielectric constant of 11.32 and conductivity of 0.072 at 2.983 GHz is reported [39] to be a good microwave absorbing material.

3.6. Theoretical Analysis

A direct three-dimensional Finite-Difference Time-Domain (FDTD) method is applied for the coplanar strip line fed bow tie antenna. It is a computationally efficient means of directly solving the Maxwell's time dependent curl equations, or their integral equations using finite difference technique. The finite difference time-domain (FDTD) technique permits the analysis of interactions of electromagnetic waves with material bodies of any desired shape. An FDTD code that can be used for calculating the scattering parameters as well as the current and field distribution over the surface and edges is generated. The accuracy of the analysis is validated through experiments.

The antenna geometry is divided into cells for which necessary boundary conditions are applied. Conducting surfaces are treated by setting the tangential electric field components to zero.

3.6.1 FDTD Modelling Theory

The direct time-domain solutions of Maxwell's equations using the FDTD technique for the analysis of electromagnetic wave interactions with arbitrary material structures appear to be suitable for simulating planar patch geometries that are too large or too complex for simulation by any other principal

numerical technique available today. The FDTD technique helps in modelling electromagnetic wave interactions by applying to the respective differential operators of the curl equations of simple second order accurate central-difference approximations for the space and time derivatives of the electric and magnetic fields. Space and time discretization are selected to bound errors in the sampling process and to ensure numerical stability of the problem. The electric and magnetic components are interleaved in space to permit a natural satisfaction of the tangential field continuity conditions at media interfaces. Application of FDTD techniques to various electromagnetic problems is available in the literature [8, 17-19, 40-43].

The basic steps presented in this analysis consist of the analysis of Yee algorithm [41] based on Maxwell's equations and the equivalent set of Finite Difference Equations.

Maxwell's curl Equations in an isotropic medium are:

$$\nabla \times E = -\frac{\partial B}{\partial t} \quad (3.10)$$

$$\nabla \times H = J + \frac{\partial D}{\partial t} \quad (3.11)$$

$$B = \mu H \quad (3.12)$$

$$D = \epsilon E \quad (3.13)$$

In a rectangular coordinate system, eqns. 3.10 and 3.11 are equivalent to the following system of scalar equations:

$$-\frac{\partial B_x}{\partial t} = \frac{\partial E_z}{\partial y} - \frac{\partial E_y}{\partial z} \quad (3.14)$$

$$-\frac{\partial B_y}{\partial t} = \frac{\partial E_x}{\partial z} - \frac{\partial E_z}{\partial x} \quad (3.15)$$

$$\frac{\partial B_z}{\partial t} = \frac{\partial E_y}{\partial x} - \frac{\partial E_x}{\partial y} \quad (3.16)$$

$$\frac{\partial D_z}{\partial t} = \frac{\partial H_x}{\partial y} - \frac{\partial H_y}{\partial x} - J_z \quad (3.17)$$

$$\frac{\partial D_y}{\partial t} = \frac{\partial H_z}{\partial x} - \frac{\partial H_x}{\partial z} - J_y \quad (3.18)$$

$$\frac{\partial D_x}{\partial t} = \frac{\partial H_y}{\partial z} - \frac{\partial H_z}{\partial y} - J_x \quad (3.19)$$

The boundary condition appropriate for a perfectly conducting surface is that the tangential components of the electrical fields vanish [44]. This condition also implies that the normal component of the magnetic field vanish on the surface. The conducting surface may therefore be approximated by a collection of surfaces of cubes, the sides of which are parallel to the coordinate axis. Plane surfaces, perpendicular to the x-axis will be chosen so as to contain points where, E_x and E_y are defined.

The basic Yee algorithm helps us to solve both electric and magnetic fields in time and space using the coupled Maxwell's curl equations instead of solving either one of these with a wave equation [44]. The grid points for the E-field and H-field are chosen as shown in Figure 3.7

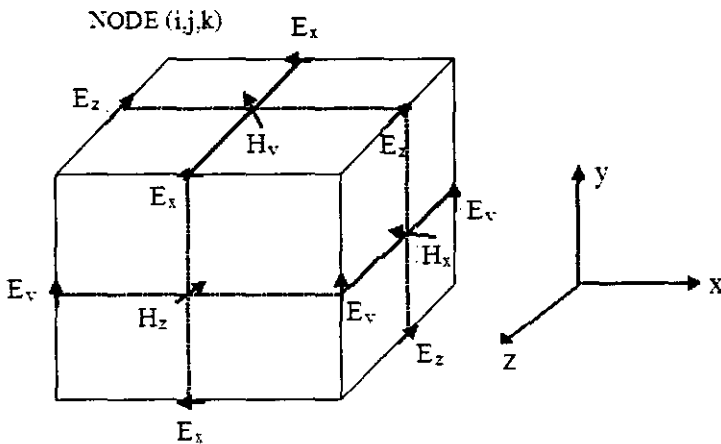


Figure 3.7. Field component placement in FDTD unit cell

The Yee algorithm centres its \vec{E} and \vec{H} components in a three dimensional space so that every \vec{E} component is surrounded by four circulating \vec{H} components, and every \vec{H} component is surrounded by four circulating \vec{E} components.

Continuity of tangential \vec{E} and \vec{H} is maintained across an interface of dissimilar materials if the interface is parallel to one of the grid coordinate axis. At the beginning of the problem, we can specify the material permittivity and permeability at each field component location. For a square Yee-mesh this yields a 'stepped', approximation of the surface and internal geometry of the antenna with a space resolution set by the size of the unit cell.

The configuration of the coplanar strip line fed bow tie antenna along with the coordinate system is shown in Figure 3.8

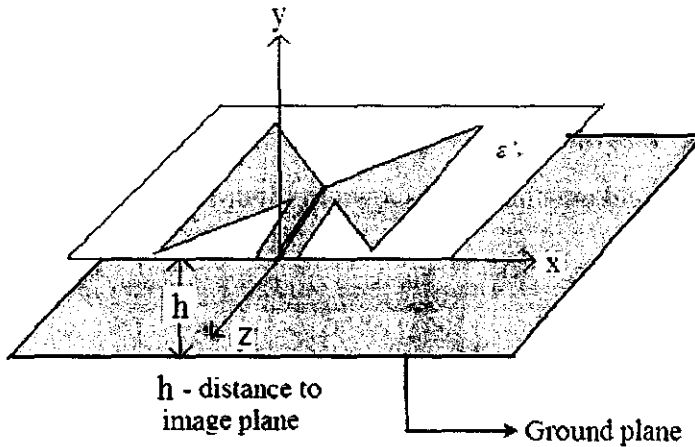


Figure 3.8 Configuration of the coplanar strip line fed bow tie antenna

3.6.2 FDTD Problem Definition

In the present analysis, space grid size is selected such that the electromagnetic field does not vary significantly over one increment. For this

the linear dimensions of the grid must be only a fraction of the wavelength. For computational stability, it is necessary to satisfy the condition between the space increments $\Delta x = \Delta y = \Delta z$, and the time increment Δt .

The notations used for the analysis are generalized into three spatial dimensions; a space point in a uniform rectangular lattice is represented as;

$$(i,j,k)=(i\Delta x,j\Delta y,k\Delta z) \quad (3.20)$$

Here, Δx , Δy and Δz are the lattice space increments in the x, y and z coordinate directions, and i,j and k are integers. The coplanar strip line fed bow tie antenna design is partitioned into six rectangular geometries and the formulation of the FDTD method begins by considering the differential form of Maxwell's two curl equations that govern the propagation of fields.

3.6.3 FDTD Source Excitation and Principal Equations

The FDTD analysis depends on the volumetric sampling of the unknown electric and magnetic fields within and surrounding the structure of interest, and over a period of time. At time $t=0$, the fields are assumed to be identically zero throughout the computational domain. A Gaussian pulse is used for the excitation as its frequency spectrum is also Gaussian in nature and will therefore provide frequency domain information from dc to the desired cut-off frequency by adjusting the width of the pulse. As the structure becomes complicated, tens or even hundreds of thousands of time steps may be required for the FDTD calculations to converge, especially for transient excitation.

For simplicity of analysis, the media are assumed to be piecewise uniform, isotropic and homogenous. The structure is assumed to be loss less, [41] (no volume currents or finite conductivity). Based on these assumptions, Maxwell's curl equations may be written as:

$$\mu \frac{\partial H}{\partial t} = -\nabla \times E \quad (3.21)$$

$$\varepsilon \frac{\partial E}{\partial t} = \nabla \times H \quad (3.22)$$

In order to find an approximate solution to this set of equations, the problem is discretized over a finite three-dimensional computational domain with appropriate boundary conditions enforced on the antenna mesh walls. The six field locations are considered to be interleaved in space as shown in Figure 3.7, which is a drawing of the FDTD unit cell [41]. Here since the domain in which the field has to be computed is unbounded an absorbing boundary condition by using a mesh of limited size, but large enough to fully contain the obstacle has to be applied.

FDTD antenna or transient calculations are excited by a voltage source in which the internal source resistance is zero. These sources can be implemented in an FDTD code for calculating the current and field distribution. The electric field at the mesh edge where the source is located is determined by a Gaussian pulse, which is significantly greater than zero amplitude for only a very short fraction of the total computation time. Once the pulse amplitude drops the source voltage becomes essentially zero, thus any reflection from the antenna, which return to the source, is totally reflected back. The introduction of a source with the implementation of an internal source resistance to excite the FDTD calculation provides an additional loss mechanism to dissipate this energy introduced into the calculation space which in turn results in reducing the FDTD calculation time appreciably.

To simulate a voltage source excitation, it is necessary to impose the vertical electrical field, E_y , in a square region above the ground plane as shown in Figure 3.7. The remaining electric field components on the source plane are to be set zero. An excitation scheme is generated to simulate a magnetic wall

directly on the source plane using image theory, then the remaining electric field components on the source plane can be calculated using the finite-difference equations, with minimum source distortion. The launched wave has nearly unit amplitude and is Gaussian in time which is given by:

$$E_y = f_s(t) = e^{-(t-t_0)^2} / T^2 \quad (3.23)$$

This excitation will result in the fundamental mode only propagating down the patch in the desired frequency range of interest.

The antenna design under investigation has a conducting ground plane attached at a distance and a single dielectric substrate with metallization on top. These electric conductors are assumed to be perfectly conducting and have zero thickness and are treated by setting the electric field components that lie on the conductors to be zero. The edge of the conductor should be modeled with electric field components tangential to the edge lying exactly on the edge of the patch as shown in Figure 3.8

3.6.4 Finite Difference Equations

To obtain discrete approximations of the continuous partial differential equations, the central difference approximation is used on both the time and space first order partial differentiations. The antenna geometry is divided into six rectangular field locations and each conducting surfaces are treated by setting tangential electric field components to zero. These six field locations are considered to be interleaved in space as illustrated in Figure 3.7. The entire computational domain is obtained by stacking these rectangular cubes, into a larger rectangular volume. The \hat{x} , \hat{y} , and \hat{z} dimensions of the unit cell are Δx , Δy , and Δz , respectively. Here the centered differences are realized in the calculation of each field component and that continuity of tangential field components is hence automatically satisfied. As there are only six unique field components within the unit cell, the six field components touching the shaded

upper corner of the unit cell in Figure 3.7 are considered to be a unit node with subscript indices i, j and k corresponding to the node numbers in the \hat{x} , \hat{y} , and \hat{z} directions. This notation implicitly assumes the $\pm 1/2$ space indices and thus simplifies the notation. The time steps are indicated with the superscript n . We can rewrite the explicit finite difference approximations to Eqns.3.21 and 3.22 as:

$$H_x^{n+1/2} = H_x^{n-1/2} + \frac{\Delta t}{\mu\Delta z}(E_y^n_{i,j,k} - E_y^n_{i,j,k-1}) - \frac{\Delta t}{\mu\Delta y}(E_z^n_{i,j,k} - E_z^n_{i,j-1,k}) \quad (3.24)$$

$$H_y^{n+1/2} = H_y^{n-1/2} + \frac{\Delta t}{\mu\Delta x}(E_z^n_{i,j,k} - E_z^n_{i-1,j,k}) - \frac{\Delta t}{\mu\Delta z}(E_x^n_{i,j,k} - E_x^n_{i,j,k-1}) \quad (3.25)$$

$$H_z^{n+1/2} = H_z^{n-1/2} + \frac{\Delta t}{\mu\Delta y}(E_x^n_{i,j,k} - E_x^n_{i,j-1,k}) - \frac{\Delta t}{\mu\Delta x}(E_y^n_{i,j,k} - E_y^n_{i-1,j,k}) \quad (3.26)$$

$$E_x^{n+1} = E_x^n_{i,j,k} + \frac{\Delta t}{\epsilon\Delta y}(H_z^{n+1/2}_{i,j+1,k} - H_z^{n+1/2}_{i,j,k}) - \frac{\Delta t}{\epsilon\Delta z}(H_y^{n+1/2}_{i,j,k+1} - H_y^{n+1/2}_{i,j,k}) \quad (3.27)$$

$$E_y^{n+1} = E_y^n_{i,j,k} + \frac{\Delta t}{\epsilon\Delta z}(H_x^{n+1/2}_{i,j,k+1} - H_x^{n+1/2}_{i,j,k}) - \frac{\Delta t}{\epsilon\Delta x}(H_z^{n+1/2}_{i+1,j,k} - H_z^{n+1/2}_{i,j,k}) \quad (3.28)$$

$$E_z^{n+1} = E_z^n_{i,j,k} + \frac{\Delta t}{\epsilon\Delta x}(H_y^{n+1/2}_{i+1,j,k} - H_y^{n+1/2}_{i,j,k}) - \frac{\Delta t}{\epsilon\Delta y}(H_x^{n+1/2}_{i,j+1,k} - H_x^{n+1/2}_{i,j,k}) \quad (3.29)$$

The half time steps indicate that the E and H are alternatively calculated in order to achieve centered differences for the time derivatives. In these equations, the permittivity and permeability are set to the appropriate values depending on the location of each field component. For the electric field

components on the dielectric air-interface the average of two permittivities $(\epsilon_0 + \epsilon_r)/2$, is used [40].

Due to the use of these centered differences, the error is second order in both the space and time steps; i.e., if Δx , Δy , and Δz and Δt are proportional to Δl , then the overall error will be $O(\Delta l)^2$. The maximum time step that may be used is limited by the stability criterion of the finite difference equations:

$$\Delta t \leq \frac{1}{V_{\max}} \left(\frac{1}{\Delta x^2} + \frac{1}{\Delta y^2} + \frac{1}{\Delta z^2} \right)^{-1/2} \quad (3.30)$$

where, V_{\max} , is the maximum velocity of light within the computational volume. Typically, V_{\max} , will be the velocity of light in free space unless the entire volume is filled within the dielectric. These equations will allow the appropriate solution of $E(\mathbf{r},t)$ and $H(\mathbf{r},t)$ in the volume of the computational domain or mesh; however, special consideration is required for the source, the conductors and the mesh walls. All of the \vec{E} -computations in the three dimensional space of interest are completed and stored in memory for a particular time point using \vec{H} -data previously stored in the system memory. The reverse process is repeated for the \vec{H} -computations.

The equations for individual unit cells are identical for lossy dielectric, perfect conductor and free space. The FDTD implementation uses pulse excitation, which provides a wide band of frequencies with a single fast Fourier Transform.

3.6.5. Absorbing Boundary Conditions for the Finite-Difference

Approximation

When time-domain electromagnetic field equations are solved using finite-difference techniques in unbounded space, there must be a method for limiting the domain in which the field is computed. This is achieved by truncating the mesh in \hat{x} , \hat{y} and \hat{z} directions and applying absorbing boundary conditions at

its artificial boundaries to simulate the unbounded surroundings. One of the six mesh boundaries is a ground plane and its tangential electric field values are forced to be zero. The tangential electric field components on the remaining five mesh walls are represented as if the outgoing waves are not reflected using the absorbing boundary conditions. In this approach, the pulses on the patch will be incident normally to the mesh walls. This results in a simple approximate continuous absorbing condition that the tangential field on the outer boundaries will obey the one-dimensional wave equation in the direction normal to the mesh wall. For the \hat{y} normal wall the one-dimensional wave equation is:

$$\left(\frac{\partial}{\partial y} - \frac{1}{v} \frac{\partial}{\partial t} \right) E_{\text{tan}} = 0 \quad (3.31)$$

The above equation is the first approximate boundary condition [43] and it may be easily discretized using only few field components on or just inside the mesh wall, yielding an explicit finite difference equation.

$$E_0^{n+1} = E_1^n + \frac{v\Delta t - \Delta y}{v\Delta t + \Delta y} (E_1^{n+1} - E_0^n) \quad (3.32)$$

Here, E_0 represents the tangential electric field components on the mesh wall and E_1 represents the tangential electric field components on node inside the mesh wall. This normal incidence assumption is not valid for the fringing fields, which are propagating tangential to the walls, so the sidewalls should be far enough in order to make the fringing fields negligible at the walls. Moreover, radiation will not be exactly normal to the mesh walls. Second order absorbing boundary conditions that account for oblique incidence will not work on the mesh walls because these absorbing boundary conditions are derived in uniform space.

The finite difference equations (3.24-3.29) are used with the above boundary and source conditions to simulate the propagation of a broadband Gaussian pulse on the patch.

Here the reflections from the antenna edges will be reflected by the source wall. This is avoided by placing the source wall patch at a sufficient distance from the source, and after the Gaussian pulse has been fully launched, the absorbing boundary condition is turned ON at the boundary walls.

To excite an FDTD calculation with a voltage source mentioned above, which corresponds to an electric field E in the z -direction at a certain mesh location $i_s\Delta x$, $j_s\Delta y$, and $k_s\Delta z$. To converge the FDTD calculation time steps at a faster rate, a source resistance is included along with the voltage source and the equivalent source is depicted in Figure 3.9

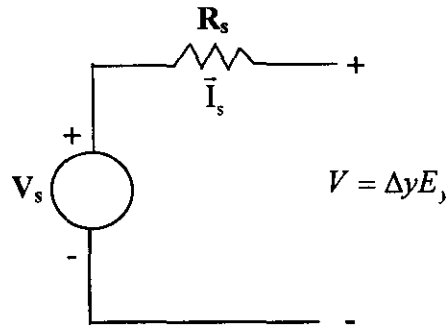


Figure 3.9. FDTD Source with source Resistance ‘ R_s ’

If the source resistance R_s is set to zero, then the usual FDTD electric field at the source location is given by:

$$E_s^n(i_s, j_s, k_s) = V_s(n\Delta t) / \Delta y \quad (3.33)$$

V_s is the Gaussian Pulse.

With the source resistance included, the calculation of the source field $E_s^n(i_s, j_s, k_s)$ becomes complicated and to determine the terminal voltage in the circuit and the source field the current through the source must be

determined by applying Ampere's circuital law. The current through the source is given by:

$$I_s^{n-1/2} = [H_z^{n-1/2}(i_s, j_s, k_s) - H_z^{n-1/2}(i_s - 1, j_s, k_s)]\Delta z + [H_x^{n-1/2}(i_s, j_s, k_s) - H_x^{n-1/2}(i_s, j_s, k_s - 1)]\Delta x \quad (3.34)$$

Now, by applying Ohm's law, to the circuit of Figure 3.10, the electric field source is given by,

$$E_s^n(i_s, j_s, k_s) = V_s(n\Delta t) / \Delta y + I_s^{n-1/2} R_s / \Delta y \quad (3.35)$$

The value of the source resistance cannot be made too large; otherwise instabilities can occur due to neglecting the displacement current through the FDTD cell containing the source.

The value of the internal resistance does not appear to be critical. A reasonable choice of for R_s is to implement the value of the characteristic impedance depending on the particular antenna geometry.

3.6.6. Calculation of Scattering Parameters

The frequency dependant scattering matrix coefficients can be calculated.

$$[V]^r = [S][V]^i \quad (3.36)$$

where, $[V]^r$ and $[V]^i$ are the reflected and incident voltage vectors, and $[S]$ is the scattering matrix. It is assumed that this field value is proportional to the voltage considering the propagation of the fundamental mode. To obtain the scattering parameters $S_{11}(\omega)$, the incident and reflected waveforms must be known. The FDTD simulation calculates the sum of the incident and the reflected waveforms. To obtain the incident waveform, calculation is performed using only port 1 of the patch, which will now be of infinite extent and the incident waveform is noted. This incident waveform is then subtracted from the total waveform (incident + reflected) to yield the reflected waveform for port1. The scattering parameters, S_{jk} , can be calculated by simple Fourier Transform of the transient waveform as;

$$S_{jk}(w) = \frac{FT[V_j(t)]}{FT[V_k(t)]} \quad (3.38)$$

Here the reference planes are selected with enough distance from the patch discontinuities to eliminate evanescent waves. These distances are included in the definition of the circuit so that no phase correction is performed for the scattering coefficients. For all of the circuits considered, the only unique coefficients are in the first column of the scattering matrix such as $S_{11}(w)$, $S_{21}(w)$, $S_{31}(w)$...etc.

3.6.7 Flow Chart of the Algorithm

The important aspects of the time-domain algorithm are as follows:

- Initially (at $t=n=0$) all fields are 0.
- The following steps are repeated until the response is ≈ 0 :
 - Gaussian Impulse is imposed the source plane.
 - $H^{n+1/2}$ is calculated from FD equations.
 - E^{n+1} is calculated from FD equations.
 - Tangential E is set to 0 on conductors.
 - Save desired field equations.
 - $n \rightarrow n+1$
- Compute the scattering matrix coefficients from time domain results.

3.6.8 FDTD design of bowtie antenna

The numerical analysis has been computed based on the FDTD code formulated in Matlab 7.0. The volume in which the simulation for the antenna geometries is to be performed is depicted in Figure 3.10. The slanted edges of the antenna are approximated using stair casing with millimeter spatial grid resolution. The computation domain consists of 100 x 40 x 100 Yee cells in the x, y, and z directions respectively. Space step of

1 mm is chosen to accommodate the antenna structure conveniently. As per the quasi static analysis of the coplanar strip feed, the substrate thickness h is considered to be of very large compared to the width of the strip ($2.16 \text{ cm} > 0.005 \text{ cm}$). This analysis is incorporated in the FDTD design by considering 40 cells of 1mm each in the y direction of which 30 cells are considered in the $-y$ direction and 10 cells in the $+y$ direction. The time step selected is 0.25 ps to ensure Courant Stability condition. The Gaussian half width T and the time delay t_0 are set to be 15 ps and 45 ps respectively.

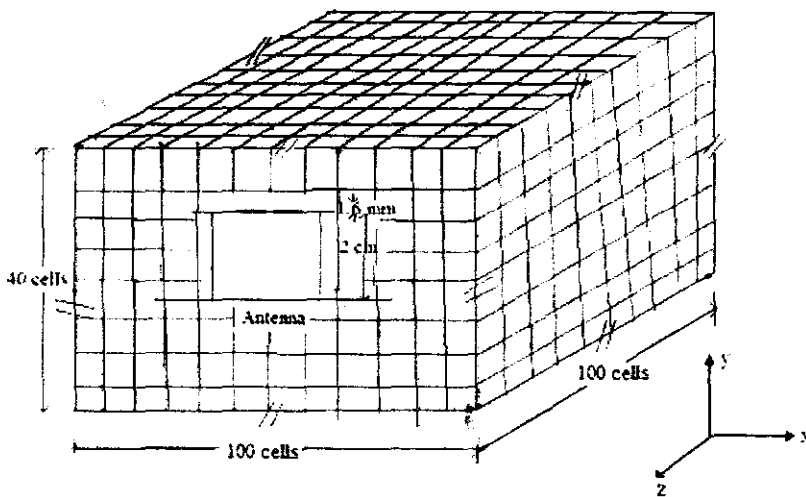


Figure 3.10. Computational Domain for Antenna Simulation

An internal source resistance ($R_s=50\Omega$) is also incorporated into the geometry. This helps us to reduce the computational time significantly thereby enhancing computational efficiency.

The FDTD design indicates the material properties in terms of ϵ and μ (equations 3.24 to 3.29). The values taken for $\epsilon = \epsilon_0 \epsilon_r$ where $\epsilon_r = 4.28$ for FR4 Glass epoxy substrate and 1 for air. At the dielectric air-

interface the average of two permittivities $(\epsilon_0 + \epsilon_r)/2$, is used. μ is taken as μ_0 , as the material is non magnetic.

3.7. Results and Discussions

The experimental analysis of the antenna is performed using the experimental set up shown in Figure 2.4 of Chapter 2. As the first step, the set up is calibrated using the TRL calibration procedure explained in Section 2.6. The antenna is then connected to port 1 of the experimental set up for the measurement of S11. For this, the start frequency is selected as 1.5 GHz, stop frequency as 4 GHz and number of points selected as 201 in the network analyzer.

At first, a printed dipole antenna of dimension 4 x 4 cm is optimized to have a resonant frequency of 3GHz by experimental iterations. The edges of the dipole are then flared to enhance the band width. The performance of the antenna for different flare angles are shown in Table 3.1. As the flare angle of the bow is increased, the bandwidth increases, with the resonant frequency remaining almost constant. The flare angle is optimized as 90 degrees for maximum band width and a resonant frequency of 3 GHz.

Table 3.1 Performance of the antenna for different flare angles.

Flare angle degrees	Operational band (GHz)	Resonant frequency(GHz)	Return Loss (dB)	Bandwidth %
30	2.22 – 2.73	2.93	-20	17.46
60	2.27 – 3.12	2.95	-35	28.81
90	1.85 – 3.435	3.0	-42	52.8

Table 3.2 Performance of the antenna for different distances of the image plane

Distance to the image plane (cms)	Operational band (GHz)	Resonant frequency (GHz)	Return Loss (dB)	Bandwidth %
0.8	2.425 – 3.27	3.02	-18	27.98
1.4	2.275 – 3.25	2.95	-32	33.05
2	1.85 – 3.435	3.0	-52	52.8
2.6	1.875 – 3.750	2.9	-41	64.6
without image plane	2.2 – 4.29	2.95	-42	70.84

The flared coplanar antenna without conductor backing, exhibited high 2:1 VSWR bandwidth of 71%, but a figure of eight radiation pattern. Hence to reduce these back radiations, a conductor backing of dimension 8 x 8 cm is provided and is fixed to the bow tie patch using low loss Teflon screws. The performance of the antenna for various distance of this image plane is studied. Table 3.2 shows this result. Thus the antenna is optimized to have a dimension 4x4 cm, flare angle 90° and a distance of 2 cm with the image plane.

The S11 characteristics of the optimized bow tie antenna exhibited lossy performance, which is due to the edge reflections. To minimize this, a 1mm wide polyaniline coating is provided at the antenna edges and the results are shown in Figure 3.11. The polyaniline coating reduces the edge reflections and provides good matching.

The S21 characteristics of the antenna are measured by connecting bow tie antenna to port 1 and standard wide band Horn antenna to port 2. The number of measurement points is selected as 201 in the network analyzer with the center frequencies selected as 2.2 GHz, 3 GHz and 3.2

GHz. Figures 3.12 (a, b, c) show the E and H - plane radiation patterns of

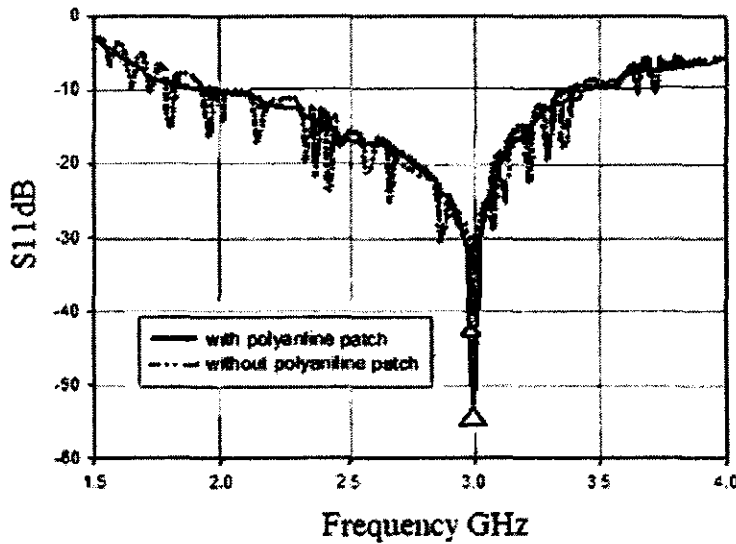


Figure 3.11. Effects of polyaniline strip on return loss

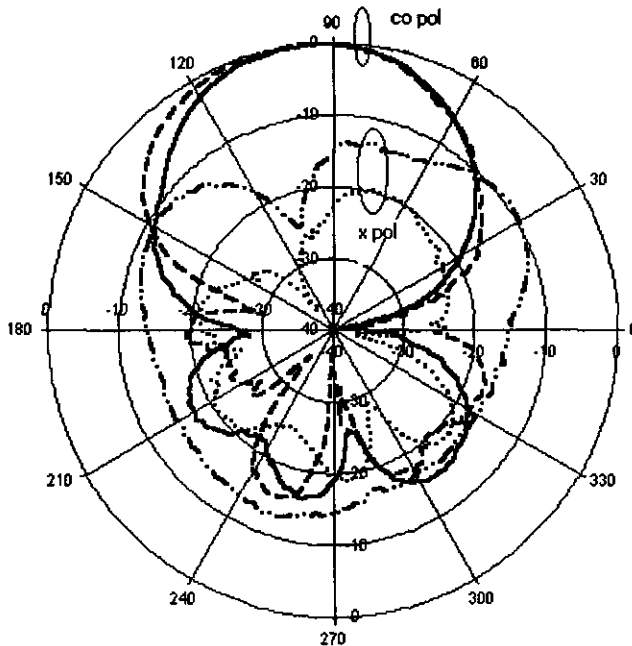


Figure 3. 12 (a) Radiation pattern of the antenna measured at 2.2 GHz.

— Eco ; Ecross ; - - Hco ; - · - Hcross

the antenna. It is observed that the pattern remains similar throughout the operational band. A reduction of around 20 dB in cross polarization is observed on the on-axis of both E and H planes. The antenna exhibits a HPBW of 53° and 55° for E and H planes respectively at 2.2 GHz, 55° and 56° for E and H planes respectively at 3 GHz, and, 53° and 56° for E and H planes respectively at 3.2 GHz. It is observed that at all the frequencies, E and H plane radiation patterns exhibit slight squint. Also some back lobes are also observed, even after the usage of image plane.

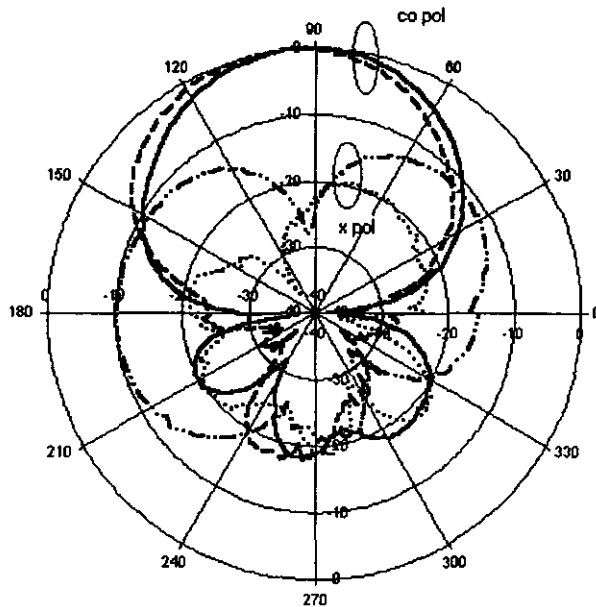


Figure 3. 12 (b) Radiation pattern of the antenna measured at 3 GHz.

— E_{co} , E_{cross} , -- H_{co} : - · - · H_{cross}

In the microwave imaging studies presented in this thesis, all the measurements performed are relative and not absolute. So the effects of back lobes and squint in the measurement are relative and hence the errors in the measurement are cancelled. To substantiate this, the antenna has been used to image the dielectric contrasts of known samples like wax with

inclusion of water and is shown in Table A.1.(f) of Appendix A. Accurate results obtained for the dielectric constants of wax and water with clear discrimination at the boundary, shows that the error in the measurement is relative and gets cancelled.

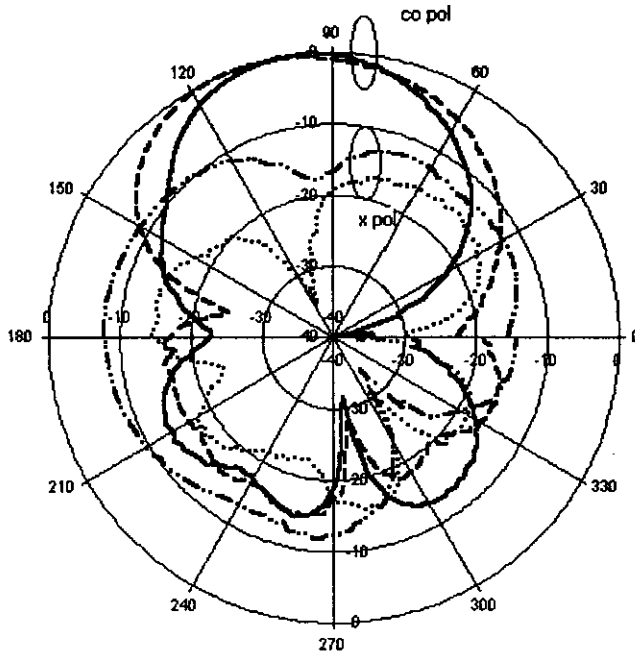


Figure 3.12 (c) Radiation pattern of the antenna measured at 3.2 GHz.

— E_{co} ,E_{cross} , -- H_{co} : -·-· H_{cross}

To measure the gain of the antenna, the network analyzer is calibrated using a circular microstrip patch antenna having a resonant frequency of 3 GHz. It is observed that the bowtie antenna exhibits a gain of 1 dB less than that of the circular patch antenna at 3 GHz.

Numerical evaluation of the antenna is performed using FDTD analysis. The computation is performed for 2500 time steps till the field stabilizes. Figure 3.13 shows the return loss of the optimized antenna. The FDTD computed bandwidth of 59 % in the operational band of 1.77 – 3.55

GHz, complements the experimentally obtained bandwidth of 53 % in the operational band of 1.85 – 3.425 GHz while the resonant frequency remains unchanged as 3 GHz.

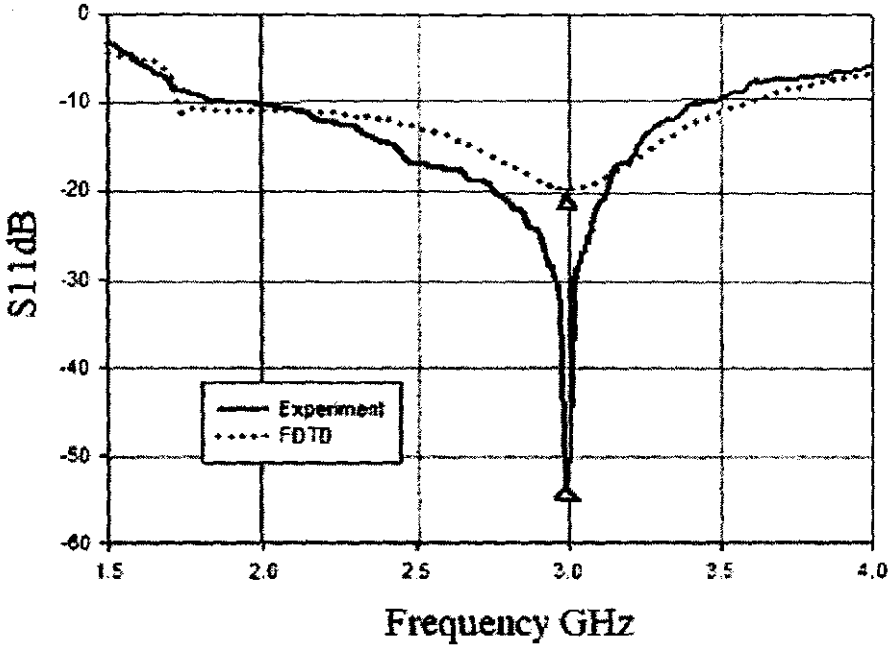


Figure 3. 13. Return loss of the antenna

The stabilized voltage computed at the feed point of the antenna using FDTD analysis is shown in Figure 3.14. The field stabilizes with 2500 time steps. The end reflection of the antenna is computed by taking the power ratio of one half of the peak to peak amplitude [16] between A and B marked in the Figure 3.14. It is observed that the antenna exhibits end reflection of -24 dB which is much less than the reported -6 dB for the simulated bow tie antenna reported by Hagness et al [16]. Figure 3.15 shows the stabilized spatial waveform of the E_y component sampled just

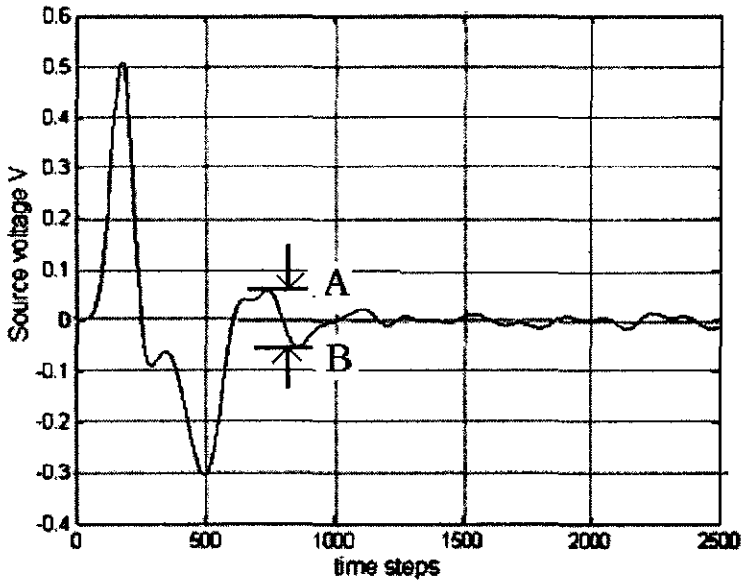


Figure 3. 14. Stabilized voltage computed at the feed point of the antenna

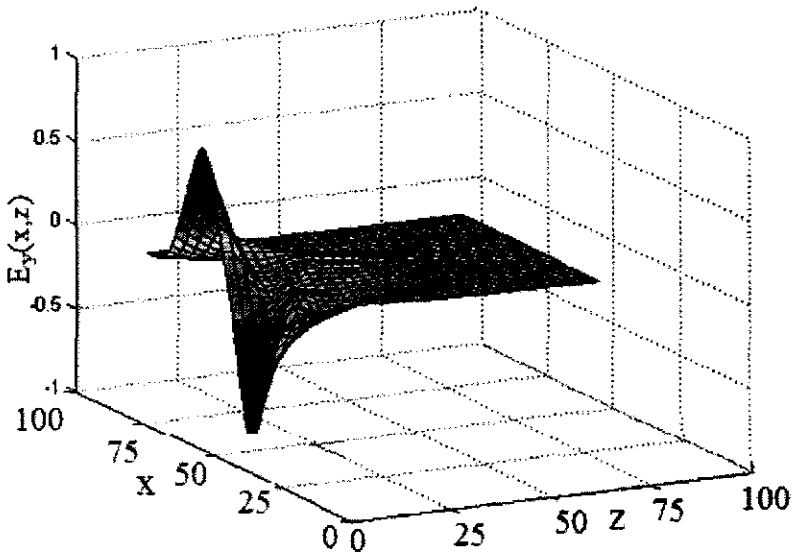


Figure 3. 15. Spatial waveform of the E_y component sampled just below the strips

below the strips, computed using FDTD analysis. It is observed that the field stabilizes perfectly with 2500 time steps.

The overall performance of the optimized antenna at 3 GHz is summarized in Table 3.3.

Table 3.3 Performance of the optimized antenna at 3GHz

Band width		Return Loss		HPBW		Back lobe level	Gain
Experiment	FDTD	Experiment	FDTD	E - Plane	H-Plane		
53%	59%	-52 dB	-20 dB	55 ⁰	56 ⁰	-20 dB	< 1dB of circular patch antenna

3.8. Conclusion

A novel planar bow tie antenna with coplanar strip line feed is developed. The new antenna exhibits wide operational band of 1.575 GHz with a resonant frequency of 3 GHz, and a HPBW of 55⁰ and 57⁰ for E and H planes respectively. Moreover the antenna is compact and easy to fabricate. Theoretical analysis of the antenna is performed using Finite Difference Time Domain Analysis and good agreement is obtained with the experimental results. The antenna is ideal for time domain confocal microwave imaging where short transient pulses are required for illuminating the target. For microwave tomographic imaging the antenna can be operated at the resonant frequency of 3 GHz where good matching is observed.

3.9 References

1. A.W.Guy, J.F.Lehman, J.B.Stonebridge, C.C.Soreson, "Development of a 915 MHz direct contact applicator for therapeutic heating of tissues", *IEEE Transactions on Microwave Theory and Techniques*, vol. MTT 26, pp. 550 - 556, 1978.
2. A.Y.Cheung, T. Dao, J.E.Robinson, "Dual beam TEM applicator for direct contact heating of dielectrically encapsulated malignant mouse tumor", *Radio Science*, vol. 12, pp. 81 - 85, 1977.
3. F. Sterzer, R.W.Pagilone, J.Mendecki, E.Friedenthal, C.Botstein, "RF therapy for malignancy", *IEEE Spectrum*, pp. 32 - 37, 1980.
4. I.J.Bahl, S.S.Stuchly, J.J.W. Lagendijk, M.A.Stuchly, "Microstrip loop radiators for medical applications," *IEEE Transactions on Microwave Theory and Techniques*, vol. MTT 30, pp. 1090 - 1093, 1982.
5. Xu Li, S.C.Hagness, M.K.Choi, D.W.van der Weide, "Numerical and experimental investigation of an ultra wideband pyramidal horn antenna with curved launching plane for pulse radiation", *IEEE Antennas and Wireless Propagation Letters*, vol.2, pp. 259 - 262, 2003.
6. Xu Li, S.K.Davis, S.C.Hagness, D.W.van der Weide, B.D.Van Veen, "Microwave imaging via space time beamforming: experimental investigation of tumor detection in multiplayer breast phantoms", *IEEE Transactions on Microwave Theory and Techniques*, vol. 52, 1856 - 1865, 2004.
7. Xu Li, S.C.Hagness, "A confocal microwave imaging algorithm for breast cancer detection", *IEEE Microwave and Wireless Components Letters*, vol.11, pp. 130 - 132, 2001.
8. Xu Li, S.C.Hagness, E.C. Fear, M.A.Stuchly, "FDTD analysis of planar and cylindrical antenna- array configuration for 3D breast tumor localization using confocal microwave imaging", *Proc. of IEEE APS*, pp. 246 - 249, 2001.
9. P.M.Meaney, K.D.Paulsen, A. Hartov, R.K.Crane, "An active microwave imaging system for reconstruction of 2-D electrical property distributions", *IEEE Transactions on Biomedical Engineering*, vol. 42, pp. 1017 - 1026, 1995
10. P.M.Meaney, K.D.Paulsen, A. Hartov, R.K.Crane, "Microwave imaging for tissue assessment: initial evaluation in multitarget tissue-equivalent phantoms", *IEEE Transactions on Biomedical Engineering*, vol. 43, pp. 878 - 890, 1996.
11. P.M.Meaney, M.W.Fanning, D. Li, S.P.Poplack, K.D.Paulsen, "A clinical prototype of active microwave imaging of the breast", *IEEE*

- Transactions on Microwave Theory and Techniques, vol. 48, pp. 1841 – 1853, 2000.
12. P.M.Meaney, K.D.Paulsen, J.T. Chang, M.W.Fanning, “Initial microwave imaging experiments in ex-vivo breast tissue”, Proc. of First Joint IEEE BMES/ EMBS Conference Serving Humanity, Advancing Technology, pp. 1130 , 1999.
 13. E.C.Fear, M.A. Stuchly, “Microwave detection of breast cancer”, IEEE Transactions on Microwave Theory and Techniques, vol. 48, pp.1851 – 1863,2000
 14. E.C.Fear, M.A. Stuchly, “Microwave detection of breast cancer: a study of tumor response variations”, Proc. of IEEE EMBS Intl. Conference, pp. 74 – 77, 2000.
 15. E.C.Fear, J.M.Sill, “Preliminary investigations of tissue sensing adaptive radar for breast tumor detection”, Proc. of IEEE EMBS, pp. 3787 – 3790, 2003.
 16. S.C.Hagness, A.Taflove, J.E.Bridges, “Wideband ultra low reverberation antenna for biological sensing”, Electronics Letters, vol. 33, pp. 1594 – 1595, 1997.
 17. S.C.Hagness, A. Taflove, J.E.Bridges, “Three-dimensional FDTD analysis of a pulsed microwave confocal system for breast cancer detection: design of an antenna array element”, IEEE Transactions on Antennas and Propagation, vol. 47, pp. 783 – 791, 1999.
 18. S.C.Hagness, A.Taflove, J.E.Bridges, “FDTD analysis of a pulsed microwave confocal system for breast cancer detection”, Proc. of IEEE EMBS Conf., pp. 2506 – 2508, 1997.
 19. S.C.Hagness, A.Taflove, J.E.Bridges, “FDTD modeling of a coherent addition antenna array for early-stage detection of breast cancer”, Proc. of IEEE APS , pp. 1220 – 1221, 1998
 20. L. Jofre, M.S. Hawley, A. Broquetas, E de los Reyes, M. Ferrando, A.R.E. Fuster, “Medical imaging with a microwave tomographic scanner”, IEEE Transactions on Biomedical Engineering, vol. 37, pp. 303 – 311, 1990.
 21. K.D.Paulsen, P.M.Meaney , “Nonactive antenna compensation for fixed array microwave imaging – Part I: Model development,” IEEE Transactions on Medical Imaging, vol. 18, pp. 496 – 507, 1999
 22. K.D.Paulsen, P.M.Meaney , J.T.Chang, M.W.Fanning, A.Hartov, “Nonactive antenna compensation for fixed array microwave imaging – Part II: Imaging results”, IEEE Transactions on Medical Imaging, vol. 18, pp. 508 - 518, 1999
 23. K.D.Paulsen, P.M.Meaney, S. D. Geimer, S.A. Haide, M.W.Fanning, “Quantification of 3-D field effects during 2-D microwave imaging”,

- IEEE Transactions on Biomedical Engineering, vol. 49, pp. 708 – 720, 2002
24. Dun Li, P.M.Meaney, T. Raynolds, S.A.Pendegrass, M.W.Fanning, K.D.Paulsen, “A broadband microwave breast imaging system”, Proc. of IEEE EMBS, pp. 83 – 84, 2003
 25. Dun Li, P. M. Meaney, T. Raynolds, S. Pendergrass, M. Fanning, K. D. Paulsen, “A parallel-detection microwave spectroscopy system for breast imaging”, Review of Scientific Instruments, vol. 75, pp. 2305 – 2313, 2004
 26. M.A. Stuchly, E.C.Fear, “ Microwave breast tumor detection: antenna design and characterization”, Proc. of IEEE APS, pp. 1076 – 1079, 2000
 27. M.A. Stuchly, E.C.Fear, A. Low, J. Sill, “Microwave system for breast tumor detection: experimental concept evaluation”, Proc. of IEEE APS, pp. 819 – 821, 2002.
 28. M.A. Stuchly, E.C.Fear, J. Sill, “Experimental feasibility of breast tumor detection and localization”, IEEE MTT-S Digest, pp. 383 – 386, 2003
 29. X. Yun, E.C.Fear, R. Johnston, “Broadband cross-polarized bowtie antenna for breast cancer detection”, Proc. of IEEE APS, pp. 1091 – 1094, 2003.
 30. X. Yun, E.C.Fear, R. Johnston, “Radar based microwave imaging for breast cancer detection: tumor sensing with cross-polarized reflections”, Proc. of IEEE APS, pp. 2432 – 2434, 2004.
 31. S. Y.Semenov, R.H.Svenson, A.E.Boulyshev, A.E.Souvorov, V.Y.Borisov, A.N.Starostin, K.R.Dezen, G.P.Tatsis, V.Y.Baranov, “Microwave Tomography: two dimensional system for biological imaging”, IEEE Transactions on Microwave Theory and Techniques, vol. 43, pp. 869 – 877, 1996
 32. S. Y.Semenov, R.H.Svenson, A.E.Boulyshev, A.E.Souvorov, A.G.Nazarov, Y.E.Sizov, A.V.Pavlovsky, V.G.Posukh, G.P.Tatsis, “Microwave Tomography: experimental imaging on two and three dimensional systems”, IEEE MTT-S Digest, pp. 763 – 766, 1998.
 33. S. Y.Semenov, R.H.Svenson, A.E.Boulyshev, A.E.Souvorov, A.G.Nazarov, Y.E.Sizov, V.Y.Borisov, V.G.Posukh, I.M.Kozlov, A.G.Nazarov, G.P.Tatsis, “Microwave Tomography: experimental investigation of the iteration reconstruction algorithm”, IEEE Transactions on Microwave Theory and Techniques, vol. 46, pp. 133 – 141, 1998.
 34. S. Y.Semenov, R.H.Svenson, A.E.Boulyshev, A.E.Souvorov, A.G.Nazarov, Y.E.Sizov, A.V. Faviovsky, V.Y.Borisov, B.A.Voinov,

- G.I.Simonova, A.N.Staostin, V.G.Posukh, G.P.Tatsis, V.Y.Baranov, "Three dimensional microwave tomography: experimental prototype of the system and vector born reconstruction method", IEEE Transactions on Biomedical Engineering, vol. 43, pp. 937 – 945, 1999.
35. E.A.Oral, A.V.Sahakian, " 3-D microwave imaging of breast tumors with matched filtering", Proc. of IEEE EMBS, PP. 1423 – 1426, 2004
 36. Y. Zhao, W. Shao, G.Wang, "UWB microwave imaging for early breast cancer detection: effect of two synthetic antenna array configurations", IEEE conf. On Systems, Man and Cybernetics, pp. 4468 – 4473, 2004.
 37. C.J.Shannon, M.okoniewski, E.C.Fear, "A dielectric filled ultra wideband antenna for breast cancer detection", Proc. of IEEE APS, pp. 218 – 221, 2003.
 38. K.C.Gupta, R.Garg, I.J.Bahl, Microstrip lines and slotlines, Artech House Inc, 1979.
 39. Honey John, Ph. D thesis "Studies on selected conducting polymers for microwave and electrical applications", Cochin University of Science and Technology, September 2003.
 40. D.M.Sheen, S.M.Ali, M.D.abouzahra, J.A.Kong, "Application of the three-dimensional finite difference time domain method to the analysis of planar microstrip circuits", IEEE Transactions on Microwave Theory and Techniques, vol. 38, pp. 849 – 855, 1990.
 41. K.S.Yee,,"Numerical solution of initial boundary value problems involving Maxwell's equations in isotropic media", IEEE Transactions on Antennas and Propagation, vol. AP-14, pp. 302 – 307, 1966.
 42. G.Liang, Y.Liu, K.K.Mei, "Full-wave analysis of coplanar wave guide and slot line using time-domain finite difference method", IEEE Transactions on Microwave Theory and Techniques, vol. 37, pp. 1949 – 1957, 1989.
 43. G.Murr, "Absorbing boundary conditions for the finite difference approximation of the time domain electromagnetic field equations", IEEE Transactions on Electromagnetic Compatibility, vol. EMC – 23, 377 – 382, 1981.
 44. Allen Taflove, "Computational Electromagnetics" Artech House, 1995.

Chapter 4

IDENTIFICATION OF SUITABLE PHANTOM AND COUPLING MEDIUM FOR MICROWAVE MAMMOGRAPHY

4.1 Introduction

Active microwave imaging for breast cancer detection has gathered momentum in recent years because of the better tissue characterization when compared to conventional mammographic techniques. Many prototypes for active microwave imaging for breast cancer detection are proposed [1-5]. Evaluation of the performance of these prototypes requires imaging and interpretation of test objects or phantoms. These phantoms could be simple uniform blocks or steps or more complex designs containing embedded objects to provide tests of resolution and shape detection. It is desirable that the phantom should respond to microwaves in a similar fashion to the anatomical areas they represent, particularly in tests which measure or calibrate microwave exposures, or when used for optimization of system parameters over the required frequency range. The dielectric properties of the breast equivalent material should yield close

match to the actual tissue conditions. Also the phantom should be well adapted when intermediate compositions are desired.

In microwave imaging, the object immersed in a coupling medium is subjected to microwave illumination and the reflected / transmitted energy is analyzed to study the dielectric profile of the object. The specific use of suitable coupling medium enhances the coupling of electromagnetic energy to the object as well as increases the resolution [6]. It also approximates the dielectric properties of the medium to that of the object in order to minimize the reflection, thereby reducing the propagation loss. Thus the medium provides an easily implemented anechoic environment to prevent interference and also a reasonably good match to water dominated biological samples. It also accomplishes wavelength contraction without propagation loss penalty [7].

In the present work, dielectric studies of glycerine and corn syrup are made to assess the suitability of using these materials as phantoms and coupling media for microwave breast imaging.

4.2 Review of the past work

A description of the various materials that are used as phantoms and coupling media in microwave mammography is given here.

Dun Li et al [3] conducted a parallel detection microwave spectroscopy using corn syrup as breast phantom. A 5 cm. radius corn syrup cylinder with an inclusion of 1.5 cm. radius tube filled with the tumor phantom was the sample profile. The tumor phantom was simulated by adding 0.4 mol of sodium chloride in a mixture of glycerine and water in the ratio 65:13. The coupling medium used for the study was a mixture of glycerine and water in the ratio 87:13. At 2.1 GHz the dielectric constants and conductivities of normal breast phantom, tumor phantom and coupling

medium were 28, 50 and 46 and, 0.08 S/m, 1.5 S/m and 1.2 S/m respectively. Satisfactory image reconstruction was possible using these materials.

Fear et al [8, 9] studied the experimental feasibility of radar based techniques for breast tumor localization and detection. They used an experimental set up consisting of PVC pipe of radius 12 cm and height 92 cm which represents the skin, inside which a circular wooden tumor phantom of radius 5 cm is placed. The normal breast tissue as well as the coupling medium used was air. The PVC pipe and wood had dielectric constants of 2.6 and 4, and conductivities of 0.01 S/m and 0.015 S/m, at a frequency of 10 GHz. Even though satisfactory image reconstruction was achieved with this phantom, a conclusion could not be drawn from these results. This was because the dielectric constant and conductivity of the phantom used were no where near that of the breast tissue values.

Microwave breast imaging was investigated using Soyabean oil and diacetin solution as normal and malignant breast tissue phantoms by Xu Li et al [10, 11]. Diacetin solution poured in a cylindrical PVC container of radius 2 mm and height 4 mm was suspended in a PVC box containing soyabean oil using nylon thread. The skin layer of the phantom was created at the top of the box using uncladed FR4 glass epoxy board. Antennas immersed in soyabean oil were used for the transmission and reception of microwave energy. Thus soyabean oil served as the coupling medium too, in this set up. The dielectric constants of soyabean oil, diacetin solution, FR4 glass epoxy and PVC were 2.6, 8.7, 4.34 and 2.7 respectively, and the corresponding conductivities were 0.05 S/m, 1.9 S/m, 0.067 S/m and 0.01 S/m at a frequency of 6 GHz. Even though good image reconstruction was

possible, the dielectric constant and conductivity of the phantom used were in no match to that of the breast tissue values.

A microwave system for breast tumor detection, using water filled PVC pipe of radius 2 mm and height 10 cm. as the breast tumor phantom was evaluated by Andrew Low et al [12]. The phantom was immersed in another PVC pipe of radius 5cm. and height 50 cm. Air was used as the normal tissue phantom and coupling medium. The dielectric constants and conductivities of water and PVC used in the study were 77 and 2.8, and 2.09 S/m and 0.01 S/m respectively at a frequency of 3 GHz. The reconstructed images were not good as significant dielectric contrast exists between the phantom and the coupling medium.

The effects of coupling medium in confocal microwave imaging were studied by Sill et al [13] and Fear et al [14]. They performed simulations using breast phantom having ϵ_r ' as 50 and σ as 4 S/m. The coupling media considered for the study had ϵ_r ' as 36 and σ as 4 S/m, and ϵ_r ' as 9 and σ as 0.4 S/m. Images of the breast phantom were reconstructed using both the coupling media and better resolution was reported using the former.

Semenov et al [4, 5, 15] conducted experimental imaging of phantoms and biological objects using three dimensional microwave tomography. The study was performed at 2.4 GHz. They used de-ionized water of ϵ_r ' as 78 and σ as 1.3 S/m, as the coupling medium and foam soaked with water having ϵ_r ' as 70 and σ as 1.19 S/m, as the phantom. Same group also conducted two dimensional microwave tomographic imaging using cooled gel having ϵ_r ' as 68 and σ as 0.79 S/m as the phantom and water having ϵ_r ' as 77.8 and σ as 1.35 S/m, as the coupling

medium [16]. The experiment was performed at 900 MHz and the results were promising.

Multi target tissue equivalent materials of breast were evaluated by mixing agar and distilled water by Meaney et al [17]. Experiments were conducted by holding this phantom in plexi glass tubes at a frequency range of 300 MHz – 700 MHz. Saline was selected as coupling medium for the study. The range of dielectric constants and conductivities of saline were from 75 - 73.89 and 1.757 S/m - 1.935 S/m, that of phantom were from 5.8 - 5.57 and 0.0136 S/m - 0.0187 S/m, that of agar were from 69.69 - 68.95 and 0.7898 S/m - 0.8714 S/m, that of distilled water were from 75.59 - 75.54 and 0.0197 S/m - 0.1070 S/m, and that of plexiglass were from 2.44 - 2.39 and 0.00842 S/m - 0.00931. The profiles of dielectric constant of the reconstructed images were not good, as the phantom exhibited significant conductivity values and hence high dielectric loss.

Dewald et al [18] performed a study of complex resonant frequencies in dispersive media to classify suspicious growths in breast cancer diagnosis. In this simulation they considered a cancerous tissue having dielectric constant variation of 50 – 35 from static to optical values and corresponding conductivity variation of 0.15 S/m – 1.5 S/m. The respective variations for the normal tissue were from 10 - 7 and from 0.13 – 0.15 S/m.

Arthur W Guy [19] simulated muscle by mixing 76.5 % saline solution, 15.2 % poly ethylene powder and 8.4 % jelling agent. The frequency range used for the study was from 50 MHz -10 GHz. In this range the phantom exhibited a variation of dielectric constant from 58 - 49 and that of conductivity from 0.33 – 1.7 S/m. He also showed that dielectric constant over a wide range could be obtained by varying the

percentage of polyethylene powder and that of conductivity by varying the salinity of the material. The material could also be used to simulate other high water content tissues like breast. He also simulated fat and bone by mixing 84.81 % laminac polyster resin, 14.5 % aluminium powder, 0.24 % acetylene black, 0.24 % methyl ethyl ketone peroxide for the catalyst. In the frequency range of 50 MHz - 10 GHz, this material showed a dielectric constant variation of 6.2 – 4.6 and conductivity variation of 0.17 - 0.55 S/m. A wide range of low water content tissues were also simulated by varying the amounts of aluminum powder to control the dielectric constant and that of acetylene black to control the conductivity.

A dry phantom composed of ceramic (BaTiO_3) powder, graphite powder and bonding resin was synthesized to simulate high water content biological tissues like muscle, brain and breast by Tamura etal [20]. The studies performed at 900 MHz showed that the dielectric constant of the phantom was 50 and conductivity was 0.5 S/m. Also the specific heat of the phantom was small enough to make it possible to observe specific absorption rate (SAR) pattern created by weaker output power of the radiation source.

Kobayashi etal [21] developed dry phantom for human head, composed of ceramic powder (CaSnO_3), graphite powder and bonding resin made of poly vinylidene fluoride. The dielectric constant and conductivity of the material measured using coaxial line S-parameter method at a frequency of 900 MHz were 52 and 0.5 S/m. The phantoms were reported to be highly stable and also had reliable SAR estimation.

A soft and dry phantom model was developed by mixing raw silicone rubber, carbon fiber and a curing agent, by Nikawa etal [22]. In the frequency range of 0.43 – 2.45 GHz a dielectric constant variation of 85 -

7 and conductivity variation of 0.1 – 2.8 S/m was obtained by varying the composition ratio of carbon fiber. Tissues having low water content like fat and bone, and that having high water content like breast, skin and muscle could be simulated using this phantom.

Robinson et al [23] developed muscle phantom using 48% ethanediol, 40 % water, 2% salt, and 10% gelatine. The gelatine was allowed to slowly dissolve in other ingredients at a temperature of 55 – 60°C. The material exhibited dielectric constant variation of 53.6 – 39.5 and conductivity variation of 0.85 – 1.35 S/m in the frequency range of 500 – 2450 MHz. The material could also be used as a simulant of breast tissues as the dielectric parameters were in good match. They also simulated fat tissue by mixing 55% ethanediol, 5% gelatine, 40% polyethylene powder, and a drop of detergent. The detergent was added to wet the polyethylene powder. Studies showed that this material exhibited low dielectric constant similar to that of fat. The dielectric constant measurements were made using open ended coaxial sensor.

Chang et al [24] synthesized a phantom from compressed carbon black and conductive thermoplastic. Polyethyl methacrylate (PEMA) powder and isobutyl methacrylate liquid monomer were used for the fabrication of conductive thermoplastic. In the frequency range of 100 MHz – 1 GHz the dielectric constant of the material could be varied from 72 – 7.5 and conductivity from 0.02 – 1.5 S/m, by varying the composition ratio of PEMA and carbon black. Hence the material could be used as a simulant of low water content as well as high water content tissues.

Phantoms for high water content tissues like breast and muscle were simulated by mixing acrylamide (C_3H_5NO), ammonium persulfate ($(NH_4)_2S_2O_8$) solution in water and salt by Andreuccetti et al [25]. In the

frequency range of 0.75 – 5.5 GHz, its dielectric constant could be varied from 52 – 44.5 and conductivity from 0.675 – 1.19 S/m by varying the concentrations of acylamide and salt in the mixture.

A gel based brain and breast phantoms were developed using agar, de-ionized water, sodium chloride, sodium azide, and TX-151 polyethylene powder by Okano et al [26]. In the frequency range of 0.3 – 3 GHz, the material exhibited dielectric constant variation of 12 – 32 and conductivity variation of 2.1 – 2.5 S/m. He also developed skull phantoms using silicone, agar, silicone emulsion, glycerol, TX-151 and polyethylene powder. For the same frequency range this material showed dielectric constant variation of 3 – 14 and conductivity variation of 1.3 – 0.8 S/m.

A coupling medium using sodium meta-silicate (SMS) gel was proposed for medical imaging applications by Hamsakutty et al [27, 28]. A variation of 18 – 7 in dielectric constant and 0.89 – 1 S/m in conductivity was reported in the frequency range of 2 – 3 GHz by varying the pH of the gel sample.

Meaney and Paulsen [29] performed near field microwave imaging at 700 MHz using phantoms having high values of dielectric parameters. They used saline having ϵ_r' and σ as 77.44 and 2.198 S/m as the coupling medium and agar with 0.3 % NaCl having ϵ_r' and σ as 71.11 and 0.992 S/m as the phantom. Due to the high conductivity value of the saline phantom, the dielectric constant profile was distorted.

Microwave image reconstruction using breast phantom at the frequency of 900 MHz was performed using cylindrical molasses phantom with saline inclusion and 50:50 glycerine: water mixture as the coupling medium by Fang et al [30]. Molasses, saline and coupling medium used had ϵ_r' and σ as, 62 and 1.2 S/m, 80 and 1.5 S/m, and, 21 and 0.12 S/m

respectively. Satisfactory image reconstruction was possible using these phantoms.

Jannicke Hilland [31] studied the dielectric properties of saline solutions for its feasibility of using as phantom and coupling medium in microwave medical imaging. As the percentage of NaCl in saline was varied from 0.3 to 3.5, the dielectric constant showed a variation from 15 to 40 and conductivity from 0.5 to 5 S/m at a frequency of 3 GHz.

4.3 Motivation for the present work

From the works described in the previous section it is understood that different materials were used as phantoms and coupling media in microwave breast imaging. Using different materials having different dielectric constants as phantom and coupling medium, decreases the measurement accuracy, increases attenuation and creates temperature drifts and unpredictable local temperature gradients. Also, the dielectric properties of the phantoms and coupling media reported in the review, agrees only roughly with that of the breast tissue values reported [32-33,35-36]. Even though some simulations gave satisfactory results, their experimental feasibility was not validated.

This work is an attempt to identify a single material to be used as both phantom and coupling medium in microwave breast imaging. Experimental validity of its usage is given in Chapters 5 and 6.

4.4. Sample preparation

The samples considered for the study are Glycerine and Corn Syrup.

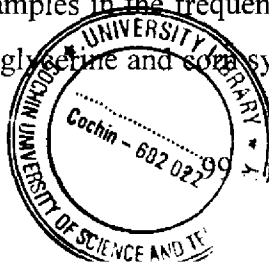
Commercially available glycerine is treated as G-Sample 1. G-Samples 2, 3 and 4 are prepared by diluting G-Sample 1 with 30%, 55% and 80% of water.

Corn flour mixed with water in the ratio 1:1 is heated till it changes in to a thick consistent jelly like form. This jelly form is treated as C-Sample 1. C-Samples 2, 3 and 4 are prepared by diluting C-Sample 1 with 30%, 55% and 80% of water. Water used for the study has a dielectric constant of 77.5 and conductivity of 2.05 S/m at 3 GHz.

4.5 Experimental analyses

As the first step, the dielectric constant and conductivity studies of glycerine and corn syrup samples are done using rectangular cavity perturbation technique in the frequency range of 2–3 GHz. This frequency range is selected as it conveniently includes the ISM band. The rectangular cavity resonator used for the study has a dimension of 36 x 7 x 4 cms. The diameter of the coupling hole is 1.28 cm, length of the slot on the broad wall is 22.5 cm and width of the slot is 0.4 cm. The experimental set up described in Section 2.6 is used for this study. The system is first calibrated using TRL procedure described in Section 2.6. The resonator is then connected between ports 1 and 2 and the analyzer is set for S21 measurement. A capillary tube made of low loss silica ($\tan \delta = 0.002$ at 3 GHz) having volume 0.063 cm^3 is used to hold the liquid sample. The sample is inserted and moved in the cavity and measurements are taken for the positions of maximum perturbation. The details of the rectangular cavity measurement technique and the various equations used in the analysis of dielectric parameters are discussed in Section 2.5.2 of Chapter 2. The resonant frequency spectrum of the S-band rectangular cavity used for the study is shown in Figure 4.1.

Figures 4.2 (a,b) and 4.2 (c,d) show the dielectric characteristics of glycerine and corn syrup samples in the frequency range of 2-3 GHz. The measured dielectric data of glycerine and corn syrup samples at 2.983 GHz



are compared with that of the dielectric parameters of breast tissue samples given in literature [32,33] and is shown in Table 4.1.

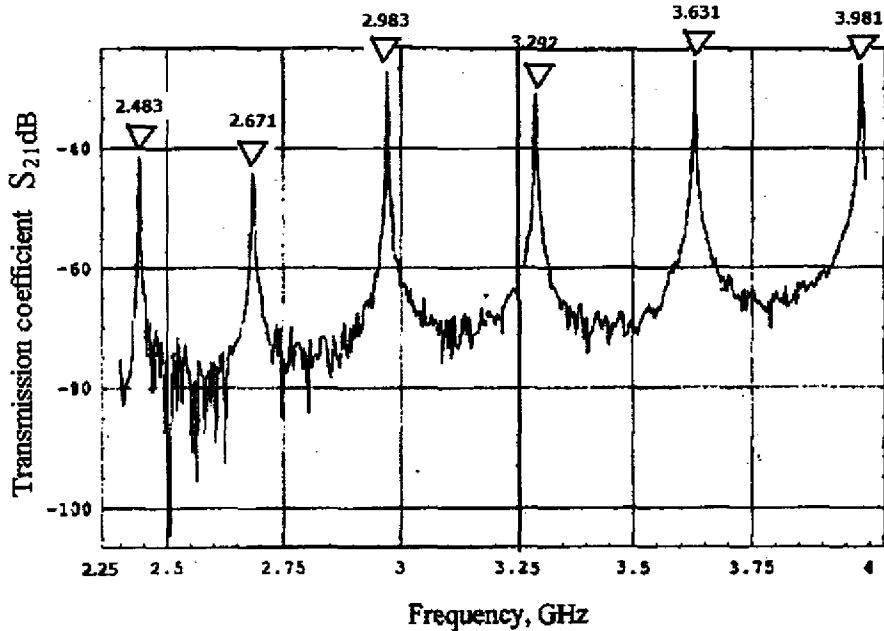


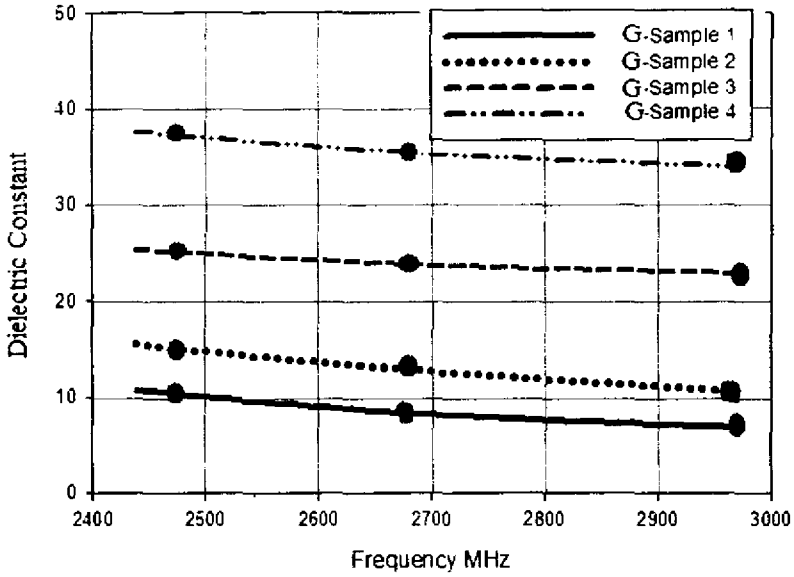
Figure 4.1. Resonant frequency spectrum of the S-band rectangular cavity

It is observed that among the glycerine samples only G-Sample 4 exhibits comparable values of dielectric constant with that of breast tissues. But this sample shows high value of conductivity which is an indication of larger dielectric loss, and thereby of increased propagation loss. So, even though G-Sample 4 can be used as a breast phantom, the usage of this material as an efficient coupling medium is restricted. However, corn syrup samples exhibit matching values of dielectric constant with that of the breast tissues while the conductivity values are lesser. Hence these samples can be used as both breast phantoms and coupling medium for microwave breast imaging studies. Also, corn syrup is cheaper than glycerine.

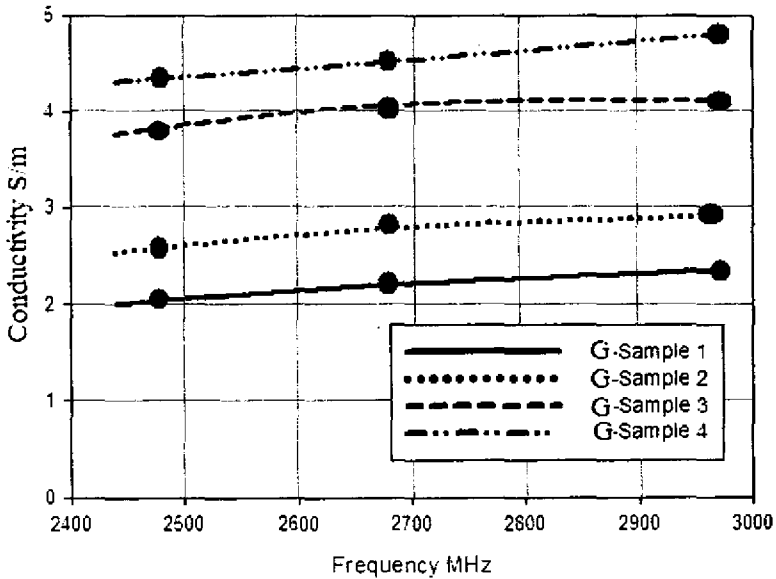
For the microwave breast imaging studies performed in thesis, corn syrup samples are used as the breast phantoms and C-sample 1 is used as the coupling medium due to their matching electrical properties with that of the breast tissue samples.

Table 4.1 Comparison of the dielectric parameters of glycerine and corn syrup samples with that of breast tissue at 3 GHz.

Sample	Dielectric Constant	Conductivity S/m
G-Sample 1	6.25	2.35
G-Sample 2	13.41	2.85
G-Sample 3	24.85	4.1
G-Sample 4	34.63	4.81
C-Sample 1	18.7	0.98
C-Sample 2	29.8	1.1
C-Sample 3	38.1	1.91
C-Sample 4	42.2	2.38
Normal Breast Tissue [32-33, 35-36]	~20	~2.3
Malignant Breast Tissue [32-33, 35-36]	~32	~2.7
Benign Breast Tissue [32-33, 35-36]	~35	~3.1

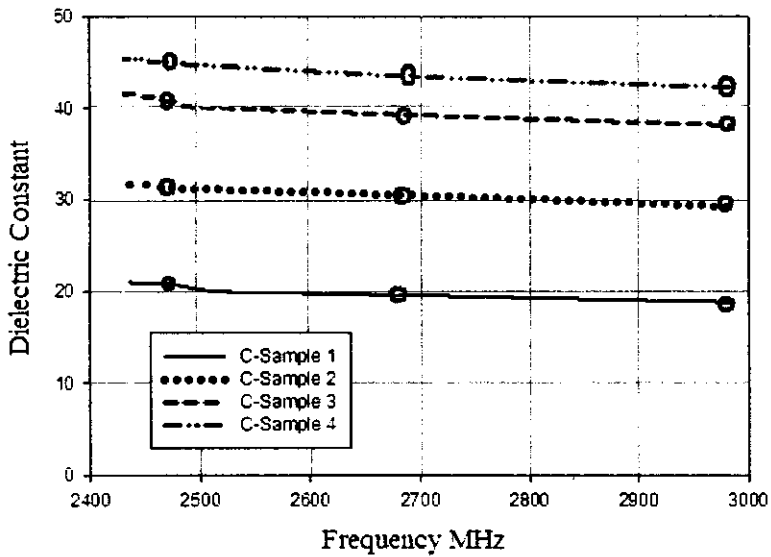


(a)

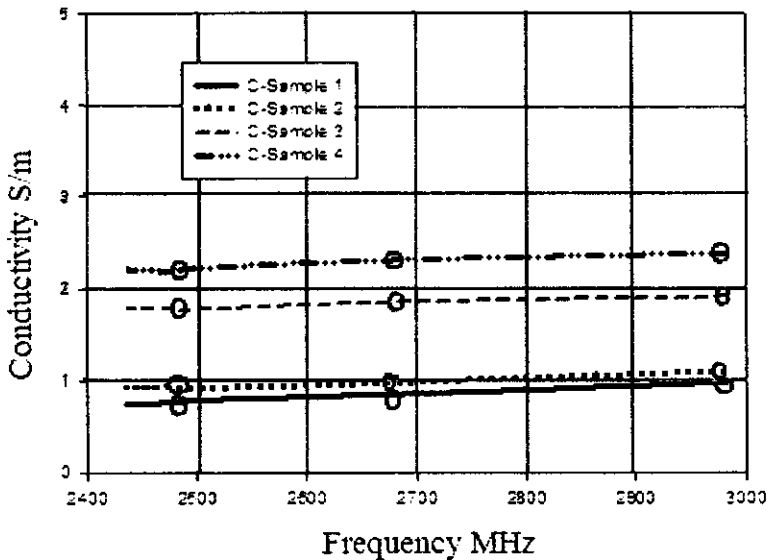


(b)

Figure 4.2 Variation of dielectric parameters with frequency for glycerine samples measured using rectangular cavity perturbation method



c)



d)

Figure 4.2 Variation of dielectric parameters with frequency for corn syrup samples measured using rectangular cavity perturbation method

As the rectangular S-band cavity has limited operational band, dielectric properties of corn syrup samples are further explored using a coaxial cavity resonator to evaluate its performance over a broader range of 0.422–3 GHz. For this, the coaxial cavity is connected to Port 1 of the experimental set up. The details of the experimental set up used and the calibration procedure adopted for the measurement are discussed in Section 2.6 of Chapter 2. Details of the coaxial cavity and the various equations used for the analysis are described in Section 2.5.1. The coaxial cavity used for the study has a length of 25 cm and diameter 8 cm. The central conductor has a length of 118 cm and diameter 3.2 cm. The network analyzer is set for S11 measurements as coaxial cavity resonator is of reflection type. The cavity exhibits resonant frequencies at 0.422 GHz, 1.888 GHz and 2.983 GHz. The resonant frequency spectrum of the coaxial cavity is shown in Figure 4.3.

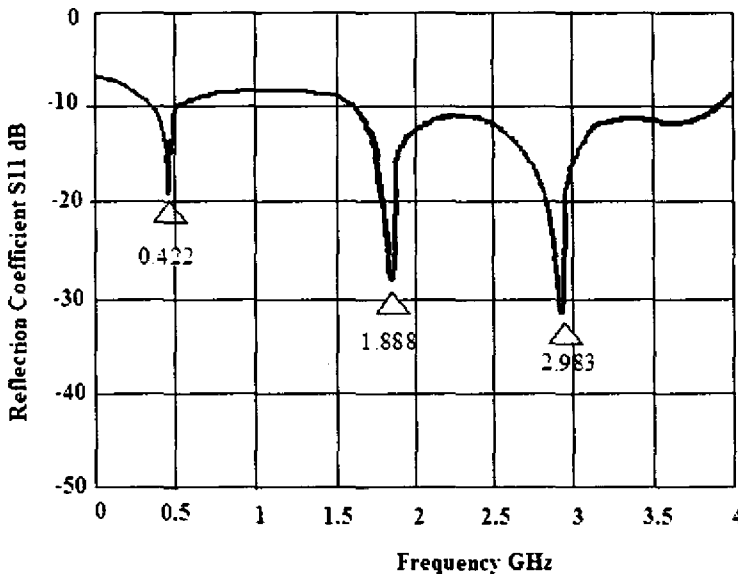
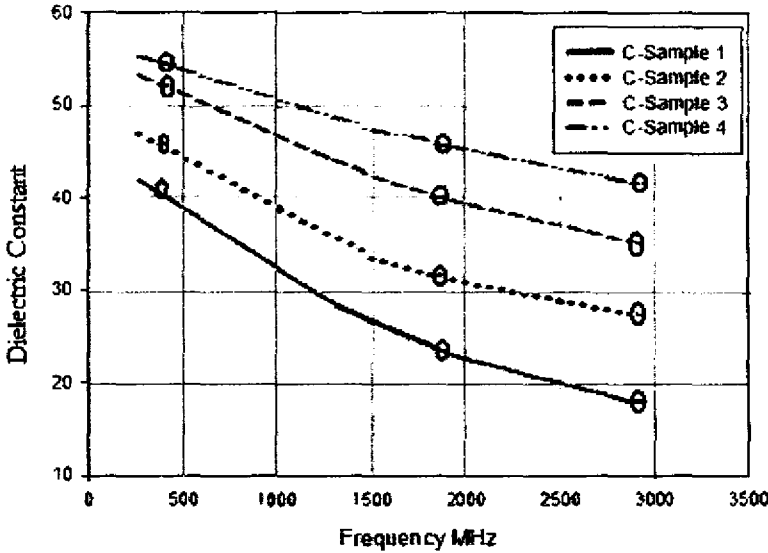
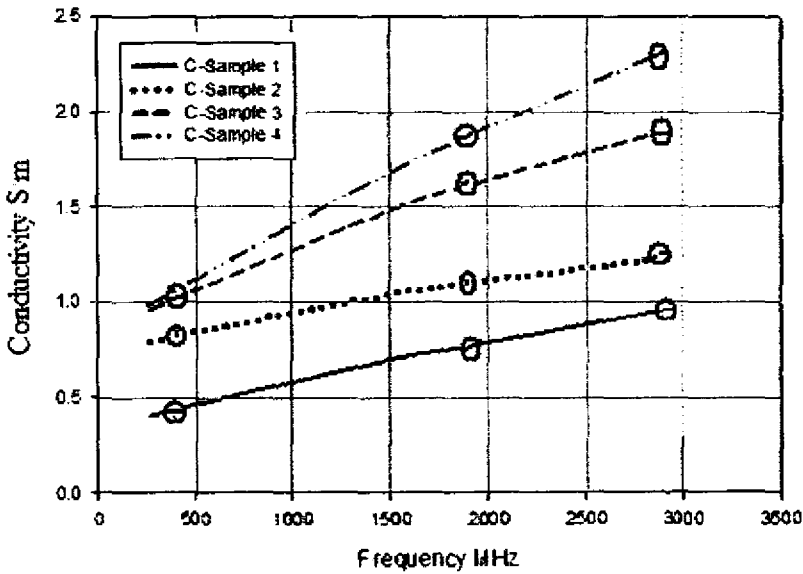


Figure 4.3. The resonant frequency spectrum of the coaxial cavity

Figures 4.4 (a,b) show the variations of dielectric constant and conductivity of corn syrup samples measured using coaxial cavity, with frequency. For a given corn syrup sample the dielectric constant decreases and the conductivity increases, with increase in frequency. This result matches with the dielectric properties of biological tissues [35, 36]. The decrease of dielectric constant with increase of frequency is due to the orientation of polarization in the microwave field. The higher the polarizability of the material greater will be the dielectric constant. In the case of orientation polarization, the applied field causes a net orientation of the dipoles parallel to the field. As the frequency of the applied field is increased, net polarization is reduced due to orientation polarization and total polarizability falls to $\alpha_T - \alpha_o$ where α_T is the total polarizability and α_o is the polarizability of orientation polarization [37]. This fall in polarizability leads to dielectric relaxation which in turn, leads to a decrease in dielectric constant. In other words at higher frequencies due to the rotational displacement of polar groups under the influence of the electric field, frictional loss increases and it reduces dielectric constant. The conductivity of dielectric materials in a microwave field depends upon the dielectric loss factor ϵ_r'' . As frequency increases, the dielectric loss factor increases. The dielectric loss is a direct function of the relaxation process, which is due to the local motion of the polar groups. At high frequencies the friction between the molecular chains increases, which leads to higher dielectric loss. This dielectric loss factor leads to the so called "conductivity relaxation". At the relaxation region, the polarization acquires a component out of phase with the field and a displacement current in phase with the field, resulting in thermal



(a)



(b)

Figure 4.4. Variation of dielectric parameters with frequency for corn syrup samples measured using coaxial cavity perturbation method

dissipation of energy. This generates dielectric loss which in turn generates conductivity. Hence conductivity increases with frequency [37].

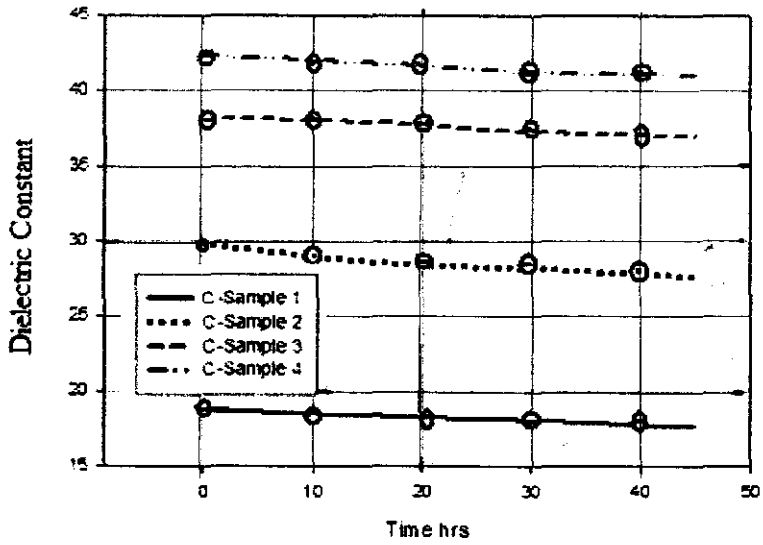
A comparison of the dielectric properties of various breast tissues with that of corn syrup samples and conventional coupling media in the frequency range of 0.4 – 3 GHz is given in Table 4.2. It is seen that all types of breast tissues can be simulated from corn syrup by varying its concentration, as good match in dielectric constant is observed. As the conductivity values are less for corn syrup samples, its propagation loss will be less and hence can be used as an efficient coupling medium too. The dielectric parameters of conventional coupling media like water, saline and SMS gel, in the frequency range of 0.4 – 3 GHz are also compared with that of corn syrup samples. While water and saline [31, 34] exhibit a higher range of dielectric constant than that of the breast tissue samples, SMS gel [27, 28] exhibits a lower range. Hence these materials if used as coupling media provide significant reflections which result in poor coupling of the electromagnetic energy into the tissues.

It is seen from Table 4.2 that in the frequency range of 0.4 – 3 GHz, normal female breast tissue exhibits dielectric constant variation from 46 - 20 and conductivity from 0.2 – 2.3 S/m. In the same range, benign breast tumors exhibit a broad distribution of dielectric constant from 67 - 30 and conductivity from 0.32 – 2.7 S/m, and for malignant tumors the variations are from 65 - 35 and from 0.5 –3.1 S/m respectively. These variations of dielectric parameters depend on the bound water content of the tissue as well as with the applied frequency. The bound water content of the breast tissue is also a function of the age of the person. As high breast cancer rate is reported for women in the age group of 45 - 55, the bound water content values and dielectric parameters reported in the table are for women in this age group [32,33].

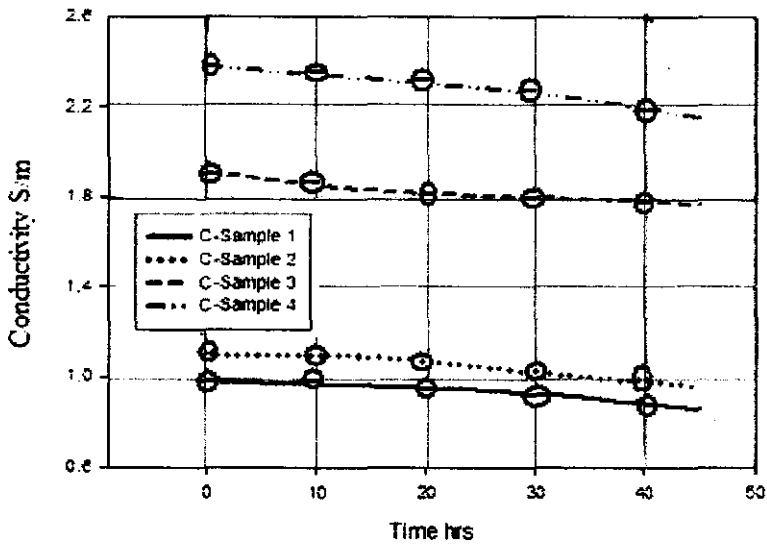
Figure 4.5 shows that corn syrup samples exhibit almost stable performance over the variations of time.

Table 4.2. Comparison of the dielectric properties of various breast tissues with that of corn syrup samples and conventional media in the frequency range of 0.4 – 3 GHz.

Sample		Range of dielectric constant (average)	Range of conductivity $S\ m^{-1}$ (average)
Normal breast tissue (water content varies from 40 - 50 % by weight) [32-33,35-36]		46 – 20	0.2 – 2.3
Benign breast tumor (water content varies from 60 - 70 % by weight) [32-33,35-36]		67 – 30	0.32 – 2.7
Malignant breast tumor (water content varies from 62 - 75 % by weight) [32-33,35-36]		65 - 35	0.5 – 3.1
Corn syrup	C-Sample 1	41.2 – 18.7	0.4 – 0.98
	C-Sample 2	47.8 – 29.8	0.72 – 1.1
	C-Sample 3	52.1 - 38.1	1.01 - 1.91
	C-Sample 4	55.7 – 42.2	1.12 - 2.38
Water [31-34]		82 - 77.5	1.6 – 2.05
Saline (0.5 % NaCl) [31-34]		71.7 – 67.4	0.63 - 0.74
SMS gel [27-28]		16.6 – 8.2	0.52 – 0.71



(a)



(b)

Figure 4.5 Variation of dielectric parameters with time for various corn syrup samples measured at 3 GHz

Figure 4.6 shows the variation of absorption coefficient of the samples with frequency. It is observed that absorption coefficient increases with frequency which is due to the increase of conductivity.

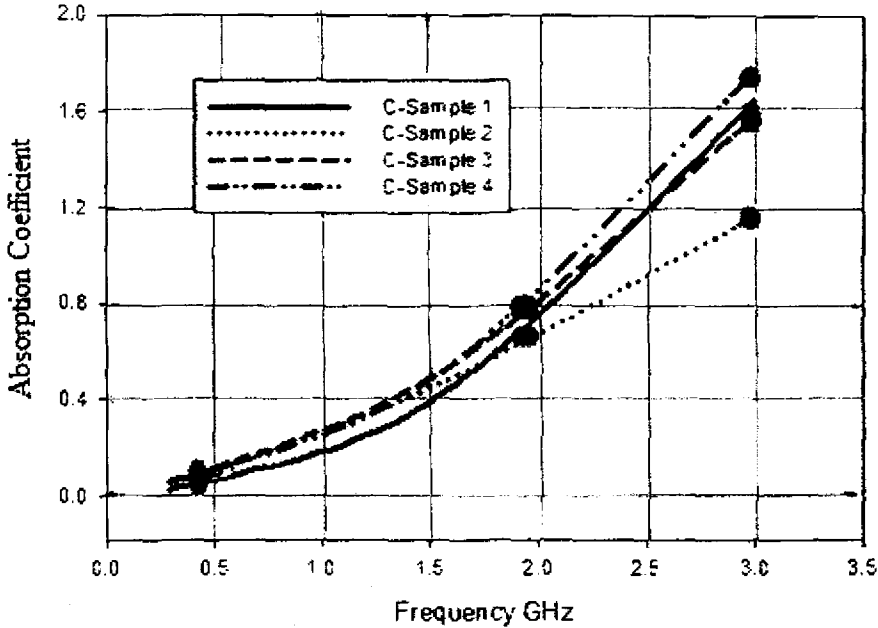


Figure 4.6 Variation of absorption coefficient of corn syrup samples with frequency

For biological materials, relaxation time τ decreases and dipole moment increases with the increase in water content of the tissues [35, 36]. To check whether corn syrup samples also show a similar profile, these parameters are calculated for corn syrup samples at a frequency of 3 GHz using eqns. 2.29– 2.40 and are reported in Table 4.3. The frequency is so selected that it matches with the center frequency of the antenna designed for the microwave imaging studies.

It is observed from Table 4.3 that increasing the water content of the corn syrup sample makes a decrease in the relaxation time. This reduction

is caused by the decrease in viscosity and hence a reduction in the hindering forces. The highly polar nature of the water molecule contributes more to the intra-molecular relaxation process, thereby reducing the most probable relaxation time [35].

Table 4.3. Relaxation time and dipole moment of corn syrup samples at 3 GHz.

Sample	τ ps	Dipole moment $\mu \times 10^{-30}$ C m
C-Sample 1	0.75	1.30
C-Sample 2	0.53	2.5
C-Sample 3	0.42	3.65
C-Sample 4	0.37	4.8

As the water content of the sample is increased, the polarity increases and the dipole moment approaches towards that of the water molecule which is 0.69×10^{-29} C m. The increase of dielectric constant with the dilution of water also causes an increase of the dipole moment.

The complex relative permittivity of a dielectric material can be written as

$$\epsilon_r = \epsilon_r' - j\epsilon_r'' \quad (4.1)$$

where ϵ_r is the dielectric constant or permittivity and ϵ_r'' is the dielectric loss of the medium

The loss tangent

$$\tan \delta = \epsilon_r'' / \epsilon_r' \quad (4.2)$$

The conductivity σ is given by

$$\sigma = \omega \epsilon_0 \epsilon_r'' \quad (4.3)$$

The propagation constant

$$\gamma = \sqrt{j\omega\mu_0(\sigma + j\omega\epsilon_0\epsilon_r')} = \alpha + j\beta \quad (4.4)$$

where α represents the attenuation factor and β the phase factor.

Substituting Eqns. (4.1- (4.3) in (4.4) and simplifying, we get

$$\alpha = 2\pi f \sqrt{\mu_0 \epsilon_0 \epsilon_r'} \left[\sqrt{1 + \tan^2 \delta} - 1 \right] \quad (4.5)$$

and

$$\beta = 2\pi f \sqrt{\mu_0 \epsilon_0 \epsilon_r'} \left[\sqrt{1 + \tan^2 \delta} + 1 \right] \quad (4.6)$$

If the wave considered is traveling in the + z direction, $e^{-\alpha z}$ represents the decaying envelope of the wave and $e^{-j\beta z}$ represents the sinusoidal nature of the wave whose phase is βz . The total loss encountered by the wave over a distance z consists of dissipation loss L_{diss} due to conduction currents being excited in the medium and diffusion loss L_{diff} due to the spherical spreading of energy [7].

They are given by,

$$L_{diss} = 20 \log_{10} e^{\alpha z} \quad (4.7)$$

$$L_{diff} = 20 \log_{10} (\beta z) - 29.14 (dB) \quad (4.8)$$

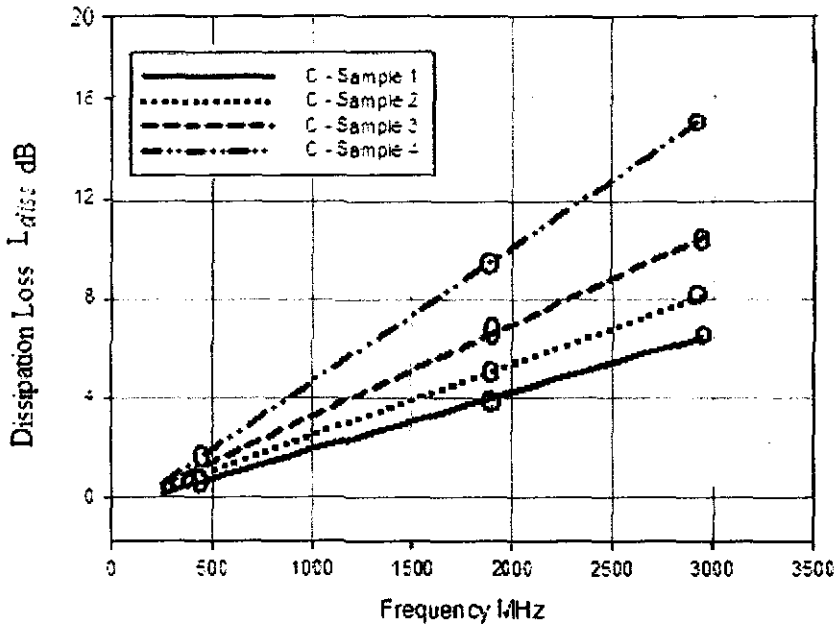
Hence the total loss $L_{total} = L_{diss} + L_{diff} \quad (4.9)$

Table 4.4 shows a comparison of the loss parameters of corn syrup samples with that of water and saline, at 3 GHz. A distance z of 12 cm is

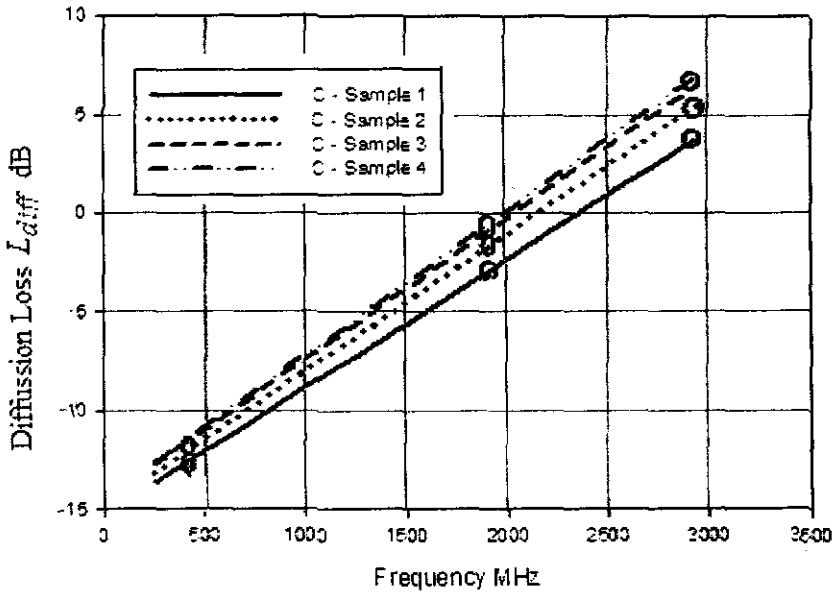
selected as this is the maximum distance between transmitting and receiving antenna in the microwave imaging studies presented in this thesis. A loss of 9.8 dB to 21.8 dB is an acceptable range when compared to the loss parameters of conventional coupling media like water and saline [7]. Figures 4.7 (a, b, c) show the variation of propagation losses associated with the samples as a function of frequency. It is seen that losses increase with frequency, which is due to the increase of conductivity. The high lossy nature of water increases the losses with the dilution of corn syrup sample with water.

Table 4.4 Propagation loss parameters of water, saline and corn syrup at 3 GHz.

Sample		Total loss dB Dissipation Loss + Diffusion Loss
Corn syrup	C-Sample 1	9.8
	C-Sample 2	13.1
	C-Sample 3	17.6
	C-Sample 4	21.8
Water		180
Saline (0.5 % NaCl)		165



(a)



(b)

Figure 4.7 Propagation loss characteristics of corn syrup samples with frequency.

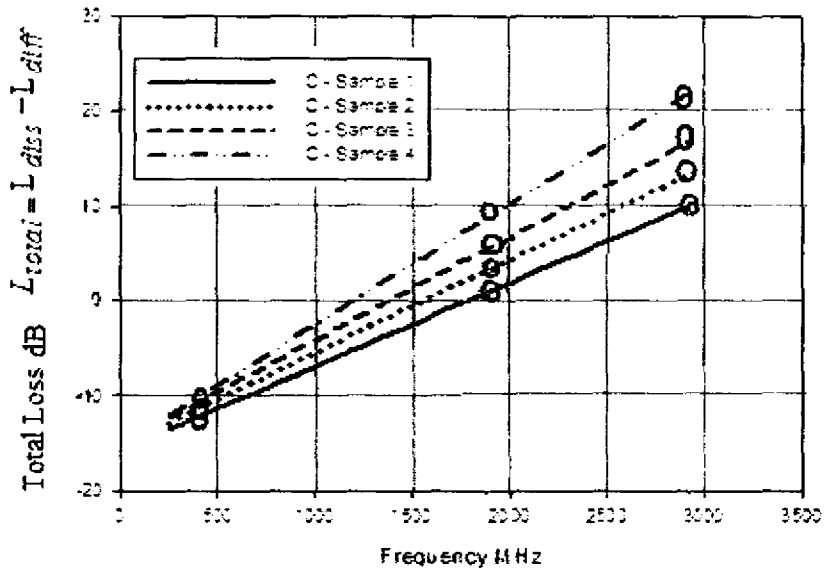


Figure 4.7(c) Total loss suffered by corn syrup samples with frequency.

To evaluate the performance of the antenna in the medium, the antenna is immersed in C-Sample 1 and is connected to port 1 of the experimental set up. C-Sample 1 is used as the medium as this is the coupling medium used in the subsequent microwave imaging studies. Prior to this measurement, the system is calibrated using the TRL calibration procedure discussed in section 2.6 and is then set for S11 measurement. Figure 4.8 shows the comparison of the reflection (S11) characteristics of the bowtie antenna in air and in the medium. In air, the antenna exhibits a return loss of -53 dB at a resonant frequency of 3 GHz with a 2:1 VSWR bandwidth of 53 % in the range of 1.875 . – 3.475 GHz, while in corn syrup, the bandwidth is enhanced to 91 % in the range of 1.215 – 3.810 GHz with resonant

frequency of 2.855 GHz and return loss of - 41 dB. This enhanced bandwidth is beneficial to transmit short transient pulses in time domain confocal microwave imaging applications.

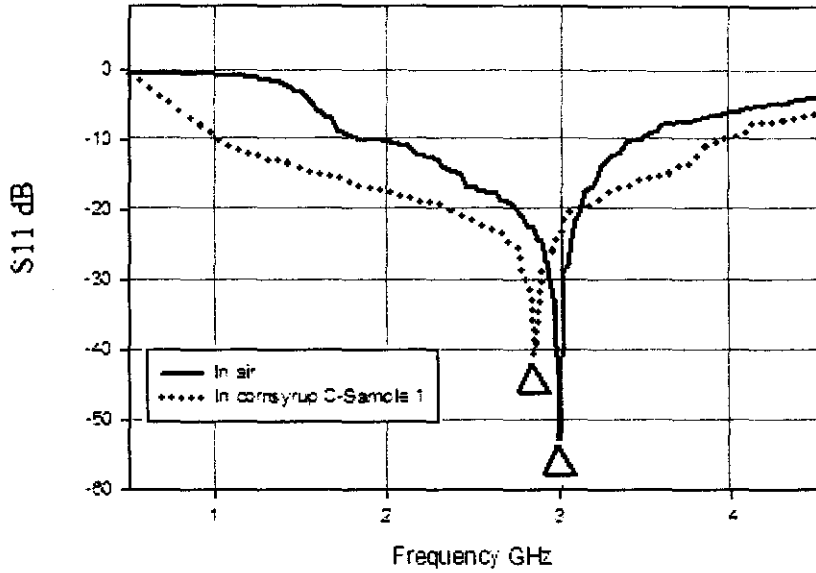


Figure 4.8 Reflection characteristics of the bowtie antenna

Figure 4.9 shows the transmission (S_{21}) characteristics of the antenna in air and in C-Sample 1. No significant reduction in power is observed at 3GHz when the antenna is immersed in the medium.

4.6 Conclusion

Dielectric properties of glycerine and corn syrup samples are studied to check the feasibility of using them as breast phantom and coupling medium in microwave breast imaging. The dielectric constants of glycerine samples do not match with that of breast tissues. Also, glycerine suffers more

dielectric loss than corn syrup and is costly. Hence it is not selected as coupling medium and breast phantom for further studies. Studies show that

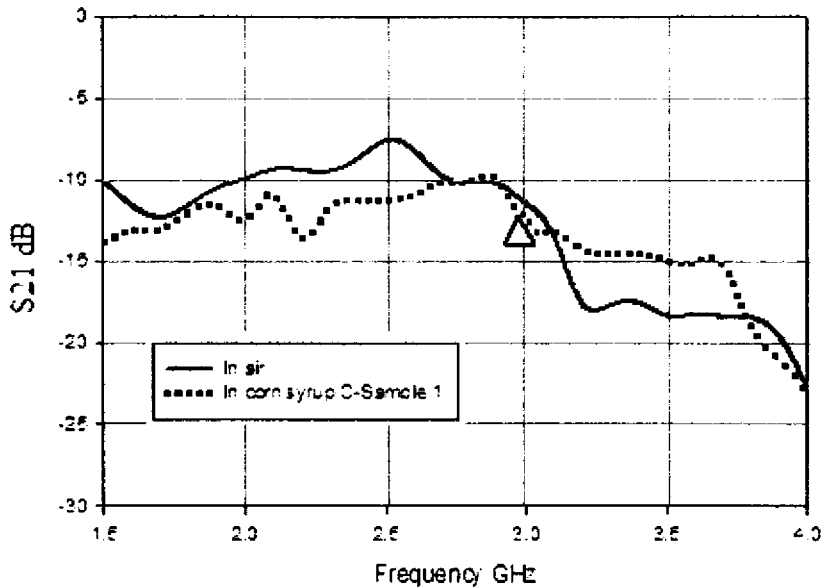


Figure 4.9 Transmission characteristics of the antenna

dielectric constant of corn syrup samples match with that of breast tissues, with less conductivity values. Also the samples exhibit stable performance over the variations of time. Relaxation time and dipole moment of the samples agree with that of high water content biological tissues. Hence these samples can be used as an excellent breast substitute and its usage as coupling medium minimizes the scattering, enhances coupling of electromagnetic energy and improves the resolution in microwave breast imaging.

4.7 References

1. P. M. Meaney, M. W. Fanning, Dun Li, S.P. Poplack, K.D. Paulsen, "A clinical prototype of active microwave imaging of the breast," *IEEE Transactions on Microwave Theory and Techniques*, vol. 48, pp. 1841 – 1853, Nov. 2000.
2. P.M.Meaney, K.D.Paulsen, A. Hartov, R.K.Crane, "An active microwave imaging system for reconstruction of 2-D electrical property distributions", *IEEE Transactions on Biomedical Engineering*, vol. 42, pp. 1017 – 1026, 1995.
3. Dun Li, P. M. Meaney, T. Raynolds, S. Pendergrass, M. Fanning, K. D. Paulsen, "A parallel-detection microwave spectroscopy system for breast imaging," *Review of Scientific Instruments*, vol. 75, pp. 2305 – 2313, 2004
4. S.Y.Semenov, R.H.Svenson, A.E.Boulyshev, A.E.Souvorov, V.Y.Borisov, A.N.Starostin, K.R.Dezen, G.P.Tatsis, V.Y.Baranov, "Microwave Tomography: two dimensional system for biological imaging", *IEEE Transactions on Microwave Theory and Techniques*, vol. 43, pp. 869 – 877, 1996
5. S.Y.Semenov, R.H.Svenson, A.E.Boulyshev, A.E.Souvorov, A.G.Nazarov, Y.E.Sizov, A.V. Faviovsky, V.Y.Borisov, B.A.Voinov, G.I.Simonova, A.N.Staostin, V.G.Posukh, G.P.Tatsis, V.Y.Baranov, "Three dimensional microwave tomography: experimental prototype of the system and vector born reconstruction method" *IEEE Transactions on Biomedical Engineering*, vol. 43, pp. 937 – 945, 1999.
6. Meaney P.M, Pendergrass S.A, Fanning M.W, Li D, Paulsen K.D, "Importance of using a reduced contrast coupling medium in 2D microwave breast imaging", *Journal of Electromagnetic Waves and Applications*, vol. 17, pp.333 – 355, 2003.
7. S.J.Foti, R.P.Flam, J.F.Aubin, L.E.Larsen, J.H. Jacobi, "A water immersed microwave phased array system for interrogation of biological targets" in *Medical Applications of Microwave Imaging*, IEEE Press, New York, (1986), 148 – 166.
8. Fear E.C, Jeff Sill, Stuchly M.A, "Experimental feasibility of breast tumor detection and localization", *IEEE MTT-S Digest*, TU5D-2, pp. 383 – 386, 2003.
9. Fear E.C, Jeff Sill, Stuchly M.A, "Experimental feasibility study of confocal microwave imaging for breast tumor detection", *IEEE Transactions on Microwave Theory and Techniques*, vol. 51, pp. 887 - 892 , 2003.

10. Xu Li, Hagness S.C, Van Veen B.D, van der Weide D, "Experimental investigation of microwave imaging via space time beam forming for breast cancer detection", *IEEE MTT-S Digest, TU5D-1*, 2003.
11. Xu Li, Shakti S.K, Hagness S.C, van der Weide D, Van Veen B.D, "Microwave imaging via space time beam forming: experimental investigation of tumor detection in multiplayer breast phantoms", *IEEE Transactions on Microwave Theory and Techniques*, vol. 52, pp. 1856 – 1865, 2004.
12. Andrew Low, Fear E.C, Jeff Sill, Stuchly M.A, "Microwave system for breast tumor detection: experimental concept evaluation", *IEEE APS*, pp. 819 – 821, 2002.
13. Sill J.M, Fear E.C, "Tissue sensing adaptive radar for breast cancer detection: study of immersion liquids", *Electronics Letters*, vol. 41, pp. 113 – 115, 2005.
14. Fear E.C, Stuchly M.A, "Confocal microwave imaging for breast tumor detection: comparison of immersion liquids", *IEEE APS*, pp:250 – 253, 2001.
15. Semenov S.Y. Bulychev A.E, Souvorov A.E, Nazarov A.G, Sizov Y.E, Svenson R.H, Posukh V.G, Pavlovsky A, Repin P.N, Tatsis G.P, "Three-dimensional microwave tomography: experimental imaging of phantoms and biological objects", *IEEE Transactions on Microwave Theory and Techniques*, vol. 48, pp. 1071 – 1074, 2000.
16. Semenov S.Y. Bulychev A.E, Souvorov A.E, Sizov Y.E, Svenson R.H, Posukh V.G, Borisov V.Y, Kozlov I.M, Nazarov A.G Tatsis G.P, "Microwave tomography: A theoretical and experimental investigation of iteration reconstruction algorithm" , *IEEE Transactions on Microwave Theory and Techniques*, vol. 46, pp. 133 – 141, 1998.
17. Meaney P.M, Paulsen K.D, Hartov A, Crane R.K, "Microwave imaging of tissue assessment: initial evaluation in multitarget tissue equivalent phantoms," *IEEE Transactions on Biomedical Engineering*, vol. 43 , pp. 878 – 890, 1996.
18. Dewald S, Bansal R, "Complex resonant frequencies of biological targets for microwave imaging applications", *Electronics Letters*, vol.38, pp. 1633 – 1634, Dec. 2002.
19. Arthur W Guy, "Analyses of electromagnetic energy induced in biological tissues by thermographic studies on equivalent phantom models", *IEEE Transactions on Microwave Theory and Techniques*, vol. MTT-19, pp. 205 – 214, 1971.
20. Tamura H, Ishikawa Y, Kabayashi T, Nojima T, "A dry phantom material composed of ceramic and graphite powder", *IEEE*

- Transactions on Electromagnetic Compatibility, vol. 39, pp. 132 – 140, 1997.
21. Kobayashi T, Nojima T, Yamada K, Uebayashi S, “Dry phantom composed of ceramics and its application to SAR estimation”, IEEE Transactions on Microwave Theory and Techniques, vol. 41, pp. 136 – 140, 1993.
 22. Yoshio Nikawa, Chino M, Kikuchi K, “Soft and dry phantom modeling material using silicone rubber with carbon fiber”, IEEE Transactions on Microwave Theory and Techniques, vol. 44, pp. 1949 – 1953, 1996
 23. Robinson M.P, Richardson M.J, Green J.L, Preece A.W, “New materials for dielectric simulation of tissues”, Physics in Medicine and Biology, vol.36, pp. 1565 – 1571, 1991.
 24. Chang J.T, Fanning M.W, Meaney P.M, Paulsen K.D, “ A conductive plastic for simulating biological tissue at microwave frequencies”, IEEE Transactions on Electromagnetic Compatibility, vol. 42, pp. 76 – 81, 2000.
 25. Andreuccetti, Bini M, Ignesti A, Olmi R, Rubino N, Vanni R, “Use of polyacrylamide as a tissue equivalent material in the microwave range”, IEEE Transactions on Biomedical Engineering, vol. 35, pp. 275 – 277, 1988.
 26. Y.Okano, K. Ito, I. Ida, M. Takahashi, “ Te SAR evaluation method by a combination of thermographic experiments and biological tissue equivalent phantoms”, IEEE Transactions on Microwave Theory and Techniques, vol. 48, pp. 2094 – 2103, 2000.
 27. Hamsakutty V, Lonappan A, Thomas V, Bindu G, Jacob J, Yohannan J, Mathew K.T, “ Coupling medium for microwave medical imaging”, Electronics Letters, vol.39, pp. 1613 - 1614, 2003.
 28. Hamsakutty V, Lonappan A, Bindu G, Thomas V, Jacob J, Yohannan J, Mathew K.T, “Biomedical applications of sodium meta silicate gel as coupling medium for microwave medical imaging”, IEEE APS, 0-7803-8302-8/04, 2004.
 29. Paul M.Meaney, Keith D.Paulsen, “Near field microwave imaging of biologically based materials using a monopole transceiver system”, IEEE Transns. of Microwave Theory and Techniques, vol. 46, pp.31 – 44, 1998.
 30. Fang Q, Meaney P.M, Paulsen K.D, “Microwave image reconstruction of tissue property dispersion characteristics utilizing multiple frequency information”, IEEE Transactions on Microwave Theory and Techniques, vol. 42, pp.1866 -1875, 2004.

31. Jannicke Hilland, "Simple sensor system for measuring the dielectric properties of saline solutions", *Measurement Science and Technology*, vol. 8, pp. 901 – 910, 1997.
32. A.M.Campbell, D. V. Land, Dielectric properties of female human breast tissue measured in vitro at 3.2 GHz, *Physics in Medicine and Biology*, vol. 37, pp.193 – 209, 1992.
33. S. S. Chaudhary, R. K. Mishra, A. Swarup, J. M. Thomas, "Dielectric properties of normal and malignant human breast tissues at radiowave and microwave frequencies," *Indian Journal of Biochemistry and Biophysics*, vol.21, pp. 76 – 79, 1981
34. Jacques Thuery, *Microwaves: Industrial Scientific and Medical Applications*, Artech House, 685 Canton Street, Norwood, MA 02062, 1992.
35. S.Gabriel, R. W.Lau, C.Gabriel, Dielectric properties of biological tissues: II Measurements in the frequency range 10 Hz to 20 GHz, *Physics in Medicine and Biology*, vol. 41, pp. 2251 – 2269. 1996
36. S.Gabriel, R. W. Lau, C. Gabriel, Dielectric properties of biological tissues:III. Parametric models for the dielectric spectrum of tissues, *Physics in Medicine and Biology*, vol.41, pp. 2271 – 2293, 1996.
37. T.A.Ezquerria, F.Kremmer, G.Wegner, *Progress in electromagnetic research*, 6, Elsevier, NewYork, 1992.

Chapter 5

TWO DIMENSIONAL MICROWAVE TOMOGRAPHIC IMAGING OF BREAST PHANTOMS AND BREAST TISSUES

5.1 Introduction

Microwave tomographic imaging is a promising approach for breast cancer detection due to the high dielectric contrast between normal and malignant breast tissues when exposed to microwaves. The technique is highly desirable as it provides quantitative information about the electrical properties of tissues which potentially relates the physiological states of tissues.

The microwave imaging solutions involve the measurement of energy transmitted through an object. These measurements are then used to reconstruct the dielectric properties of the object. Initially X-ray based reconstruction technique has been tried for microwave imagery. But the images were seriously faulted due to inaccurate reconstruction. The reason for the inapplicability of X-ray based methods to microwave forward scattered methods is the fact that a single, linear ray path cannot be

reasonably presumed to connect the transmitter and receiver. Neither can a single, curved path be assumed for this. Minor changes in launch angle have a dramatic effect upon the receiver site where the ray is terminated. Also the multiple scattering effects that take place inside the object upon encounter with microwaves are ignored in X-ray image reconstruction methods. Thus the problem of ray linkage presents a barrier to successful application of ray-based methods to microwave systems.

Another class of numerical technique is then considered which is stated in radar terminology as inverse scattering methods. Here the object profile is reconstructed by solving the inverse scattering problem using iterative methods. In addition to obtaining the shape of the object, a quantitative description of the dielectric constant profile is also obtainable, which is extremely valuable diagnostic information.

Microwave tomographic imaging of breast phantoms and breast tissue samples based on inverse scattering method is presented in this chapter. Evaluation of two-dimensional tomographic images and their dielectric constant profiles show that microwave tomographic imaging can resolve regions of dielectric contrast with reasonable accuracy.

5.2 Review of the past work

The various techniques used in microwave imaging are discussed in this section.

A 2.45 GHz microwave camera was developed by Franchois etal [1] where they used method of moments combined with distorted Born iterative method for image reconstruction.

In microwave imaging algorithm developed by Sourov etal [2], the direct solution for the scattering problem was obtained by fast forward iterative method and inverse solution by Newton iterative method.

Chew et al [3] developed a time domain approach that incorporated the FDTD method in distorted Born iterative method to the reconstruct images.

A microwave imaging system that operated at 2.45 GHz was developed by Joefre et al [4]. Phantoms having dielectric constants 45, 49, 46 and 32 with water as the coupling medium was considered. The image reconstruction algorithm was formulated in two dimensions using Born approximation. It was assumed that scattering acted as a small perturbation on the illumination and therefore the field within the body was approximated by the incident field. The spectrum of the plane wave induced currents in the object was obtained from the measurements on a circular line with a set of cylindrical wave illuminations. Using a double convolution operator the problem was reduced to a conventional reconstruction in linear geometries. The images were not good, due to the limitations of Born approximation [5] and due to the dielectric contrast between water and phantoms.

Meaney et al [6] developed a dual mesh scheme for image reconstruction where the field variables were decoupled form the reconstruction parameters thereby minimizing the amount of observational data needed to recover electrical property profiles without sacrificing the quality of the reconstructed images. The work was extended [7] using Newton's iterative scheme based on finite element (FE) representation, which was coupled with boundary element (BE) formulation for finding the forward solution of the electric fields. It utilized FE discretization of only the area of interest while incorporating the BE method to match the conditions of the homogeneous background region extending to infinity. They also developed an active microwave imaging system [8] in the

frequency range of 0.3 – 1.1 GHz and 2-D electrical property distributions of phantom were reconstructed using the above algorithm. Coupling media used for the study were water and saline. Multi target tissue equivalent phantoms [9] were also investigated in the same frequency range, using the same coupling media. A weighted least squares minimization involving pre and post multiplying of the Jacobian matrix with diagonal weights had been used to improve matrix conditioning. In addition, low pass filtering was applied during the iterative reconstruction process by spatially averaging the updated reconstruction parameters at each iteration, which reduced the effects of noise and measurement imprecision. The electrical properties were found to be frequency dependent and an error of ~50% was reported for a dielectric constant variation of 10 – 20% between the phantom and the background medium. The same group modified the hybrid element strategy by modifying the forward solution problem in microwave tomographic imaging [10]. The electric fields were calculated at each iteration and the Jacobian matrix calculations were updated with the new electrical property values. These forward solution modifications affected the boundary element part of the numerical algorithm, which was then coupled to the existing finite element discretization yielding a new complete hybrid element discretization. They also performed ex-vivo microwave imaging experiments in normal breast tissue sample with saline inclusion, immersed in saline [11]. Due to the contrast between the breast tissue and the saline, the reconstructed images were not clear. Single object investigations were performed to isolate the 3-D effects without additional perturbations from scattering interactions from multiple targets. The hybrid element approach was further explored [12-13] where finite element method was deployed inside the biological imaging region of interest. The

electromagnetic property distribution was expressed in a piecewise linear basis function expansion whose coefficients were to be determined. The uniform surrounding space that consisted of the attenuating medium containing the electromagnetic radiators was discretized using boundary element method. This method accounted for the unbounded wave propagation of any scattered fields and efficiently approximated the computational domain where finite walls confined the external attenuating medium. Non-active antenna compensation model too, was incorporated in the image reconstruction algorithm. The compensation model parameters were predetermined from the measurement data obtained from a homogeneous medium and then applied in the imaging results involving the reconstruction of heterogeneous regions. Same group realized a water-coupled prototype microwave imaging system [14] to perform multislice examinations of the breast over a broad frequency range of 0.3 – 1 GHz. Hybrid element approach was used for image reconstruction. The obtained relative permittivities of the breast tissues were considerably higher than those previously reported [15]. They also studied the 3-D effects in 2-D microwave imaging using a wide range of phantom and simulation experiments [16]. The frequency range is enhanced to 0.5 – 3 GHz by developing a parallel detection microwave system for breast imaging [17]. High quality reconstructions of inclusions embedded in phantoms were achieved up to 2.1 GHz.

Conformal microwave imaging algorithm for breast cancer detection was investigated by Li et al [18]. They used Gauss-Newton iterative scheme for microwave breast image reconstruction where the heterogeneous target zone within the antenna array was represented using finite element method while the surrounding homogeneous coupling

medium was modeled with boundary element method. The interface between the two zones was arbitrary in shape and position with the restriction that the boundary element region contained only the homogeneous coupling liquid. Their studies showed that the detection of tumor was enhanced as the target zone approached the exact breast perimeter. Also the central artifacts that often appear in the reconstructed images that might potentially confound the ability to distinguish benign and malignant conditions were reduced.

Slaney et al [19] developed a microwave imaging algorithm by relating Fourier transformation of projection views to samples of two-dimensional Fourier transformation of the scattering object. They also discussed the limitations of first order Born and Rytov approximations in scalar diffraction tomography.

Tseng et al [20] simulated quasi monostatic microwave imaging using multi source illumination. The object rotation angle was reduced but multiple sets of the object Fourier domain data were received from multiple sources at the same time.

An iterative algorithm to solve the non-linear inverse scattering problem for two-dimensional microwave tomographic imaging using time domain scattering data was developed by Moghaddam et al [21]. The method was based on performing Born iterations on volume integral equation and then successively calculating higher order approximations to the unknown object profile. Wide band time –domain scattered field measurements made it possible to use sparse data sets, and thus reduced experimental complexity and computation time.

Tijhuis et al [22] conducted 2-D inverse profiling with the Ipswich data provided by the Institut of Fresnel, France. The distorted Born

iterative approach was applied for the image reconstruction. They observed that the dynamic range was large and resolution was limited for low frequency, where as at high frequencies the resolution was increased at the cost of dynamic range. They also developed a technique for solving 2-D inverse scattering problem in microwave tomographic imaging by parameterizing the scattering configuration and determining the optimum value of the parameters by minimizing a cost function involving the known scattered fields [23]. The efficiency of the computation was improved by using CGFFT iterative scheme.

Born iterative method was proposed for solving the inverse scattering problem in microwave tomographic imaging by Wang et al [24]. The Green's function was kept unchanged in the iterative procedures. As the method failed for imaging strong scatterers, they proposed an alternative method called distorted Born iterative method [25] wherein the Green's function and the background medium were updated in every iteration. The new method showed faster convergence rate.

Liu et al [26] developed fast forward and inverse methods to simulate 2-D microwave imaging for breast cancer detection. The forward methods were based on extended Born approximation, fast fourier transform, conjugate gradient and bi-conjugate gradient methods. The inverse methods were based on a two step non-linear inversion. Numerical results demonstrated the efficiency of the algorithm. The work was extended [27] to 3-D imaging of the breast using stabilized biconjugate gradient technique (BiCGSTAB) and FFT algorithm, to compute electromagnetic fields. The computational domain of the electric field integral equation was discretized by simple basis functions through the weak form discretization.

Multiple frequency information was utilized for performing microwave image reconstruction of tissue property dispersion characteristics by Fang et al [28]. They adopted Gauss-Newton iterative strategy which facilitated the simultaneous use of multiple frequency measurement data in a single image reconstruction.

Caorsi et al [29] proposed a multi-illumination multi view approach for 2-D microwave imaging based on Genetic algorithm. The inverse problem was recasted as an optimization problem, solved in the frame work of Born approximation.

Multiplicative regularization scheme was introduced to deal with the problem of detection and imaging of homogeneous dielectric objects by Abubakar et al [30].

Contrast source inversion method was introduced for reconstructing the complex index of refraction of a bounded object immersed in a known background medium by Van den Berg et al [31]. The method accommodated spatial variation of the incident fields and allowed *a priori* information about the scatterer.

Newton- Kantorovitch iterative reconstruction algorithm was developed for microwave tomography by Joachimowicz et al [32]. The results of biological imaging provided a quantitative estimation of the effect of experimental factors such as temperature of the immersion medium, frequency and signal to noise ratio.

Multi frequency scattering data was utilized for image reconstruction in 2-D microwave imaging by Belkebir et al [33]. Newton – Kantorovich (NK) and Modified Gradient (MG) methods were used for image reconstruction. Both methods used *a priori* information and the same initial guess that the characteristic function was non-negative.

Semenov et al [34, 35] developed a 2-D quasi real time tomographic system for microwave imaging. The Rytov approximations were modified to take into account of the radiation pattern as well as the locations of the antenna for 2-D microwave tomography. Images of water immersed gel phantom were developed. Better results were reported with objects of high contrast. The same group also [36] developed vector Born reconstruction method for developing 3-D microwave tomographic images. The method utilized only one component of the vector electromagnetic field for image reconstruction. They also studied Newton method for reconstructing 2-D images of breast phantoms and Modified Gradient method for reconstructing 3-D images [37].

5.3 Motivation for the present work

Review shows that extensive research goes on in the field of microwave tomographic imaging to solve the inverse scattering problem, to realize a viable system for medical imaging. Most of the works reported were simulations and a few were tested experimentally on phantoms. Reconstruction of 2-D tomographic images from experimentally collected scattered fields on breast tissues (normal tissue with cancerous inclusion) in the presence of a matching coupling medium is not tried elsewhere.

The present chapter analyses distorted Born iterative method to solve the inverse scattering problem using experimentally collected scattered data on breast tissues and on breast phantoms. This method is adopted as it is simple, easy to implement and could develop images with reasonable accuracy, even for strong scatterers.

The analysis of the wave equations for inhomogeneous media and that of the inverse scattering method are discussed in detail in the following sections.

5.4 The Wave Equation

In a homogeneous medium, electromagnetic waves, $\phi(\vec{r})$, satisfy a homogeneous wave equation of the form,

$$(\nabla^2 + k_0^2)\phi(\vec{r}) = 0 \quad (5.1)$$

where the wave number k_0 represents the spatial frequency of the plane wave and is a function of the wavelength λ or $k_0 = 2\pi/\lambda = \omega\sqrt{\mu\epsilon_0}$. A solution to eqn. 5.1 is given by a plane wave as

$$\phi(\vec{r}) = e^{j\vec{k}_0\vec{r}} \quad (5.2)$$

where $\vec{k}_0 = (k_x, k_y)$ is the wave factor of the wave and satisfies the relation $|\vec{k}_0| = k_0$. For imaging, an inhomogeneous medium is of interest and hence the wave equation is written in more detailed form as,

$$(\nabla^2 + k^2(\vec{r}))\phi(\vec{r}) = 0 \quad (5.3)$$

For electromagnetic fields, if the effects of polarization are ignored, $k(\vec{r})$ can be considered to be a scalar function representing the refractive index of the medium. It can then be written as,

$$k(\vec{r}) = k_0 n(\vec{r}) = k_0 (1 + n_s(\vec{r})) \quad (5.4)$$

The parameter $n_s(\vec{r})$ represents the deviation from the average refractive index. In general it is assumed that the object of interest has finite support and hence $n_s(\vec{r})$ is zero outside the object.

Re-writing eqn. 5.4 in terms of the dielectric constant,

$$k^2(\vec{r}) = k_0^2 \epsilon(\vec{r}) = k_0^2 (1 + \delta\epsilon(\vec{r})) \quad (5.5)$$

where $\delta\epsilon(\vec{r})$ represents the difference in dielectric constants between object and the background medium, which is also represented as object function

$O(r')$. If the second order terms in $\delta\epsilon(\bar{r})$ are ignored the wave equation becomes,

$$(\nabla^2 + k_o^2)\phi(\bar{r}) = -\phi(\bar{r})k_o^2\delta\epsilon(\bar{r}) \quad (5.6)$$

This scalar propagation equation implies that there is no depolarization as the electromagnetic wave propagates through the medium.

In addition, the incident field $\phi_{inc}(\bar{r})$ can be defined using eqn. 5.1 as,

$$(\nabla^2 + k_o^2)\phi_{inc}(\bar{r}) = 0 \quad (5.7)$$

Thus $\phi_{inc}(\bar{r})$ represents the source field or the field present without any object inhomogenities. The total field is then expressed as the sum of the incident field and the scattered field.

$$\phi(\bar{r}) = \phi_{inc}(\bar{r}) + \phi_{scat}(\bar{r}) \quad (5.8)$$

with $\phi_{scat}(\bar{r})$ satisfying the wave equation

$$(\nabla^2 + k_o^2)\phi_{scat}(\bar{r}) = -\phi(\bar{r})O(r') \quad (5.9)$$

which is obtained by substituting eqns. 5.7 and 5.8 in eqn. 5.6.

This scalar Helmholtz equation cannot be solved directly for $\phi_{scat}(\bar{r})$, but a solution for this can be written in terms of Green's function [38].

The Green's function which is a solution of the differential equation

$$(\nabla^2 + k_o^2)g(\bar{r}/\bar{r}') = -\delta(\bar{r} - \bar{r}') \quad (5.10)$$

is written as

$$g(\bar{r}/\bar{r}') = \frac{e^{jk_oR}}{4\pi R} \quad (5.11)$$

with $R = |\bar{r} - \bar{r}'|$. The representations of r and r' are given in Figure 5.1.

In 2 -D, the solution of eqn.5.10, which is the Green's function is written in terms of Hankel function of the first kind as,

$$g(\bar{r}/\bar{r}') = \frac{j}{4} H_0^1(k_0 R) \quad (5.12)$$

In both the cases the Green's function, $g(\bar{r}/\bar{r}')$ is only a function of the difference $\bar{r} - \bar{r}'$, so the argument of the Green's function will often be represented as simply $g(\bar{r}/\bar{r}')$. As the eqn. 5.10 represents a point inhomogeneity, the Green's function can be considered to represent the field resulting from a single point scatterer.

Eqns. 5.9 – 5.10 can be represented in terms of linear integral equations as there is close correspondence between linear integral equations, which specify linear, integral relations among functions in an infinite-dimensional function space, and plain old linear equations, which specify analogous relations among vectors in finite dimensional vector space. An inhomogeneous Fredholm integral equation of the first kind has the form,

$$g(t) = \int_a^b K(t, s) f(s) ds \quad (5.13)$$

where $f(t)$ is the unknown function to be solved for, while $g(t)$ is a known right hand side.

This is analogous to the matrix equation

$$G = K \cdot f \quad (5.14)$$

As eqn. 5.10 represents the radiation from a 2-D impulse source, the total radiation from all the sources on the right hand side of eqn. 5.9 can be given by the Fredholm integral equation as,

$$\phi_{scat}(\bar{r}) = \int g(\bar{r} - \bar{r}') \mathcal{O}(r') \phi(r') dS = \omega^2 \mu \int g(\bar{r} - \bar{r}') \delta \epsilon(r') \phi(r') dS \quad (5.15)$$

In general it is impossible to solve eqn. 5.15, so some approximations need to be made.

5.4.1 Inverse scattering

In inverse scattering the profile of the scattering object is inferred from the measurement data collected at a distance from the scatterer. In addition to obtaining the shape of the object, a quantitative description of profile of dielectric constant is also obtainable from the inverse scattering experiment.

The inverse scattering depends on the multiple scattering effects that take place within the object. These effects cause the scattered fields to non-linearly relate to the object function; which is a function that describes the velocity, relative permittivity and conductivity distribution of the object. A solution to the inverse scattering is sought from the field perturbation, or the scattered field induced by object. The inverse scattering measurement configuration is shown in Figure 5.1.

A solution to the inverse problem is non-unique, due to the generation of evanescent waves by high spatial frequency portions of the object. These waves are exponentially small at the receiver locations and in practice not measurable unless the receivers are very close to the object. This gives rise to the concept of near field imaging in microwave tomography.

The relationship between the scattered field and the scattering object is a non-linear one. This non-linearity arises from the multiple scattering effects within the object as shown in Figure 5.2.

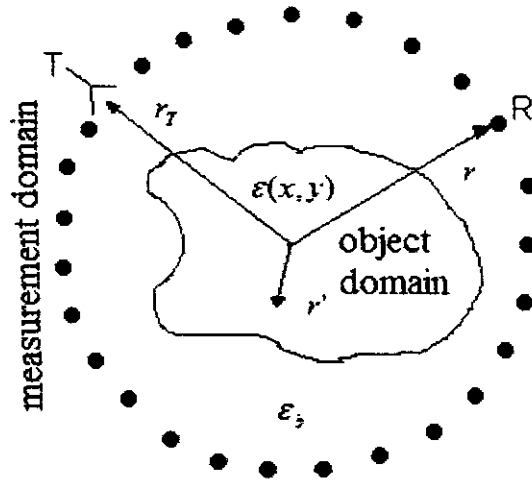


Figure 5.1 Inverse scattering measurement configuration

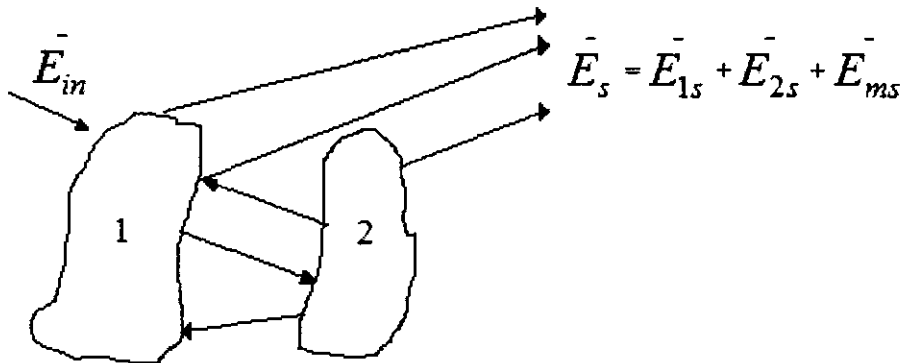


Figure 5. 2. Multiple scattering effects inside the object

When only scatterer 1 is present, the scattered field is \vec{E}_{1s} and when only scatterer 2 is present the scattered field is \vec{E}_{2s} . However when both the

scatterers are simultaneously present, the scattered field is $\bar{E}_{1s} + \bar{E}_{2s} + \bar{E}_{ms}$ where \bar{E}_{ms} is a result of multiple scattering between the scatterers.

5.4.2 Non-linear inverse scattering method

Non-linear inverse scattering theories deal with problems involving multiple scattering effects.

As given in eqns 5.8 and 5.13, the scattering by an inhomogeneous body is represented by the equation,

$$\phi_{scat}(\bar{r}) = \omega^2 \mu \int g(\bar{r} - \bar{r}') \delta\epsilon(r') \phi(r') dS \quad [3]$$

$$\text{where } \phi_{scat}(\bar{r}) = \phi(\bar{r}) - \phi_{inc}(\bar{r}) \quad (5.16)$$

\bar{r} stands for a point in the measurement domain and \bar{r}' for the object domain. In general it is impossible to solve the non linear eqn. 5.13, hence some approximations need to be made. The Born Approximation is the simpler approach to linearise this inverse scattering equation.

Eqn 5.16 shows that total field $\phi(\bar{r})$ is expressed as the sum of the incident field $\phi_{inc}(\bar{r})$ and a small perturbation $\phi_{scat}(\bar{r})$. In a similar way, eqn.5.15 can be written as,

$$\phi_{scat}(\bar{r}) = \omega^2 \mu \int g(\bar{r} - \bar{r}') \delta\epsilon(r') \phi_{inc}(r') dS + \omega^2 \mu \int g(\bar{r} - \bar{r}') \delta\epsilon(r') \phi_{scat}(r') dS \quad (5.17)$$

If the scattered field $\phi_{scat}(\bar{r})$ is small compared to the incident field $\phi_{inc}(\bar{r})$, the effects of the second integral can be ignored to arrive at the approximation,

$$\phi_{scat}(\bar{r}) = \omega^2 \mu \int g(\bar{r} - \bar{r}') \delta\epsilon(r') \phi_{inc}(r') dS \quad (5.18)$$

This constitutes the first order Born Approximation. This approximation is valid only if the magnitude of the scattered field is smaller than the incident field.

Eqn. 5.10, represents radiation from a two-dimensional impulse source and the Green's function is considered to represent the field from a single point scatterer. Hence the incident field can be considered to that generated by a uniform line source, which is given by the Hankel function as,

$$\phi_{inc}(\vec{r}_T|\vec{r}') = \frac{j}{4} H_0^1(k_o(\vec{r}_T|\vec{r}')) \quad (5.19)$$

For eqn. 5.18, it is assumed that the medium is homogeneous and hence Green's function is known in the closed form. The field inside the scatterer is found numerically for an initial guess of the permittivity profile. Then an improved profile is obtained by comparing the differences between the estimated and the measured scattered field. This process is repeated until a convergent solution is reached. This iteration procedure is called as the Born iterative method.

While the Born iterative method is simple to implement, it does not offer second order convergence and hence not suitable to solve non linear inverse scattering problem. Also eqns. 5.12 and 5.19 represents the homogeneous medium, which is not suitable for breast imaging. Hence Distorted Born Iterative Method is developed for the image reconstruction of breast tissues. The method is described in detail in the following section.

5.4.3 Distorted Born Iterative Method

In this method, the back ground medium is considered inhomogeneous and is updated with each iteration. Hence the equation for Green's function (eqn. 5.12) and the equation for incident field (eqn. 5.19) are updated with each iteration.

The wave equation for the inhomogeneous medium can be written as

$$(\nabla^2 + k_b^2)\phi(\vec{r}) = 0 \quad (5.20)$$

where the wave number k_b represents the spatial frequency of the plane wave in the medium and is a function of the wavelength λ or $k_b = 2\pi/\lambda = \omega\sqrt{\mu\epsilon_b}$. A solution to this equation is given by a plane wave as

$$\phi(\vec{r}) = e^{jk_b\vec{r}} \quad (5.21)$$

which on simplification using eqns. 5.3 – 5.16 and using the Green's function becomes,

$$\phi(\vec{r}) = \phi_{inc,b}(\vec{r}) + \omega^2 \mu \int_S dS g_b(\vec{r}, \vec{r}') \delta\epsilon(\vec{r}') \phi(\vec{r}') \quad (5.22)$$

where \vec{r} stands for a point in the measurement domain and \vec{r}' for the object domain. $\phi(\vec{r})$ is the total field at \vec{r} , $\phi_{inc,b}(\vec{r})$ is the incident field measured at \vec{r} in the presence of the background inhomogeneity, ω represents the angular frequency and μ the permeability. As biological materials are non-magnetic, the relative permeability is unity and hence $\mu = \mu_0$, the permeability of free space.

The $\delta\epsilon(\vec{r}')$ is defined as

$$\delta\epsilon(\vec{r}') = \epsilon(\vec{r}') - \epsilon_b(\vec{r}') \quad (5.23)$$

where $\epsilon(\vec{r}')$ is the complex relative permittivity of the object and $\epsilon_b(\vec{r}')$ is the complex relative permittivity of the background medium. $g_b(\vec{r}, \vec{r}')$ is the Green's function and $\phi(\vec{r}')$ is the total field inside the scatterer. The integral term in Eqn. 5.22 is the scattered field due to the dielectric contrast of the scatterer. Hence,

$$\phi_{scat,b}(\vec{r}) = \phi(\vec{r}) - \phi_{inc,b}(\vec{r}) \quad (5.24)$$

$$\text{Therefore } \phi_{scat,b}(\bar{r}) = \omega^2 \mu \int_S dS g_b(\bar{r}, \bar{r}') \delta\epsilon(\bar{r}') \phi(\bar{r}') \quad (5.25)$$

This scattered field is a non-linear functional of $\delta\epsilon(\bar{r}')$ because $\phi(\bar{r}')$ in the integral is also a function of $\delta\epsilon(\bar{r}')$. In the inverse scattering problem, $\delta\epsilon(\bar{r}')$ need to be solved from the measurement of the scattered field outside the scatterer.

To linearize the non-linear relation between the scattered field and the object function, it is assumed that $\epsilon(\bar{r})$ is close to $\epsilon_b(\bar{r})$ [38]. Hence $\phi_{scat,b}(\bar{r}) \ll \phi_{inc,b}(\bar{r})$. Therefore $\phi(\bar{r}')$ in Eqn 5.25 is approximated with $\phi_{inc,b}(\bar{r}')$, which is the incident field inside the scatterer. This approximation is called as distorted Born approximation. The scattered field is written as

$$\phi_{scat,b}(\bar{r}) = \omega^2 \mu \int_S dS g_b(\bar{r}, \bar{r}') \delta\epsilon(\bar{r}') \phi_{inc,b}(\bar{r}') \quad (5.26)$$

Substituting Eqn. 5.22 in Eqn. 5.26,

$$\phi_{scat,b}(\bar{r}) = k_0^2 \int_S dS g_b(\bar{r}, \bar{r}') (\epsilon_r(\bar{r}') - \epsilon_{rb}(\bar{r}')) \phi_{inc,b}(\bar{r}') \quad (5.27)$$

where $k_o^2 = \omega^2 \mu \epsilon_o$. The singularity that exists in the Green's function when observation point is in the object domain, is taken care by using Richmond approximation [39] where the square cells in the computation domain are approximated with circular cells of same cross sectional area.

Hence $k_0^2 \int_S dS g_b(\bar{r}, \bar{r}')$ in Eqn 5.27 is modified as,

$$\frac{j\pi k_o}{2} \sum_{n=1}^N a_n J_1(k_b a_n) H_0^{(1)}(k_b(\bar{r} - \bar{r}_n')) \quad \text{for } \bar{r} \neq \bar{r}' \quad (5.28)$$

$$\frac{j\pi k_o}{2} \sum_{n=1}^N a_n H_1^{(1)}(k_b a_n) - 2j \quad \text{for } \bar{r} = \bar{r}' \quad (5.29)$$

where N stands for the total number of cells in the computation domain and a the radius of the circular cell. $H_0^{(1)}$ represents zeroth order Hankel function of first kind, $H_1^{(1)}$ represents first order Hankel function of first kind and k_b represents the wave number $\omega \sqrt{\mu\epsilon_b}$.

In 2-D, the incident field inside the scatterer is written using eqn. 5.19 as,

$$\phi_{inc,b}(\bar{r}') = \frac{j}{4} H_0^{(1)}(k_b(\bar{r}' - \bar{r}_T)) \quad (5.30)$$

where \bar{r}_T represents the transmitter location. Eqns. 5.28 - 5.30 are substituted in the linearized eqn 5.27 and is solved numerically to obtain the value of $\delta\epsilon(\bar{r}')$. This method to obtain $\delta\epsilon(\bar{r}')$ from $\phi_{scat,b}(\bar{r})$ is termed as the inverse scattering solution. $\epsilon(\bar{r}')$ can be calculated from $\delta\epsilon(\bar{r}')$ using Eqn. 5.23. This value of $\epsilon(\bar{r}')$ is then used as the new $\epsilon_b(\bar{r}')$ and using this, the incident field and Green's function inside the object are updated. The total field inside the scatterer is then updated using the equation,

$$\phi(\bar{r}') = \phi_{inc,b}(\bar{r}') + \omega^2 \mu \int_S dS g_b(\bar{r}, \bar{r}') \delta\epsilon(\bar{r}') \phi_{inc,b}(\bar{r}') \quad (5.31)$$

Computing $\phi(\bar{r}')$ using Eqn. 5.31 is termed as the forward scattering solution. This value of $\phi(\bar{r}')$ is then substituted as $\phi_{inc,b}(\bar{r}')$ in the Eqn. 5.26. The entire procedure is repeated by first obtaining the inverse scattering solution and then the forward scattering solution. This iterative procedure where the dielectric properties of the background medium are also updated with each iteration is called as the distorted Born iterative method. The iteration is continued until convergence is reached, that is the difference between the estimated and the measured scattered field is less than 5%.

5.4.4 Discretization of the integral equation

The Eqn. 5.26 is to be solved to obtain the unknown $\delta\mathcal{E}(\bar{r}')$. The $\phi_{scat,b}$ is a function of frequency, transmitter and receiver locations. Hence Eqn. 5.24 is re written as,

$$\phi_{scat,b}(\bar{r}, \bar{r}_T, \omega) = \omega^2 \mu \int_S dS g_b(\bar{r}, \bar{r}', \omega) \delta\mathcal{E}(\bar{r}') \phi_{inc,b}(\bar{r}', \bar{r}_T, \omega) \quad (5.32)$$

This equation is discretized as

$$\phi_{scat,b}(\bar{r}_i, \bar{r}_{T_j}, \omega_k) = \sum_{n=1}^N \Delta s \omega_k^2 \mu g_b(\bar{r}_i, \bar{r}_n, \omega_k) \delta\mathcal{E}(\bar{r}_n) \phi_{inc,b}(\bar{r}_n, \bar{r}_{T_j}, \omega_k) \quad (5.33)$$

where r_n is a location within the object to be reconstructed.

If a vector \bar{f} is nonlinearly related to another vector \bar{g} via the function G , the relationship is written as,

$$\bar{f} = G(g) \quad (5.34)$$

where $f_i = G_i(g_{1,2,\dots,N})$, $i = 1, 2, \dots, M$. The first variation of f_i induced by the first variation of g_j can be written as,

$$\delta f_i = \sum_{j=1}^N \frac{\partial G_i}{\partial g_j} \delta g_j \quad (5.35)$$

This relation is represented in the matrix notation as,

$$\delta \bar{f} = \bar{F} \delta \bar{g} \quad (5.36)$$

$$\text{where} \quad [\bar{F}]_{i,j} = \frac{\partial G_i}{\partial g_j} \quad (5.37)$$

\bar{F} is the gradient of the multidimensional function known as its Frechet derivative.

So, from Eqn. 5.33,

$$\bar{\phi}_{scat,b} = \bar{M} \cdot \delta \bar{\mathcal{E}} \quad (5.38)$$

where M is called as the Freschet derivative operator. Hence

$$\delta\bar{\mathcal{E}} = M^{-1}\bar{\phi}_{scat,b} \quad (5.39)$$

$[\bar{\phi}_{scat,b}]_m$ represents the data measured for all transmitter, receiver and frequency combinations. That is

$$[\bar{\phi}_{scat,b}]_m = \phi_{scat,b}(\bar{r}_i, \bar{r}_{T_j}, \omega_k) \quad (5.40)$$

$$[\bar{M}]_{mn} = \Delta s \omega_k^2 \mu g_b(\bar{r}_i, \bar{r}_n, \omega_k) \phi_{inc,b}(\bar{r}_n, \bar{r}_{T_j}, \omega_k) \quad (5.41)$$

$$[\delta\bar{\mathcal{E}}]_n = \delta\mathcal{E}(\bar{r}_n) \quad (5.42)$$

where index m represents all combinations of (i, j, k) .

5.4.5 Minimization of Cost (Error) Functional

A solution to Eqn. 5.39 is difficult to obtain because matrix M is ill-conditioned and might not have a unique inverse. There are two reasons for this ill-conditioning

1. \bar{M} is a $M \times N$ matrix. If $M < N$, the number of measurement data points are less than the number of pixels used to approximate the object function. Then the range space \bar{M} would have a smaller dimension than the domain, implying that the inverse does not exist.
2. \bar{M} maps the object function $\delta\bar{\mathcal{E}}$ to the measurement data $\phi_{scat,b}$. Many high spatial frequency components of \mathcal{E} are not mapped to $\phi_{scat,b}$ because these components generate evanescent waves that do not reach the receiver locations. Therefore these fine details are lost in the inversion process.

The induced current in the scatterer is produced via the term $\delta\bar{\mathcal{E}}(r')\phi_{inc,b}(\bar{r}')$. Hence if $\delta\bar{\mathcal{E}}(\bar{r}')$ has high spatial frequency components, so does the induced current. This induced current radiates via Green's function $g_b(\bar{r},\bar{r}')$ which accounts for multiple scattering within the inhomogeneous background ϵ_b . The induced current contains Fourier components corresponding to the evanescent waves, whose information is lost if the data is measured at the far field.

From eqn. 5.38, $\bar{\phi}_{scat,b} - \bar{M} \cdot \delta\bar{\mathcal{E}} = 0$. But this will not hold good due to the presence of evanescent waves. Hence to solve Eqn. 5.38 an optimization technique is adopted where the error is minimized as well as the norm of the solution $\delta\bar{\mathcal{E}}$. To solve the error function of any non singular matrix equation of type $Ax=b$, it is necessary to define an inner product as a Euclidean Scalar function [38] whose error functional is defined as

$$I_n(x_n) = \|Ax_n - b\|_{\bar{A}}^2 \quad (5.43)$$

whose norm is defined to be,

$$\|Ax_n - b\|_{\bar{A}}^2 = (Ax_n - b)^\dagger \cdot \bar{A} \cdot (Ax_n - b) \quad (5.44)$$

where \bar{A} is a positive definite matrix and the dagger \dagger represents the transpose conjugate of the matrix.

This optimization technique is applied to the function $\bar{\phi}_{scat,b} = \bar{M} \cdot \delta\bar{\mathcal{E}}$ where $\bar{\phi}_{scat,b}$ is a $M \times 1$ matrix with M representing all combinations of transmitter and receiver locations. $\delta\bar{\mathcal{E}}$ is a $M \times N$ matrix with M

representing all combinations of transmitter and receiver locations and N representing the number of pixels considered in the computational domain. $\delta\bar{\mathcal{E}}$ is a $N \times 1$ matrix with N representing the number of pixels in the computational domain. Single frequency operation is considered here.

Hence error functional I for eqn.5.38 is defined using eqn.5.43 as,

$$I = \|\bar{\varphi}_{scat,b} - \bar{M} \delta\bar{\mathcal{E}}\|_{\bar{C}}^2 + \delta_i \|\delta\bar{\mathcal{E}}\|_{\bar{D}}^2 \quad (5.45)$$

where δ_i is called as the Tikhonov regularization parameter which is used to smoothen the data. \bar{C} and \bar{D} are positive definite matrices chosen to scale the measured scattered data. \bar{C} is so chosen that equal weights are given to the data irrespective of their measured amplitudes and \bar{D} is chosen to enforce some regularity in $\delta\bar{\mathcal{E}}$. If \bar{D} is an identity matrix, then the second term in the Eqn 5.45 correspond to the energy norm of $\delta\bar{\mathcal{E}}$. If \bar{D} is a finite difference operator, then $\delta\bar{\mathcal{E}}$ has to be sufficiently smooth so that its norm as defined would not be overly large. Such a method of determining the solution to eqn 5.45 is known as the Tikhonov regularization method [38]. Cross validation analysis based on the noise property of the experimental data is used to determine an optimal values of \bar{D} and δ_i . Further δ_i has to be chosen small enough so that the goal of solving eqn 5.45 is not over whelmed by the need to minimize the norm of $\delta\bar{\mathcal{E}}$. However if δ_i is chosen to be too small, the resultant equation may be ill-conditioned again. The optimal choice of δ_i is related to the noise characteristic of the measurement data.

Rewriting Eqn 5.45, using Eqn. 5.44,

$$I = (\bar{\phi}_{scat}^\dagger - \delta\bar{\epsilon}^\dagger \cdot \bar{M}^\dagger) \cdot \bar{C} \cdot (\bar{\phi}_{scat} - \bar{M} \cdot \delta\bar{\epsilon}) + \delta_i \delta\bar{\epsilon}^\dagger \cdot \bar{D} \cdot \delta\bar{\epsilon} \quad (5.46)$$

Taking the first variation of I with respect to the first variation of $\delta\bar{\epsilon}$ and then setting the first variation to zero to obtain the minima of I , we obtain,

$$[\bar{M}^\dagger \bar{C} \bar{M} + \delta_i \bar{D}] \cdot \delta\bar{\epsilon} = \bar{M}^\dagger \cdot \bar{C} \cdot \bar{\phi}_{scat} \quad (5.47)$$

which is solved iteratively to obtain $\delta\bar{\epsilon}$.

5.4.6 Flow Chart of the algorithm

1. Collect the scattered fields from the breast tissues and phantoms by experimental procedure.
2. Compute $\delta\epsilon(\bar{r}')$ from the scattered fields by solving the inverse scattering solution. The background permittivity value is taken as that of the coupling medium used.
3. Obtain $\epsilon(\bar{r}')$ from the computed $\delta\epsilon(\bar{r}')$.
4. Update the incident field and the Green's function by substituting the obtained $\epsilon(\bar{r}')$ as $\epsilon_b(\bar{r}')$.
5. Compute the total field inside the scatterer using the updated values of incident field inside the scatterer and the Green's function by solving the forward scattering solution.
6. Substitute the obtained total field inside the scatterer as the incident field inside the scatterer .
7. Repeat steps 2 – 6 until convergence is obtained (the difference between the estimated and the measured scattered field is less than 5%)

The 2-D tomographic image reconstruction algorithm is coded using Matlab 7.0. For this, the computational domain having the tissue sample is discretized as 16 x 16 pixels. The sampling rate, Δs in eqn. 5.33 is

considered as $\lambda/10$. The sampling rate is so selected to ensure good resolution of the reconstructed image. A resolution of 2.3 mm is achieved in this work with the usage of corn syrup sample of dielectric constant 18.7 as the coupling medium. Three iterations are performed to obtain the convergence. \bar{C} and \bar{D} are chosen as identity matrices to ease the computation. An optimum value of the Tikhonov regularization parameter δ , is selected as 55×10^{-2} by experimental iterations to smoothen $\delta\bar{E}$. Single frequency operation at 3 GHz is performed to collect the scattered fields.

5.5 Measurement set up

The set up used for measurement is shown in Figure 5.3.

It consists of a tomographic chamber made of plastic coated inside with a mixture of carbon black powder, graphite powder and poly vinyl acetate based adhesive in the ratio 20:30:50. The mixture exhibits good absorption coefficient and hence is used as the inner coating to minimize the reflections. Microwave studies of this material are given in detail in Appendix B. Supporting holders made of Perspex are used to hold the bow tie antennas and immerse them in the coupling medium made of corn syrup sample having ϵ_r ' and σ as 18.7 and 0.98 S/m respectively. The transmitting antenna is fixed at a distance of 6 cm from the center of the tomographic chamber, while the receiving antenna is capable of rotating around the object at a radius of 6 cm.

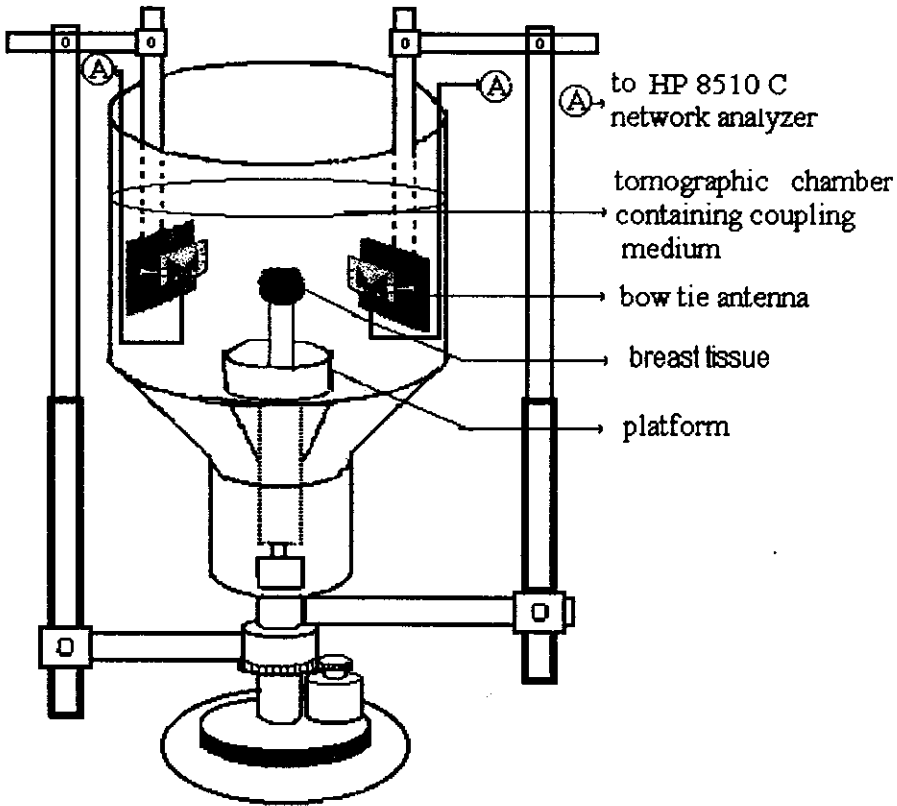


Figure 5.3 Measurement set up

A platform made of Perspex is provided at the center of the tomographic chamber to hold the sample. For data acquisition, the set up is equipped with two stepper motors – the inner motor having Torque 20 kg-cm is used for rotating the platform holding the sample and the outer one having Torque 5 kg-cm is used for rotating the antenna. The speed of the outer motor is controlled by using a 4:1 gear mechanism, to ensure accurate measurements. The details of the driver circuit used to activate the stepper motor are provided in Appendix C. The set up is interfaced with computer which in turn is interfaced with network analyzer using GPIB bus.

5.5.1 System calibration

The experimental setup discussed in Section 2.6 is used for data acquisition. The two bow tie antennas having same radiation characteristics and center frequency of 3 GHz are fixed on the antenna holders of the measurement set up (Figure 5.3), and are immersed in the tomographic chamber filled with coupling medium. The antennas are then connected to Ports 1 and 2 of the experimental set up (Figure 2.4) and THRU calibration is performed. For this, the antennas are kept on the on-axis and the network analyzer is set to perform S_{21} measurements. The transmission coefficient in the THRU position without out any sample will be a flat response, if the calibration is correct.

5.5.2. Data Acquisition

For data acquisition, the network analyzer is set to S_{21} mode and the sample under study is illuminated by the transmitting bow-tie antenna at a frequency of 3 GHz. The driver circuit of the outer motor alone is first activated so that the receiving antenna can now be moved around the sample to make measurement. For every 18° (20 steps) of rotation of the outer motor, the receiving antenna makes the S_{21} measurements. Once one set of measurement for a particular sample position is over, the driver circuit of the inner motor is activated so that the sample is now rotated for 18° (20 steps). The inner motor is then disabled and the outer motor is enabled for the S_{21} measurements. The process is repeated till the sample completes 360° of rotation.

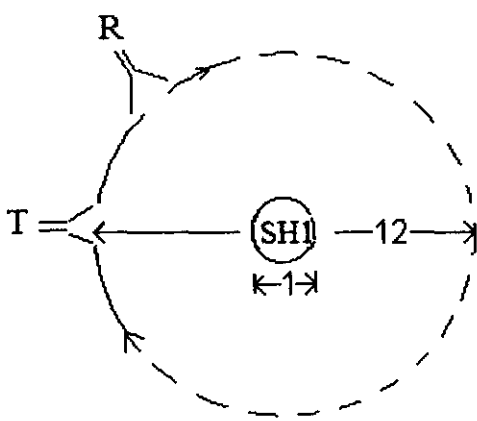
5.5.3 Measurement configuration

Measurements are performed using breast phantoms as well as with breast tissues.

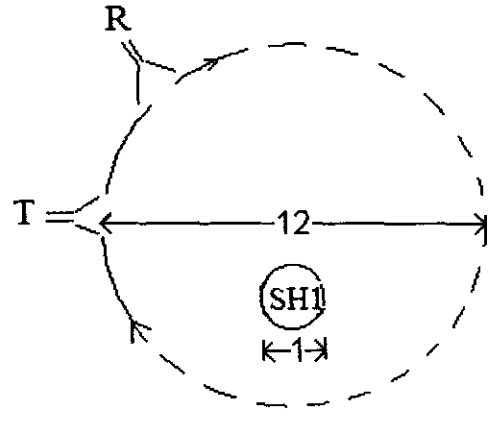
5.5.3.1 Using breast phantoms

Corn syrup of different dielectric constants and conductivities are used as breast phantom and coupling medium for the study. Cylindrical sample holders are used to hold the phantom. The sample holders are made of poly vinyl chloride having dielectric constant 2.84 and conductivity 0.005 S/m at 3 GHz. Two types of sample holders (SHs) are considered. SH1 is a circular cylinder of radius 0.5 cm and height 25 cm. SH2 consists of concentric circular cylinders of height 25 cm. and radii 5 cm. and 0.5 cm.

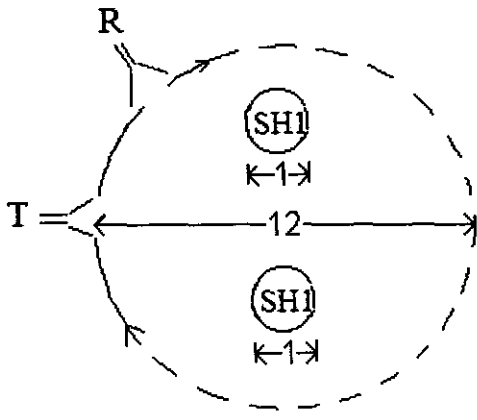
The measurement configurations shown in Figure 5.4 are used. In Fig. 5.4 (a), SH1 kept at the center is used to hold the breast tumor phantom of ϵ_r ' and σ as 38.1 and 1.91 S/m. In Fig. 5.4 (b) off centered SH1 is used to hold the same breast tumor phantom of ϵ_r ' and σ as 38.1 and 1.91 S/m. In Fig. 5.4 (c), two off centered SH1s holding tumor phantoms ϵ_r ' and σ as 38.1 and 1.91 S/m and ϵ_r ' and σ as 29.8 and 1.1 S/m are used. SH 2 is used in Fig 5.4 (d). Two measurement configurations are considered with SH2. 1) Outer and inner cylinders are filled with corn syrup samples of ϵ_r ' and σ as, 29.8 and 1.1 S/m S/m. 2) Outer and inner cylinders are filled with corn syrup samples of ϵ_r ' and σ as 29.8 and 1.1 S/m, and 38.1 and 1.91 S/m respectively



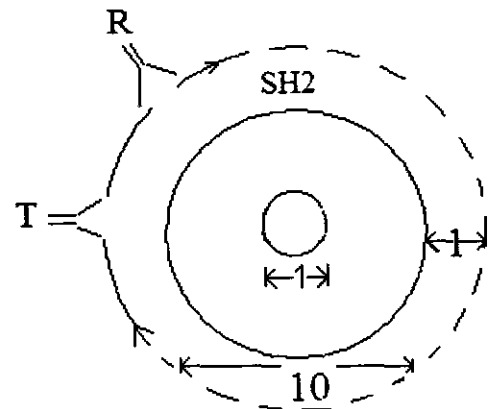
(a)



(b)



(c)



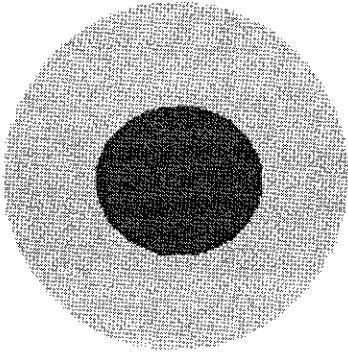
(d)

Figure. 5.4 Measurement configurations for breast phantoms
T – Transmitting antenna, R – Receiving antenna
All dimensions given are in cms.

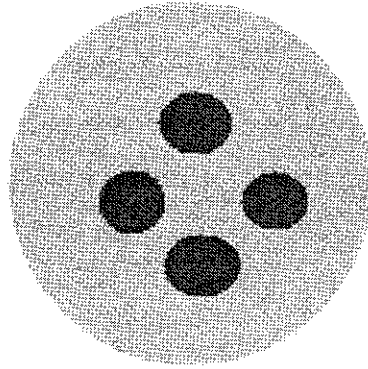
5.5.3.2 Using breast tissues

Samples of breast tissues of four patients are subjected to study within 45 minutes of mastectomy. It is reported that [40-42] the bound water content of breast tissue depends on the age and physical structure of a person. In the present study the age group selected is 45 – 55, as breast cancer is more common in women of this age group.

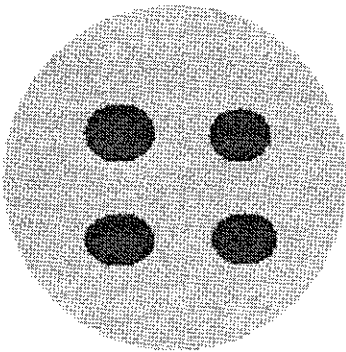
The samples are supported on SH1 and are fixed at the center /off-center of the tomographic chamber. Scattered fields from normal and malignant breast tissues of all four patients are measured separately. A normal breast tissue of radius ~ 1 cm and cancerous tissue of radius ~ 0.25 cm are used for the measurement. Also a real time cancerous breast model is created by inserting cancerous tissue in normal breast tissues. Four cases of this are studied – (1) A cancerous breast tissue of radius ~ 0.5 cm inserted in normal breast tissue of radius ~1 cm, of patient 1, is taken as B-Sample 1. (2) Four tumorous inclusions of radius ~ 0.25 cm each inserted in normal tissue of radius ~ 1 cm, of patients 2 and 3 are treated as B - Samples 2 and 3. (3) Scattered inclusions of cancerous tissue of ~ radius 0.1 cm. each inserted in normal tissue of radius ~ 1 cm, of patient 4 is treated as B-Sample 4. B- Samples are represented in Figure 5.5



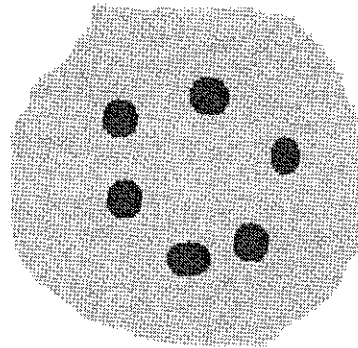
B-Sample 1



B-Sample 2



B-Sample 3



B-Sample 4

Figure. 5.5 Schematic representation of breast tissue samples

 Normal tissue,  Cancerous tissue

To check the feasibility of using corn syrup sample of ϵ_r' and σ as 18.7 and 0.98 S/m as coupling medium for studying the dielectric contrast of breast tissues, dielectric studies of breast tissues are done using rectangular

cavity perturbation method discussed in Section 2.5.2. The experimental set up used for this study is given in detail in Section 2.6. The samples are subjected to dielectric studies after calibrating the experimental set up using the TRL calibration procedure discussed in Section 2.6. The rectangular cavity is then connected between ports 1 and 2 of the experimental set up and the samples are suspended in to the cavity. A cylindrical cup made of low loss Teflon ($\tan \delta = 0.0015$ at 3 GHz) having volume 0.052 cm^3 is used to hold the breast tissue sample. The response of the cavity for maximum perturbation when the sample is inserted is noted. The dielectric parameters of the breast tissue samples obtained at 2.983 GHz are tabulated in Table 5.1 (a). This frequency is selected as it is the nearest resonant frequency of the rectangular cavity to the resonant frequency of the antenna.

The bound water contents of the breast samples are determined by subjecting 10 gm. of each of the sample in a pre-heated oven at 70° C , for 5 seconds [40]. The estimated water content of each of the sample is shown Table 5.1(a)

5.6 Results and Discussions

Table 5.1 (a) shows the dielectric parameters of breast tissues and their bound water content. It is observed from the table that for women in the age group of 45 – 55, normal breast tissue exhibits variation of dielectric constant from 18.85 – 24.98 and conductivity variation from 2.64 S/m – 3.25 S/m. The respective variations for the cancerous breast tissues are 30 – 40.1 and 3.34 S/m – 4.31 S/m. The estimated variation of bound water content for normal breast tissues is from 41 – 45 % and that for cancerous breast tissue is from 61 – 65 %. For the same person, cancerous tissue exhibits a higher value dielectric constant than that of the normal tissue,

due to the higher rate of bound water content.

Table 5.1 (a) Dielectric parameters and bound water content of breast tissues

Sample		Dielectric constant	Conductivity S/m	Bound water content %
Breast tissue, Patient 1 - Age 47	Normal	20.43	3.12	43
	Cancerous	36.31	3.52	62
Breast tissue, Patient 2 - Age 49	Normal	18.85	2.64	42
	Cancerous	38.73	4.12	65
Breast tissue, Patient 3 - Age 51	Normal	24.98	3.25	45
	Cancerous	40.1	4.31	65
Breast tissue, Patient 4 - Age 45	Normal	19.5	2.71	41
	Cancerous	30	3.34	61
Corn syrup (C-Sample 1)		18.7	0.98	NA

Table 5.2 shows the reconstructed 2-D tomographic images and dielectric constant profiles of breast phantoms. Images are good and regions of dielectric contrast are clearly distinguishable. The obtained dielectric constant of the breast phantom is in good match with that obtained by rectangular cavity perturbation technique discussed in Chapter 4.

The reconstructed 2-D tomographic images and profiles of dielectric constant of normal breast tissues are shown in Table 5.3. The images are not clear as there exists very less contrast in the dielectric constants of the coupling medium and that of the normal tissue samples of patients 1, 2 and 4. The dielectric constant profiles show some sharp peaks, whose values match with that of the respective tissues reported in Table 5.1(a). There exists a dielectric contrast between the coupling medium and the normal breast tissue of patient 3, and hence the image is better with distinct peaks in the dielectric constant profile whose values match with the reported values in Table 5.1(a). In all the cases the profiles of dielectric constant are not smooth and uniform, due to the highly heterogeneous nature of the tissue. The tissue contains fat deposits and minor blood vessels that are of low water contents.

Table 5.4 shows the 2-D tomographic images and dielectric constant profiles of cancerous tissues. Cancerous tissues of patients 1-3 have high values of dielectric constants compared to that of the coupling medium and are clearly distinguishable from the figure. To minimize the effect of tissue heterogeneity in the study, each of the tissue samples used has a radius of ~ 0.25 cm. For the tissue sample of patient 4, the dielectric contrast is less compared to that of other three tumor samples and hence the image is not good as that of the other samples. Still, the peak of the profile shows a value corresponding to the dielectric constant of the tissue reported in Table 5.1(a).

The reconstructed 2-D tomographic images and profiles of dielectric constant of normal breast tissues with cancerous tissue inclusions are shown in Table 5.5. The cancerous inclusions as well as the dielectric contrast are clearly distinguishable in all the images. B-Sample 4 is

enclosed in a conical polythene envelope and imaged. This is done to ensure that the shape of the sample too is detected properly by this imaging technique. The black border in the image is due to the low value of dielectric constant of polythene, which is 2.84 at 3 GHz. The dielectric constant obtained for all the profiles match well with that measured using cavity perturbation technique.

For the dielectric constant profiles shown in Tables 5.2 – 5.5, it is seen that the range of values on the z axes are not uniform. This is due to the fact that these values are automatically generated by the Matlab when the algorithm is run, depending on the intensity of the dielectric constant computed from the collected scattered field from different breast tissues. The increase in dielectric constant of the cancerous tissue in the case of each of the patient is clear from the respective figures, which was the aim of the work. A comparison of the results of different patients does not give any useful information as the nature of the cancerous tissue varies from person to person. Normal breast tissue exhibits very low dielectric constant compared to the malignant tissues and providing uniformity in the z -axis, results in reducing the clarity of the profile and hence it is not attempted.

Convergence is achieved with three iterations. The qualitative improvement of the images with iteration is shown Figure 5.6. To ensure that global convergence is achieved, four iterations are performed and the same result as with the third iteration is obtained.

5.6.1 Comparison of the results

Most of the algorithms reported in the literature review were tried only for solving the inverse scattering problem in microwave imaging and not tested for microwave mammography. However Joeffre etal [14] tried Born Approximation, Li etal [18] tried Gauss Newton Iterative Method, Liu etal

[26] tried Biconjugate Gradient Method for simulating breast cancer model. Meaney et al [9-14] tried Hybrid Element Method and Semenov et al [36-37] tried Modified Gradient Method for imaging breast tissues in saline medium. A comparison of these results with that obtained by the author is given in Table 5.1 (b). The error in dielectric constant in the author's work is estimated by comparing the values of the dielectric constants obtained by 2-D tomographic imaging reported in Table 5.2 with that obtained using cavity perturbation technique reported in Table 5.1(a).

Table 5.1 (b) Comparison of the 2-D tomographic imaging results with literature values

Name	Quality of image	Type of work & Medium	Error in dielectric constant
Author	Excellent	Real time - Corn Syrup	4.2 – 7.8 %
Joeffre etal [14]	Good	Simulation – Air	26 %
Li etal [18]	Good	Simulation – Air	34 %
Liu etal [26]	Good	Simulation – Air	24 %
Meaney etal [9-14]	Blurred	Real time – Saline	72 %
Semenov etal [36-37]	Blurred	Real Time - Saline	64 %

From Table 5.1 (b) it is clear that the author's approach reports the least error with the quality of image being excellent. The simulations performed by Joeffre etal, Li etal and Liu etal reports good quality images with significant error in the dielectric constants. If put to real time applications, this high error rate cause false signals in early stage cancer detection. The

real time approach performed by Meaney et al and Semenov et al reports blurred images with high variations in the dielectric constants. This is due to the usage of saline as the coupling medium, which causes significant propagation losses and poor matching of the dielectric parameters with that of the breast tissues.

The effects of using a reduced contrast coupling medium in microwave breast imaging are shown in Figure 5.7. For all the samples, the reconstructed images are not clear, when coupling medium is absent. This is due to the poor coupling of electromagnetic energy into the sample. As air is having a relative permittivity of unity, high dielectric contrast exists between air and the samples, and hence significant reflections result. Also resolution of the image is poor, when samples are imaged in air.

5.7 Conclusion

The reconstruction of 2-D tomographic images of normal and cancerous breast tissues using distorted Born iterative algorithm is performed here. The obtained dielectric parameters of the breast tissues are compared with that of the already reported values and good agreement is observed. Hence it is concluded that microwave tomographic imaging is a successful imaging modality for providing valuable diagnostic information about the shape of the tissues and quantitative description about the dielectric constant profile of the object, rather than identifying the location of the object.

Table 5.2. 2-D Tomographic images and dielectric constant profiles of breast phantoms

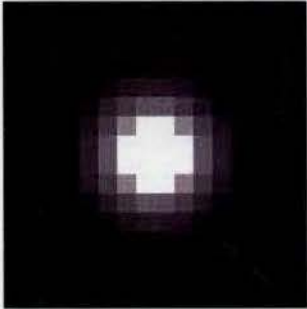
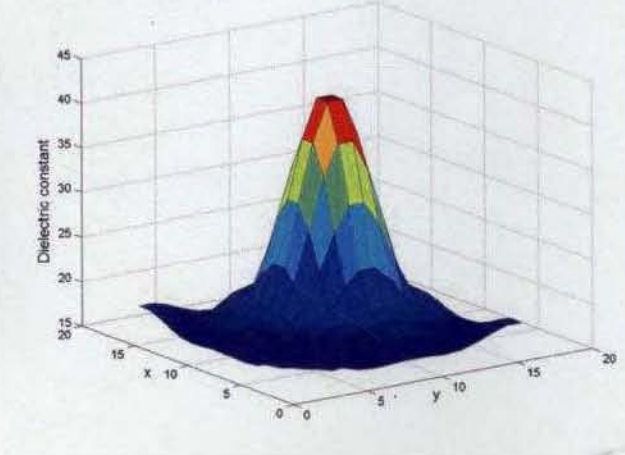
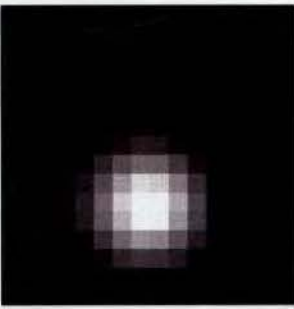
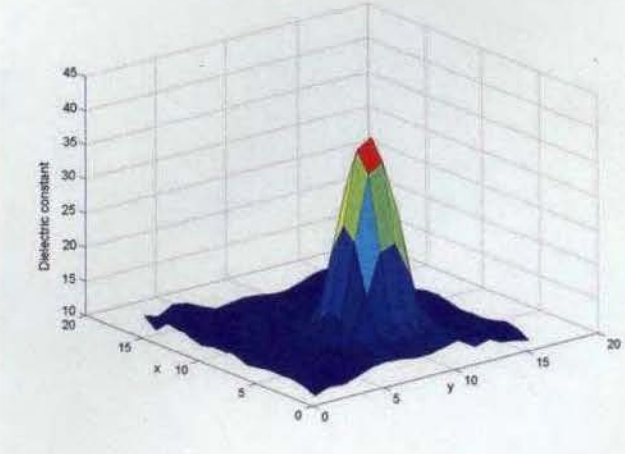
Corn syrup as breast phantom	2-D Tomographic image	Dielectric constant profile
Centered SH1 holding breast tumor phantom of ϵ_r' 38.1		
Off-centered SH1 holding breast tumor phantom of ϵ_r' 29.8		

Table 5.2. continued

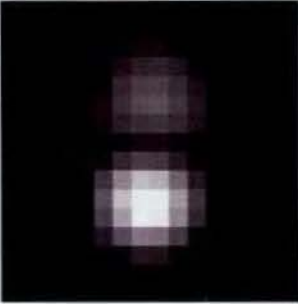
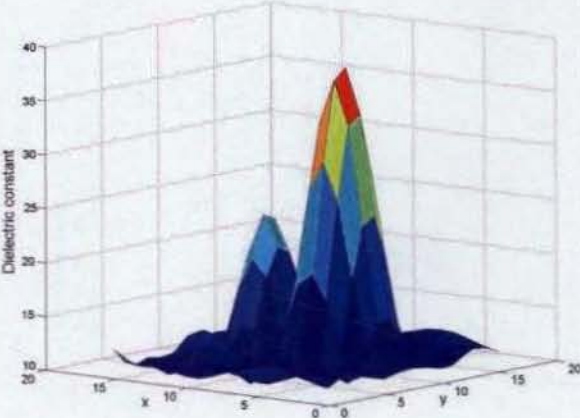

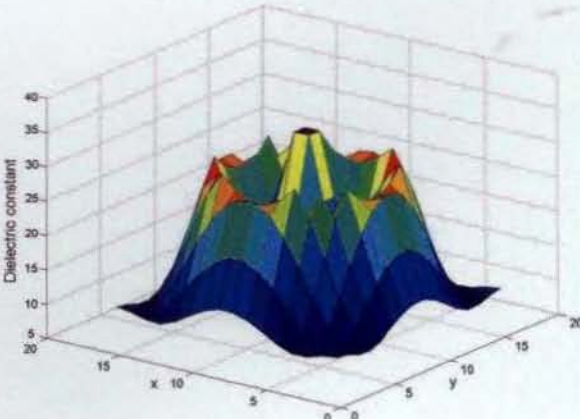
<p>Two off centered SH1s holding breast tumor phantoms ϵ_r' 38.1 and 29.8</p>		
<p>SH2 where outer and inner cylinders are filled with corn syrup samples of ϵ_r' 29.8</p>		

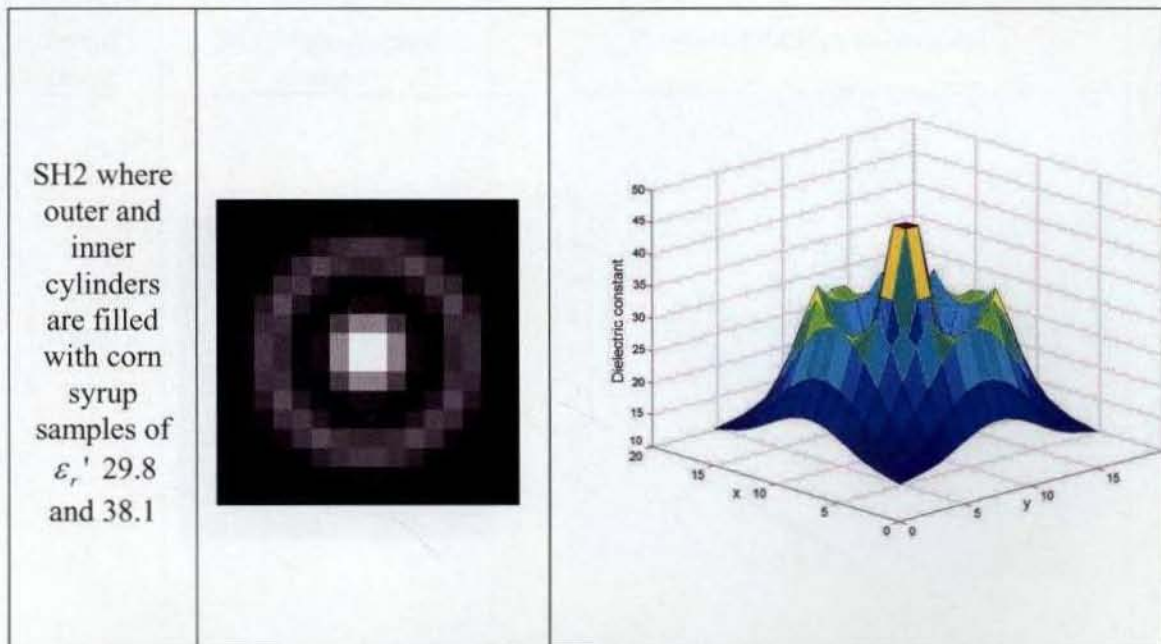
Table 5.2 (continued)

Table 5.3. 2-D Tomographic images and dielectric constant profiles of normal breast tissues

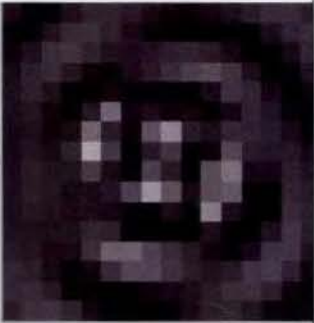
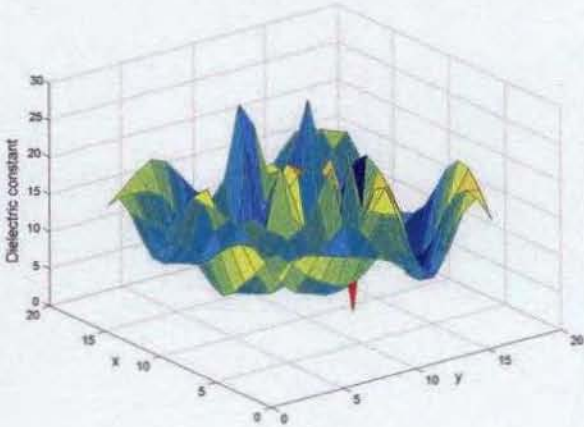
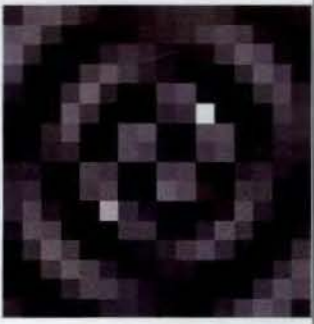
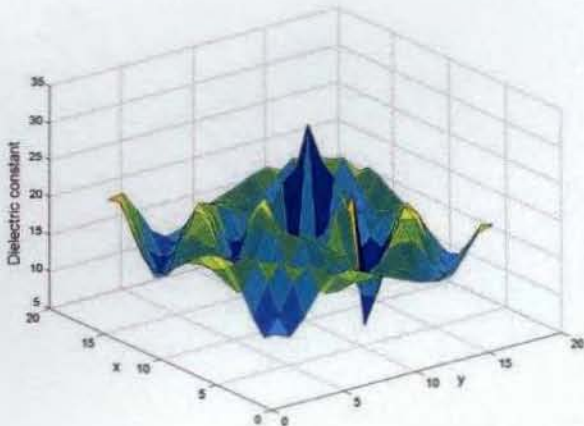
Normal breast tissue	2-D Tomographic image	Profile of dielectric constant
Patient 1		
Patient 2		

Table 5.3 -continued


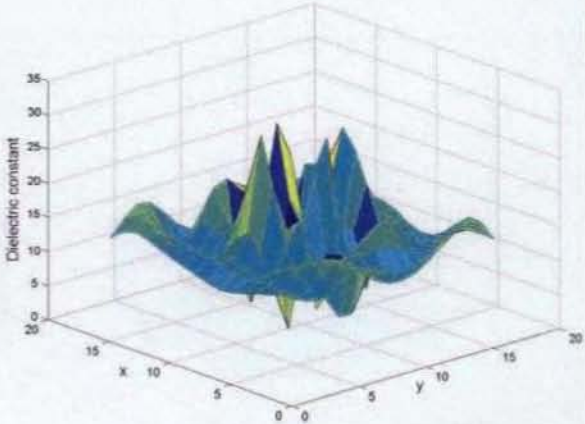
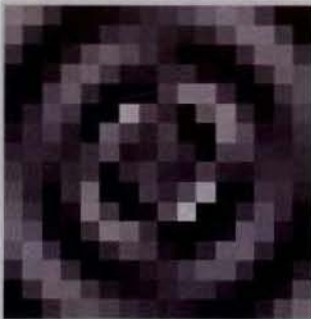
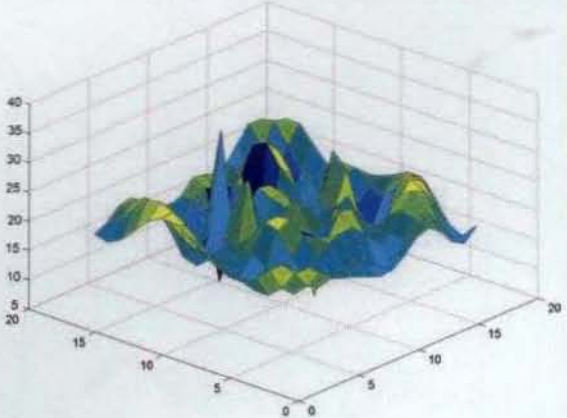
<p>Patient 3</p>		
<p>Patient 4</p>		

Table 5.4. 2-D Tomographic images and dielectric constant profiles of cancerous breast tissues


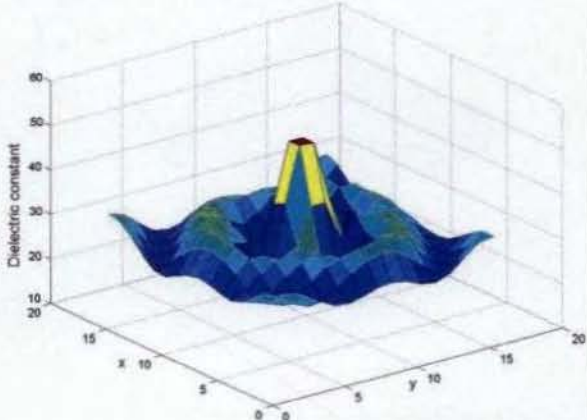

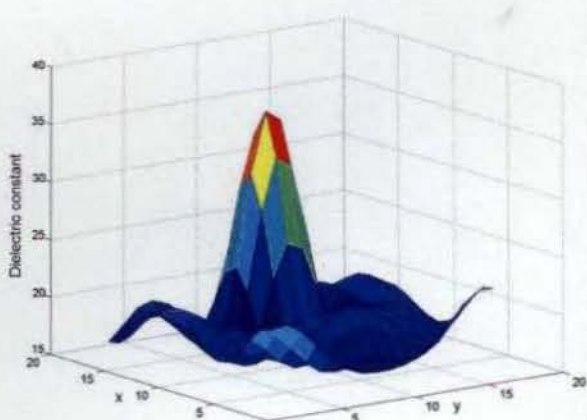
Cancerous breast tissue	2-D Tomographic image	Profile of dielectric constant
Patient 1		
Patient 2		

Table 5.4 - continued


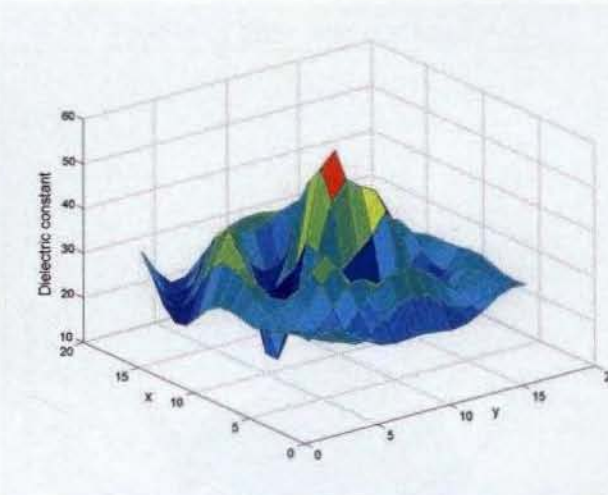

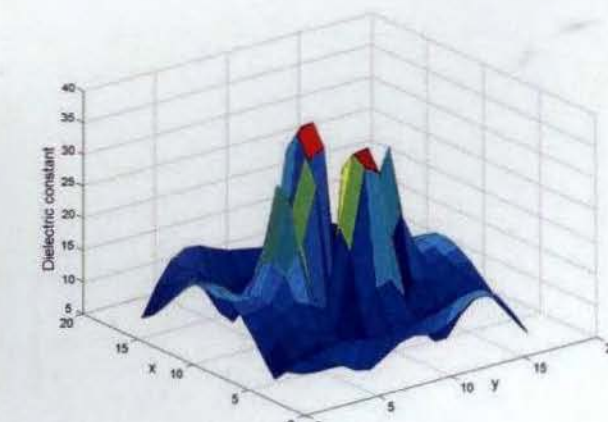
<p>Patient 3</p>		
<p>Patient 4</p>		

Table 5.5. 2-D Tomographic images and dielectric constant profiles of normal breast tissues with inclusions of cancerous tissue

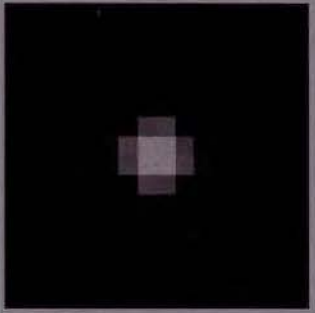
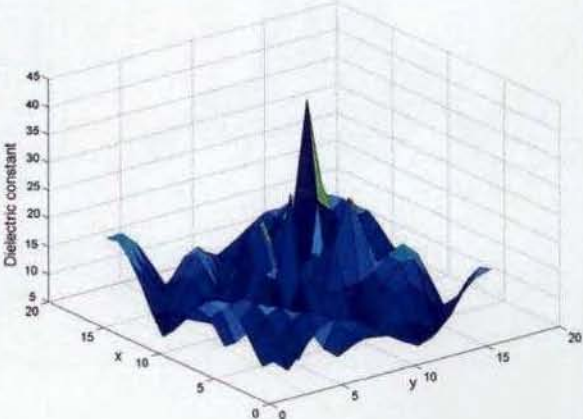
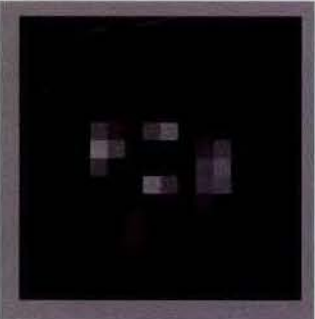
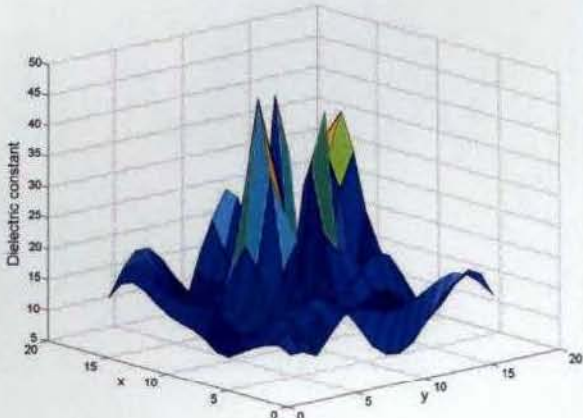

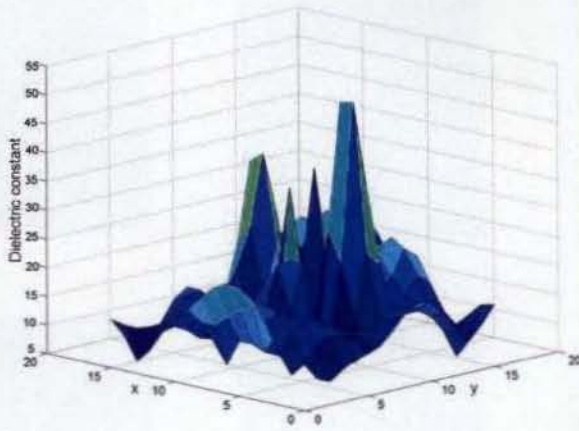

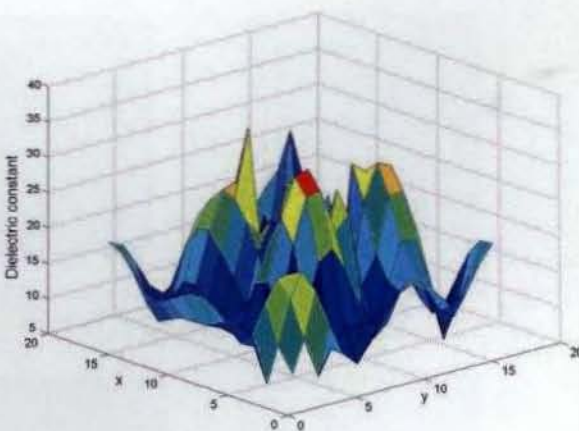
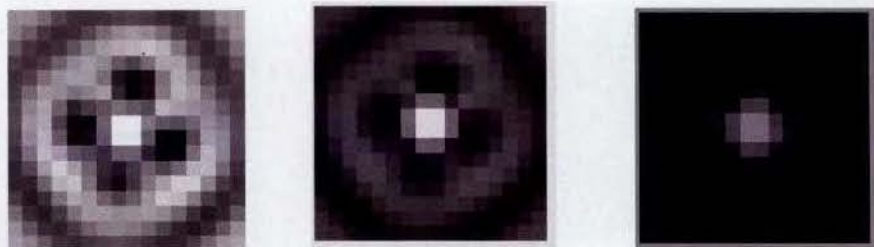
Sample	2-D Tomographic image	Profile of dielectric constant
Patient 1. B - Sample 1		
Patient 2. B - Sample 2		

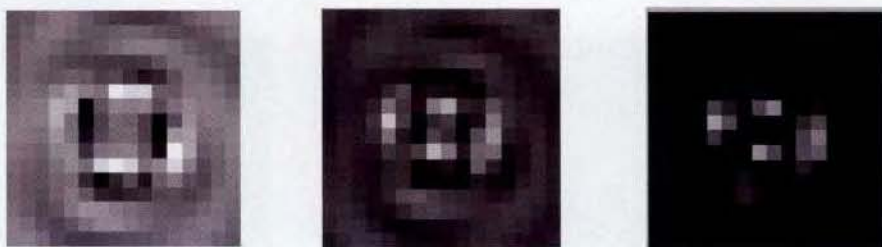
Table 5.5 - continued

<p>Patient 3. B - Sample 3</p>		
<p>Patient 4. B - Sample 4</p>		

B-Sample 1



B-Sample 2



B-Sample 3



B-Sample 4

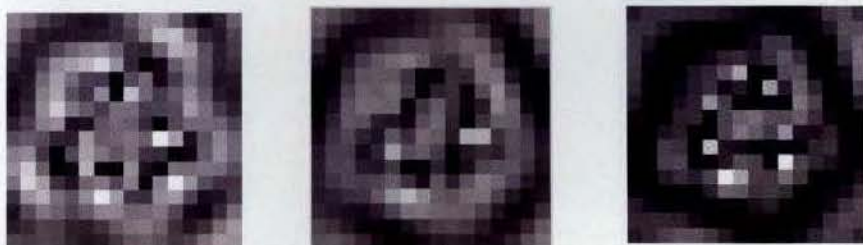
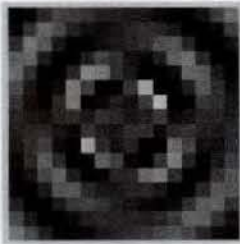
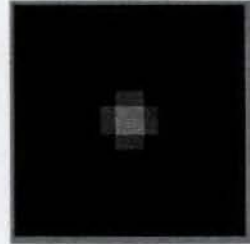


Figure 5.6. Improvement in the quality of images with iteration 1 - 3

B-Sample 1

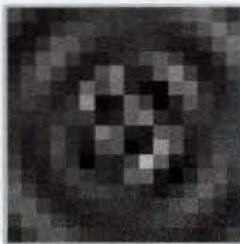


a)

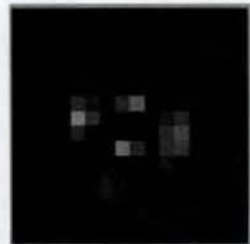


b)

B-Sample 2

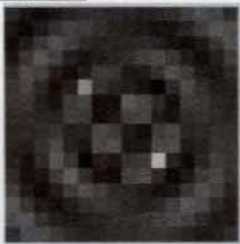


a)



b)

B-Sample 3



a)

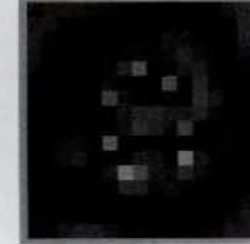


b)

B-Sample 4



a)



b)

**Figure 5. 7 Effects of coupling medium in microwave breast imaging.
(a) without coupling medium.(b) with coupling medium**

5.8 References

1. A. Franchois, A.Joisel, C.Pichot, J.C.Bolomey, "Quantitative microwave imaging with a 2.45 GHz planar microwave camera", *IEEE Transactions on Medical Imaging*, vol. 18, pp. 550 – 561, 1998.
2. A.E Souvorov, A.E.Bulyshev, S.Y.Semenov, R.H.Svenson, A.G.Nazarov, Y.E.Sizov, G.P.Tatsis, "Microwave Tomography: A two-dimensional Newton iterative scheme", *IEEE Transactions on Microwave Theory and Techniques*, vol. 46, pp. 1654 – 1658 , 1998.
3. W.C.Chew, "Imaging and inverse problems in electromagnetics", in *Advances in Computational Electrodynamics: The Finite Difference Time Domain Method*, A.Taflove, Ed. Norwood, MA: Artech House, 1998, Chapter 12.
4. L. Jofre, M.S. Hawley, A. Broquetas, E de los Reyes, M. Ferrando, A.R.E. Fuster, "Medical imaging with a microwave tomographic scanner", *IEEE Transactions on Biomedical Engineering*, vol. 37, pp. 303 – 311, 1990.
5. M.Slaney, A.C.Kak, L.E.Larson, " Limitations of imaging with first order diffraction Tomography", *IEEE Transactions on Microwave Theory and Techniques*, vol. 39, pp. 836 – 844, 1991.
6. P.M.Meaney, K.D.Paulsen, M.J.Moskowitz, J.M.Sullivan, "A dual mesh scheme for finite element based reconstruction algorithms", *IEEE Transactions on Medical Imaging*, vol. 14, pp. 504 – 514, 1995.
7. P.M.Meaney, K.D.Paulsen, T.P.Ryan, "Two-dimensional hybrid element image reconstruction for TM illumination", *IEEE Transactions on Antennas and Propagation*, vol. 43, pp. 239- 247, 1995.
8. P.M.Meaney, K.D.Paulsen, A. Hartov, R.K.Crane, "An active microwave imaging system for reconstruction of 2-D electrical property distributions", *IEEE Transactions on Biomedical Engineering*, vol. 42, pp. 1017 – 1026, 1995.
9. P.M.Meaney, K.D.Paulsen, A. Hartov, R.K.Crane, "Microwave imaging for tissue assessment: initial evaluation in multitarget tissue-equivalent phantoms", *IEEE Transactions on Biomedical Engineering*, vol. 43, pp. 878 - 890, 1996.
10. P.M.Meaney, K.D.Paulsen, J.T.Chang, "Near-field microwave imaging of biologically based materials using a monopole

- transceiver system”, IEEE Transactions on Microwave Theory and Techniques, vol. 46, pp. 31 – 44, 1998.
11. K.D.Paulsen, P.M.Meaney, J.T. Chang, M.W.Fanning, “Initial microwave imaging experiments in ex-vivo breast tissue”, Proc. of First Joint IEEE BMES/ EMBS Conference Serving Humanity, Advancing Technology, pp. 1130 , 1999.
 12. P.M.Meaney , K.D.Paulsen “ Nonactive antenna compensation for fixed array microwave imaging – Part I: Model development,” IEEE Transactions on Medical Imaging, vol. 18, pp. 496 – 507, 1999.
 13. P.M.Meaney , K.D.Paulsen, J.T.Chang, M.W.Fanning, A.Hartov, “Nonactive antenna compensation for fixed array microwave imaging – Part II: Imaging results,” IEEE Transactions on Medical Imaging, vol. 18, pp. 508 - 518, 1999
 14. P.M.Meaney, M.W.Fanning, D. Li, S.P.Poplack, K.D.Paulsen, “ A clinical prototype of active microwave imaging of the breast”, IEEE Transactions on Microwave Theory and Techniques, vol. 48, pp. 1841 – 1853, 2000
 15. S. S. Chaudhary, R. K. Mishra, A. Swarup, J. M. Thomas, “ Dielectric properties of normal and malignant human breast tissues at radiowave and microwave frequencies”, Indian Journal of Biochemistry and Biophysics, vol.21, pp. 76 – 79, 1981.
 16. P.M.Meaney, K.D.Paulsen, S. D. Geimer, S.A. Haide, M.W.Fanning, “Quantification of 3-D field effects during 2-D microwave imaging”, IEEE Transactions on Biomedical Engineering, vol. 49, pp. 708 – 720, 2002.
 17. Dun Li, P. M. Meaney, T. Raynolds, S. Pendergrass, M. Fanning, K. D. Paulsen, “A parallel-detection microwave spectroscopy system for breast imaging”, Review of Scientific Instruments, vol. 75, pp. 2305 – 2313, 2004
 18. D. Li, P.M.Meaney, K.D.Paulsen, “Conformal microwave imaging for breast cancer detection”, IEEE Transactions on Microwave Theory and Techniques, vol. 51, pp. 1179 - 1186, 2003.
 19. M. Slaney, M. Azimi, A.C.Kak, L.E. Larsen, “Microwave imaging with first order diffraction Tomography”, in Medical Applications of Microwave Imaging, IEEE Press, New York, pp. 183 – 212, 1986.
 20. C.H.Tseng, T.H.Chu, “Quasi- monostatic microwave imaging using multi-source illumination”, Proc. of IEEE APS, pp. 179 – 181, 2003.

21. M.Moghaddam, W.C.Chew, "Non linear two dimensional velocity profile inversion using time domain data", *IEEE Transactions on Geoscience and Remote Sensing*, vol. 30, pp. 147 – 156, 1992.
22. A.G.Tijhuis, K.Belkebir, A.S.Litman, B.P.de Hon, "Multiple frequency distorted Born approach to 2-D inverse profiling", *Inverse Problems*, vol. 17, 1635 – 1644, 2001.
23. A.G.Tijhuis, K.Belkebir, A.S.Litman, B.P.de Hon, "Theoretical and computational aspects of 2-D inverse profiling", *IEEE Transactions on Geoscience and Remote Sensing*, vol. 39, pp. 1316 - 1329, 2001.
24. Y.M.Wang, W.C.Chew, "An iterative solution of the two-dimensional electromagnetic inverse scattering problem", *International Journal of Imaging Systems and Technology*, vol. 1, pp. 100 – 108, 1989.
25. W.C.Chew, Y.M.Chang, "Reconstruction of two-dimensional permittivity distribution using the distorted Born iterative method", *IEEE Transactions on medical Imaging*, vol. 9, pp. 218 – 225, 1991.
26. Q.H.Liu, Z.Q.Zhang, T.T.wang, J.A.Bryan, G.A.Ybarra, L.W.Nolte, A.T.Joines, "Active microwave imaging I – 2 D forward and inverse scattering methods", *IEEE Transactions on Microwave Theory and Techniques*, vol. 50, pp. 123 – 132, 2002.
27. Q.H.Liu, Z.Q.Zhang, T.T.wang, C. Xiao, E. Ward, G. Ybarra, A.T.Joines, "Active microwave imaging II – 2 D reconstruction and a 3-D fast volume integral equation method", *IEEE Transactions on Microwave Theory and Techniques*, vol. 50, pp. 223 – 232, 2002.
28. Q.Fang, P.M.Meaney, K.D.Paulsen, "Microwave image reconstruction of tissue property dispersion characteristics utilizing multiple frequency information", *IEEE Transactions on Microwave Theory and Techniques*, vol. 52, pp.1866 – 1875, 2004.
29. S. Caorsi, M. Pastorino, "Two-dimensional microwave imaging approach based on a genetic algorithm", *IEEE Transactions on Antennas and Propagation*, vol. 48, pp. 370 – 373, 2000.
30. A. Abubakar, P.M. Van den Berg, "The contrast source inversion method for location and shape reconstruction", *Inverse Problems*, vol. 18, pp.495 – 510, 2002.
31. P.M. Van den Berg, A. Abubakar, "A contrast source inversion method", *Inverse Problems*, vol. 13, pp. 1607 – 1620, 1997.
32. N. Joachimowicz, J.J.Mallorqui, J.C.Bolomey, A. Broquetas, "Convergence and stability assessment of Newton-Kantorovich reconstruction algorithms for microwave tomography", vol. 17, pp. 562 – 569, 1998.

33. K.Belkebir, R.E.Kleinman, C.Pichot, "Microwave imaging-location and shape reconstruction from multifrequency scattering data", *IEEE Transactions on Microwave Theory and Techniques*, vol. 45, pp. 469 – 476, 1997.
34. S.Y.Semenov, R.H.Svenson, A.E.Boulyshev, A.E.Souvorov, A.G.Nazarov, Y.E.Sizov, V.Y.Borisov, V.G.Posukh, I.M.Kozlov, A.G.Nazarov, G.P.Tatsis, "Microwave Tomography: experimental investigation of the iteration reconstruction algorithm", *IEEE Transactions on Microwave Theory and Techniques*, vol. 46, pp. 133 – 141, 1998.
35. S.Y.Semenov, R.H.Svenson, A.E.Boulyshev, A.E.Souvorov, V.Y.Borisov, A.N.Starostin, K.R.Dezen, G.P.Tatsis, V.Y.Baranov, "Microwave Tomography: two dimensional system for biological imaging", *IEEE Transactions on Microwave Theory and Techniques*, vol. 43, pp. 869 – 877, 1996
36. S.Y.Semenov, R.H.Svenson, A.E.Boulyshev, A.E.Souvorov, A.G.Nazarov, Y.E.Sizov, A.V. Faviovsky, V.Y.Borisov, B.A.Voinov, G.I.Simonova, A.N.Staostin, V.G.Posukh, G.P.Tatsis, V.Y.Baranov, "Three dimensional microwave tomography: experimental prototype of the system and vector born reconstruction method", *IEEE Transactions on Biomedical Engineering*, vol. 43, pp. 937 – 945, 1999.
37. Semenov S.Y. Bulychev A.E, Souvorov A.E, Nazarov A.G, Sizov Y.E, Svenson R.H, Posukh V.G, Pavlovsky A, Repin P.N, Tatsis G.P, "Three-dimensional microwave tomography: experimental imaging of phantoms and biological objects", *IEEE Transactions on Microwave Theory and Techniques*, vol. 48, pp. 1071 – 1074, 2000.
38. Allen Taflove, "Advances in computational electrodynamics: The finite difference time domain method", Chapter 12, Artech House, Boston, USA, 1998.
39. J.K.Richmond, "Scattering by dielectric cylinder of arbitrary cross section shape", *IEEE Transactions on Antennas and Propagation*, vol. 13, pp. 334 – 341, 1965.
40. A.M.Campbell, D. V. Land, "Dielectric properties of female human breast tissue measured in vitro at 3.2 GHz", *Physics in Medicine and Biology*, vol. 37, pp.193 – 209, 1992.
41. S.Gabriel, R. W. Lau, C. Gabriel, "Dielectric properties of biological tissues:II. Measurements in the frequency range 10 Hz to 20 GHz", *Physics in Medicine and Biology*, vol. 41, pp. 2251 – 2269. 1996

42. S.Gabriel, R. W. Lau, C. Gabriel, "Dielectric properties of biological tissues: III. Parametric models for the dielectric spectrum of tissues", *Physics in Medicine and Biology*, vol.41, pp. 2271 – 2293, 1996

Chapter 6

DETECTION OF DIELECTRIC CONTRAST OF BREAST PHANTOMS AND BREAST TISSUES USING CONFOCAL MICROWAVE TECHNIQUE

6.1 Introduction

Video pulse radars operating at air-earth interface have been used to detect buried structures such as pipes, cables and mines [1]. Versions of these radars were introduced for medical applications as a means to detect malignancy in internal biological tissues [2]. Dielectric imaging using this pulsed radar technology was studied for early detection of breast cancer [3, 4].

Confocal microwave technique (CMT) uses the principle of video pulse radars to distinguish the regions of dielectric contrast in breast tissues [5, 6]. A wide band antenna capable of transmitting short transient pulses is used for the transmission and reception of microwave energy for this application. Upon encountering a tumor, microwave energy is scattered because tumor has a significantly greater dielectric constant and conductivity than normal tissue. In CMT, backscatter method is adopted,

where the measured reflected signals are used to infer the location of significant microwave scatterers.

However this technique only identifies the presence and location of strong scatterers in the breast rather than completely reconstructing the dielectric properties profile.

This chapter discusses experimental and theoretical investigations of confocal microwave technique to detect regions of dielectric contrast of breast phantoms and breast tissues.

6.2 Review of the past work

Hagness et al [5-6] performed two and three-dimensional FDTD analysis of a pulsed confocal microwave system for breast cancer detection. The system used pulsed backscatter technique and time gating to enhance the detection of tumors while suppressing the effects of tissue heterogeneity and absorption. The backscattered waveforms were subjected to simple time shift and add algorithm to extract the tumor response. The FDTD model used a uniform grid with square unit cells of size 2mm x 2mm. Published data for the dielectric properties of normal and malignant breast tissues were used for the simulation. Their studies showed that tumors as small as 2 mm in diameter could be detected in the presence of background clutter. Lateral spatial resolution of the tumor was reported as 1 cm. They also studied the effect of back ground clutter in breast tumor detection [7] using FDTD simulations. The antennas were excited one at a time and the collected backscattered responses were time-shifted and summed coherently to achieve the synthetic focus. The signal to clutter ratio was computed by comparing the peak back scattered responses with and without the presence of tumor. Debye dispersion relation was also incorporated in the FDTD equations and no degradation in the signal to clutter ratio with respect to the

results from the non-dispersive model was reported. They also performed [8] FDTD computations of a confocal microwave system using co and cross polarized waveforms and obtained a cross polarized backscatter response of a spherical tumor phantom positioned directly below the antenna feed point as zero. When the tumor was off the central perpendicular axis of the two antennas, a non zero cross polarized component of the tumor backscatter response was obtained. With this configuration, they were able to detect tumors adjacent to the chest wall.

A confocal microwave algorithm for breast cancer detection was realized by Xu Li et al [9]. They adopted a calibration process to remove the skin reflections and incident signal artifacts. A reference waveform was created by averaging the stored backscattered waveforms. The skin backscatter and incident signals remain dominant in this reference waveform while the tumor backscatter and clutter signals were reduced to negligible levels. The reference waveform was then subtracted from each original backscatter waveforms resulting in calibrated backscatter waveforms that contain only the tumor response and clutter signals. The image was created by time shifting and summing data points from each integrated waveform for each synthetic focal point in the breast. They also performed [10] FDTD analysis for 3-D tumor localization using confocal microwave technique. The collected backscattered signals were first processed, to remove the early-time content consisting of incident pulse, skin reflections and residual antenna reverberations. The signals were then integrated to achieve a signal maximum at the center point of the incident pulse, allowing for the detection of tumor. This was done by identifying the local maxima and determination of object location using time delays between maxima. Compensation was also provided to correct the decrease

in signal amplitude due to radial spreading and propagation through lossy breast tissue. Space time beam forming with confocal microwave technique for breast cancer detection was also proposed by the same group [11, 12]. The backscattered signals were first processed to remove antenna reverberations and reflections from the skin interface. The signals were then time shifted to align the return from a hypothesized point scatter at that location. The waveforms were then transformed to frequency domain using FFT algorithm and passed through frequency domain beam formers. The outputs were then added, transformed back to time domain and time gated. By appropriately changing the time shifts, gating and FIR filter weights, the beam former focus was scanned throughout the breast region to obtain 3-D image of backscattered energy as a function of location. Experimental investigation of the technique was performed [11] on multi layer breast phantoms with malignant to normal dielectric constants in the ratio 1.5: 1. Good agreement was observed between measurements and FDTD simulations.

Converse et al [13] conducted a computational study of confocal microwave technique for hyperthermia treatment of breast cancer. A train of ultra wide band pulses was passed through a space time beam former and transmitted simultaneously from multiple antennas into the breast phantom. The filters in the space time beam former were designed to compensate for dispersive propagation through breast tissue so that pulses from each antenna add coherently at the treatment location and add incoherently elsewhere. Thus the transmitted energy was tightly focused at the treatment location to produce localized heating. The effectiveness of this procedure was substantiated by calculating the power density deposited in the breast using FDTD.

A confocal microwave system for detection of breast cancer was simulated by Fear et al [14, 15]. They illuminated the breast with an ultra wide band pulse and the recorded backscattered signals were first calibrated and then applied a skin subtraction algorithm. The signals were then time shifted and added to find the response at a particular point in the domain of interest. They also performed FDTD analysis of CMT using a synthetic planar array which spanned 6 cm in the x direction and 8.2 cm in the y direction [16,17]. The backscattered signals were first calibrated by averaging the returns at each antenna in a row. Subtraction of this signal from the actual response recorded at each antenna in that row was done to suppress early time content. The signals were then integrated and compensation was applied to account for radial spreading and path loss. The processed signals were then synthetically focused at a specific point in the breast. The distances from each antenna to the focal point were computed and then converted it into time delays. These time delays were used to identify the contribution from each processed signal. All the contributions were added and the squared value of the sum is assigned to the pixel value at the focal point. Successful detection of 6 mm. diameter spherical tumors was achieved with this method. Experimental verification of CMT using breast phantoms was also performed by the same group [18, 19]. The backscattered signals were noted for various locations of the phantom. The synthetic focus was accomplished by computing the distance between each antenna and the selected focus, converting this into time delay and adding the time delayed data. The resulting signal was filtered to remove the clutter. The signals were then time shifted and the average response of the data set was subtracted from each set. Finally the data was integrated and focused.

The displayed image was proportional to the field intensity and in good shape.

Yun et al [20, 21] examined cross polarization in CMT to detect tumors axially asymmetric to the antenna structure thereby allowing the detection of tumors near the chest wall while rejecting co-polarized reflections. The frequency signatures of various tumor shapes were also examined.

6.3 Motivation for the present work

In CMT, transmission and reception of microwave energy are done using the same antenna. For good spatial resolution, the breast need to be illuminated from a number of antenna locations; one at a time. This spatial selectivity ensures accurate detection of tumor by masking the clutter from adjacent breast regions.

All the works reported in the review were either FDTD simulations or experimental observations using breast phantoms. No attempt was made to investigate wide band CMT using breast tissues in the presence of a matching coupling medium.

The present work investigates CMT on breast tissues as well as on breast phantoms. Wide band pulse is used to illuminate the sample from many locations; one at a time. The relative arrival times and amplitudes of the backscattered signal measured at each antenna position provide information to accurately determine the scatterer location. Experimental results are substantiated by FDTD analysis and good agreement is observed.

6.4 Measurement set up

The set up used for measurement is shown in Figure 6.1. It is the same measurement set up as shown in Figure 5.3, except that a single antenna is used for both transmission and reception of microwave energy. The

antenna is capable of rotating around the object at a radius of 6 cm. The sample as well as the antenna are immersed in a coupling medium, which is corn syrup sample of dielectric constant and conductivity 18.7 and 0.98 S/m at 3 GHz.

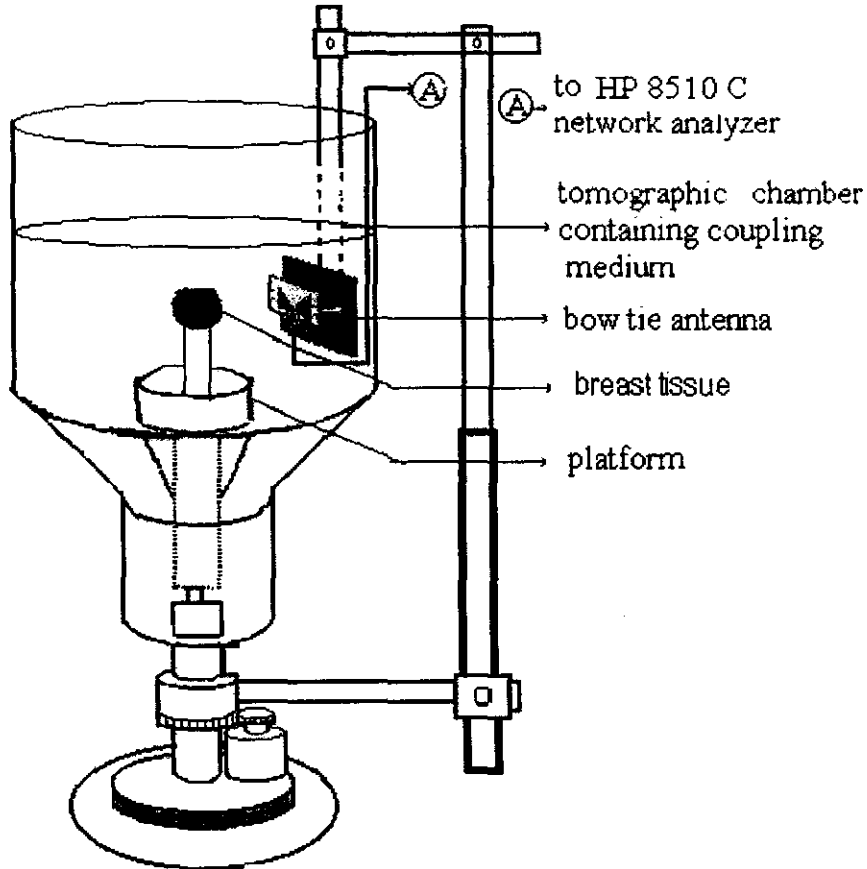


Figure 6.1 Measurement set up

6.4.1 System Calibration

The transmitting antenna of the measurement set up is connected to Port 1 of the experimental set up discussed in Section 2.6. The bow tie antenna having center frequency of 3 GHz is fixed on the antenna holder of the set up, and is immersed in the tomographic chamber filled with coupling

medium. A metal plate is placed at the platform of the measurement set up where sample is to be kept, and the key board entry of the network analyzer is given for S_{11} . The whole calibration is stored in any one of the CAL set available in the network analyzer. Error correction is automatically turned on. The time domain band pass response is then taken to verify the calibration. If the calibration is correct, the maximum of the time domain response will be at zero seconds for S_{11} . This indicates that the reference position is set at the position of the metallic plate. While taking measurements with the sample, a time gating of 9 ns is applied for better accuracy.

6.4.2 Data acquisition

For data acquisition, the network analyzer is set to the time domain mode. The analyzer does the measurement in the frequency domain and is then converted to time domain. The integral high speed computer in the HP 8510 C network analyzer performs this calculation using the Chirp Z Fourier Transform computation techniques [22]. The time domain data will then be displayed in near real time.

The sample under study is mounted on the platform and is illuminated by the transmitting bow-tie antenna at a frequency of 3 GHz and the same antenna collects the back-scattered waves. The driver circuit (Appendix C) of the outer motor is activated so that the antenna can now be rotated around the object. For every 18° (20 steps) of rotation, the antenna collects the back scattered waves and the network analyzer displays time domain response of this reflected signal.

6.4.3 Measurement configuration

Measurements are performed using breast phantoms as well as with breast tissues. Two types of sample holders (SHs) are considered to hold the breast

phantoms. SH1 is a circular cylinder of radius 0.5 cm and height 25 cm and SH2 consists of concentric circular cylinders of height 25 cm and radii 5 cm and 0.5 cm. The SHs are made of Polyvinyl chloride (PVC) having a dielectric constant of 2.84 and conductivity 0.005 S/m.

6.4.3.1 Using breast phantoms

The measurement configurations considered are - 1) SH1 kept at the center of the tomographic chamber is used to hold the breast tumor phantom of ϵ_r and σ as 38.1 and 1.91 S/m. 2) SH2 kept at the center of the tomographic chamber where the outer and inner cylinders are filled with corn syrup samples of ϵ_r and σ as, 18.7 and 0.98 S/m, and 38.1 and 1.91 S/m respectively. 3) SH2 kept at the same position with the outer and inner cylinders are filled with corn syrup samples of ϵ_r and σ as, 18.7 and 0.98 S/m ϵ_r and σ as 29.8 and 1.1 S/m respectively. These configurations are shown in Figures 5.4 (a) and 5.4(d) of Chapter 5.

6.4.3.2 Using breast tissues

Breast tissue samples of the four patients used for microwave tomographic imaging discussed in Section 5.5.3.2 of Chapter 5 are used for CMT studies too. The samples are supported on SH1 and are fixed at the center of the tomographic chamber. Time domain responses of normal and cancerous breast tissues are measured separately. For this, normal breast tissue of radius ~ 1 cm and cancerous tissue of radius ~ 0.25 cm are used. A real time cancerous breast model is created by inserting cancerous tissue in normal breast tissues. Four cases of this are studied - (1) A cancerous breast tissue of \sim radius 0.5 cm inserted in normal breast tissue of \sim radius 1 cm, of patient 1, is taken as B-Sample 1. (2) Four tumorous inclusions of \sim radius 0.25 cm. each inserted in normal tissue of \sim radius 1 cm, of patients 2 and 3 are treated as B-Samples 2 and 3. (3) Scattered inclusions

of cancerous tissue of ~ radius 0.1 cm each inserted in normal tissue of ~ radius 1 cm, of patient 4 are treated as B-Sample 4. These configurations are the same as described in Section 5.5.3.2 of Chapter 5. A schematic diagram of the B-Samples is also shown in Figure 5.5.

6.5 Analyses

6.5.1 Experimental analysis

The time domain response of the reflected signal obtained when the antenna is on the on-axis of the object is taken as the reference signal at 0° . The antenna is then rotated around the object and the responses are collected for every 18° (20 steps) positions of the antenna. The responses consist of reflections from the regions of dielectric contrast with shifted time axis, depending on the position of the antenna with respect to the object. Each of the obtained responses is then time shifted with respect to the reference time domain response and added, to enhance the returns from high contrast regions and to reduce clutter.

6.5.1.1 Flow chart of the algorithm

Matlab 7.0 is used to code the algorithm

1. Collect the time domain response at the on axis and treat this as the reference
2. Collect the time domain response for the next 18° (20 steps) position of the antenna.
3. Shift the time axis to that of the reference
4. Add the two responses.
5. Repeat steps 2 - 4 till the antenna completes 360° rotation.

6.5.2 Numerical analysis

To validate the experimental investigation, the theoretical analysis is done using finite difference time domain (FDTD) method. The aim of this analysis is to simulate the scattering of waves by tissue samples and to obtain the amplitude of the reflected signal. The FDTD technique permits the analysis of interactions of electromagnetic waves with material bodies of any arbitrary shape. Space and time discretization are selected to bound errors in the sampling process and to ensure numerical stability of the problem. The electric and magnetic components are interleaved in space to permit a natural satisfaction of the tangential field continuity conditions at media interfaces. The space time gridding underlying the FDTD method was first proposed by Yee [23] (Yee's algorithm) and the associated boundary conditions used [24] are discussed in detail in Section 3.6 of Chapter 3.

For the simulation, a dielectric medium is assumed to be filled in an area and the tissue sample is immersed in it. A pulse is excited in the dielectric medium and the reflected signal is obtained from the sample. In the present study a Gaussian pulse is considered to propagate from the source plane and the information about the sample is obtained from the analysis of the reflected signal. A 2- D analysis of this model is presented here using FDTD technique.

6.5.3 FDTD Analysis

The Maxwell's curl equations are the basis of the FDTD analysis.

$$\nabla \times \bar{H}(x, y, z, t) = \frac{\partial \bar{D}(x, y, z, t)}{\partial t} \quad (6.1)$$

$$\nabla \times \bar{E}(x, y, z, t) = -\frac{\partial \bar{B}(x, y, z, t)}{\partial t} \quad (6.2)$$

where $\bar{B}(t)$ and $\bar{D}(t)$ are the inverse Fourier Transform of $\bar{B}(w)$ and $\bar{D}(w)$.

The incident wave is assumed to be a Transverse Magnetic wave having $H_z = E_x = E_y = 0$. This wave is considered as a + y directed plane wave whose electric field vector is in the z direction. The scatterer geometry is assumed to be uniform in the z direction; hence the problem is treated as a 2-D scattering of the incident wave with only E_z , H_x and H_y fields present.

Discretizing the eqns 6.1 – 6.2, we get,

$$\frac{\partial H_x}{\partial t} = -\frac{\partial E_z}{\mu_0 \partial y} \quad (6.3)$$

$$\frac{\partial H_y}{\partial t} = \frac{\partial E_z}{\mu_0 \partial x} \quad (6.4)$$

$$\frac{\partial E_z}{\partial t} = \frac{\partial H_y}{\epsilon \partial x} - \frac{\partial H_x}{\epsilon \partial y} \quad (6.5)$$

As the medium considered here is non magnetic, the permeability is taken as μ_0 . But the dispersive nature of the dielectric medium need to be incorporated in the constitutive FDTD equations using first order Debye dispersion relation [25 -27] which is given in detail in Section 2.3.1 of Chapter 2.

Debye has related the dielectric relaxation time with the complex relative permittivity in his equation (Eqn. 2.38 of Chapter 2)

$$\epsilon_r(\omega) = \epsilon_{\infty} + \frac{\epsilon_{rs} - \epsilon_{\infty}}{1 + j\omega\tau} \quad (6.6)$$

where ϵ_{rs} is the static relative permittivity measured at dc / low frequencies, ϵ_{∞} is the optical relative permittivity measured at optical / very high frequencies, ω the angular frequency and τ the relaxation time.

Also the dielectric susceptibility of the medium χ is derived as eqn.2.10 in Chapter 2 is,

$$\chi(\omega) = \epsilon_r \epsilon_0 - \epsilon_0 = \epsilon_0 (\epsilon_r - 1) \quad (6.7)$$

As eqn. 6.6 is in the spatial domain, inverse Fourier Transform is performed to translate it to the time domain.

$$\epsilon_r(t) = \epsilon_{\infty} \delta(t) + \frac{\epsilon_{rs} - \epsilon_{\infty}}{\tau_o} e^{-t/\tau_o} u(t) \quad (6.8)$$

Using eqn. 6.8 $\bar{D}(t)$ is written as,

$$\bar{D}(t) = \epsilon_0 \epsilon_{\infty} \bar{E}(t) + \epsilon_0 \int \bar{E}(t - \tau) \chi(\tau) d\tau \quad (6.9)$$

If the pulse takes n time steps with each time step of size Δt to travel in the computational domain, the total time required is $n\Delta t$. Using this Yee's notation [23], eqn 6.9 is re-written as,

$$\bar{D}(t) = D(n\Delta t) = D^n = \epsilon_0 \epsilon_{\infty} E^n + \epsilon_0 \int_0^{n\Delta t} E(n\Delta t - \tau) \chi(\tau) d\tau \quad (6.10)$$

All field components are assumed to be constant over each time interval Δt . There fore, we have, assuming $\bar{D}(t)$ and $\bar{E}(t)$ are zero for $t < 0$,

$$D^n = \epsilon_0 \epsilon_{\infty} E^n + \epsilon_0 \sum_{m=0}^{n-1} E^{n-m} \int_{m\Delta t}^{(m+1)\Delta t} \chi(\tau) d\tau \quad (6.11)$$

The value of D at the next time step is

$$D^{n+1} = \epsilon_0 \epsilon_{\infty} E^{n+1} + \epsilon_0 \sum_{m=0}^n E^{n+1-m} \int_{m\Delta t}^{(m+1)\Delta t} \chi(\tau) d\tau \quad (6.12)$$

Let number of spatial steps in the x and y directions be i and j respectively. So $x=i\Delta x$ and $y=j\Delta y$. Incorporating these Yee notations [23] of spatial steps and time steps in the Maxwell's curl equation 6.1,

$$\frac{D_z^{n+1}(i, j) - D_z^n(i, j)}{\Delta t} = - \frac{H_x^{n+1/2}(i+1/2, j) - H_x^{n+1/2}(i-1/2, j)}{\Delta y}$$

$$+ \frac{H_y^{n+1/2}(i, j+1/2) - H_y^{n+1/2}(i, j-1/2)}{\Delta x} \quad (6.13)$$

Substituting eqns. 6.11 and 6.12 in the right hand side of eqn. 6.13 we get,

$$\begin{aligned} D_z^{n+1}(i, j) - D_z^n(i, j) &= \varepsilon_{\infty}(i, j)\varepsilon_0[E_z^{n+1}(i, j) - E_z^n(i, j)] \\ &+ \varepsilon_0 E_z^{n+1}(i, j) \int_0^{\Delta t} \chi(\tau, i, j) + \varepsilon_0 \sum_{m=0}^{n-1} E_z^{n-m}(i, j) \\ &\left\{ \int_{(m+1)\Delta t}^{(m+2)\Delta t} \chi(\tau, i, j) d\tau - \int_{m\Delta t}^{(m+1)\Delta t} \chi(\tau, i, j) d\tau \right\} \end{aligned} \quad (6.14)$$

To simplify the notation, let

$$\chi_m(i, j) = \int_{m\Delta t}^{(m+1)\Delta t} \chi(\tau, i, j) d\tau \quad (6.15)$$

Then eqn. 6.14 becomes,

$$\begin{aligned} D_z^{n+1}(i, j) - D_z^n(i, j) &= \varepsilon_0 \varepsilon_{\infty}(i, j) + \varepsilon_0 \chi_0(i, j) E_z^{n+1}(i, j) \\ &- \varepsilon_0 \varepsilon_{\infty} E_z^n(i, j) - \varepsilon_0 \sum_{m=0}^{n-1} E_z^{n-m}(i, j) (\chi_m(i, j) - \chi_{m+1}(i, j)) \end{aligned} \quad (6.16)$$

To further simplify the notation, let

$$\Delta \chi_m(i, j) = \chi_m(i, j) - \chi_{m+1}(i, j) \quad (6.17)$$

Substituting eqns. 6.16 and 6.17 in 6.13 and solving for $E_z^{n+1}(i, j)$,

$$\begin{aligned} E_z^{n+1}(i, j) &= \frac{\varepsilon_{\infty}(i, j)}{\varepsilon_{\infty}(i, j) + \chi_0(i, j)} E_z^n(i, j) \\ &+ \frac{1}{\varepsilon_{\infty}(i, j) + \chi_0(i, j)} \sum_{m=0}^{n-1} E_z^{n-m}(i, j) - m) \Delta \chi_m(i, j) \\ &+ \frac{\Delta t}{\varepsilon_{\infty}(i, j) + \chi_0(i, j) \varepsilon_0 \Delta x} (H_y^{n+1/2}(i, j+1/2) - H_y^{n+1/2}(i, j-1/2)) \end{aligned}$$

$$+ \frac{\Delta t}{\epsilon_{\infty}(i, j) + \chi_0(i, j)\epsilon_0\Delta y} (H_x^{n+1/2}(i+1/2, j) - H_x^{n+1/2}(i-1/2, j)) \quad (6.18)$$

The Yee equations for the magnetic fields in a non-magnetic medium are unchanged and is obtained by discretizing eqns. 6.3 and 6.4 using the time and spatial representations. Hence

$$H_x^{n+1/2}(i+1/2, j) = H_x^{n-1/2}(i+1/2, j) - \frac{\Delta t}{\mu_0\Delta y} (E_z^n(i+1, j) - E_z^n(i, j)) \quad (6.19)$$

$$H_y^{n+1/2}(i, j+1/2) = H_y^{n-1/2}(i, j+1/2) - \frac{dt}{\mu_0\Delta x} (E_z^n(i, j+1) - E_z^n(i, j)) \quad (6.20)$$

6.5.3.1 Analytical Model

A Gaussian pulse of unit amplitude is selected as the source of excitation. It is given by,

$$E_z = e^{-(t-t_0)^2/T^2} \quad (6.21)$$

where t_0 is the time delay and T the pulse width. T is selected as 18 ps and t_0 as 54 ps. The computational domain is discretized as 130 x 130 Yee cells. Space steps of 1 mm each in x and y directions and time step of 6.05 ps are chosen to ensure propagation of the waves in the entire domain. Tangential component of E is set to 0 at the boundary which is defined by Mur's absorbing boundary conditions. This is discussed in detail in Section 3.6.5 of Chapter 3. Computation is performed for 940 time steps so that the field stabilizes.

The material properties are indicated in the FDTD design in terms of ϵ and μ . μ is taken as μ_0 , as the material is non magnetic. ϵ is taken as $\epsilon_0\epsilon_r$ where ϵ_r is the relative permittivity of the medium. ϵ_r takes the value of 18.7 (dielectric constant of the coupling medium) in the domain except inside the tissue sample and at the tissue boundary. Inside the tissue

sample, the dielectric constant of the tissues obtained by cavity perturbation technique discussed in Table 5.1(9) is taken. At the coupling medium-tissue interface, average of the two permittivities is used.

6.5.3.2 Flow Chart of the FDTD Algorithm

Matlab 7.0 is used to code the FDTD algorithm.

The important aspects of the time-domain algorithm are as follows:

- Initially (at $t=n=0$) all fields are 0.
- The following steps are repeated until the response is ≈ 0 :
 - Gaussian Impulse is imposed at the source plane.
 - $H^{n+1/2}$ is calculated from FD equations.
 - E^{n+1} is calculated from FD equations.
 - Tangential E is set to 0 at the boundary.
 - Save desired field equations.
 - $n \rightarrow n+1$

6.6 Results and Discussions

Figures 6.2- 6.12, show the time domain responses of the samples. In all the figures, the markers are given for the peaks in the experimental results. The FDTD results are normalized.

Figure 6.2 shows the time domain responses of SH1 holding breast tumor phantom of ϵ_r and σ as 38.1 and 1.91 S/m. The peaks A and B in the figure are attributed to the reflections from the edges of the tumor phantom used. The amplitude of the peak B is smaller than A due to the decrease in the strength of the reflected signals with distance. The FDTD and experimental results are in reasonable agreement.

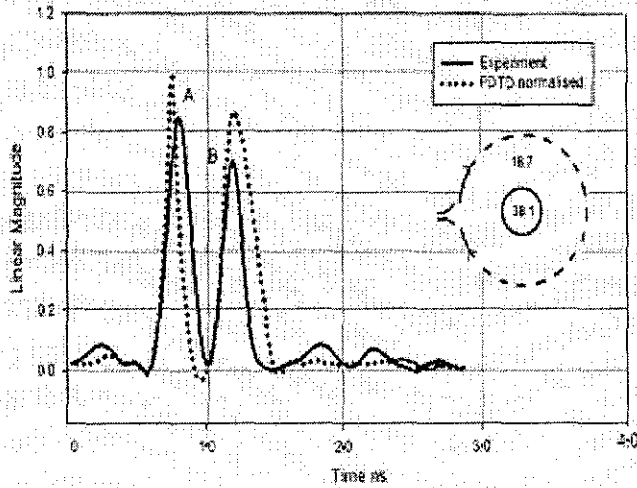


Figure 6.2. Time domain response of SH1 holding the breast tumor phantom

Figure 6.3 shows the time domain responses of the tumor phantom using SH2 given in Section 6.4.2.1. The outer and inner cylinders of SH2 are filled with corn syrup samples of ϵ_r and σ as, 18.7 and 0.98 S/m, and 38.1 and 1.91 S/m respectively. Experimentally obtained results complement the FDTD computed results.

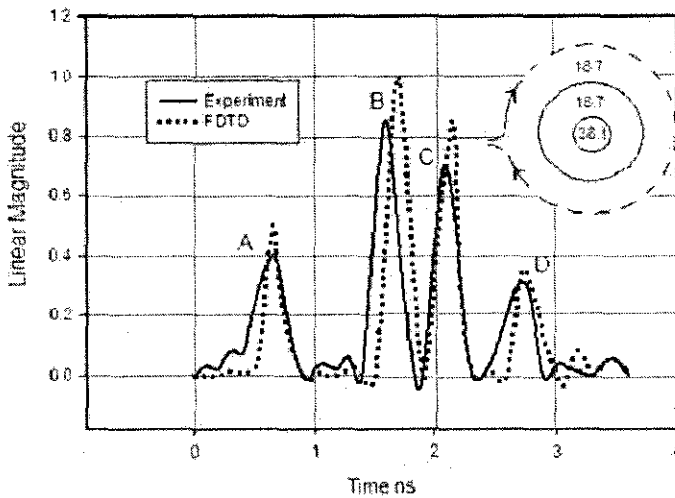


Figure 6.3. Time domain responses of SH2 holding normal and malignant breast phantoms

Even though the coupling medium, and the corn syrup sample used in the outer cylinder are same, reflections A and D are observed. This is due to the fact that the PVC cylinder exhibits significant dielectric contrast with the corn syrup sample resulting in reflections. Sharp peaks B and C are due to the reflections from the tumor phantom. These peaks have larger amplitude compared to A and D due to greater reflection from the corn syrup medium of higher dielectric constant.

Figure 6.4 shows the time domain response of the tumor phantom using SH2 given in Section 6.4.2.1, with the outer and inner cylinders filled with corn syrup samples of ϵ_r ' and σ as, 18.7 and 0.98 S/m ϵ_r ' and σ as 29.8 and 1.1 S/m respectively. Experimental observation shows that the amplitude of the peaks B and C are less compared to that in Figure 6.3. This is due to the reduced value of the dielectric constant of the corn syrup sample used as the tumor phantom here.

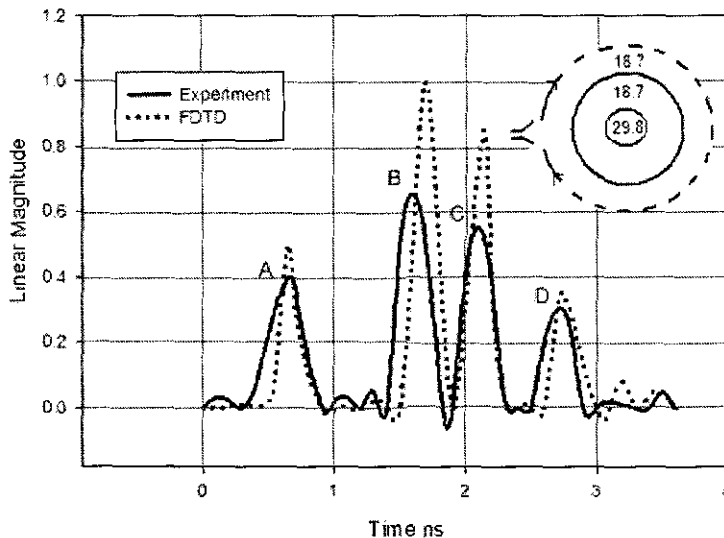
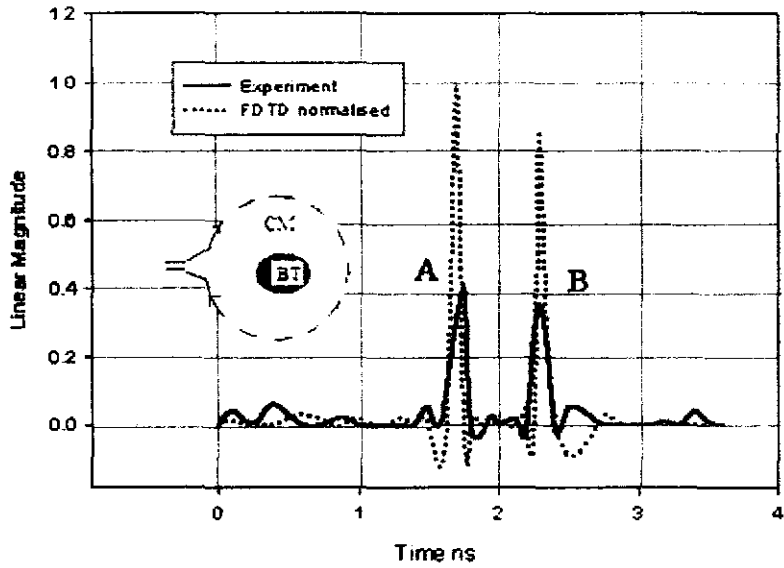
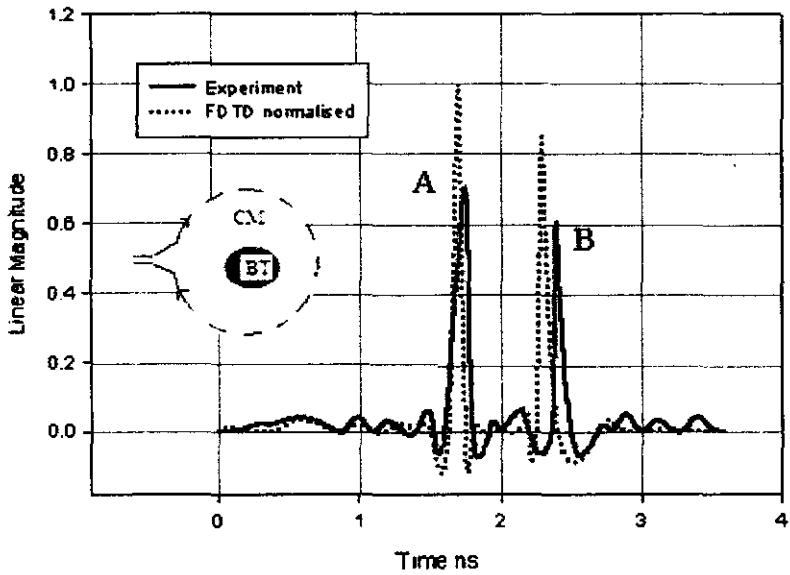


Figure 6.4. Time domain responses of SH2 holding normal and malignant breast phantoms

Figures 6.5 – 6.8 show the time domain responses of the normal and cancerous breast tissue samples of patients 1 – 4. Regions of dielectric contrast are clearly visible from the graphs. Peaks A and B represent the reflections from the boundaries of coupling medium and the tissue. In all the cases theoretical and experimental results are in good agreement. Reflections from the cancerous breast tissue have higher amplitude than that of the normal tissue due to the higher value of dielectric constant and conductivity, which is in turn a function of the bound water content.

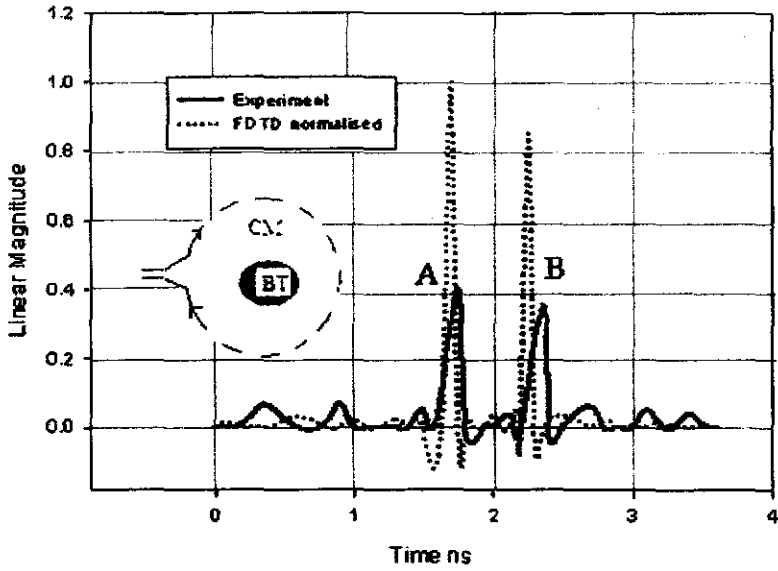


a)

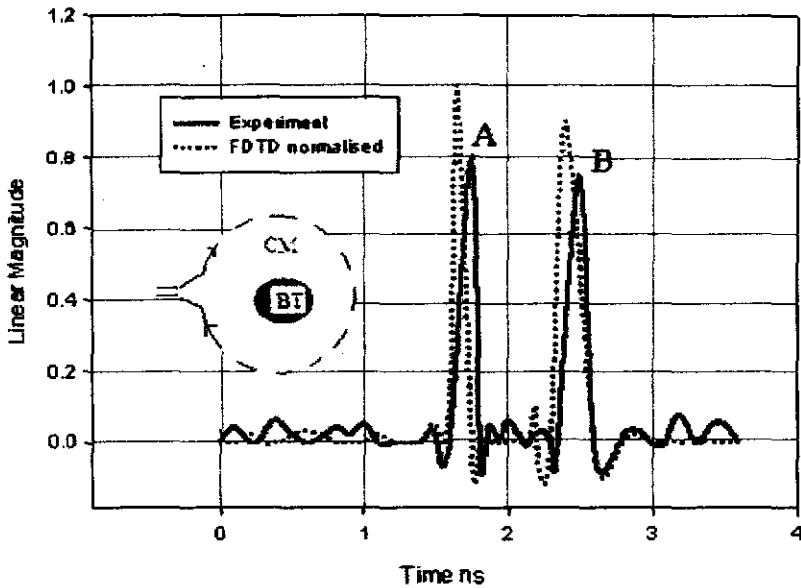


b)

Figure 6.5. Time domain responses of breast tissue of patient 1.
 (a) normal tissue (b) cancerous tissue.
 CM – Coupling medium, BT – Breast tissue



a)

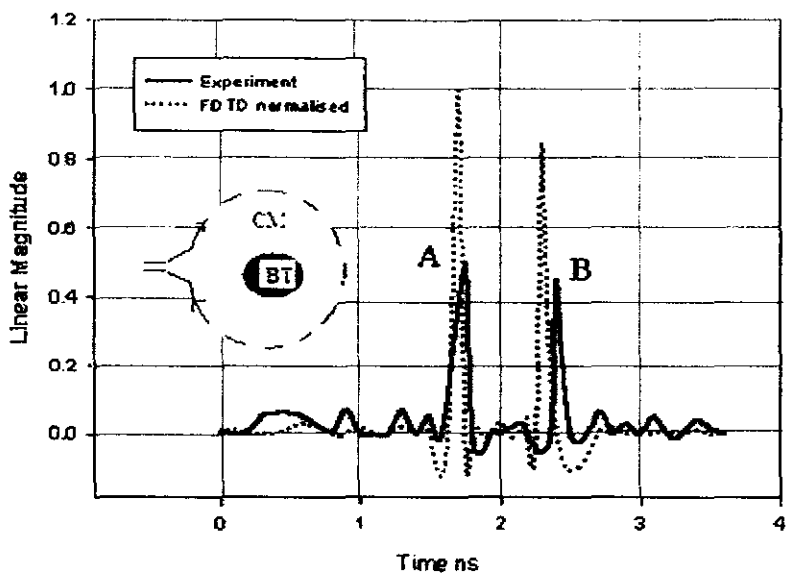


b)

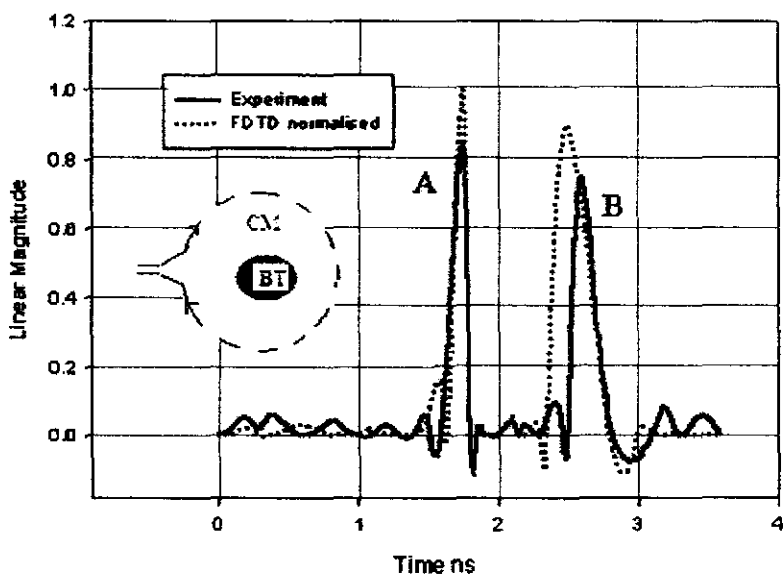
Figure 6.6. Time domain responses of breast tissue of patient 2.

(a) normal tissue (b) cancerous tissue.

CM - Coupling medium, BT - Breast tissue



a)



b)

Figure 6.7. Time domain responses of breast tissue of patient 3.
 (a) normal tissue (b) cancerous tissue.
 CM – Coupling medium, BT – Breast tissue

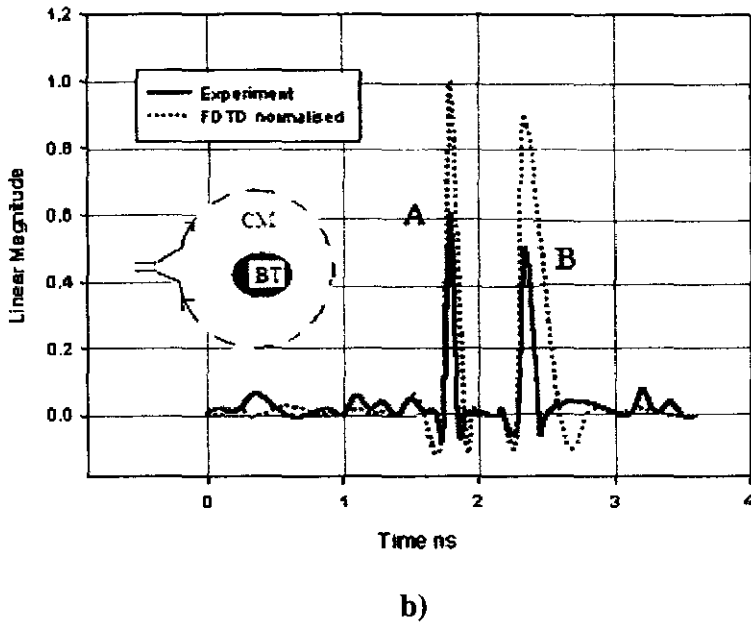
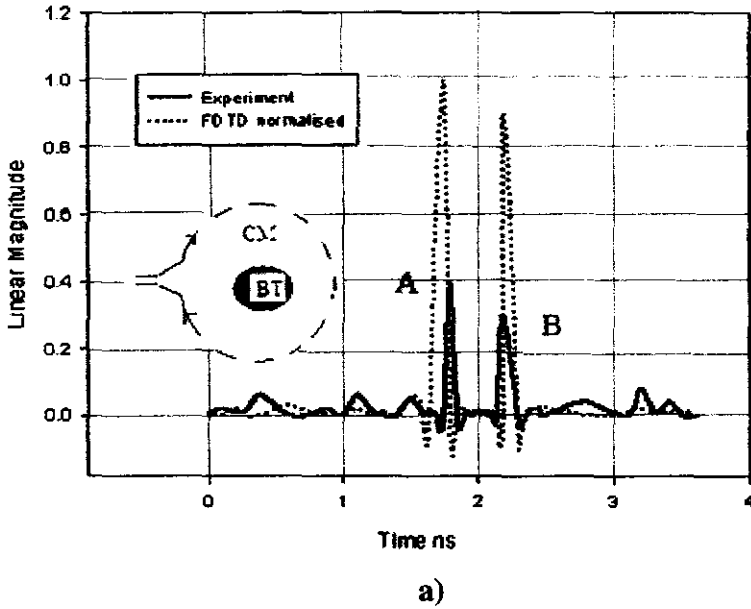


Figure 6.8. Time domain responses of breast tissue of patient 4.

(a) normal tissue (b) cancerous tissue.

CM – Coupling medium, BT – Breast tissue

Figures 6.9 - 6.12 show the time domain responses of normal breast tissue with cancerous inclusions, i.e of B-Samples 1- 4. In Figure 6.9 of B-Sample 1 (normal breast tissue with a single cancerous inclusion), the peaks A and D in the encircled region, represent reflections from the coupling medium - normal tissue interface.

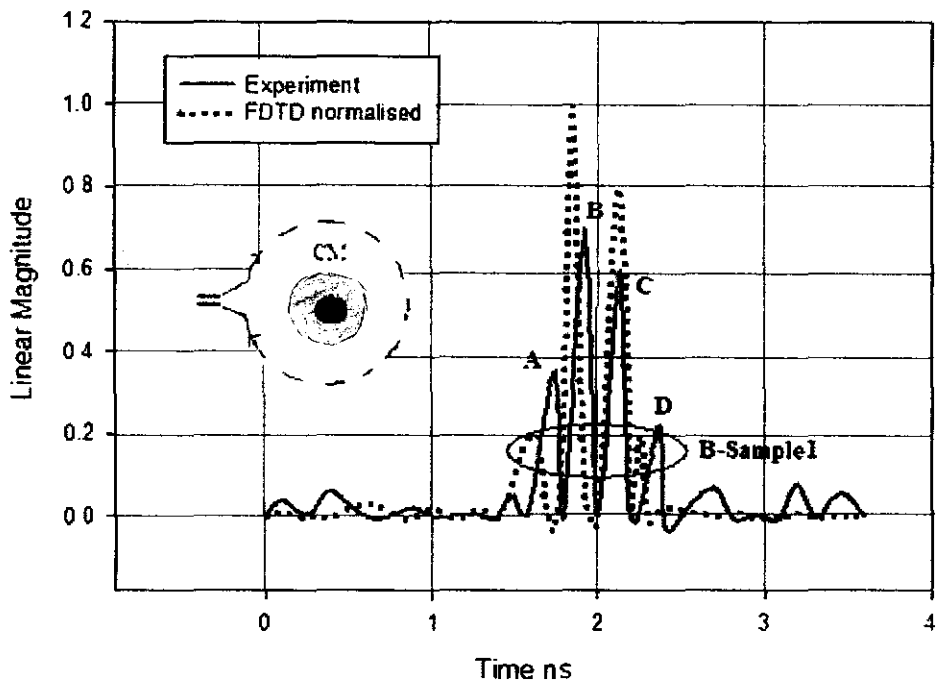


Figure 6.9. Time domain responses of B-Sample 1 (of patient 1)

 Normal tissue,  Cancerous tissue

CM- Coupling Medium

As the dielectric contrast is less here, the reflections are less compared to the reflections produced by the cancerous tissues. Peaks B and C correspond to reflections from the tumor inclusions. Peak C exhibits lesser

amplitude compared to B, due to the decrease in the signal strength with distance of propagation. Experimental and FDTD results show good agreement as there is only a single tumor inclusion in B-Sample 1.

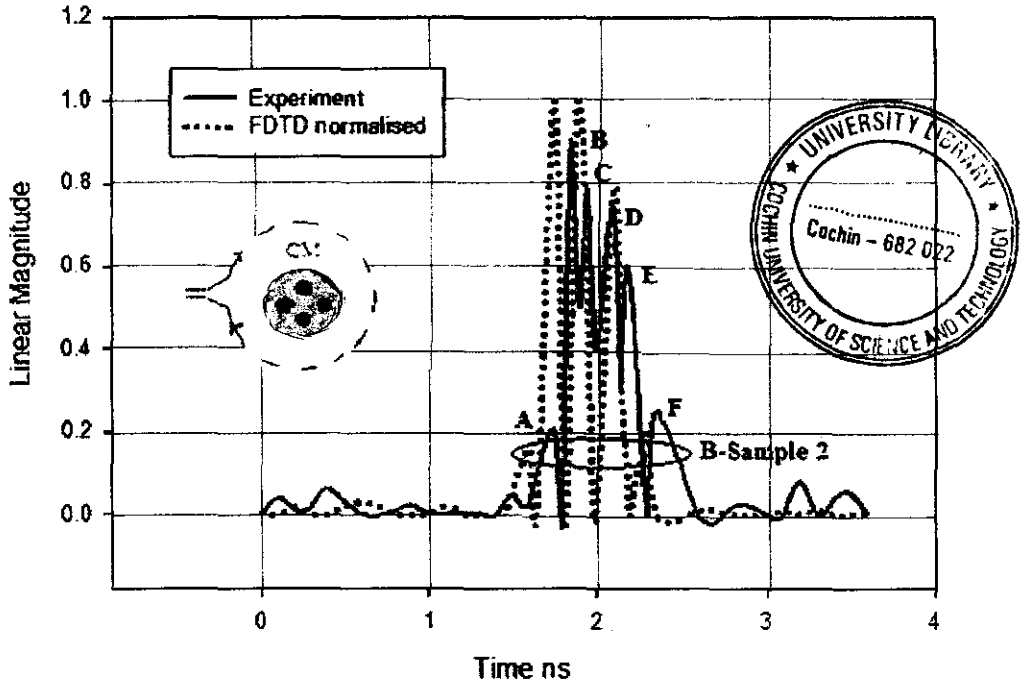


Figure 6.10. Time domain responses of B-Sample 2 (of patient 2)

 Normal tissue,  Cancerous tissue

CM- Coupling Medium

In Figures 6.10 – 6.12 of B-Samples 2 - 4, the peaks A and F in the encircled region represent reflections from the normal breast tissue and the remaining peaks B,C,D and E are reflections from the tumor inclusions. The FDTD and experimental results do not agree well in these figures due to the presence of multiple inclusions. Reflections from nearby contrast points overlap and get represented as a single point. The time shift and add

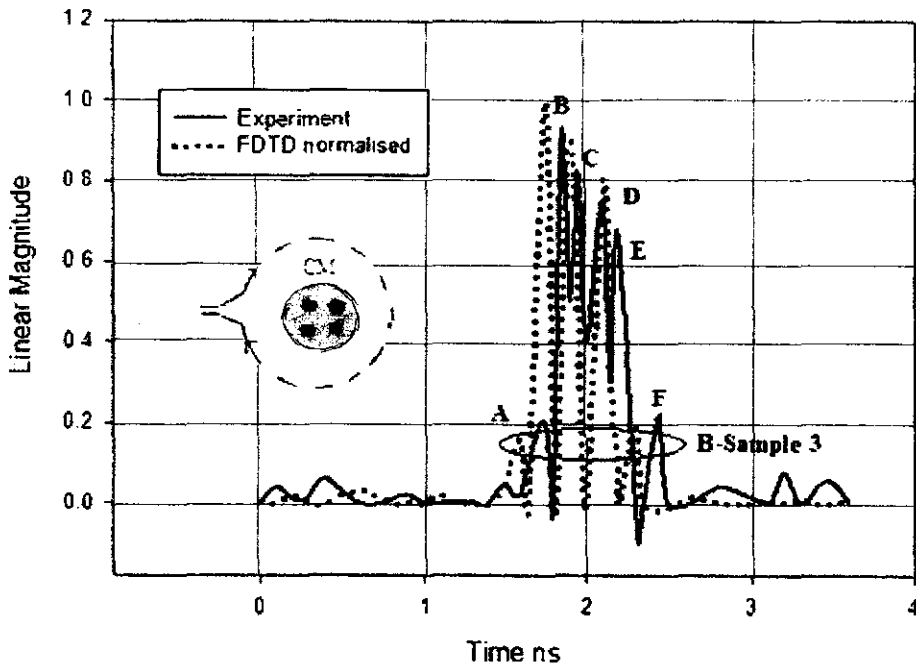


Figure 6.11. Time domain responses of B-Sample 3 (of patient 3)

 Normal tissue,
  Cancerous tissue

CM- Coupling Medium

algorithm applied to the experimental data makes the reflected signals from tumors located opposite to each other to overlap. Even though exact tumor locations are difficult to figurize, regions of dielectric contrast are satisfactorily detected using this time domain confocal microwave technique. The amplitudes of the tumor reflections B in Figures 6.10 and 6.11 are higher than that in Figures 6.9 and 6.12 due to the higher dielectric constant of the cancerous tissue in B-Samples 2 and 3 compared to that in B-Samples 1 and 4.

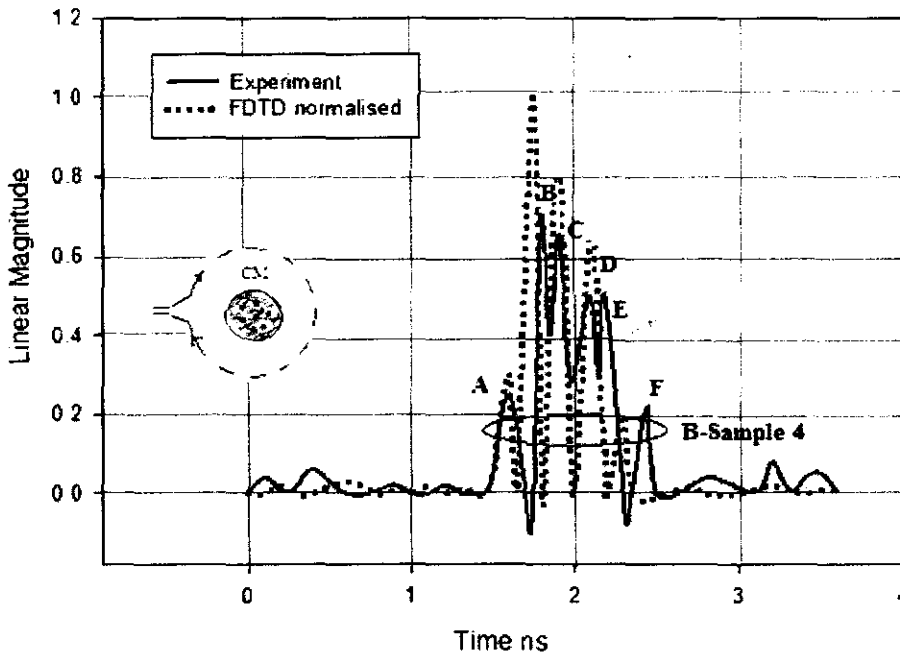


Figure 6.12. Time domain responses of B-Sample 4 (of patient 4)
 [Hatched Box] Normal tissue, [Solid Black Box] Cancerous tissue
 CM- Coupling Medium

Approximate tumor locations represented by the tallest peak in Figures 6.9- 6.12 are calculated from the following equation.

The velocity of propagation depends on the dielectric constant of the medium given by,

$$v = \frac{c}{\sqrt{\epsilon_r}}, \quad (6.22)$$

where
$$v = \frac{2d}{t} \quad (6.23)$$

d is the distance, t is the time taken for propagation, ϵ_r is the dielectric constant and c is the velocity of light in free space. The results are tabulated in Tables 6.1 and Table 6.2. The percentage of error between the actual

tumor location and the experimentally obtained value is less than 5%. The FDTD results also give an error percentage of less than 5%

Table 6.1. Approximate tumor locations with respect to the first tumorous inclusion in Figures 6.9 -6.12 (i.e with respect to the tallest peak in time domain graphs)

B - Sample	Actual distance of nearest tumorous inclusion from the antenna cm	Approximate distance calculated from experimental time domain data cm	Percentage error
1	6	6.28	4.6
2	6	6.16	2.6
3	6	6.23	3.8
4	6	6.21	3.5

Table 6.2. Approximate tumor locations with respect to the first tumorous inclusion in Figures 6.9 -6.12 computed from FDTD (i.e with respect to the tallest peak in time domain graphs)

B - Sample	Actual distance of nearest tumorous inclusion from the antenna cm	Approximate distance calculated from FDTD	Percentage error
1	6	6.25	4.2
2	6	6.14	2.4
3	6	6.2	3.5
4	6	6.19	3.1

6.6.1 Comparison of the results

None of the time domain techniques reported in the literature review was tested on real breast tissues and hence no data are available for comparison. However the percentage of error obtained in estimating the tumor depths using the simulations performed by Hagness etal [5,6], Xu Li etal [9,10] and Fear etal [16 – 18] are compared here with. The results of the comparison are reported in Table 6.3. The tumor depth estimation method presented in this thesis reports the least error, even when tested on real breast tissues.

Table 6.3 Comparison of the percentage of error in estimation of tumor depths of breast tissues with the reported simulation values

	Author		Hagness etal	Xu Li etal	Fear etal
	Experiment	FDTD			
Percentage of error	<4.6% (2.6 - 4.6)	<4.2% (2.4 - 4.2)	6.5%	5.8%	5.2%

6.7 Conclusion

Confocal Microwave Technique is investigated on actual breast tissues as well as on breast phantoms to estimate the location of the region of dielectric contrast. An error of less than 5% is obtained between the actual depths of the tumor and the experimentally obtained results. Experimental results are substantiated by FDTD analysis and good agreement is observed

6.8 References

1. G.A.Burrell, L.Peters “Pulse propagation in lossy media using the low frequency window for video pulse radar application”, Proc. IEEE, vol. 67, pp. 981 – 990, 1979.
2. J. D. Young, L. Peters, Jr., “Examination of video pulse radar systems as potential biological exploratory tools”, Medical Applications of Microwave Imaging, L. E. Larson, and J. H. Jacobi, Eds. New York: IEEE Press, pp 82 -105, 1986.
3. A.W.Preece, H. Johnson, F.L.Green, M.P.Robinson, “Dielectric imaging for localization and detection of breast tumors”, IEEE MTT –S Digest, pp. 1145 – 1146, 1993.
4. N.M.Pothecary, C.J.Railton, R.H.Johnson, A.W.Preece, “FDTD analysis of a noninvasive sensor for the detection of breast tumors”, IEEE MTT-S Digest, pp. 527 – 530, 1994.
5. S.C.Hagness, A.Taflove, J.E.Bridges, “FDTD Analysis of a pulsed confocal microwave system for breast cancer detection”, Proc. 19th Intl. Conference on IEEE/EMBS, Chicago, USA, pp. 2506 – 2508, 1997.
6. S. C. Hagness, A.Taflove, J. E. Brdiges, “Two -Dimensional FDTD analysis of a pulsed microwave confocal system for breast cancer detection: fixed-focus and antenna array sensors,” IEEE Transactions of Biomedical Engineering, vol.45, pp.1479 – 1429, 1998.
7. S.C.Hagness, A.Taflove, J.E.Bridges, “FDTD modeling of a coherent addition antenna array for early stage detection of breast cancer”, IEEE APS, pp. 1220 – 1223, 1998
8. S. C. Hagness, A.Taflove, J. E. Brdiges, “Three-Dimensional FDTD analysis of a pulsed microwave confocal system for breast cancer detection: design of an antenna-array element”, IEEE Transactions of Antennas and Propagation, vol.47, pp.783 – 791, 1999.
9. Xu Li, S.C.Hagness, “A confocal microwave imaging algorithm for breast cancer detection”, IEEE Microwave and Guided Wave Letters, vol. 11, pp. 130 – 132, 2001.
10. Xu Li, S.C.Hagness, E.Fear, M.A.Stuchly, “FDTD analysis of planar and cylindrical antenna – array configurations for 3D breast tumor localization using confocal microwave imaging”, IEEE APS, pp. 246 – 249, 2001.
11. Xu Li, S.C.Hagness, B.D. Van Veen, D. van der Weide, “ Experimental investigation of microwave imaging via space time beam forming for breast cancer detection”, IEEE MTT-S Digest, pp. 379- 382, 2003.
12. Xu Li, S.K.Davis, S.C.Hagness, D.van der Weide, B.D.Van veen, “Microwave imaging via space time beam forming: experimental

- investigation of tumor detection in multiplayer breast phantoms”, IEEE Transactions on Microwave Theory and Techniques, vol. 52, pp. 1856 – 1865, 2004.
13. M. Converse, E.J.Bond, S.C.Hagness, B.D.Van veen, “Ultra wide band microwave space time beam forming for hyperthermia treatment of breast cancer: a computational feasibility study”, IEEE Transactions on Microwave Theory and Techniques, vol. 52, pp. 1876 – 1889, 2004.
 14. E.C.Fear, M.A.Stuchly, “Microwave system for breast tumor detection”, IEEE Microwave and Guided Wave Letters, vol. 9, pp. 470 – 472, 1999.
 15. E.C.Fear, M.A.Stuchly “Microwave detection of breast cancer”, IEEE Transactions on Microwave Theory and Techniques, vol. 48, pp. 1854 – 1863, 2000.
 16. E.C.Fear, A. Low, J. Sill, M.A. Stuchly, “Microwave system for breast tumor detection: experimental concept evaluation”, Proc. of IEEE APS, pp. 819 – 821, 2002.
 17. E.C.Fear, J. Sill, M.A. Stuchly, “Experimental feasibility of breast tumor detection and localization”, IEEE MTT-S Digest, pp. 383 – 386, 2003
 18. E.C.Fear, Xu Lii, S.C.Hagness, M.A.Stuchly, “Confocal microwave imaging for breast cancer detection: localization of tumors in three dimensions”, IEEE Transactions on Biomedical Engineering, vol. 49, pp. 812 – 821, 2002.
 19. E.C.Fear, J. Sill, M.A.Stuchly, “Experimental feasibility study of confocal microwave imaging for breast tumor detection”, IEEE Transactions on Microwave Theory and Techniques, vol. 51, pp. 887 – 892, 2003
 20. X. Yun, E.C.Fear, R. Johnston, “Broadband cross-polarized bowtie antenna for breast cancer detection”, Proc. of IEEE APS, pp. 1091 – 1094, 2003.
 21. X. Yun, E.C.Fear, R. Johnston, “Radar based microwave imaging for breast cancer detection: tumor sensing with cross-polarized reflections”, Proc. of IEEE APS, pp. 2432 – 2434, 2004.
 22. HP 8510C Network Analyzer Operating and Programming Manual, Manual part. No. 08510-90070, Hewlett Packard.
 23. K.S.Yee,,”Numerical solution of initial boundary value problems involving Maxwell’s equations in isotropic media”, IEEE Transactions on Antennas and Propagation, vol. AP-14, pp. 302 – 307, 1996.
 24. G.Murr, “Absorbing boundary conditions for the finite difference approximation of the time domain electromagnetic field equations”,

- IEEE Transactions on Electromagnetic Compatibility, vol. EMC – 23, 377 – 382, 1981.
25. P. Kosmas, C. M. Rappaport, E. Bishop, “Modeling with the FDTD method for microwave breast cancer detection”, IEEE Transactions on Microwave Theory and Techniques, vol. 52, pp. 1890 – 1897, 2004.
 26. R. Luebbers, F. P. Hunsberger, K. S. Kunz, R. B. Standler, M. Schneider, “A frequency dependent finite-difference time domain formulation for dispersive materials”, IEEE Transactions on Electromagnetic Compatibility, vol. 32, pp. 222 – 227, 1990.
 27. R. Luebbers, F. Hunsberger, “FDTD for N^{th} order dispersive media”, IEEE Transactions on Antennas and Propagation, vol. 40, pp. 1297 – 1301, 1992.

Chapter 7

CONCLUSION AND FURTHER EXTENSION OF THE WORK

7.1 Conclusion

The invention of non-invasive microwave technique, to reveal the internal structure of biological objects was a break through in the field of medical diagnostics. Electrical properties of biological tissues and their interaction with electromagnetic waves have direct impact on human life. Extensive research is already been done and is still going on in this field.

Breast cancer is the most common non-skin malignancy in women and a leading cause of female mortality. A potentially important strategy for reducing this menace is the detection at an early stage. Despite its recognized value in detecting and characterizing breast disease, X-ray mammography has serious limitations in the evaluation of soft tissues that motivate the quest for alternatives to augment the diagnostic tools that are currently available to the radiologist. The rationale for pursuing electromagnetic methods are – 1) significant difference in the electrical properties of normal and malignant breast tissues in the microwave

spectrum, 2) microwave illumination can effectively penetrate the breast, 3) as breast is a small readily accessible tissue volume, it is an ideal site for deploying advanced near field imaging concepts that exploit model based image reconstruction methodology.

This thesis focuses on theoretical and experimental investigations of active microwave imaging techniques for breast cancer detection. The unique features of microwave breast imaging are that it

- offers low health risk
- is sensitive to tumors and specific to malignancies
- detects breast cancer at a curable stage
- is non-invasive and simple to perform
- is cost effective and widely available
- involves minimal discomfort
- provides easy to interpret and consistent results.

The challenges involved in microwave breast imaging are -

- design and development of low reverberation transmitter and receiver.
- identification of suitable, cost-effective coupling medium, to enhance the resolution.
- development of algorithms for target detection and image reconstruction.

A coplanar strip line fed bow tie antenna that exhibits wide band and unidirectional radiation pattern is developed to use as transmitter and receiver. Wide bandwidth is essential to transmit short transient pulses in confocal microwave technique. Microwave tomographic imaging is done at 3 GHz which is the resonant frequency of the antenna. Use of low

frequencies increases the antenna size, whereas high frequencies increase the propagation loss and reduce the penetration strength of the signal into the object. Hence, as a compromise, the antenna is designed to have a resonant frequency of 3 GHz, which is found successful in detecting and imaging regions of dielectric contrast in breast tissues.

Dielectric properties of corn syrup are studied to check its feasibility of using as coupling medium and phantom in microwave breast imaging. The studies show that the dielectric constant of corn syrup is in good agreement with that of breast tissues, while the conductivity is less. This underlies its application as an efficient coupling medium with less propagation loss. As the dielectric constant and conductivity of the material can be varied by proper dilution with water, both normal and malignant breast tissues can be easily simulated using the same material.

The two approaches of active microwave imaging, microwave tomographic imaging with measured transmitted signals and confocal microwave technique (CMT) with measured reflected signals are addressed in Chapters 5 and 6. Studies are made on both breast phantoms and on breast tissue samples. Results show that microwave tomographic imaging provides valuable diagnostic information about the shape and quantitative description of the dielectric constant profile of the object, while the time domain CMT identifies the presence and location of regions of dielectric contrast of the object rather than completely reconstructing the dielectric property profile. Analyzing the 2-D tomographic images and dielectric constant profiles of the breast samples, the presence of malignancy is easily ascertained. This evaluation is substantiated by cross checking with the time domain confocal microwave response. The presence of sharp peaks in the reflected signal undoubtedly shows the

occurrence of dielectric contrast in breast samples, which is due to none other than a cancerous growth. Thus the two techniques should go hand in hand for a reliable, assertive detection of breast cancer. As normal breast tissues exhibit low bound water content and hence low dielectric constants than the malignant tissues, a comparison of the microwave images and dielectric constant profiles of both the breasts can easily detect the presence of tumor.

It can thus be concluded that microwave techniques developed in this work for breast cancer detection are coming of age. Enough reason is there to be optimistic that a clinically viable system will be developed soon. It is not expected that such a system will replace X-ray mammography as a screening tool. But these systems if used together can improve detection and limit false findings. Perhaps for young women for whom mammography is not recommended, a microwave system will become useful as a painless low risk diagnostic aid. At present, there is still a great deal of research and engineering design to be completed before this becomes a reality.

7.2 Sources of error

The sources of errors and accuracy conditions encountered in the work are discussed below.

As early stage tumor detection is the attractive feature of microwave breast imaging, care is taken to eliminate all possible types of errors. In the present study HP 8510 network analyzer is used. Accuracy of this instrument is 0.001dB for power measurement, 1 Hz for frequency measurement and 0.01 ns for time domain measurement [1]. Main sources of experimental errors are

- Edge reflections from the antenna: The FDTD computed end-

reflections observed at the feed point of the bowtie antenna relative to the exciting pulse is -24 dB. For the CMT, a time gating of 9.07 ns is provided from the network analyzer to remove these reflections. Moreover, calibration of the system was performed in the coupling medium in the absence of the samples.

- **Reflections from the sample holder:** The tissue samples are supported on a low loss PVC pipe having loss tangent ($\tan \delta$) 0.0017. Hence reflections are negligible.
- **Medium reflections:** As the tumor under study is immersed in a matching coupling medium, reflections are minimized and good resolution of the reconstructed image is ensured.
- **Error in using distorted Born approximation to linearize the inverse scattering problem:** This method is adopted to reduce the computational complexity. Acceptable values of dielectric constant profiles are obtained with in vitro breast studies. The matter has to be further investigated with strong scatterers and fast forward iterative solvers.
- **False convergence:** To ensure convergence, iterations are continued until global convergence is achieved.

7.3 Future extensions of the work

With a variety of promising approaches, there are good reasons to believe that microwave breast cancer detection will become a successful complement to conventional mammography. The techniques explained in this thesis provide a solid foundation for improved design of a microwave breast cancer diagnostic tool. In addition to the further development of the existing technologies, new solutions are also likely to emerge. One may hope that clinical systems already in place will pave the road for clinical

acceptance of the new system.

The possible extensions of the work are summarized as follows.

- Development of a viable microwave breast imaging system for real time application. Even though many prototypes of microwave breast imaging system have been realized, a clinically viable system is yet to be realized. As microwave technology is non-hazardous and can detect and image breast tumor at an early curable stage itself, a clinically viable microwave breast imaging system is definitely a boon to breast cancer patients.
- To develop three-dimensional tomographic images of the breast. In the present work, two-dimensional microwave tomographic images of breast tissues are developed. Even though tumor locations can be satisfactorily detected and imaged using the 2-D method, a better analysis of the size of the cancerous region is possible with 3-D images.
- In the present work characterizing and analyzing of normal and malignant breast tissues using microwaves are reported. Some benign breast tumors too respond to microwaves in a similar fashion to that of malignant tumors. Studies with these benign breast tumors and development of a technique to distinguish benign and malignant tumors need to be done.
- In the present work, distorted Born iterative method is used to solve the non-linear inverse scattering problem. Even though this method is easy to implement, it is computationally intensive. Hence fast forward iterative solvers need to be developed to reduce the computation time.
- The time domain confocal microwave method discussed in the thesis could satisfactorily detect cancerous regions in the breast. A technique

to develop 2-D / 3-D images from this time domain data could substantiate these results. Development of images using the time domain data can also save the computation time.

- Tikhonov regularization technique is used in the present work to solve the inverse scattering problem. Proper selection of the associated regularization parameter is a difficult task in this method. Development of a regularization technique based on a stochastic model of the reconstruction process can be tried.

7.4 References

1. HP 8510C Network Analyzer Operating and Programming Manual
1988 Hewlett-Packard.

Appendix A

**2-D MICROWAVE TOMOGRAPHIC IMAGING
OF SOME BIOLOGICAL OBJECTS AND WAX
SAMPLE**

A.1 Introduction

The applications of microwave tomographic imaging to detect the electrical properties of low water content biological tissues like bone, bone marrow and wood sample are discussed in this section. Dielectric study of wax cylinder with inclusion of a high dielectric constant medium is also done.

A.2 Models

The same system configuration as discussed in Chapter 5 is used for the study. Samples are fixed at the center of the tomographic chamber as shown in Figure A.1, and are illuminated by the bow tie antenna at 3 GHz. No coupling medium is used as the samples have low bound water contents. 2-D images and dielectric constant profiles of the samples are reconstructed from the collected scattered fields using distorted Born iterative method.

A.3 Samples

The samples considered for study are, femur of calf, thigh of chicken, bark of rubber tree and wax cylinder with inclusion of water. The femur of calf is

imaged, when freshly excised, after seven days and after fourteen days of natural drying.

A.4 Results and discussion

The reconstructed 2-D tomographic images and dielectric constant profiles of the femur of calf from the collected scattered fields are shown in Table 1. It is reported that [1] freshly excised (within 1hr. of extraction) femur and bone marrow of calf has permittivities of 6 and 10. The corresponding values obtained in the present experiment are 4 and 8. In Table A.1(a), both bone and bone marrow exhibit smooth dielectric constant profiles whereas the profiles are non-uniform when the bone is kept for natural drying, as shown in Table A.1(b) and A.1(c). These variations are attributed to the non-uniform decrease in the bound water content with drying. It is observed that after seven days of natural drying the peak value of the dielectric constant of the bone marrow decreases by 37 % and after fourteen days the drop is by 66 %. The corresponding values for the bone are 37% and 50% respectively. Tissue water contents of the samples are determined by weighing sections of bone and bone marrow before and after drying. For bone marrow, the bound water content decreases by 35 % and 70 % where as for the bone the decrease is by 40 % and 52 % when weighed after seven days and fourteen days of natural drying. A linear variation of dielectric constant with bound water content is observed in Figure A.2.

2-D tomographic image of thigh of chicken is shown in Table A.1(d). The dielectric constant profile is almost smooth with the flesh exhibits a dielectric constant of ~ 18. As bone is a low water content tissue having smaller cross section area and exhibits low dielectric constant compared to that of flesh, it is not easily distinguishable from the dielectric constant profile, even though it is visible in the 2-D image.

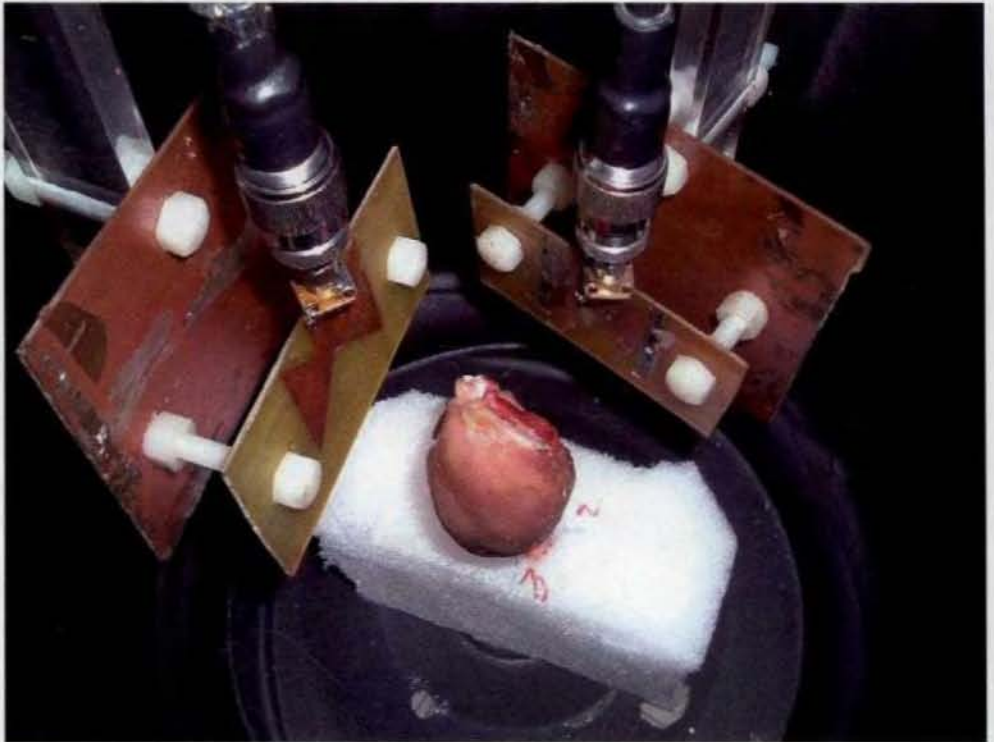


Figure A. 1. Measurement configuration for imaging chicken thigh

Table A.1. 2-D Tomographic images and dielectric constant profiles of biological samples


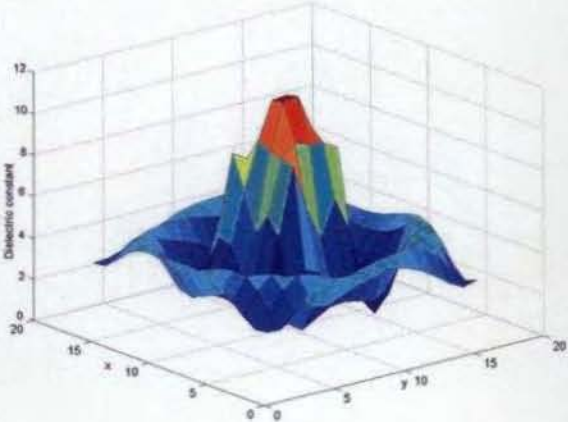
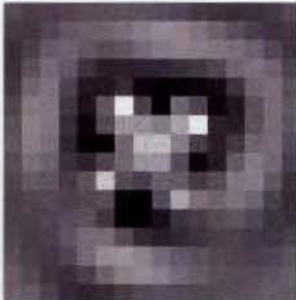
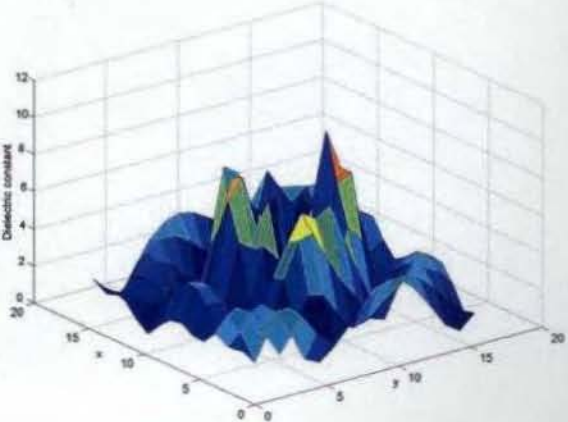
Sample	2-D Tomographic image	Profile of dielectric constant
<p>(a)</p> <p>Femur of calf (Freshly excised)</p>		
<p>(b)</p> <p>Femur of calf (after 7 days of natural drying)</p>		

Table A.1 continued

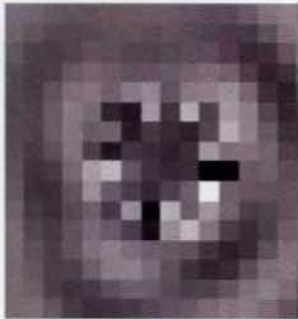
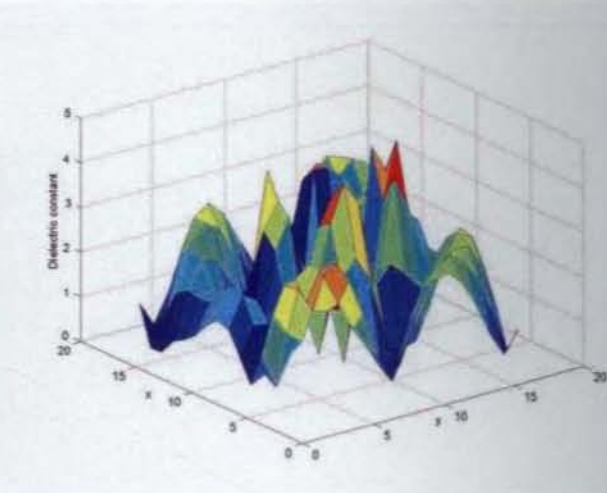
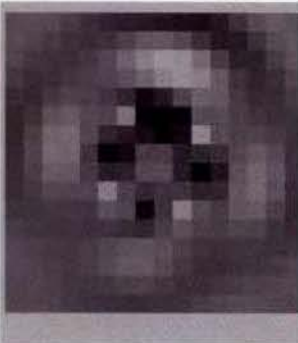
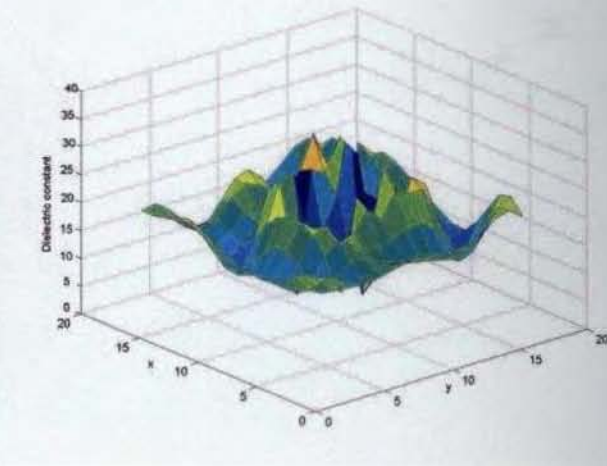
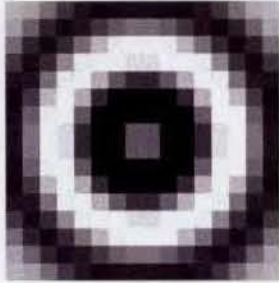
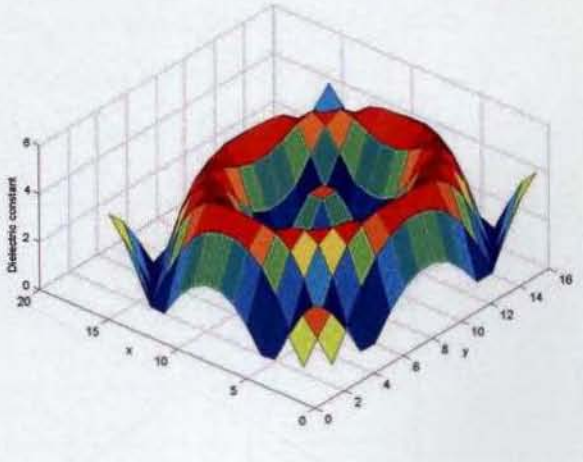
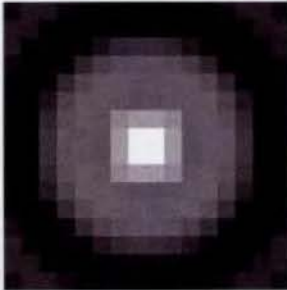
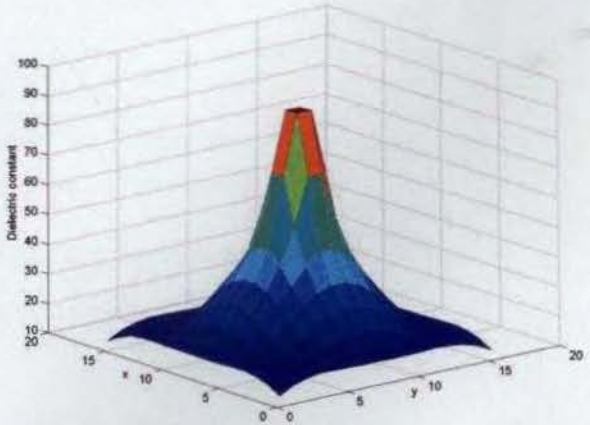
<p>(c) Femur of calf (after 14 days of natural drying)</p>		
<p>(d) Thigh of chicken</p>		

Table A.1 continued

<p>(e)</p> <p>Freshly cut bark of rubber tree</p>		
<p>(f)</p> <p>Wax cylinder with inclusion of water</p>		

Freshly cut bark of rubber tree exhibits a low value of dielectric constant of ~ 1.4 with the core having a still lower dielectric constant of ~ 1.1 , as seen in Table .1(e).

The reconstructed 2-D image and dielectric constant profile of wax cylinder of radius 2.5 cm with 0.2 cm. radius inclusion of water is shown in Table A.1(f). Published data shows that wax has a low value of dielectric constant of 3, whereas water has a dielectric constant of 77.8 at 3 GHz. Reasonable agreements of these values are obtained from the experiment.

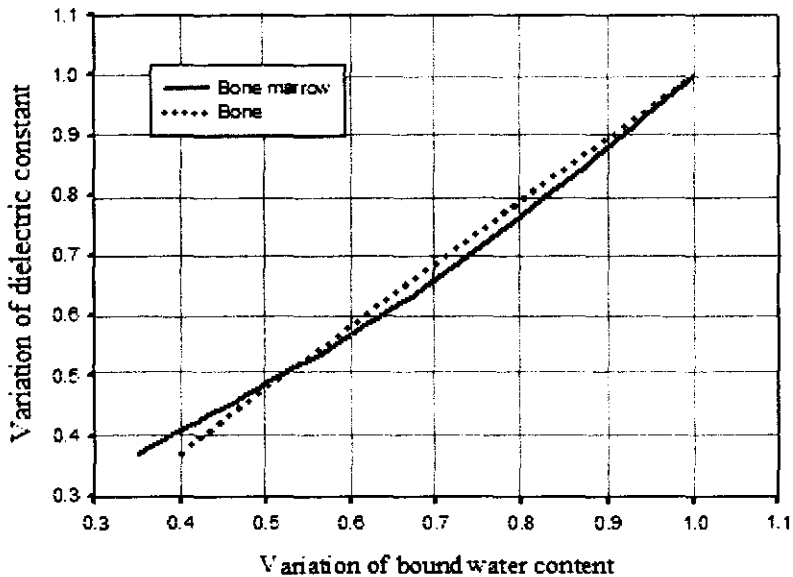


Figure A. 2. Variation of dielectric constant with bound water content of calf femur

A.5 References

1. Susan Rae Smith, Kenneth R. Foster, "Dielectric properties of low water content tissues", *Physics in Medicine and Biology*, vol. 30, pp. 965 – 973, 1985.

Appendix B

**MICROWAVE STUDIES OF POLY VINYL ACETATE
BASED PHANTOM FOR APPLICATIONS IN MEDICAL
IMAGING**

B.1 Introduction

Development of phantoms to simulate low water content biological tissues is an extensive research area. To study the interaction of electromagnetic energy with human tissue, it is necessary to use models that simulate the electrical properties of real tissue. It is also important that these models are reproducible, long lasting, non- corrosive, easy to make and use, and cost – effective.

A non-hydrated phantom that overcomes the inherent problems in conventional phantoms like decomposition and deterioration due to the invasion of bacteria or mold is developed, to simulate low water content biological tissues. The material is composed of polyvinyl-acetate-based adhesive, carbon black powder and graphite powder. The complex permittivity of the phantom can be controlled by adjusting the composition ratio. The absorption coefficient of the material is studied for its feasibility of using as microwave absorber for interior coating of tomographic chamber in microwave imaging applications. A frequency range of 2–3 GHz is

selected for the study to conveniently include the Industrial, Scientific and Medical Applications (ISM) band of 2.45 GHz.

B.2 Sample preparation and procedure

The samples are prepared by mixing polyvinyl-acetate-based adhesive (PVA), carbon black powder and graphite powder in different known proportions of weight. Diamond and graphite are the two natural crystalline allotropes of carbon. Both of them are extracted by conventional mining techniques.

Diamond has a three-dimensional structure, while graphite is composed of a series of parallel planes. The structure of carbon black powder is intermediate between these two forms and is termed 'quasi-graphitic', as a series of layers are formed during the nucleation process. Carbon black powder is intensely black in colour, and is manufactured by subjecting natural gas to extremely high temperatures in carefully controlled combustion process. Natural gas is composed of 80 % to 95 % of methane, and the balance is composed of varying amounts of ethane, propane, butane and other hydrocarbon compounds.

In the present study commercially available carbon black powder, graphite powder and PVA are used. PVA is easily available in the brand name Fevicol. Carbon black and graphite powder are mixed in various composition ratios (C: G) of 50: 0, 40: 10, 30: 20, 20: 30, 10: 40 and 0: 50 with the PVA content in all the samples fixed as 50%. It is found that if the PVA content is more than 50% there is difficulty in setting the compound. Cylindrical pellets of diameter 3 mm and height 2 mm are made for all the mixture samples by compressing them in a 3 mm die using hand press. Microwave studies of the pellets are done using rectangular cavity perturbation technique described in Chapter 2.

B.3 Results and Discussions

To study the variations of dielectric constant and conductivity of the mixture compared to their elemental values, dielectric properties of carbon black, graphite powder and PVA are studied separately. Cylindrical pellets of same dimensions as the mixture samples are made for the study. In the frequency range of 2–3 GHz, carbon black powder exhibits dielectric constant variation from 3.8 to 2.67. The respective variation of graphite powder is from 4.8 to 3.87 and for PVA from 5.74 to 4.02. For the same frequency range, the conductivity variation for, carbon black powder is from 0.0024 to 0.0067, graphite powder is from 0.003 – 0.005 and for PVA from 0.003 to 0.015. When these materials are mixed in definite proportions, the dielectric constant and conductivity increases and behaves as an ideal simulant of low water content biological tissues. The variations of dielectric constant and conductivity with frequency for mixture samples are shown in Figures B.1 and B.2. It is observed that for all the samples, the dielectric constant decreases and conductivity increases, with increase in frequency. This result coincides with the studies on dielectric properties of biological tissues [2].

When carbon black, graphite powder and PVA are mixed in definite proportions, the conductivity and dielectric constant increases compared to their corresponding elemental values due to interfacial polarization. In heterogeneous dielectrics where a dielectric material is composed of two or more phases, space charge build up occurs at the macroscopic interface as a result of the differences in the conductivities and dielectric constants of the materials at the interface. This accumulation of space charge leads to field distortions and dielectric loss; this interfacial loss depends on the quantity of filler present as well as on the dispersion. The magnitude of the

interfacial loss is particularly susceptible to the length of the dispersed phase geometry in the direction of the field. Due to this interfacial loss, the conductivity increases [1]. In the presence of microwave field, dielectric constant depends on the dipolar polarization. The accumulation of polar charges at the interface leads to dipolar polarization, which in turn increases the dielectric constant. The absorption coefficient of a dielectric material depends on dielectric constant, conductivity and resonant frequency. The absorption coefficients of the samples for various composition ratios of graphite to carbon black powder are plotted in Figure B.3. It is observed that a combination of 50% PVA, 20% carbon black powder and 30% graphite powder exhibits good absorption rate and is ideal to use as microwave absorbing material in microwave tomographic imaging.

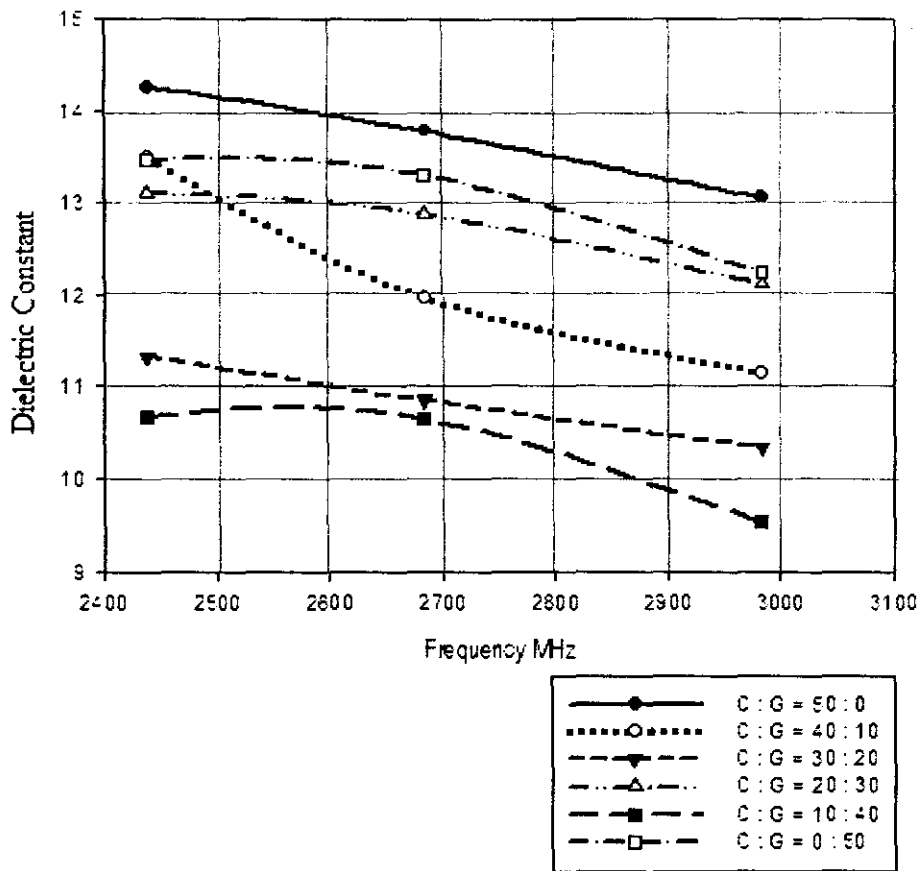
The equivalent phantoms for various low water content biological samples [3] in the frequency range of 2–3 GHz are given in Table B1. It is observed that, mixing carbon black powder and graphite powder in definite proportions with PVA can simulate phantoms of any of these biological tissues.

B.4 Conclusion

Polyvinyl-acetate-based composite of carbon black and graphite powder is identified as suitable phantom for low water content biological tissue in microwave medical imaging. The dielectric constant and conductivity of the phantom samples exhibit good matching with the available literature data on biological tissues. High value of absorption coefficients of the samples suggest their another application as microwave absorbing material in medical imaging.

Table B.1. Equivalent phantoms of various biological tissues in the frequency range of 2–3 GHz

Biological Sample	Range of dielectric constant	Range of conductivity $S m^{-1}$	Equivalent ratio of carbon black:graphite with 50%PVA
Bladder, Human	13.5 - 13.1	0.21 – 0.215	C : G = 40 : 10, C : G = 0 : 50
Breast Fat, Human	10.2 - 9.8	0.052 – 0.062	C : G = 10 : 40
Bone, Cancellous, Human	12.6 -12.14	0.15 – 0.17	C : G = 20 : 30
Bone, Cortical, Ovine	11.78 - 11.299	0.17 – 0.23	C : G = 30 : 20
Bone, cortical, Human	12.44 - 10.96	0.068 – 0.71	C : G = 20 : 30
Bone marrow (infiltrated), Ovine	13.31 - 14.76	0.175 – 0.182	C : G = 50 : 0



**Figure B.1. Variation of dielectric constant with frequency for different composition ratios of the phantom.
(C – carbon black powder, G – graphite powder)**

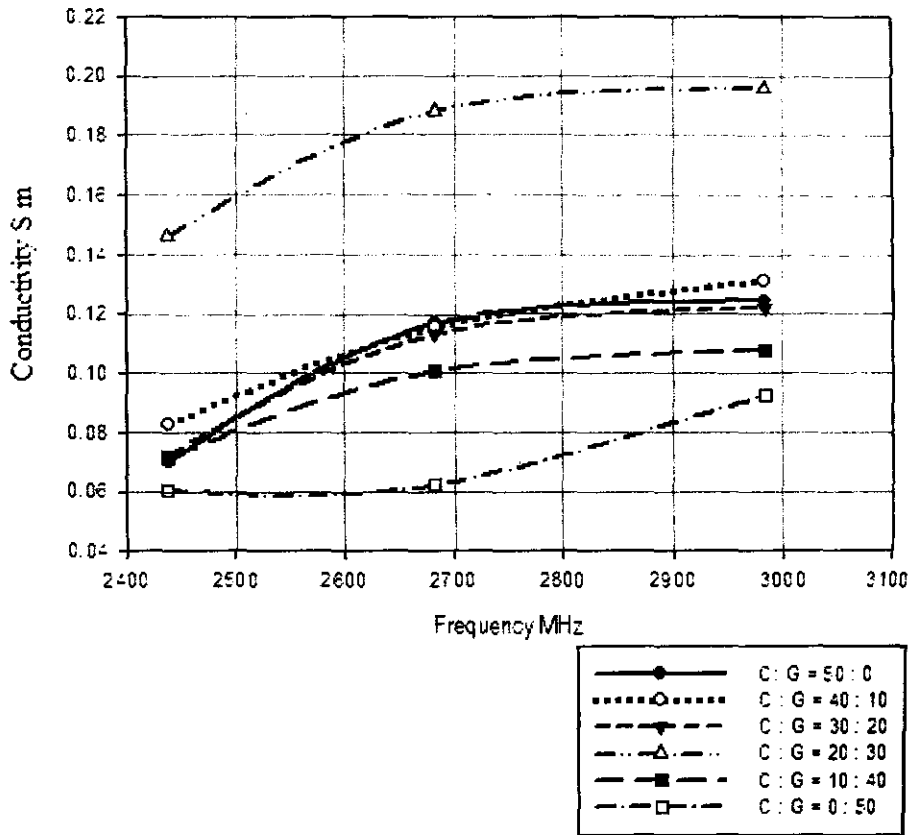


Figure B.2. Variation of conductivity with frequency for different composition ratios of the phantom (C – Carbon black powder, G – graphite powder)

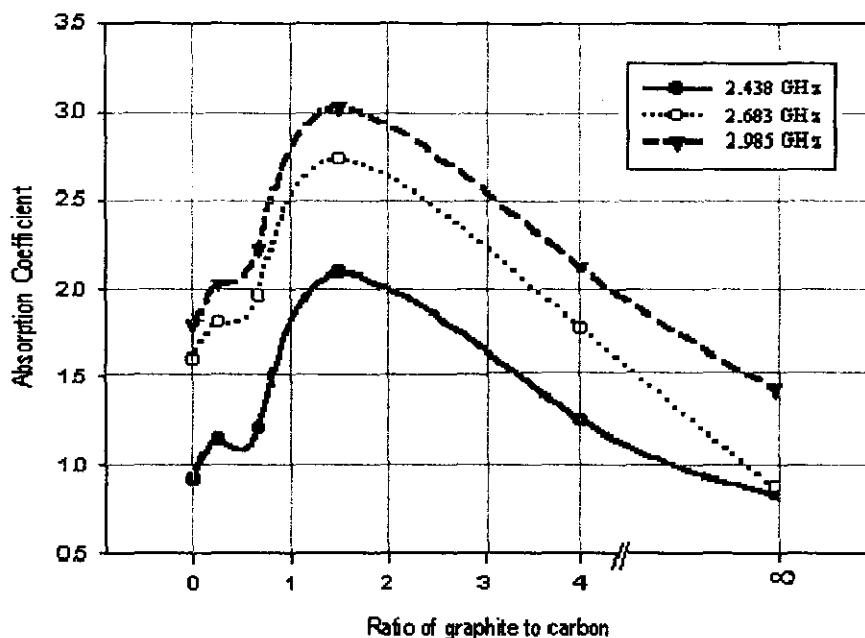


Figure B.3. Variation of absorption coefficient for different composition ratios of carbon black powder and graphite powder. In all the samples PVA constitutes 50% of the composition

B.5 References

1. T.A.Ezquerro, F.KRemmer and G.Wegner: Progress in electromagnetic research, (Elsevier, NewYork,), 1992.
2. S.Gabriel, R. W. Lau, C. Gabriel, Dielectric properties of biological tissues:II. Measurements in the frequency range 10 Hz to 20 GHz, Physics in Medicine and Biology, vol. 41, pp. 2251 – 2269. 1996
3. S.Gabriel, R. W. Lau, C. Gabriel, Dielectric properties of biological tissues:III. Parametric models for the dielectric spectrum of tissues, Physics in Medicine and Biology, vol.41, pp. 2271 – 2293, 1996



Product Specifications And Features

Bipolar Stepper Driver

Product Code: ML-STEPR-23

Revision Status: Rev-A-030820

Specifications

Motor Supply Voltage	: AC: 12 - 30V / 3Amps DC: 15 - 40V / 3Amps (Not to exceed 45VDC as it can cause component failure) <i>Note: Only Single winding is required.</i>
Aux. DC Output	: Unprotected +5VDC regulated supply for connecting external inputs. <i>Note: It can source up to 25mA of current. Do not short circuit or overload.</i>
External Logic Input Levels	: Low: 0 - 0.7V High: 5- 12V. <i>Note: Applying beyond 15V from an external source may damage the components</i>
PWM Frequency	: 22 kHz.
Maximum Clock Frequency	: 12 kHz in Half Step Mode with a minimum pulse width of 10us.
Maximum Phase Current	: 3A per phase
Current Level Adjustment	: Through on-board DIP Switches, 8 levels (Refer layout diagram on how to select the operating current)
Step Selection	: Through on-board DIP Switches, - Full, Half (Refer layout diagram on how to select the step)
Speed Setting	: Speed can be preset using on-board Speed setting potentiometer in Auto mode. On enable, motor will ramp to set speed and stay there. Optional external potentiometer control can be provided.
Operating Temperature	: 0 - 60°C
Storage Temperature	: 0 - 80°C



INSTRUCTION MANUAL
Bipolar Stepper Motor Driver
Model: ML-STEPR-23

Auto/ Manual Mode (A/M+, A/M-):

- **Auto Mode** - When Auto/ Manual input (A/M+, A/M-) is open or GND, the drive is in Auto Mode. The Drive runs on internal oscillator and speed can be set using the on board Potentiometer. On enabling the drive, Motor runs from Low RPM to maximum set RPM with soft start.
- **Manual Mode** - When Auto/Manual is connected to the supply (5V-12V DC), the driver is in Manual Mode. For the motor to run in this mode, External Clock is required. The Clock frequency determines the motor speed, depending on the step selection and Step angle of the motor. Minimum ON time should be 50 μ seconds.

*Note: In manual mode, when pulsing is removed, current will be flowing in the motor.
To avoid drive heating, disable the drive if drive is not in use.*

Enable (ENA+, ENA-):

- **Disabling** - When the Enable input (ENA+, ENA-) is open or GND, Drive is disabled and motor is de-energized.
- **Enabling** - When Motor is connected to 12V, then Drive is enabled which is indicated by the glow of Green LED.

Direction selection (DIR+, DIR-):

- **Forward** - When the Direction Selection input (DIR+, DIR-) is open or GND, Forward Direction is selected.
- **Reverse** - When Direction Selection input is connected to supply, Reverse Direction is selected.

External Clock (PULSE+, PULSE-):

If the drive is in Manual mode, then the speed is decided by the frequency of the external clock. For more details on clock setting refer the Auto/ Manual Mode section.

Current Selection

Levels of Motor Current can be selected as given in the table below. (NOTE the Direction of 4321)

2	3	4	1	Amps
B	C	D	A	
0	0	0	X	0
1	0	0	X	0.8
0	1	0	X	1.7
1	1	0	X	1.9
0	0	1	X	2.4
1	0	1	X	2.6
0	1	1	X	2.8
1	1	1	X	3.0

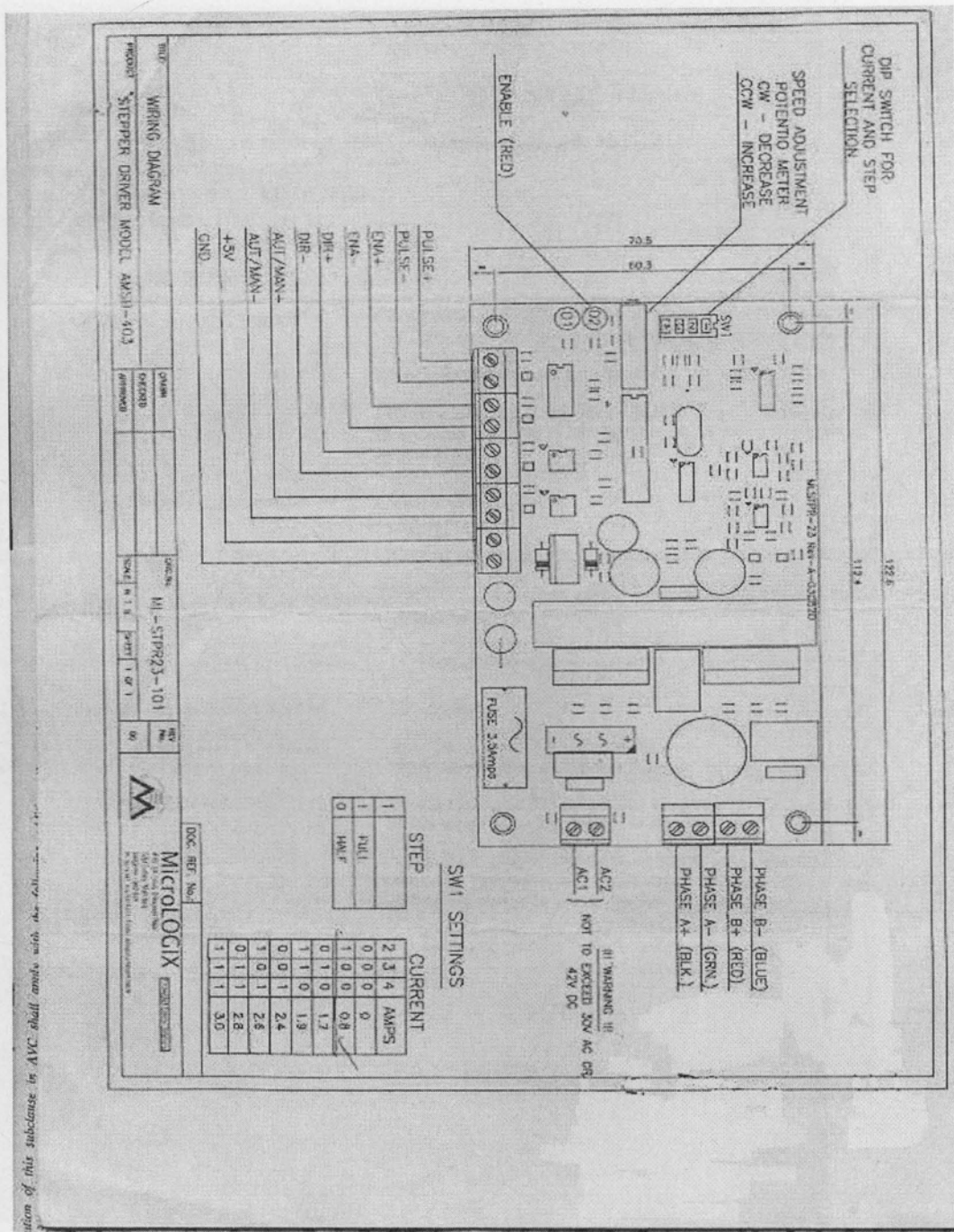
Step Selection:

2	3	4	1	
B	C	D	A	
X	X	X	1	FULL STEP
X	X	X	0	HALF STEP

Speed Setting Potentiometer: The motor speed can be set using 10K Multi-turn Potentiometer which is located close to the DIP switches. Refer the layout diagram for pot location

DC output (+5V): It is unprotected 5V/25mA DC output. It can also be looped back for external logic inputs.

*Note: Refer Layout diagram for electrical connections, DIPswitch selection and other details.
Direction, Pulse, Enable and Auto Manual are opto isolated inputs with differential GND.*



INDEX

A

absorption coefficient
31,110,146,221,224,228.

antenna

- bow tie
60,67,68,83,85,146,148,181,208,214
- dipole
52,54,55,56,60,78.
- gain
82,85
- microstrip
52,59,60,82
- monopole
52,54, 57, 58.
- ridged horn
51,52
- wave guide
59, 50,51,53

application

- industrial
4,5,6,7,8, 222.
- medical
5,6, 8,9,48, 49,222.
- Scientific
8, 222.

B

back scatter
14,15,17,54,175,178,179,180

band width
51,52,53,58,60,63,78,79,83,85,115,116

Bark rubber
214, 219, 220.

bone marrow, calf
214, 215, 225.

bound water
12,13,32,107,151,153,154,193,210,214,
215

breast

- benign
101,107,108,212

- malignant
9,12,13,16,92,101,107,108,122,151,156,17
8,191,192,207.
- normal
57,91,101,107,108,130,151,153,155,156,1
62,166,175,176,183,191-199,207.

breast cancer
12,13,15,53,90,96,107,126,151,157,175.

C

cancerous tissue
94,151,154,165,156,166,183,184,194-200

cavity perturbation
16,33,34,38,41,102,106,153,155,156,15
7,190,222

chicken thigh
17,216

complex permittivity
15,24,221

conductivity
14,16,24,31,37,40,64,68,93,98,99,100,101,
107,108,110,112,113,114,134,149,153,154,
175,181,183,193,209,224

confocal microwave technique
14, 16, 52, 59, 175, 176, 177, 178, 200,
203, 208, 209.

convergence
128,137,141,146,156,211

corn syrup
34,91,98,99,100-117,146,149,152,154,157 -
161, 181,183,191,192,209.

cost functional
142-144

coupling medium
145,146,148,149,153,155,158,180,181,190,
192 - 01, 209.

D

dielectric

- constant
13,16,31,32,37,49,50,57,60,64,82,
91,93-101, 105, 107, 111, 112, 116,
117,118,134, 146, 153-166, 178,
181, 183, 189, 190, 192, 193, 201,
209, 210, 211.

contrast
10, 13, 17, 81, 93, 122, 123, 124, 153,
154, 155, 156, 158, 175, 176, 184, 192,
198, 200, 203, 209, 210
loss
31, 32, 37, 94, 100, 105, 107, 117, 223.
dipole moment
23, 25, 26, 27, 28, 30, 32, 110, 111, 117.
dispersion
23, 33, 59, 176, 186, 223.
distorted Born iterative method
16, 123, 124, 128, 130, 137, 140, 212, 214.
domain
frequency
59, 68, 107, 178, 182.
time
76, 85, 116, 124, 127, 173, 178, 182,
183,
184, 185, 190-205, 209, 210.
driver circuit
17, 147, 148, 49, 182.

E

evanescent wave
76, 134, 142, 143.
experimental set up
17, 41, 78, 92, 99, 104, 115, 148, 153,
181.

F

FDTD
54, 55, 64, 65, 66, 68, 69, 72, 74, 75, 76, 77,
82, 83, 85, 124, 176, 177, 178, 180, 185, 186,
189, 190, 199, 202, 203, 206, 210.
flare angle
55, 78, 79.
forward solution
125.

G

Gaussian

54, 56, 68, 69, 70, 74, 76, 77, 185, 189, 190.
glycerine
34, 91, 97, 98, 99, 100, 101, 102, 116.
Green's function
128, 132, 133, 137, 138, 139, 143, 145.

I

image
plane
60, 63, 79, 8.
reconstruction
11, 14, 92, 97, 123, 124, 126, 129, 137,
146, 208.
imaging
magnetic resonance
11.
microwave
12, 13, 14, 15, 16, 32, 33, 41, 48, 50,
58, 81, 85, 90, 91, 93, 110, 113, 115,
123, 124-130, 157, 209, 221.
medical
48, 56, 91, 98, 130, 224.
optical
11.
ultra sound
11.
x-ray
10, 11, 12, 13, 14, 122, 123, 207, 210.
inverse problem
129, 134.
inverse scattering
15, 123, 127, 128, 130, 134, 135, 136, 137,
139, 140, 149, 157, 211, 212.
iteration
60, 78, 125, 127, 128, 137, 140, 141, 146,
156, 168, 211

M

mammography
17, 85, 87, 204, 207, 209.
mastectomy
148.
measurement
configuration
133, 134, 145, 146, 147, 180, 216.
setup

144, 178, 179.
 Microwave band
 3, 4, 15, 25.
 Microwave - noninvasive
 9, 11, 12, 13, 207, 208
 microwave imaging
 active
 7, 13, 14, 15, 48.
 hybrid
 13, 14.
 passive
 13.
 multiple scattering
 11, 15, 123, 134, 135, 136, 143.

O

object function
 131, 134, 139, 142.
 optimization technique
 143, 144.

P

permeability
 67, 71, 138, 186.
 permittivity
 24, 27, 29, 31, 32, 33.
 polarization
 16, 24, 25, 26, 27, 28, 29, 30, 33, 81, 105,
 131, 132, 180, 223, 224.
 Polianiline
 64, 79, 80
 poly vinyl acetate
 146, 221.
 powder
 carbon black powder
 17, 96, 146, 221, 222, 223, 224, 225,
 226, 227, 228.
 graphite powder
 17, 95, 146, 221, 222, 223, 224, 225,
 226, 227, 228.
 propagation loss
 91, 100, 107, 113, 114, 158, 209.
 propagation velocity
 11.

R

radiation pattern
 53, 58, 79, 80, 81, 82, 130, 208.
 Reflection characteristics
 116.
 reflection - edge
 59, 64, 79, 210.
 relaxation time
 30-33, 110, 111, 117, 186,
 resolution
 58, 67, 76, 90, 91, 93, 117, 128, 146, 158,
 176, 180, 208, 211.
 resonant frequency
 11, 34, 35, 39, 56, 59, 60, 78, 79, 82, 83, 85,
 99, 100, 104, 115, 116, 153, 208, 224
 return loss
 78, 79, 80, 82, 83, 85, 115, 116.

S

Scattering
 117, 123, 124, 125, 127, 130, 134, 135,
 136, 137, 140, 145, 157, 185, 186, 211,
 212, 213.

T

Tikhonov regularization
 144, 146, 213.
 tomography
 microwave
 93, 130, 134.
 X - ray
 10.
 tumor, breast
 54, 55, 56, 92, 107, 108, 149, 159, 160,
 176, 183, 190, 191, 212.

V

video pulse radar
 175.

List of Publications

International Journals

1. **G.Bindu**, Anil Lonappan, C.K. Aanandan, K.T Mathew, "Dielectric studies of corn syrup for application microwave breast imaging" Progress in Electromagnetics Research, PIER 59, pp.175- 186, 2006.
2. **G.Bindu**, Anil Lonappan, C.K. Aanandan, K.T Mathew, "Dielectric studies of polyvinyl acetate based phantom for application in medical imaging", Journal of Material Science, Springer, Netherlands, 20th Sept.2006, pp. 1573 – 1578.
3. **G.Bindu**, Santhosh John Abraham, C.K. Aanandan, K.T Mathew, "Two-Dimensional microwave tomographic imaging of breast tissues", International Journal of Cancer Research 2 (1), pp. 57 -68, 2006.
4. **G.Bindu**, Santhosh John Abraham, C.K. Aanandan, K.T Mathew, "Detection of dielectric contrast of breast tissues using confocal microwave technique", Microwave and Optical Technology Letters, vol. 48, no. 6, June 2006.
5. **G.Bindu**, Santhosh John Abraham, C.K. Aanandan, K.T Mathew, "Active microwave imaging for breast cancer detection", Progress in Electromagnetics Research, PIER 58, pp. 149 – 169, 2006.
6. **G.Bindu**, Vinu Thomas, C.K. Aanandan, K.T Mathew, "Microwave studies of poly vinyl acetate based phantom for application in medical imaging", Microwave and Optical Technology Letters, vol. 48, no. 1, pp. 180 – 183, January 20th 2006
7. **G.Bindu**, Santhosh John Abraham, C.K. Aanandan, K.T Mathew " Effects of reduced contrast coupling medium in microwave breast imaging", Microwave and Optical Technology Letters, vol. 47, no.6, pp. 443 – 446, December 5th 2005
8. **G.Bindu**, Santhosh John Abraham, C.K. Aanandan, K.T Mathew "A pulsed confocal microwave technique for the detection of dielectric contrast of breast tissues", Microwave and Optical Technology Letters, vol. 47, no.3, pp. 209–212, November 5th 2005.
9. **G.Bindu**, Vinu Thomas, Anil Lonappan, C.K. Aanandan, K.T Mathew " Two Dimensional microwave tomographic imaging of low water content tissues" , Microwave and Optical Technology Letters Vol. 46, No.6, pp. 599 – 601, September 20th 2005.

10. **G.Bindu**, Anil Lonappan, Vinu Thomas, C.K. Aanandan, K.T Mathew "Microwave characterization of breast phantom materials" , Microwave and Optical Technology Letters ,Vol. 43, No.6, pp 506-508, December 20th 2004
11. **G.Bindu** , Vinu Thomas, C.K. Aanandan, K.T Mathew "Wide band bowtie antenna with coplanar stripline feed" , Microwave and Optical Technology Letters, Vol. 42, No. 3, pp 222-224, August 5th 2004
12. Vinu Thomas, **G. Bindu**, V. Hamsakutty, K. T. Mathew "A novel technique for localizing the scatterer in inverse profiling of two dimensional circularly symmetric dielectric scatterers using degree of symmetry and neural networks" Journal of Electromagnetic Waves and Applications, vol. 19, no.15, Dec.2005, pp. 2113- 2121.
13. V Hamsakutty, **G.Bindu**, Vinu Thomas, K.T Mathew "A multi-frequency coaxial fed metal coated dielectric resonator antenna," , Microwave and Optical Technology Letters, vol. 47, No.6, pp. 573-575, December 20th 2005
14. Vinu Thomas, **G. Bindu**, Anil Lonappan, K. T. Mathew "A novel technique for reducing the imaging domain in microwave imaging of two dimensional circularly symmetric scatterers" , Microwave and Optical Technology Letters Vol. 44, No. 5, pp 423-427, March 5th 2005
15. Anil Lonappan, **G. Bindu**, Vinu Thomas, K. T. Mathew "Analysis of human semen using microwaves", Progress in Electromagnetics Research, PIER 57, pp. 277 – 284, 2006.
16. Vinu Thomas, **G.Bindu**, Anil Lonappan, K.T Mathew " Microwave imaging of two-dimensional dielectric cylinders with a multiscaled frequency hopping approach", Microwave and Optical Technology Letters Vol. 43, No. 4, pp 353-355, November 20th 2004
17. Anil Lonappan, **G.Bindu**, Vinu Thomas, K.T Mathew " Dielectric properties of human urine at microwave frequencies" , Microwave and Optical Technology Letters, Vol. 42, No.6, pp 500-503, September 20th 2004
18. V.Hamsakutty, Anil Lonappan, **G.Bindu**, Vinu Thomas, K.T Mathew " A novel coupling medium for microwave medical imaging", IEE Electronic Letters, Vol. 39, No. 21, pp 1498-1499, October 16th 2003
19. Anil Lonappan, **G. Bindu**, Vinu Thomas, K. T. Mathew "Dielectric properties of human cerebro spinal fluid at microwave frequencies", Journal of Electromagnetic Waves and Applications, vol. 20, no.6, pp. 773 -779, 2006.

20. Anil Lonappan, **G.Bindu**, Vinu Thomas, K.T Mathew, "Analysis of human breast milk at microwave frequencies", Progress in Electromagnetics Research, PIER 60, pp. 179 - 185, 2006.
21. V Hamsakutty, Praveen Kumar, **G.Bindu**, Jaimon Yohannan, K.T Mathew, "Coaxial fed dielectric resonator antenna for multi frequency operation", Microwave and Optical Technology Letters, vol.8, no.5, pp. 878 - 880, May 2006.
22. Vinu Thomas, Jaimon Yohannan, **G.Bindu**, Anil Lonappan, K.T Mathew, "Localization of the investigation domain in inverse profiling of buried 2-D dielectric pipelines with circular cross section using electromagnetic scattering data" Progress in Electromagnetics Research, PIER 61, pp.11 - 131, 2006.

Symposia

1. **G. Bindu**, K. T. Mathew, "Two-dimensional microwave tomographic imaging of breast tissues", IEEE AP-S International Symposium and USNC / URSI National Radio Science meeting, APS/URSI 2006, July 9 -11, 2006, Albuquerque, USA
2. **G.Bindu**, C.K.Aanandan, K.T.Mathew, "Detection of dielectric contrast of breast tissues using confocal microwave technique", Asia Pacific Microwave Conference, APMC, Yakohama, Japan, Dec. 12-15, 2006.
3. **G. Bindu**, C. K. Aanandan, K. T. Mathew, "Characterization of Female Human Breast Tissues at ISM Band", Progress in Electromagnetics Research Symposium PIERS, 26th - 30th March 2007, Beijing, China
4. T.K.Padmashri, **G.Bindu**, "Localization of the Object Domain in Microwave Medical Imaging Using Probabilistic Neural Network", Progress in Electromagnetics Research Symposium PIERS, 26th - 30th March 2007, Beijing, China
5. Jaimon Yohannan, V. Hamsakutty, **G. Bindu**, K.T. Mathew, "A rectangular dielectric resonator band stop filter", IEEE AP-S International Symposium and USNC / URSI National Radio Science meeting, APS/URSI 2006, July 9 -11, 2006, Albuquerque, USA
6. **G. Bindu**, Anil Lonappan, Vinu Thomas, C. K. Aanandan, K. T. Mathew, "Microwave studies of poly vinyl acetate based phantom for application in medical imaging" 12th European Conference of Composite Materials, Aug. 28th - 3rd Sept. 2006, Biarritz, France.

7. **G. Bindu**, K. T. Mathew, "Analysis of Female Human Breast Tissues at Microwave Frequencies", 40th annual Microwave Symposium, International Microwave Power Institute, August 9- 11, 2006, Boston, USA.
8. **G. Bindu**, C. K. Aanandan, K. T. Mathew, "Microwave characterization of female human breast tissues" European Conference on Wireless Technology, September 10 -12, 2006, Manchester, UK.
9. **G. Bindu**, Anil Lonappan, Vinu Thomas, C. K. Aanandan, K. T. Mathew, "A pulsed confocal technique for breast cancer detection" Asia Pacific Microwave Conference Proceedings, APMC, China, vol. 5, pp. 1 – 4, 04 -07, Dec. 2005
10. **G. Bindu**, Anil Lonappan, C. K. Aanandan, K. T. Mathew "Coplanar stripline fed wide band bowtie antenna for ground penetrating radar" XXVIIIth General Assembly of International Union of Radio Science, URSI 2005, October 23-29, 2005, New Delhi, India.
11. V. Praveen Kumar, **G. Bindu**, Anil Lonappan, K. T. Mathew, "Microstripline fed circular sector dielectric resonator antenna", IEEE AP-S International Symposium and USNC / URSI National Radio Science meeting Proceedings, APS/URSI 2005, July 3-8, 2005, Washington DC, USA, vol. 2A, 3-8 July 2005, pp :192 – 195.
12. V Hamsakutty, **G. Bindu**, Vinu Thomas, K.T Mathew " Biomedical applications of sodium meta silicate gel as coupling medium for microwave medical imaging", 2004 IEEE AP-S International Symposium and USNC/URSI National Radio Science Meeting, APS/URSI 2004 Proceedings, June 20-26, 2004, Monterey, California, USA, vol. 3, 20-25 June 2004 pp.2448 – 2451.
13. **G. Bindu**, Anil Lonappan, C. K. Aanandan, K. T. Mathew, "Wideband bowtie antenna for confocal microwave imaging" Asia Pacific Microwave Conference, APMC 2004, December 15-18, 2004, Department of Electronic Science, University of Delhi South Campus, New Delhi, India
14. **G. Bindu**, Vinu Thomas, K.T.Mathew, "Microwave Tomography – a novel 2 –D imaging technique for medical applications", 16th Kerala Science Congress, Kerala, India, January 2004.
15. **G. Bindu**, Vinu Thomas, C. K. Aanandan, K. T. Mathew "Microwave imaging of dielectric wax cylinders" 9th National Symposium on Antennas and Propagation, APSYM 2004, December 21-23, 2004, Department of Electronics, Cochin University of Science & Technology, Cochin, Kerala, India
16. Anil Lonappan, **G. Bindu**, Vinu Thomas, K. T. Mathew "Dielectric properties of human semen at microwave frequencies" 6th Conference on Electromagnetic Wave Interactions with Water and Moist Substances, ISEMA 2005, May 29- June 1, 2005, Weimar, Germany

17. Vinu Thomas, **G. Bindu**, Anil Lonappan, K. T. Mathew "A novel technique for localizing the scatterer in inverse profiling of two dimensional circularly symmetric dielectric scatterers using degree of symmetry and neural networks" Electromagnetics Research Symposium, PIERS 2005, August 22-26, 2005, Hangzhou, China
18. Jaimon Yohannan, **G.Bindu**, Vinu Thomas, Anil Lonappan, K. T. Mathew "Half-Split cylindrical dielectric resonator antenna" 5th Conference on Ferroelectrics, Ferroelectrics UK 2005, April 26- 27, 2005, University of Paisley, Scotland, UK
19. Vinu Thomas, **G. Bindu**, K.T.Mathew, " Microwave tomographic imaging of 2-D dielectric wax cylinders", Proc.of 1st International Conference of Microwave Antennas and Radio Science, ICMARS 2003, Dec. 2003, Jodhpur, India.

Resume

Senior Research Fellow

Department of Electronics,

Cochin University of Science and Technology,

Kochi – 682 022

E mail # bindhu_g@cusat.ac.in

Objective:

To involve in research activities in the field of microwave medical imaging, microwave antennas and microwave material characterization.

Educational Qualifications:

Degree	University	Year	Subject	% Marks
B.E	Madurai Kamaraj University	1989	Electronics & Commn.	73.7
M.Tech	Kerala University	1991	Electronics & Commn. (Microwave Commn)	73.3

Academic Honours:

Awarded Senior Research Fellowship by the Council of Scientific and Industrial Research, Govt. of India for pursuing Ph.D.

Details of Employment: 14 years of teaching experience from August 1991 – till date, with the Dept. of Electronics, Manipal Institute of Technology, Manipal, Karnataka. Presently holding the designation of Assistant Professor.

